ABSTRACT

Title of Dissertation: Advanced Quantum Magnetic Microscopy with Solid-state Spin Ensemble in Diamond

Zechuan Yin
Doctor of Philosophy, 2026

Dissertation Directed by: Professor Ronald L. Walsworth
Department of Electrical and Computer Engineering

Solid-state electronic spin systems offer powerful platforms for sensitive magnetic-field detection. A prominent example is the negatively charged nitrogen-vacancy (NV^-) center in diamond, which provides long spin-coherence times, direct optical readout, and robust operation under ambient conditions. These properties have enabled NV centers to serve as high-performance magnetometers across diverse application areas. The development of the quantum diamond microscope (QDM) has further expanded these capabilities, introducing a wide-field imaging modality that delivers high-spatial-resolution magnetic images enabled by the minimal stand-off distance between the diamond sensor and the sample.

Over the past decade, QDM technology has matured significantly, demonstrating broad utility in bioscience, electronic diagnostics, geology, and condensed-matter physics, and is now transitioning from laboratory instruments to commercial products. However, two major challenges remain. First, most QDM-based magnetic microscopy still relies on optically detected magnetic resonance (ODMR), which constrains both sensitivity and sensing bandwidth. Second, the use of CCD cameras in typical

QDM implementations limits temporal resolution and restricts access to advanced pulsed-sensing techniques.

This work advances a next-generation QDM for quantum magnetic microscopy. On the hardware side, we design and construct a QDM platform incorporating a high-speed lock-in camera operating at kiloframes per second and an arbitrary waveform generator (AWG) for executing advanced quantum sensing protocols. These improvements enable the application of established pulsed sensing techniques, previously not demonstrated in a wide-field imaging format, to QDM. We demonstrate static and broadband magnetic imaging using Ramsey sequences, narrowband signal imaging with dynamical decoupling protocols, and nuclear magnetic resonance (NMR) imaging using the coherently averaged synchronized readout (CASR) technique. Finally, we benchmark the system's sensitivity and spatial resolution, demonstrating substantial improvements enabled by the advanced hardware and pulsed-sensing capabilities. With the enhanced sensitivity and temporal resolution, this work expands the range of signals and phenomena that QDM can image, paving the way for broader scientific and technological applications.

ADVANCED QUANTUM MAGNETIC MICROSCOPY WITH SOLID-STATE SPIN ENSEMBLE IN DIAMOND

by

Zechuan Yin

Dissertation submitted to the Faculty of the Graduate School of the
University of Maryland, College Park in partial fulfillment
of the requirements for the degree of
Doctor of Philosophy
2026

Advisory Committee:
Professor Ronald Walsworth, Chair/Advisor
Professor John Cumings, Dean's Representative
Professor Edo Waks
Professor Saikat Guha
Professor Yanne Chembo

© Copyright by
Zechuan Yin
2026

Acknowledgments

I owe my deepest gratitude to all the people who have made this thesis possible, and because of whom my graduate experience has been one I will cherish forever.

First and foremost, I would like to thank my advisor, Professor Ronald L. Walsworth, for giving me the invaluable opportunity to work on challenging and exciting projects over the past five years. I still remember the night Ron and members of the former Walsworth group at Harvard interviewed me. I said, "It's my dream to work with you." As Ron often reminds us, a Ph.D. is a marathon. Instead of pushing from behind, he leads from the front: encouraging us, supporting us, and providing the most comfortable and empowering environment to grow. Ron always ensured we had the best resources for conducting experiments, including financial support, an excellent lab environment, and top-tier instruments. Despite his extremely busy schedule, he was always available to guide our research direction. And he helped us to polish the paper so detail, I always very appreciate when I see hundreds of red circles on my manuscript. I am grateful and fortunate to be Ron's student. He made my Ph.D. journey both satisfying and joyful.

My colleagues in the Walsworth group have been the best teammates I could ask for. I owe special thanks to Jner Tzern Oon, my first mentor in the group. When I joined during the COVID pandemic, I worked remotely for a whole year, a tough time for a rookie with no hands-on experience, limited English, and a 12-hour time difference. Yet JJ patiently guided me, helped me find simulation projects I could contribute to, and taught me the fundamentals of NV physics. After I arrived in the U.S., he taught me essential experimental skills as we built the Keysight AWG setup together. I am also grateful to Xiechen Zheng, who helped me adapt to life in a new country and navigate graduate school. In the lab, I learned so much while working with Jiashen Tang, Connor Hart, Matthew Turner, John Blanchard, and Stephen DeVience, who shaped my understanding of scientific research. As I

grew more experienced, I had the opportunity to mentor junior group members, an experience that enriched me as much as it helped them. Saipriya Satyajit has a stronger theoretical foundation than I do, guiding Sai in experiments taught me the value of his thoughtful and careful approach. Smriti Bhalerao joined the group with a biology background, but through her dedication she quickly learned quantum fundamentals and optical experimental techniques, eventually growing into a leader in our quantum biosensing project. Justin Welter learns new things fast and has a great engineering intuition, his chip designs have helped many group members. Camille McDonnell is patient and hardworking, the project we worked on together was the most challenging of my Ph.D. Although we struggled to obtain signals early on, she never lost her positivity and pursued every detail with dedication. I could not have completed that project without her. I am truly proud to see all of them grow. I also appreciate everyone in the Walsworth group who, even if not working with me directly, created such a warm atmosphere and supportive environment. I am profoundly grateful for this research community.

I would also like to thank my friends for their help and companionship. My housemates—Zhiyin Tu, Haowei Deng, Chenghao Deng, Jiashen Tang, Ding Hua and Haoyi You have been like family, creating a comfortable home and a wonderful life outside the lab. My gym buddies—Hanbing Liu, Geyang Wang, Ziteng Wen, Gengzhi Yang, Ruochen Yang, and Junshan Liu guided me in training and helped me build a strong and healthy body.

Finally, I thank my family—my parents Wei Yin and Yuhong Li, my sister Zeyue Yin, and my girlfriend Lin Zhu for their unwavering love and support. Although an ocean has separated us for the entire five years of my Ph.D., they have supported me emotionally and financially through every difficulty. Especially Lin, my greatest half. Time has never passed faster than during our daily video calls. Thank you for accompanying me every day, comforting me when I'm sad, encouraging me when I'm disappointed, entertaining me when I'm tired, and kissing me when I'm lonely. I cannot imagine

this journey without you, and I look forward to many more years together.

Table of Contents

Acknowledgements ii

Table of Contents v

List of Tables viii

List of Figures ix

Abbreviations xxv

Chapter 1: Introduction 1
- 1.1 Nitrogen-Vacancy Centers in Diamond . . . 1
- 1.2 NV-diamond for Quantum Sensing . . . 6
  - 1.2.1 Static and Broadband Magnetic Sensing Protocols . . . 7
  - 1.2.2 AC and Narrowband Magnetic Sensing Protocols . . . 10
- 1.3 Quantum Diamond Microscope . . . 12
  - 1.3.1 Basic Components and Design Consideration of QDM . . . 13
  - 1.3.2 Established QDM Applications and Limitations . . . 17
- 1.4 Organization of this Dissertation . . . 19

Chapter 2: Ramsey-based Static Magnetic Microscopy 22
- 2.1 Protocols and Techniques for Ramsey Magnetometry with QDM . . . 22
  - 2.1.1 Sensitivity of Ramsey Magnetometry with NV Ensembles . . . 22
  - 2.1.2 Implementation of the Spin-bath Driving Technique . . . 24
  - 2.1.3 Implementation of the DQ4R Protocol Using a Lock-In Camera . . . 27
- 2.2 Electromagnetic Design and Simulation of QDM Components . . . 30
  - 2.2.1 Design and Simulation of the Coplanar Microwave Waveguide . . . 30
  - 2.2.2 Simulation of the Magnetic Field Generated by the Circuit Phantom . . . 33
- 2.3 Experimental Details and Results . . . 37
  - 2.3.1 Static Magnetic Field Imaging and Comparison with Simulation . . . 40
  - 2.3.2 Dynamic Magnetic Field Imaging . . . 41
  - 2.3.3 Spin Dephasing Time and Sensitivity . . . 43
  - 2.3.4 Spatial Resolution and Spatial Noise . . . 46

Chapter 3: Dynamical-Decoupling-Based AC Magnetic Microscopy 49
- 3.1 Protocols and Techniques for AC Magnetometry with QDM . . . 50
  - 3.1.1 Dynamical Decoupling Sequences for AC Sensing . . . 50
  - 3.1.2 Coherent Averaged Synchronized Readout (CASR) . . . 52
  - 3.1.3 Implementation of XY8 AC Magnetometry with a Lock-In Camera . . . 56
- 3.2 Experimental Details and Calibrations . . . 59
  - 3.2.1 Experimental Setup and Device Fabrication . . . 59
  - 3.2.2 Calibration of AC Magnetometry . . . 62

3.3 Experimental Results . . . 64
3.3.1 In-Phase RF Magnetic Imaging . . . 64
3.3.2 Simultaneous Amplitude and Phase Imaging . . . 66
3.4 Performance of the RF-QDM . . . 73
3.4.1 Spatial Resolution and Frequency Range . . . 73
3.4.2 AC Magnetic Sensitivity Optimization . . . 76
3.4.3 Noise Source Analysis . . . 79
3.4.4 Spatial Noise and Spatial Resolution . . . 80
3.5 Potential Applications of the RF-QDM . . . 82

Chapter 4: High-Resolution and Wide-Frequency-Range Magnetic Spectroscopy 87
4.1 QFM-CASR Spectroscopy Protocol . . . 89
4.1.1 Rotating Frame Hamiltonian Approximation in the Floquet Picture . . . 89
4.1.2 QFM-CASR Experimental Design and Signal Processing . . . 94
4.2 Sensitivity Assessment Across a Wide Signal Frequency Range . . . 97
4.2.1 AC bias-field calibration and target-signal amplitude control . . . 99
4.2.2 Example sensitivity calibration and polarization considerations . . . 100
4.3 Demonstration and Performance of QFM-CASR Spectroscopy . . . 101
4.3.1 Detection of Multi-frequency RF Signals with Hz-scale Spectral Resolution . . . 101
4.3.2 Precise Phase Measurement of RF Signals . . . 104
4.3.3 Demonstration of Sub-Hz Spectral Resolution . . . 107
4.4 Effective Signal Validation with Rabi and DEER-Rabi . . . 108
4.5 Performance Comparison, Optimization, and Applications of QFM-CASR . . . 113
4.5.1 Comparison of NV-Diamond AC Sensing Techniques . . . 113
4.5.2 QFM-CASR Performance Limitations, Trade-Offs, and Optimization . . . 115
4.5.3 QFM-CASR Applications and Outlook . . . 116

Chapter 5: Real-Space Nuclear Magnetic Resonance Microscopy 118
5.1 Detection of NMR Signals with NV Centers in Diamond . . . 119
5.1.1 Development of NV-NMR . . . 119
5.1.2 Challenges Toward NMR Imaging . . . 121
5.1.3 Overhauser Dynamic Nuclear Polarization . . . 123
5.2 Experimental Setup for QDM-NMR . . . 126
5.2.1 Integrated Inductive NMR and NV-NMR . . . 127
5.2.2 Nuclear CPMG Sequence with Lock-in Camera Demodulation . . . 130
5.3 QDM-NMR Experimental Results . . . 132
5.3.1 Inductive NMR Measurement for Pulse Optimization . . . 132
5.3.2 Simultaneous NV and Inductive Nuclear CPMG Measurements . . . 135
5.3.3 Proof-of-Principle CPMG-Shaped Signal Imaging . . . 141
5.4 Next Steps for QDM-NMR Applications . . . 146
5.4.1 Potential QDM-NMR Applications in Hydrogels . . . 148
5.4.2 Potential QDM-NMR Applications in Bio-systems . . . 149

Chapter 6: Quantum Magnetic Microscopy for Industrial Applications 157
6.1 Development of Compact NV-diamond Magnetic Sensors . . . 157

6.1.1 Industrial Requirements and Low-SWaP Constraints . . . 157
6.1.2 Comparison with Alternative Magnetometer Technologies . . . 158
6.1.3 Examples of Low-SWaP NV Magnetometers . . . 159
6.1.4 Design Considerations for Industrial QDM Systems . . . 161
6.2 Development of a Compact Quantum Magnetic Camera . . . 162
6.2.1 Components of the camera . . . 162
6.2.2 Design and Simulation of the Illumination Module . . . 165
6.2.3 Design and Simulation of the Imaging Module . . . 166

Chapter 7: Outlook and Future Experiments 170
7.1 Ramsey DC Sensing Improvement via Decoupling of NV–NV Interactions . . . 170
7.1.1 Spin-Bath Driving of Off-Axis NV Centers . . . 171
7.1.2 Magic-Angle Spinning for NV-diamond System . . . 178
7.2 Potential Improvements in AC Magnetic Sensing . . . 182
7.2.1 Double-Quantum Dynamical Decoupling Sequences . . . 183
7.2.2 Vector AC Magnetometry . . . 185
7.3 Future Directions in QDM-NMR Experiments . . . 188
7.3.1 Diffusion NMR Imaging . . . 188
7.3.2 Nutation-Based Longitudinal Sensing for High-Field NMR Imaging . . . 190

Appendix A: Lock-in Camera Demodulated CASR 193
A.1 Double-alias Process . . . 193
A.2 Optimization of the Modulated-CASR Performance . . . 197
A.3 Numerical Simulation Results . . . 199

Appendix B: Bias Magnetic Field Alignment 201
B.1 Determination of NV Orientation . . . 201
B.2 Alignment and Optimization of the Bias Field . . . 204

Appendix C: MW CPW and Phantom Fabrication 206
C.1 Phantom Layer Fabrication . . . 206
C.2 Ω Loop Layer Fabrication . . . 208
C.3 Post-Fabrication Process . . . 209

List of Tables

6.1 Comparison of magnetometer technologies. 158

List of Figures

1.1 (a) Model of the carbon diamond lattice featuring a substitutional nitrogen adjacent to a vacancy, forming an NV center. The NV symmetry axis is aligned with the crystallographic axis. (b) Energy level diagram for the negatively charged NV center (NV^-). The ground state $^3A_2$ spin triplet has a zero-field splitting (ZFS) of approximately 2.87 GHz between the $m_s = 0$ ($|0\rangle$) and $m_s = \pm 1$ ($|\pm 1\rangle$) states. Under optical illumination (532 nm, green arrows), NV^- is excited to the first excited state ^3E, from which it radiatively decays back to the ground state, emitting fluorescence in the 638–800 nm range (red arrows) through a mostly spin-conserving process. NV^- in $m_s = \pm 1$ can also decay to the $^3A_2$ state via an alternative, spin-selective ISC pathway (dashed gray arrows), passing through the $^1A_1$ and ^1E states, which does not produce visible fluorescence. Expanded view: $^3A_2$ sublevels, where the $|0\rangle$ state is split from the $|\pm 1\rangle$ states by the ZFS D. The $|\pm 1\rangle$ sublevels further exhibit a Zeeman splitting proportional to the component of the applied magnetic field B along the NV axis. . . . 2

1.2 NV magnetometry protocols [18]. Schematic of timing and duration of laser pulses, MW pulses, and readout sequences relative to the field being sensed for common NV-diamond protocols. Swept parameters are indicated by arrows. Straight lines for the bias and sample fields indicate static magnetic fields, including the swept static bias field for Rabi and T_1 relaxometry. Sinusoidal curves represent time-dependent sample fields, which are very high frequency for Rabi and T_1 relaxometry. 8

1.3 Quantum Diamond Microscope (QDM) [18]. Examples of QDM setups using (a) permanent magnets and (b) Helmholtz coils to apply a bias magnetic field. In both configurations, a 532-nm excitation laser illuminates the diamond chip, and optics collect NV fluorescence onto a camera. An interference filter is used to transmit NV fluorescence while blocking scattered excitation light. A planar gold omega-loop, fabricated onto a substrate, is shown delivering microwaves to the diamond chip for NV control. 14

1.4 QDM applications. (a) Parabolic hydrodynamic current density flow profile in graphene at the Dirac point [33]. (b) Magnetic field image of magnetite intrinsic to MTB bacteria [34]. (c) Remnant magnetization of a geological sample [35]. (d) Spatially-resolved NMR detection of ^{19}F nuclear spins on the diamond surface [36]. 17

2.1 (a) NV double electron-electron resonance (DEER) technique for measuring the $^{15}N_s^0$ and free-electron spin resonance spectrum in the QDM diamond sensor. The total free evolution intervals between the initial and final single-quantum (SQ) $\pi/2$ pulse on the NV spins is chosen to match the ensemble NV spin-echo T_2 for optimal sensitivity to bath-spin resonances. The frequency of the SQ π pulse on the bath spins is swept to measure the NV DEER spectrum by the effect on the NV ensemble fluorescence contrast (see Ref. [20] for details). (b) Energy level diagram of the coupled electron-nuclear spin system in $^{15}N_s^0$. (c) Simulated $^{15}N_s^0$ and free-electron ($g = 2$) spin resonance spectrum (red) overlaid with NV DEER measurement results (blue) and offset vertically for clarity. The simulated resonant frequencies are broadened by a Lorentzian function with linewidth and relative contrast chosen to approximate the measurement data. 26

2.2 (a) Sequence for magnetic imaging using the DQ 4-Ramsey protocol for NV interrogation together with spin-bath driving. The camera internal exposures alternate between the I and Q channel; on-chip circuitry accumulates differential results between two successive measurements in both channels. For example, the output in the I channel using the sequence in (a) will be $S_{I1}-S_{I2}+S_{I3}-S_{I4}$. (b) Left: Dual-tone MW resonant with $|m_s = 0\rangle \leftrightarrow |m_s = +1\rangle$ and $|m_s = 0\rangle \leftrightarrow |m_s = -1\rangle$ NV spin transitions is used to implement DQ pulses. Middle: Phase alternations of individual MW tones in a DQ 4-Ramsey sequence. The $\pm$X directions are defined in the effective Bloch sphere formed by the two NV spin levels $|m_s = 0\rangle$ and $|m_s = +1\rangle$ (or $|m_s = -1\rangle$). The duration of the DQ pulse is the time to change the NV spin state from $|m_s = 0\rangle$ to a superposition state with equal population between $|m_s = +1\rangle$ and $|m_s = -1\rangle$. Right: The permutation of MW-phase alternation in the Q channel results in NV fluorescence dynamics of opposite phase to that of the I channel. Differential results between these two measurements are output to an external frame. 28

2.3 Design and simulation of the CPW Ω-loop antenna. The inner diameter of the Ω-shaped structure is $800\,\mu$m. The trace width at the connector boundary is designed to be $0.9\,$mm to match the geometry of the U.FL connector, while the trace width of the antenna loop is $132\,\mu$m. The gaps between the center trace and the ground planes are optimized to achieve a $50\,\Omega$ impedance match for both regions, thereby minimizing MW reflections. Bottom left: Rabi-homogeneity simulation using Ansys HFSS. The HFSS output is a time-dependent MW magnetic field propagation; here we show a snapshot at zero phase with an input power of 44 dBm at 2.87 GHz. Bottom right: Rabi-field simulation performed using COMSOL Multiphysics, showing the spatial distribution of the magnetic flux density. Both simulations demonstrate a homogeneous Rabi driving region with a diameter of approximately $500\,\mu$m. 31

2.4 Design and simulation of the terrapin-shaped circuit phantom. (a) Geometry construction of the phantom and boundary conditions in COMSOL. (b), (c), and (d) Snapshots of the magnetic-field intensity projected onto one NV axis at stand-off distances of 1, 5, and $10\,\mu$m from the phantom. 34

2.5 Simulated phantom static magnetic-field patterns (bottom four panels) projected along the four NV axes in the diamond crystal (shown schematically in the top panel). In this study, the QDM is configured to image the magnetic field projected along the [111] axis. Simulations include NV-layer averaging over 10 μm depth and pixel binning. The NV–phantom stand-off distance is 5 μm. 36
2.6 Imaging phantom magnetic fields using a QDM. A 532 nm laser excites NV centers in a 10 μm-thick layer of a diamond chip. A gold Ω-loop delivers microwaves for NV spin control, and NV fluorescence is collected onto a photodiode or high-speed camera (not shown). A bias magnetic field is applied along one NV axis, and an RF coil drives bath spins to extend T_2^*. A driven current in the terrapin-shaped palladium phantom generates the magnetic-field pattern to be imaged. (Zoom-in) Simulated (left) and measured (right) static magnetic-field patterns acquired with the Ramsey-based QDM. The measurement uses a 25 mV excitation (436 nA) and ∼200 s averaging. SNR is computed using the peak-to-peak signal (solid box) and spatial noise in a source-free region (dashed box). Simulations include NV-layer averaging over 10 μm depth and pixel binning ($1.9 \times 1.9\,\mu\mathrm{m}^2$). The NV–phantom stand-off distance is extracted to be 5 μm. 39
2.7 Time-resolved imaging of dynamic magnetic fields using the Ramsey-based QDM and a differential measurement protocol. A voltage trace mimicking a broadband cardiac-like signal is applied to the phantom. Magnetic images are acquired with a temporal resolution of ∼2 ms and 3×3 pixel binning, and the experiment is repeated 400 times for signal averaging. (a) Temporal evolution of the peak magnetic-field amplitude extracted from the images, overlaid with the applied voltage trace scaled by 274.26 nT/V. The agreement demonstrates faithful waveform reconstruction. (b) Representative magnetic-field images at selected time points indicated in (a). The spatial magnetic noise at time point (vi) is ∼3 nT. 42
2.8 (a) QDM maps of the NV ensemble spin dephasing time T_2^* obtained from single-quantum (SQ) and double-quantum (DQ) Ramsey measurements. The SQ T_2^* is limited by heterogeneous strain in the diamond sample. Field of view: $270 \times 270\,\mu\mathrm{m}^2$. Scale bar: 50 μm. (b) Median per-pixel T_2^* and DC magnetic sensitivity η measured with and without spin-bath driving. The median T_2^* is 2.2(1) μs and 1.2(1) μs with and without spin-bath driving, respectively. The corresponding median per-pixel sensitivities are 4.1(1) nT/$\sqrt{\mathrm{Hz}}$ and 9.4(1) nT/$\sqrt{\mathrm{Hz}}$. 45
2.9 Spatial magnetic noise floor measured using the differential measurement protocol. Top: Magnetic noise images acquired with different acquisition times and pixel binning, in the absence of any applied phantom current. The acquisition time includes only the measurement duration and excludes implementation-dependent data transfer and storage overhead. The noise exhibits no significant spatial correlation across the field of view. Field of view: $270 \times 270\,\mu\mathrm{m}^2$. Scale bar: 50 μm. Bottom: Spatial magnetic noise floor $\sigma_{\mathrm{spatial}}$ as a function of acquisition time T_{acq} for each pixel binning. The dashed line indicates the expected $\propto T_{\mathrm{acq}}^{-1/2}$ scaling. 47

3.1 [38] Numerical simulation of CASR detection of an NMR free nuclear precession (FNP) signal. The top panel shows the oscillating magnetic field $B(t)$ produced by the precession of thermally polarized nuclear spins (blue) at frequency f. The middle panel illustrates the CASR protocol: a $\pi/2$ pulse (black box) applied to the nuclear spins at time $t = 0$ initiates spin precession with a well-defined phase, enabling coherent signal averaging. The protocol then consists of repeated blocks of identical NV AC magnetometry pulse sequences with central frequency f_0 (gray boxes), interleaved with optical NV spin-state readouts (green boxes). These blocks are repeated with a synchronized readout cycle period τ_{SR}. The bottom panel shows the NV fluorescence signal over successive CASR readouts, which oscillates at the aliased frequency $\delta f = f - f_0$. 53
3.2 RF magnetic field imaging protocol with a lock-in camera. Within one camera demodulation cycle, four exposures occur, with phase-modulated XY8-n sequences applied to NV spins to generate internal I & Q frames. After N_d cycles (i.e., $2N_d$ total internal frames), an external frame of the RF magnetic field image is obtained. The CASR protocol comprises interspersed blocks of single external frame measurements (red boxes) with a frame rate of f_{SR}. The RF magnetic signal (black curve) with frequency f_s is sampled via CASR readout (red dashed curve) at an alias frequency $f_s - mf_{\mathrm{SR}}$, where m is the integer closest to f_s/f_{SR}. 57
3.3 (a) Wide-field imaging of near-field patterns of narrowband magnetic fields using a QDM operated under ambient conditions. RF test signals are applied to microcoils to generate distinct magnetic field patterns across the NV-diamond surface. Laser and MW fields are used for NV electronic spin manipulation, with spin-state population readout via spin-dependent fluorescence. (b) Optical image of the spiral-shaped microcoils positioned at a stand-off distance of approximately $10\,\mu\mathrm{m}$ from the NV layer. All scale bars correspond to $50\,\mu\mathrm{m}$. (c) NV fluorescence image under CW laser excitation, illustrating the relative illumination profile (beam shape) across the FOV. The normalized fluorescence is proportional to the detected photon count. (d) Experimental apparatus. A flip mirror directs NV fluorescence to either a photodiode or a lock-in camera. An AWG provides MW pulses for NV spin control, RF signals for the microcoils, and synchronized frame triggers for camera exposure using its internal oscillator. A Sic wafer serves as a mechanical mount and thermal heat sink for the MW loop, microcoils, and NV-diamond chip. An RF test coil (not shown) is used for AC magnetometry calibration. 60
3.4 Example calibration measurements of the RF-QDM for dynamical-decoupling-based AC magnetometry, performed using photodiode detection (laser beam illumination diameter $\approx 50\,\mu\mathrm{m}$) and wide-field imaging with the lock-in camera. (a) Phase sweep of photodiode-based AC magnetometry used to determine the initial phase of a nominally in-phase AC magnetic field ($f_s = 1\,\mathrm{MHz}$) applied with the RF test coil. (b) Photodiode AC magnetometry curve showing the relative NV photoluminescence contrast measured using the XY8-8 sequence, in good agreement with a sinusoidal fit. (c) Imaged spatial distribution of the zero-crossing slope of the AC magnetometry curve, which exhibits spatial variation due to the laser illumination profile on the NV layer (see Figure 3.3(c)). The scale bar corresponds to $50\,\mu\mathrm{m}$. 62

3.5 RF-QDM imaging of narrowband, multi-frequency magnetic fields using a dynamical-decoupling (XY8-8) protocol. (a) Simultaneous application of 1 MHz (Sig1) and 0.8 MHz (Sig2) AC currents to two microcoils on the NV–diamond surface; selective detection is achieved by tuning the π-pulse spacing τ. (b) Measured (left) and simulated (right) RF magnetic field images for peak currents of $6.6\,\mu\mathrm{A}$, with SNR $\approx$ 50 after 1.2 s averaging per frequency. (c) FFT spectra of the applied signals and corresponding XY8-8 filter functions, illustrating spectral selectivity. (d) Sub-nanotesla RF magnetic imaging with peak currents of $26.4\,\mathrm{nA}$, yielding SNR $\approx$ 15 after 1 hour averaging per frequency. All scale bars are $50\,\mu\mathrm{m}$. Colorbars are not centered at zero due to asymmetry in the projection onto the sensing NV axis. 65

3.6 RF-QDM imaging of arbitrary phase, multi-frequency magnetic fields using the CASR protocol. As described in the text, a single tone alternating current (1 MHz + 125 Hz) is applied to the upper microcoil; and a two tone current (1 MHz + 65 Hz and 1 MHz + 185 Hz) is simultaneously applied to the lower microcoil. Both currents have peak amplitude $I_p = 3.3\,\mu\mathrm{A}$. The phases of each signal frequency component (tone) are arbitrary but fixed during the measurements. Total image acquisition time is 200 s. (a) CASR images of RF magnetic field amplitudes at each signal frequency component, as well as at alias frequencies (1 Hz and 250 Hz) far from any signal tone. The imaged arbitrary phase magnetic field amplitudes have SNR of approximately 70 (calculated with the same method as Figure 3.5(b) for each signal frequency component, and exhibit good agreement with images of in-phase signals shown in Figure 3.5(b). The colorbar is not centered around zero because of asymmetry in the projection of the RF magnetic field amplitude on the sensing NV axis. (b) CASR spectra (FFT) of three test pixels $\mathrm{P}_{1,2,3}$ with positions labeled in (a). Peaks corresponding to three frequency components $f_{1,2,3}$ are clearly illustrated in the spectra, with peak heights proportional to the RF magnetic field amplitude. Linewidths of all spectral peaks ≈ 1 Hz. Amplitude offsets are added to the spectra of $\mathrm{P}_{1,2}$ for a better visualization. All scale bars in (a) correspond to $50\,\mu\mathrm{m}$. 67

3.7 CASR phase imaging of multi-frequency RF magnetic fields. (a) CASR images of RF magnetic field phases at each signal frequency component, as well as at alias frequencies far from any signal tone (1 Hz and 250 Hz). Noisy phase distributions in no-signal regions are attributed to the ratio of near-zero real and imaginary amplitudes of the CASR FFT. (b) Polar plots illustrate the phases of each signal frequency component, derived from CASR measurements. ϕ_1 and ϕ_3 are determined from the real and imaginary parts of the FFT of pixel P_3; and ϕ_2 is determined from P_1. Red and blue dots represent the real and imaginary amplitudes of the associated FFT spectra, respectively, while black arrows indicate the absolute value of the amplitude as shown in Figure 3.6(a). Grids are depicted as circles with a step size equivalent to the radius of 10 arbitrary units of FFT amplitude. All scale bars in (a) correspond to $50\,\mu\mathrm{m}$. . . . 69

3.8 CASR imaging at detuned alias frequencies. (a) CASR amplitude images acquired under the same conditions as Figure 3.6, shown at alias frequencies of 66 Hz and 126 Hz (detuned by 1 Hz from the applied tones at 65 Hz and 125 Hz, respectively), and at an intermediate alias frequency of 95 Hz. All scale bars correspond to $50\,\mu$m. The colorbar is not centered at zero due to asymmetry in the projection of the RF magnetic field onto the sensing NV axis. (b) Real and imaginary components of the CASR spectrum as a function of alias frequency for three representative pixels, $\mathrm{P}_{1,2,3}$, whose locations are indicated in (a). Peaks corresponding to the applied signal tones are illustrated in the phase-offset polar plot of Figure 3.7(b). 71
3.9 RF-QDM imaging of narrowband magnetic fields with known phase using a dynamical-decoupling (XY8-8) protocol and a $1.7\,\mu$m-thick NV layer. Alternating currents at 1 MHz, 0.5 MHz, and 5 MHz with peak amplitude $I_p = 6.6\,\mu$A are applied to the upper microcoil in separate experiments. After 1.2 s of averaging per frequency, the images exhibit SNRs of approximately 50, 34, and 47, respectively, calculated using the same method as in Figure 3.5(b). The imaged RF magnetic field patterns are consistent over an order of magnitude in signal frequency and agree with numerical simulations of a DC current of $6.6\,\mu$A. All scale bars correspond to $50\,\mu$m. The colorbar is not centered at zero due to asymmetry in the projection of the RF magnetic field onto the sensing NV axis. 74
3.10 (a) Optimization of AC magnetic sensitivity as a function of XY8 sequence number, measured using photodiode detection with a $10\,\mu$m-thick NV layer diamond. Increasing the XY8-n sequence length extends the NV spin coherence time T_2. The optimal median single-pixel sensitivity across the field of view is achieved with the XY8-8 sequence. The inset shows a power-law fit of the measured coherence time T_2 versus the number of π pulses, $N_\pi = 8n$, yielding a fitted exponent $s = 0.44(1)$. (b) RF-QDM imaging using the lock-in camera with a 1 MHz signal applied via the RF test coil. Histogram of the single-pixel AC magnetic sensitivity across the field of view using the XY8-8 sequence. The median sensitivity is $0.93(1)$ nT·Hz$^{-1/2}$ for the $10\,\mu$m-thick NV layer diamond and $2.56(1)$ nT·Hz$^{-1/2}$ for the $1.7\,\mu$m-thick NV layer diamond. . . . 78
3.11 Suppression of spatial noise in RF-QDM magnetic images through temporal and spatial averaging. (a) Measured spatial magnetic noise floor, $\sigma_{\mathrm{Spatial}}$, with no RF signal applied to the microcoils and a 1 MHz detection frequency, shown as a function of data acquisition time T_{acq} for $2\,\mu$m single-pixel resolution and $10\,\mu$m (binned) super-pixel resolution. The dashed black line indicates the expected scaling $\sigma_{\mathrm{Spatial}} \propto T_{\mathrm{acq}}^{-1/2}$ as a guide to the eye. (b) Example RF-QDM images of the magnetic noise background and corresponding values of $\sigma_{\mathrm{Spatial}}$: (i) $2\,\mu$m single-pixel resolution with $T_{\mathrm{acq}} = 1.2\,$s; (ii) $10\,\mu$m super-pixel resolution with $T_{\mathrm{acq}} = 1.2\,$s; and (iii) $10\,\mu$m super-pixel resolution with $T_{\mathrm{acq}} = 3600\,$s. All scale bars correspond to $50\,\mu$m. The magnetic noise is spatially uncorrelated. Comparisons between (i) and (ii) illustrate spatial averaging, while comparisons between (ii) and (iii) demonstrate temporal averaging. The lock-in camera frame rate is identical for all measurements. 81

3.12 CASR imaging of weighted frequency and phase of RF magnetic signals generated by two microcoils under the same experimental conditions as Figure 3.6. (a) Weighted frequency image, defined as $f_w = \int f\, S_{\mathrm{CASR}}\, df / \int S_{\mathrm{CASR}}\, df$. A transparency mask based on the integrated CASR amplitude suppresses no-signal regions. The colorbar indicates the frequency integration range, which includes f_1 and f_2 but excludes f_3, revealing the near-field spatial distributions of the selected frequency components. (b) Weighted phase image, defined as $\phi_w = \int \phi\, S_{\mathrm{CASR}}\, df / \int S_{\mathrm{CASR}}\, df$, using the same mask and integration range as in (a). The spatial distributions of $\phi_1 = -6^\circ$ and $\phi_2 = 80^\circ$ are clearly resolved. The $\sim 180^\circ$ phase reversal outside each spiral arises from the opposite direction of the RF magnetic field generated by the microcoils. All scale bars correspond to $50\,\mu\mathrm{m}$. 83

4.1 (a) Bloch sphere visualization of the AC bias, target RF signal, and effective signal fields in both the laboratory and rotating frames, illustrating the general case. In the present work, the XY8 sequence is primarily sensitive to the longitudinal effective signal; and the RF signal and AC bias fields are linearly polarized and generated by the same coil, and hence are colinear in the laboratory frame. Thus, we consider only the x-component of the RF signal and AC bias fields, which contribute to the longitudinal effective signal, to simplify the Hamiltonian model. (b) Simplified schematic of quantum frequency mixer dynamics, including the effective signal amplitude Ω_e and AC Stark shift δ mediated by virtual Floquet modes. 91

4.2 (a) Wide-frequency-range RF magnetic sensing using an NV ensemble in diamond. The NV electronic spin state is initialized and read out optically, while MW control pulses are applied via an on-chip MW loop. A target RF signal and a strong AC bias field are applied through the same coil. QFM between these fields generates an effective signal within the optimal detection band ($\sim 1\,\mathrm{MHz}$) of narrowband NV sensing protocols. (b) Integration of QFM with the CASR protocol. The target signal at frequency ω_s is mixed with an AC bias field at frequency ω_b, producing an effective longitudinal signal at $\omega_e = \omega_s - \omega_b$. The CASR protocol samples the resulting NV PL at a rate ω_{SR}, yielding an aliased signal at ω_a and enabling sub-Hz spectral resolution after Fourier analysis. 95

4.3 QFM–CASR sensitivity across a wide target signal frequency range. (a) Estimated and measured QFM–CASR narrowband magnetic sensitivity for target signal frequencies from 10 MHz to 4 GHz. The AC bias field is detuned by 1 MHz from the target signal and has a fixed amplitude $\Omega_b = (2\pi)4.3$ MHz. Red and blue curves show estimated sensitivities based on the measured XY8-6 sensitivity at 1 MHz (purple diamond) and Eq. (4.18), for MW pulses resonant with the NV spin transitions at $\omega_{-1} = (2\pi)2.29$ GHz and $\omega_{+1} = (2\pi)3.45$ GHz, respectively. Circles and squares indicate experimentally measured sensitivities at selected target frequencies. Black circles ("QFM–CASR Demo.") correspond to frequencies used in the sub-Hz spectral resolution demonstrations shown in Figure 4.4. (b) Example sensitivity calibration measurement for a target signal at 2.4 GHz with an effective (mixed-down) signal frequency near 1 MHz. (c) Same data as in (a), shown with error bars derived from the standard deviation of 10 independent sensitivity measurements at each target frequency. (d) Comparison of estimated sensitivities for linearly polarized (blue) and circularly polarized (purple) AC bias fields, evaluated for the NV spin transition at ω_{+1}. Circular polarization provides a modest sensitivity enhancement for $\omega_s > \omega_{+1}$. 98

4.4 Demonstration of QFM-CASR spectroscopy of multi-frequency RF signals with sub-Hz spectral resolution over a wide frequency range. (a) QFM-CASR measurement protocol applied to a target signal consisting of two frequency components within the detection bandwidth. In a synchronized sequence of measurement periods, the NV electronic spin ensemble is initialized and read out using 532 nm laser pulses (green). A $\pi/2$ microwave pulse along the y-axis prepares the NV spin in a magnetically sensitive superposition state, followed by an XY8-k sequence ($k = 6$) resonant with a 1 MHz effective signal. A final $\pi/2$ pulse along the x or $-x$ axis projects the longitudinal spin state as signal or reference, followed by photoluminescence (PL) readout (red). During each measurement period, an AC bias field (violet) is applied to mix the two target signal frequencies, ω_{s1} and ω_{s2}, into an effective signal within the optimal detection band of the XY8-k sequence via quantum frequency mixing. (b) Time-domain QFM-CASR measurement of the two-tone target signal. A 1 Hz beating between the two signal components is clearly visible in the upper panel, while the lower zoomed-in panel resolves the higher-frequency oscillation near the CASR alias frequency (≈ 3 kHz). (c) QFM-CASR spectra obtained from FFTs of the time-domain measurements over a wide frequency range. Center: spectrum near 2.4 GHz derived from the data in (b) after DC offset removal. Left and right: spectra near 0.6 and 4 GHz, respectively. The measured effective signal amplitudes are consistent with the frequency-dependent sensitivity of the QFM-CASR protocol (black circles in Figure 4.3). (d) Top: effective-signal noise floor with a standard deviation $\sigma_e \approx 120$ pT, corresponding to $\sigma_s \approx 6$ nT for a target signal near 2.4 GHz. Bottom: zoomed-in spectrum demonstrating sub-Hz resolution, clearly resolving the two target signal peaks at ω_{a1} and ω_{a2}. 102

4.5 Precise phase measurement using QFM-CASR. (a) The effective signal generated through quantum frequency mixing has a phase ϕ_e equal to the difference between the target signal phase ϕ_s and the AC bias phase ϕ_b. By analyzing the real and imaginary components of the QFM-CASR spectrum, ϕ_e can be extracted. With ϕ_b known and controlled, the target phase is obtained as $\phi_s = \phi_e + \phi_b$. (b) Experimental demonstration with $\omega_b = (2\pi)2.4\,\mathrm{GHz}$ and $\omega_s = (2\pi)2.401\,\mathrm{GHz}$. While keeping $\phi_b = 0$, ϕ_s is swept over 360° in 1° steps. The real, imaginary, and absolute values of the QFM-CASR spectrum are shown for every 10 phase steps. (c) Histogram of the phase error between measured and applied phases. The distribution is Gaussian with standard deviation $\sigma_\phi \approx 0.4^\circ$. 105

4.6 Precise QFM-CASR phase measurements of target signals near 666 MHz (top) and 4 GHz (bottom). For the experiment near 666 MHz. For the experiment near 4 GHz, the same $\Omega_{b,s}$ is applied as for the 666 MHz experiment, with $\omega_s = (2\pi)(4\,\mathrm{GHz} + 3.125\,\mathrm{kHz})$ and $\omega_b = (2\pi)3.999\,\mathrm{GHz}$. Real (red) and imaginary (blue) components of the QFM-CASR spectra are displayed, as generated from FFT of time-domain QFM-CASR data (NV PL measurements). Polar plots illustrate the phases of each effective signal, as derived from QFM-CASR measurements. Red and blue dots represent the real and imaginary amplitudes of the associated QFM-CASR spectra, respectively, while black arrows indicate the absolute value of the amplitude. Grids are shown as circles with a radial step size equivalent to 20 arbitrary units of FFT amplitude. . . . 106

4.7 Demonstration of sub-Hz QFM-CASR spectral resolution using two test signals near 2.4 GHz + 3.125 kHz with a frequency separation of 1 mHz. (a) For an acquisition time $t_{\mathrm{acq}} = 10\,\mathrm{s}$, the frequency resolution is $\delta f \approx 100\,\mathrm{mHz}$, and the two signals are not resolved, appearing as a single peak in the FFT of the QFM-CASR time-domain data. (b) For $t_{\mathrm{acq}} = 2000\,\mathrm{s}$, corresponding to $\delta f \approx 0.5\,\mathrm{mHz}$, the two signals are clearly resolved, demonstrating a 1 mHz frequency separation. 107

4.8 (a) QFM-XY8-6 AC magnetometry curve for the effective field at 1 MHz, obtained by varying the target signal amplitude while holding the AC bias field amplitude constant. The signal and bias frequencies are 2.4 GHz and 2.399 GHz, respectively. The maximum of the curve corresponds to a $\pi/2$ phase accumulation of the NV spin due to the effective field, yielding an effective field amplitude of $0.58(1)\,\mu\mathrm{T}$. (b) NV Rabi oscillation measurements used to determine the RF amplitudes of the AC bias field, $\Omega_b = (2\pi)4.310(6)$ MHz (upper panel), and the signal field, $\Omega_s = (2\pi)0.841(2)$ MHz (lower panel). 110

4.9 (a) DEER pulse sequence used to probe P1 center spin dynamics during an NV Hahn-echo measurement. (b) DEER spectrum measured by sweeping the RF frequency around the on-axis P1 transition near 666 MHz. (c) DEER-Rabi oscillations obtained by sweeping the duration of the spin-bath RF pulse using either the AC bias field (red) or the signal field (blue). (d) Non-QFM XY8-6 AC magnetometry measurement of a 1 MHz test signal used to calibrate RF field amplitude versus AWG output amplitude. (e) (left) CASR (non-QFM) spectrum of a $1\,\mathrm{MHz} + 3.125\,\mathrm{kHz}$ test signal. (right) QFM-CASR spectrum of the effective signal generated using signal and bias fields near 666 MHz. 111

4.10 Comparison of narrowband (AC) volume-normalized sensitivity and applicable signal frequency range for state-of-the-art NV-diamond experiments, including the present QFM-CASR results (solid red line, fixed ω_0) and optimized QFM-CASR performance (red band). For non-QFM techniques, the marker indicates the reported sensitivity at the demonstrated signal frequency, while the dashed line indicates the approximate operational frequency range. All non-QFM techniques exhibit frequency-dependent AC sensitivity, typically degrading away from the reported operating point [17]. 113

5.1 Timeline of NV-NMR development, adapted from Ref. [86], highlighting major experimental milestones. 121

5.2 NV-NMR spectroscopy with integrated hyperpolarization [55]. (a) Experimental schematic: A microwave loop antenna drives both NV centers (purple) and TEMPOL electron spins (blue). Hyperpolarized NMR signals from nuclear spins in the sample (orange) are detected via NV ensemble fluorescence. Inset: The sensing area is defined by the laser spot on the diamond (scale bar: 30 μm). (b) Pulse sequence for hyperpolarized NV-NMR. Left: Overhauser DNP, where continuous microwave driving saturates the TEMPOL electron spin transition, enabling polarization transfer to nearby protons. Right: Detection of the proton FNP signal using the CASR protocol with synchronized dynamical decoupling sequences. 124

5.3 Hyperpolarization-enhanced NV NMR of water [55]. (a) Comparison of NV NMR spectra from pure water with DNP (red circles, single spectrum) and without DNP (blue circles, 10^4 spectra averaged), using a CASR pulse sequence. Line shape fits (solid lines) indicate a DNP signal enhancement factor of 230, achieving a proton number sensitivity of 10 pmol/Hz$^{1/2}$ for a signal-to-noise ratio (SNR) of 3. (b) CASR-detected signal magnitude from a pure water sample as a function of DNP drive frequency. The observed triplet structure results from hyperfine coupling between the electron and ^{14}N nuclear spins in the TEMPOL radical. (c) CASR-detected signal magnitude from pure water as a function of DNP drive power, expressed in units of the electron Rabi frequency. The maximum DNP signal enhancement occurs at a drive Rabi frequency of approximately 10 MHz. 125

5.4 Schematic of the integrated QDM-NMR experimental platform. Left: Cross-sectional view of the setup. A liquid sample containing water and dissolved TEMPOL radicals is held in a plastic tube mounted directly above the NV-diamond sensor. A slot is fabricated in the SiC wafer at the center of the Ω-shaped CPW to enable close proximity between the NV sensing layer and the sample. A multi-turn copper coil (red) surrounding the tube provides RF excitation for nuclear spin manipulation (NMR coil) as well as inductive NMR signal detection; while a separate microwave coil (yellow) delivers high-power driving for Overhauser DNP. Top right: Conceptual illustration of the sensing mechanism. Electron spins in TEMPOL radicals transfer polarization to nearby proton spins via DNP, and the resulting nuclear magnetic resonance signal is detected by the NV ensemble. Bottom right: Bottom view of the Ω-shaped CPW structure defining the microwave delivery region and the optical FOV of the QDM system. A capillary tube can be inserted into the sample volume to introduce spatially varying samples for microscopic NMR imaging. 127

5.5 Block diagram of the electronic control and signal routing for the integrated QDM-NMR system. The computer-controlled AWG serves as the central timing and control unit, generating MW pulses for NV spin manipulation and RF signals for nuclear spin excitation, while providing TTL triggers to synchronize all subsystems. NV PL is detected either by a balanced photodiode for high-sensitivity measurements or by a wide-field lock-in camera for spatial imaging. The photodiode signal is digitized by a DAQ system. For inductive NMR detection, the signal from the NMR coil is routed through a duplexer and a 90° transformer to separate the weak inductive signal from the strong RF drive, and is then recorded by the NMR DAQ. The duplexer protects the receiver while enabling simultaneous RF excitation and signal acquisition. Microwave excitation for DNP is generated by an independent MW source and amplified, providing higher output power than the AWG-based path. Additional RF and MW signals are amplified using amplifiers before being delivered to the CPW, NMR coil, or DNP coil. Arrows indicate signal flow for MW/RF delivery, TTL triggering, and data acquisition, illustrating the fully synchronized operation of NV-based sensing and inductive NMR detection. 129

5.6 Schematic of the nuclear CPMG sequence synchronized with NV-CASR detection and lock-in camera demodulation. Top: Nuclear spin control sequence. Following an initial Overhauser DNP polarization period, a $\pi/2$ pulse initializes nuclear spin coherence, followed by a train of π pulses with alternating phase (CPMG) to generate a series of spin echoes. This sequence extends the effective signal duration from the dephasing time T_2^* to the longer coherence time T_2. Middle: NV spin control using the CASR protocol. Repeated blocks of dynamical decoupling sequences (XY8-n) are synchronized to the nuclear spin evolution, enabling detection of the NMR signal. Bottom: Lock-in camera demodulation. Multiple internal frames are acquired during each camera exposure and combined to form a single external frame contains the time domain signal. This demodulation process extracts the oscillating NMR signal while suppressing static background contributions. 130

5.7 Inductive NMR measurements used for optimization of DNP and nuclear RF pulses. (a) Inductive ^{1}H NMR spectra of deionized water with (red) and without (blue) Overhauser DNP, showing an enhancement of approximately $20\times$ in signal amplitude under optimized DNP conditions. (b) NMR signal enhancement as a function of DNP drive frequency. The observed triplet structure arises from hyperfine coupling between the electron spin and the ^{14}N nuclear spin in the TEMPOL radical, with the optimal DNP frequency identified near 1.116 GHz. (c) Nuclear Rabi oscillation obtained by sweeping the RF pulse duration at fixed amplitude, used to determine the optimal π-pulse duration. (d) Nuclear Rabi oscillation obtained by sweeping the RF pulse amplitude at fixed duration, used to determine the optimal RF drive amplitude. 133

5.8 Time-domain nuclear CPMG-25 signals measured simultaneously using inductive ^{1}H NMR and NV-based detection of deionized water with Overhauser DNP. (a) Inductive NMR signal. Top: Raw signal with high-amplitude nuclear π pulses shaded; a threshold is used to identify these pulses. Bottom: Cleaned signal after removing the π-pulse contributions, revealing 25 spin-echo envelopes separated by 4 ms. (b) NV-NMR signal measured via photodiode readout. Top: Raw signal with detected spikes (corresponding to nuclear π pulses) shaded. Bottom: Cleaned signal after spike removal, showing the corresponding spin-echo train. The inductive and NV-NMR signals exhibit clear temporal alignment, confirming consistent detection of the same nuclear spin dynamics. Each spin-echo envelope decays with the nuclear dephasing time T_2^*, while the envelope peaks decrease over time according to the coherence time T_2. The NV-NMR signal shows higher noise but captures the same echo structure, demonstrating its capability for time-resolved NMR detection with microscopic sensing volume. 136

5.9 Frequency-domain analysis of a single NV-NMR spin-echo signal. (a) Raw FFT spectrum showing a clear alias peak near $f_a \approx 3.25\,\mathrm{kHz}$ (red dashed line), with the shaded region indicating the integration window. (b) Calibrated FFT spectrum converted to magnetic field units using a reference measurement, yielding a peak amplitude on the order of a few nT. (c) Amplitude spectral density (ASD), obtained by normalizing the FFT to the measurement bandwidth, highlighting the signal-to-noise characteristics. (d) Power spectral density (PSD) and integration over the signal bandwidth (shaded region), yielding a total magnetic field amplitude of $\sqrt{\int \mathrm{PSD}\, df} = 4.46\,\mathrm{nT}$. The extracted signal amplitude significantly exceeds the thermally polarized expectation, indicating $\sim 100\times$ enhancement due to Overhauser DNP. 139

5.10 Analysis of nuclear spin (^{1}H) coherence time T_2 from simultaneous NV-NMR and inductive NMR measurements using the CPMG-25 sequence for deionized water with Overhauser DNP. (a) FFT spectra of individual NV-NMR spin echoes, vertically offset and color-coded by echo time. A clear alias peak near 3.25 kHz is observed for all echoes, with the peak amplitude gradually decreasing due to nuclear spin decoherence. (b) Example integration window used for time-domain analysis of the second spin echo. The shaded region indicates the integration range centered between nuclear π pulses. (c) Comparison of T_2 extracted from the FFT peak amplitudes of each spin echo for NV-NMR and inductive NMR measurements. Dashed lines are exponential fits. (d) Comparison of T_2 obtained from time-domain integration of each spin echo. Both analysis methods yield similar coherence times, with the NV-NMR data exhibiting larger fitting uncertainty due to lower signal-to-noise ratio. The shorter NV-NMR T_2 compared with the inductive measurement is attributed to diffusion and magnetic-field gradients near the diamond surface. 140

5.11 Proof-of-principle imaging of a CPMG-shaped synthetic signal using QDM-CASR. (a) Spatial maps of the signed FFT amplitude at three frequencies: the signal frequency $f_{as} = -1071\,\text{Hz}$ (left), an off-resonant frequency $f = -571\,\text{Hz}$ (middle), and the reference/background frequency $f_{a0} = -71\,\text{Hz}$ (right). The signal map at f_{as} clearly resolves the spiral microcoil pattern, while the off-resonant map shows only noise and the background map reflects the spatial profile of the large NMR coil and illumination inhomogeneity. The circled pixel (99,61) indicates the location of maximum signal amplitude used for further analysis. (b) Time-domain CASR signal (left) and corresponding FFT real component (right) for the selected pixel. The signal exhibits an exponentially decaying envelope in time and a distinct spectral peak at f_{as} in the frequency domain. (c) Magnitude of the complex CASR signal $\sqrt{I^2 + Q^2}$ (left) and corresponding FFT amplitude spectrum (right). The spectrum shows a dominant peak at f_{as} and a smaller peak at f_{a0}, corresponding to the synthetic signal and reference background, respectively. 142

5.12 Time-resolved spectral analysis of the CPMG-shaped synthetic signal using windowed FFT. (a) Spectrogram obtained by applying FFT to successive 4 ms time windows of the CASR signal at the pixel of maximum amplitude (99,61). The dominant signal component at $f_{as} = -1071\,\text{Hz}$ (left dashed line) exhibits a clear exponential decay over time, while the reference/background component at $f_{a0} = -71\,\text{Hz}$ (right dashed line) remains approximately constant. (b) Temporal evolution of the FFT peak amplitudes extracted from (a). The signal component at f_{as} (red) is fit to an exponential decay, yielding $T_2 = 199.84 \pm 28.82\,\text{ms}$, consistent with the programmed decay constant of the synthetic signal. The reference component at f_{a0} (blue) shows no decay and remains constant within noise, confirming its origin as a steady background field. . . . 143

5.13 Magnetic-field calibration and quantitative imaging of the CPMG-shaped synthetic signal. (a) Pixel-wise AC magnetometry calibration at the selected pixel (99,61). The NV fluorescence contrast is measured as a function of applied RF magnetic field amplitude and fit to a sinusoid, yielding a calibration factor $C = 37.72\,\mu\text{T}/\text{amp}$. The vertical dashed line indicates the operating point used in the experiment. (b) Spatial map of the calibration factor (B/Amp) across the field of view, reflecting the spatial variation of the RF magnetic field generated by the NMR coil and the relative positioning of the sample within the coil. The circled pixel indicates the location used for calibration in (a). (c) Reconstructed magnetic-field amplitude images obtained by applying the calibration map to the FFT amplitudes. Left: signal component at $f_{as} = -1071\,\text{Hz}$, clearly resolving the spiral microcoil pattern with peak amplitudes on the order of 100 nT. Middle: off-resonant frequency ($f = -571\,\text{Hz}$), showing noise-limited background. Right: reference component at $f_{a0} = -71\,\text{Hz}$, corresponding to the spatial distribution of the background field generated by the large NMR coil. Horizontal artifacts arise from partial saturation of the CMOS sensor during acquisition. 145

5.14 SNR improvement through pixel binning and averaging for QDM-NMR imaging. (a) Spatial maps of the measured CASR noise floor after 1000 averages for the original image resolution (left) and after 2×2 pixel binning (right). Pixel binning reduces the effective per-pixel noise level. (b) Estimated per-pixel magnetic noise floor as a function of the number of averaged measurements for different pixel binning conditions. Curves are shown for binning factors from 1×1 ($2\,\mu$m spatial resolution) to 10×10 ($20\,\mu$m spatial resolution). The dashed lines indicate estimated signal amplitudes of 4.37 nT and 0.437 nT, corresponding to SNR = 1 and SNR = 10. (c) Estimated QDM-NMR SNR as a function of averaging number for different binning conditions. The dashed line indicates SNR = 10. Based on these estimates, an NMR image with SNR ~ 10 can be achieved at approximately $8\,\mu$m spatial resolution (4×4 binning) with 1000 averages, corresponding to a total acquisition time of approximately 6 h. 147
5.15 Adapted from Ref. [87]. PEG-based hydrogel formation and structural heterogeneity relevant to QDM-NMR imaging. (a) Schematic of PEG precursor molecules (PEG-MA and PEG-SH) used to form crosslinked hydrogel networks. (b) Comparison between homogeneous hydrogel formation (top) and gel–gel phase separation (GGPS, bottom), where dense and dilute polymer domains coexist. These structural variations lead to spatial differences in molecular diffusion and local viscosity, which can produce spatial contrast in nuclear spin coherence time T_2. 150
5.16 MRI of various biofilm geometries [94, 95]. (a) MRI visualization of different biofilm structures: autotrophic biofilm (left), granulated biofilm (middle), and granulated biofilms of varying sizes (right). (b) T_1-weighted (left) and T_2-weighted (right) MRI contrast revealing internal heterogeneity in a heterotrophic biofilm. 152
5.17 SEM images of *Staphylococcus aureus* biofilms adhered to glass under different pH conditions [97]. 153
5.18 Structural diagram of Spirogyra cells, illustrating the characteristic helical chloroplast morphology. 154
5.19 3D MRI of a single Spirogyra cell [98]. (a) Optical image of the sample. (b) Corresponding MRI reconstruction showing overall cell morphology. 155

6.1 Representative compact NV-diamond magnetometer implementations. (a) CMOS-integrated device with on-chip photodiode and microwave generation [99]. (b) Fiber-integrated sensor with compact optical and microwave components [100]. (c) PCB-level integrated system combining optical excitation, microwave delivery, and signal processing [101]. (d) Fully integrated LED-based device with compact sensor head architecture [102]. 160
6.2 Design of the compact quantum magnetic camera. (a) Cross-sectional view of the assembled device and optical layout. A fiber-coupled laser is collimated and shaped by a cylindrical lens, then directed via mirrors to illuminate the NV diamond from the side. The resulting spin-dependent fluorescence is collected by an imaging lens array, filtered, and detected by an on-chip CMOS camera. Microwave (MW) excitation is delivered through an integrated input port. (b) Exploded view of the device showing the ten-layer modular architecture, including the diamond mount **[1]**, mirror mount **[2]**, imaging lens mounts **[3]**, **[4]**, **[6]**, pinhole **[5]**, cylindrical lens and mirror mount **[7]**, fiber mount **[8]**, filter mount **[9]**, and CMOS camera board **[10]**. 163

6.3 Design and simulation of the side-illumination module. (a) Optical layout of the illumination path. A collimated Gaussian beam from the fiber output **[1]** is compressed by a cylindrical lens and directed into the diamond at position **[2]** with an incident angle of 23.4°. The beam propagates along the diamond via TIR, illuminating the target FOV of $1\,\mathrm{mm} \times 1\,\mathrm{mm}$. (b) Simulated normalized power intensity distributions at key propagation positions **[1]–[4]** using the POP method. The beam is progressively compressed along the vertical direction, with a waist reduced from 1.1 mm at the input to 66.6 μm and 45.3 μm near the diamond entry, and further confined to a $\sim$20 μm-thick layer at the sensing surface, enabling efficient and localized excitation of NV centers. 166
6.4 (a) Adapt from Ref. [104]. Room-temperature emission spectrum of a single NV center in a nanodiamond, fitted with eight Lorentzian components. The zero-phonon line (ZPL) and phonon sideband (PSB) contributions are illustrated, along with a simplified energy-level model including multiple vibronic ground states $|g_i\rangle$ and an excited state $|e\rangle$. Spectral broadening arises from spontaneous emission, pure dephasing, and phonon-assisted transitions. (b) Optical design of the finite-conjugate imaging system. Ray traces for three representative field positions (center, mid-field, and edge, shown in blue, red, and green, respectively) over a total system length of 25 mm. 168
6.5 Simulated performance of the optimized imaging system. (a) RMS wavefront error as a function of field position (+Y direction) and wavelength, showing consistently low aberrations across the full field of view. (b) Modulation transfer function (MTF) for multiple field points, demonstrating that the system maintains high contrast up to the sensor Nyquist frequency (12.8 cycles/mm in object space). (c) Seidel aberration contributions for each optical surface, indicating that third-order aberrations and chromatic effects are well corrected, with no dominant residual component. 169

7.1 Observation of off-axis NV double-quantum (DQ) transitions in DEER experiments. (a) Continuous DEER spectrum similar to Figure 2.1, where a weak off-axis NV transition is observed (red box). (b) DEER measurement reported in Ref. [105], where the off-axis NV transition is more clearly resolved. 174
7.2 Numerical simulation of off-axis NV control at $B = 200\,\mathrm{G}$. (a) Simulated pulsed ESR spectra for off-axis NV centers, showing resolved transitions arising from mixed-spin eigenstates under the applied bias field. (b) Simulated on-axis and off-axis Rabi drive corresponding oscillations 176
7.3 (a) Geometry of magic-angle spinning, showing the rotation of the internuclear vector relative to the static magnetic field. (b) Conceptual implementation of a rotating magnetic bias field using orthogonal coil pairs and permanent magnets [107]. (c) Proposed integration of the rotating-bias-field architecture into the QDM platform, enabling magic-angle spin-bath driving without mechanical rotation. 181

7.4 Suppression of strain-induced pulse errors in AC magnetic imaging by increasing the Rabi frequency. Top row: phase offset (left) and amplitude (right) images acquired with a Rabi frequency of 4.6 MHz, showing strong spatial inhomogeneity due to strain-induced detuning, highlighted by the circled region. Bottom row: corresponding images acquired with an increased Rabi frequency of 7.1 MHz, demonstrating significantly improved phase uniformity and suppression of amplitude artifacts. These results indicate that stronger microwave driving enhances robustness against detuning-induced pulse errors. The scale bar is 50 μm. 184
7.5 Double-quantum four-spin-echo protocol (DQ4S) for AC magnetic sensing. Top: pulse sequence diagram showing two microwave channels (MW1 and MW2) driving the $m_s = \pm 1$ transitions to realize double-quantum control. The sequence combines phase-alternating $\pi/2$ and π pulses to construct an effective double-quantum spin echo. Bottom: simulated AC magnetometry response under zero detuning, demonstrating sinusoidal dependence of the signal (blue) and reference (red) channels, with the normalized contrast (black) retaining high fidelity. The DQ protocol suppresses common-mode detuning effects and preserves the ideal magnetometry response, highlighting its potential for robust wide-field AC magnetic imaging. 186
7.6 [85] Pulse-gradient spin-echo (PGSE) sequence adapted for NV-based NMR detection. Gradient pulses of duration δ and separation Δ encode molecular diffusion into the accumulated phase of nuclear spins. The resulting NMR signal is detected using the CASR protocol with continuous NV optical readout. This approach enables direct measurement of diffusion coefficients. Extending this sequence to wide-field QDM detection would allow spatially resolved diffusion imaging, providing two-dimensional maps of transport dynamics in heterogeneous samples. 189
7.7 (a) Schematic of an NV ensemble NMR apparatus. A fluid sample is placed in close proximity to the NV layer in diamond and detected through optically read out NV fluorescence under microwave and RF control. (b) AERIS pulse sequence [109], where nuclear spin precession is measured through synchronized NV dynamical decoupling during RF nutation. (c) DRACAERIS pulse sequence [110], which introduces an additional reverse-nutation step to suppress common-mode noise and improve measurement robustness. (d,e) Bloch-sphere representation of nuclear spin evolution during AERIS and DRACAERIS protocols. DRACAERIS compensates leading-order off-resonance effects and restores the magnetization to its initial state more accurately. 191

A.1 Conceptual illustration of camera-demodulated CASR readout. A narrowband magnetic signal with frequency f_0 (black curve) is sampled by the CASR protocol at the repetition rate f_{SR}, producing an aliased low-frequency signal (red dashed curve with red sampling points). In the heliCam lock-in camera implementation, the camera internally averages n consecutive CASR readouts within each internal frame (top shaded regions). This internal demodulation produces a reduced set of effective samples (bottom), corresponding to an additional averaging step that lowers the effective sampling rate from f_{SR} to f_{SR}/n. Consequently, the camera-demodulated CASR signal can be interpreted as a two-stage process: first aliasing at the CASR sampling rate, followed by averaging-induced down-sampling that produces a second effective aliasing process. 194

A.2 Numerical simulation of the double-alias behavior in camera-demodulated CASR. (a) Simulated FFT peak amplitude as a function of CASR sequence length $\mathrm{Seq}_t = 1/f_{\mathrm{SR}}$. Periodically spaced maxima appear due to the synchronization condition between the signal frequency and the CASR repetition rate. The peak spacing of approximately $0.6\,\mu\mathrm{s}$ corresponds to $1/f_0$ for $f_0 \approx 1.69\,\mathrm{MHz}$. (b) Simulated contrast spectrum near the signal frequency for an optimized sequence length $\mathrm{Seq_t} = 24.28\,\mu\mathrm{s}$. The resonance peak has a full width at half maximum of approximately $3\,\mathrm{kHz}$, indicating the frequency tolerance of the double-aliased CASR detection scheme. 200

B.1 Characterization of NV orientation and diamond crystal geometry. (a) Representative ODMR spectrum of an NV ensemble without bias-field alignment, showing eight resonance dips corresponding to the Zeeman splitting of the four NV orientations (labeled NV1–NV4), neglecting hyperfine interactions. (b) Schematic illustration of two typical diamond geometries used in experiments. Laser incident into the diamond side with a total internal reflection (TIR) labeled as green arrow. (c) Measured polarization-dependent ODMR contrast for the four NV orientations as the laser polarization is rotated. The contrast modulation reflects the projection of the laser electric field onto each NV dipole, enabling identification of the crystal orientation. (d) Numerical simulation of the polarization dependence for corner-cut (left) and side-cut (right) diamonds. For corner-cut diamonds, NV orientations form two pairs with in-phase oscillations and similar amplitudes. For side-cut diamonds, one pair exhibits weak in-phase oscillations, while another pair shows strong out-of-phase oscillations. 203

B.2 Bias magnetic field homogeneity optimization via saddle-point alignment. (a) Left: magnet configuration and diamond position. Right: simulated ODMR frequency shift versus spatial detuning along x, y, and z, showing a saddle point where first-order field gradients vanish. (b) Experimental identification of the saddle point. Left: ODMR frequency versus z for different x, where the curve intersection and flattest trace determine the optimal (x, z). Right: frequency versus y with (x, z) fixed, where the minimum locates the saddle point. 205

C.1 Schematic illustration of the multi-layer fabrication process for the phantom and Ω loop structures. The process consists of seven main steps. The final device integrates a thin Pd phantom layer (typically $\sim$7 nm with $\sim$3 nm Cr adhesion) and a thicker Au microwave layer (typically $\sim$300 nm with $\sim$10 nm Cr adhesion), enabling simultaneous magnetic field generation and microwave delivery. 207

C.2 Photolithography setup used for patterning the phantom layer. (a) Spin-coating station for applying HMDS adhesion layer and S1813 photoresist, showing the spin chuck, pipetting process, and programmable spin timing. (b) UV mask aligner (Süss MicroTec MJB-3) used for pattern transfer, including photomask and wafer vacuum stages, alignment controls, and exposure timing module. These tools enable precise control of resist thickness, feature definition, and alignment accuracy in the multi-layer fabrication process. 208

C.3 Fabrication results and post-processing of the MW CPW and phantom device. 210

List of Abbreviations

AC	Alternating Current
AOM	Acousto-optic Modulator
ASD	Amplitude Spectral Density
AWG	Arbitrary Waveform Generator
CASR	Coherent Averaged Synchronized Readout
CLSM	Confocal Laser Scanning Microscopy
CPMG	Carr–Purcell–Meiboom–Gill
CPW	Coplanar Waveguide
CVD	Chemical Vapor Deposition
CW	Continuous Wave
DAQ	Data Acquisition
DEER	Double Electron-Electron Resonance
DNP	Dynamic Nuclear Polarization
DQ	Double Quantum
DQ4R	Double Quantum Four-Ramsey
EPS	Extracellular Polymeric Substances
FEM	Finite-Element Method
FFT	Fast Fourier Transform
FNP	Free Nuclear Precession
FOV	Field of View
GGPS	Gel–Gel Phase Separation
ISC	Intersystem Crossing
MRI	Magnetic Resonance Imaging
MW	Microwave
MTF	Modulation Transfer Function
NA	Numerical Aperture
NMR	Nuclear Magnetic Resonance
NV	Nitrogen-vacancy
ODMR	Optically Detected Magnetic Resonance

PEG	Polyethylene Glycol
PL	Photoluminescence
POP	Physical Optics Propagation
PSB	Phonon Sideband
PSD	Power Spectral Density
QDM	Quantum Diamond Microscope
QFM	Quantum Frequency Mixer
RF	Radio-frequency
S. aureus	Staphylococcus aureus
SEM	Scanning Electron Microscopy
SERF	Spin-exchange Relaxation-free
SNR	Signal-to-noise Ratio
SQ	Single Quantum
SQUID	Superconducting Quantum Interference Device
SWaP	Size, Weight, and Power
TIR	Total Internal Reflection
VMR	Vector Magnetoresistance
XRD	X-Ray Diffraction
ZFS	Zero-field Splitting
ZPL	Zero-phone Line

Chapter 1: Introduction

1.1 Nitrogen-Vacancy Centers in Diamond

Quantum systems composed of solid-state electronic spins can be sensitive detectors of magnetic fields. A prominent example is the nitrogen-vacancy (NV) center in diamond [1], which consists of a substitutional nitrogen adjacent to a vacancy in the carbon lattice (Figure 1.1(a)). Although NV centers exist in varies charge states (NV^-, NV^0, NV^+), in this dissertation, we use NV center to refer to the negatively-charged NV^-, which is conventionally used for sensing.

The negatively-charged NV^- features a electronic spin $S = 1$, leading to a triplet ground state ($^3A_2$) as shown in Figure 1.1(b). The ($^3A_2$) electronic ground state is an orbital singlet and spin triplet manifold, with bare ground-state Hamiltonian [2]:

$$\hat{H}_{gs}/h = \hat{S} \cdot \mathbf{D} \cdot \hat{S} + \hat{S} \cdot \mathbf{A} \cdot \hat{I} + \hat{I} \cdot \mathbf{Q} \cdot \hat{I}, \tag{1.1}$$

where h is Planck's constant, $\hat{\mathbf{S}} = (\hat{S}_x, \hat{S}_y, \hat{S}_z)$ and $\hat{\mathbf{I}} = (\hat{I}_x, \hat{I}_y, \hat{I}_z)$ are the dimensionless electron and nitrogen nuclear spin operators, respectively. The first term represents the fine-structure splitting arising from the electronic spin–spin interaction, characterized by the fine-structure tensor $\mathbf{D}$ [3]. The second term describes the hyperfine interaction between the NV electronic spin and the nitrogen nuclear spin, parameterized by the hyperfine tensor $\mathbf{A}$. The third term denotes the nuclear electric quadrupole interaction, associated with the quadrupole tensor $\mathbf{Q}$. Under the C_{3v} symmetry of the NV center, the tensors $\mathbf{D}$, $\mathbf{A}$, and $\mathbf{Q}$ are diagonal in the NV coordinate frame, and the Hamiltonian $\hat{H}_{\mathrm{gs}}$

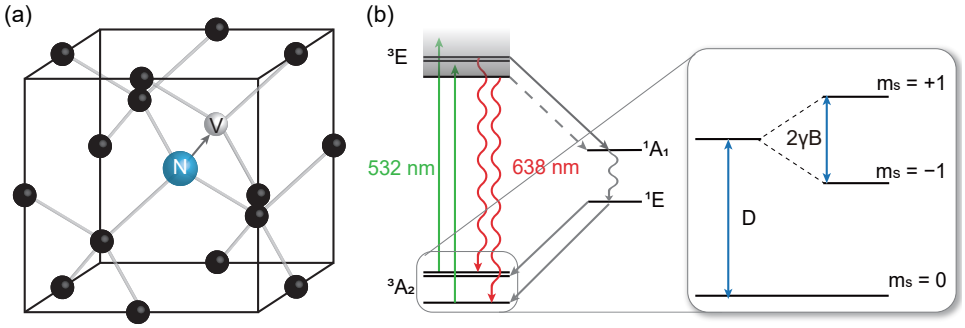


Figure 1.1: (a) Model of the carbon diamond lattice featuring a substitutional nitrogen adjacent to a vacancy, forming an NV center. The NV symmetry axis is aligned with the crystallographic axis. (b) Energy level diagram for the negatively charged NV center (NV^-). The ground state $^3A_2$ spin triplet has a zero-field splitting (ZFS) of approximately 2.87 GHz between the $m_s = 0$ ($|0\rangle$) and $m_s = \pm 1$ ($|\pm 1\rangle$) states. Under optical illumination (532 nm, green arrows), NV^- is excited to the first excited state ^3E, from which it radiatively decays back to the ground state, emitting fluorescence in the 638–800 nm range (red arrows) through a mostly spin-conserving process. NV^- in $m_s = \pm 1$ can also decay to the $^3A_2$ state via an alternative, spin-selective ISC pathway (dashed gray arrows), passing through the $^1A_1$ and ^1E states, which does not produce visible fluorescence. Expanded view: $^3A_2$ sublevels, where the $|0\rangle$ state is split from the $|\pm 1\rangle$ states by the ZFS D. The $|\pm 1\rangle$ sublevels further exhibit a Zeeman splitting proportional to the component of the applied magnetic field B along the NV axis.

can be written in the simplified form given in Ref. [2].

$$\frac{\hat{H}_{\text{gs}}}{h} = D(T)\hat{S}_z^2 + A_\parallel \hat{S}_z\hat{I}_z + A_\perp(\hat{S}_x\hat{I}_x + \hat{S}_y\hat{I}_y) + P\hat{I}_z^2. \tag{1.2}$$

The zero-field splitting (ZFS) parameter is $D(T) \approx 2.87$ GHz at room temperature, separating the $|m_s = 0\rangle$ and $|m_s = \pm 1\rangle$ sublevels. The ZFS is temperature dependent, with $dD/dT \approx -74$ kHz/K [4]. The electronic spin states exhibit additional splittings due to the hyperfine interaction with the nitrogen nuclear spin. For the naturally abundant ^{14}N isotope ($I = 1$), the axial hyperfine coupling is $A_\parallel \approx 2.14$ MHz, while for ^{15}N ($I = 1/2$) it is $A_\parallel \approx 3.03$ MHz [5, 6]. The transverse hyperfine couplings $A_\perp$ are of similar magnitude for the two isotopes, with $A_\perp \approx 2.70$ MHz for

^{14}N and $A_\perp \approx 3.65$ MHz for ^{15}N. Additionally, ^{14}N exhibits a nuclear quadrupole coupling of $P \approx -5.01$ MHz, whereas the ^{15}N isotope ($I = 1/2$) does not possess a quadrupole moment.

In the presence of an external magnetic field $\vec{B} = (B_x, B_y, B_z)$, the degeneracy of the $|m_s = \pm 1\rangle$ sublevels is lifted by the Zeeman interaction,

$$\hat{H}_{\text{Zee}}/h = g_e \mu_B (B_z \hat{S}_z + B_x \hat{S}_x + B_y \hat{S}_y), \tag{1.3}$$

where $g_e \approx 2.003$ is the NV center electronic g-factor and $\mu_B = 9.274 \times 10^{-24}$ J/T is the Bohr magneton. This corresponds to an NV electronic gyromagnetic ratio of $\gamma_e/2\pi \approx 28.04$ GHz/T.

Electric fields $\vec{E} = (E_x, E_y, E_z)$ and crystal strain also contribute additional terms to the electronic ground-state Hamiltonian with terms:

$$H_{\text{elec}}/h = d_\parallel E_z \hat{S}_z^2 - d_\perp E_x (\hat{S}_x^2 - \hat{S}_y^2) + d_\perp E_y (\hat{S}_x \hat{S}_y + \hat{S}_y \hat{S}_x), \tag{1.4}$$

where $d_\parallel = 103$ Hz/(V/m) is the axial electric dipole moment, and $d_\perp = 0.17$ Hz/(V/m) is the transverse electric dipole moment [7]; and

$$\begin{aligned} H_{\text{str}}/h = {} & M_z \hat{S}_z^2 + M_x (\hat{S}_x^2 - \hat{S}_y^2) + M_y (\hat{S}_x \hat{S}_y + \hat{S}_y \hat{S}_x) \\ & + N_x (\hat{S}_x \hat{S}_z + \hat{S}_z \hat{S}_x) + N_y (\hat{S}_y \hat{S}_z + \hat{S}_z \hat{S}_y), \end{aligned} \tag{1.5}$$

where M_x, M_y, M_z, N_x, and N_y are strain-dependent amplitudes [8]. The E_z and M_z term effectively shifts the zero-field splitting, while the remaining transverse stress terms may be negligible or suppressed depending on the experimental conditions (e.g., strong applied magnetic field). The sensitivity of the NV spin to these strain-induced interactions enables imaging of internal or external diamond

stress, which is valuable for diamond material characterization. However, for magnetic-field imaging applications [9], strain sensitivity can introduce unwanted perturbations and is therefore typically considered a potential limitation; this topic will be discussed in later chapters.

By considering only the dominant contributions, namely the zero-field splitting, axial stress, electric fields, and the Zeeman interaction, and neglecting the hyperfine and quadrupole structure, the transitions between the $|0\rangle$ and $|\pm1\rangle$ sublevels become:

$$f_\pm = |E_{\pm1} - E_0| = \big(D(T) + M_z + d_\parallel E_z\big) \pm \frac{g_e \mu_B}{h} B_z, \tag{1.6}$$

where E_{m_s} are the energy eigenstates of the corresponding $|m_s\rangle$ spin sublevels. The $|\pm1\rangle$ sublevels are shifted together relative to $|0\rangle$ by the zero-field splitting as well as axial crystal stress and electric fields, while the Zeeman interaction shifts the $|+1\rangle$ and $|-1\rangle$ levels in opposite directions. The NV ground-state spin can be coherently manipulated using microwave (MW) irradiation resonant with the $f_\pm$ transitions, which become nondegenerate when $B_z \neq 0$. Application of resonant or near-resonant MW control fields, together with continuous-wave or pulsed optical excitation, forms the basis of NV-based multimodal quantum sensing: shifts in the NV spin resonances $f_\pm$ lead to measurable changes in the detected NV fluorescence (also known as photoluminescence or PL). For sufficiently small perturbations (compared to the measurement dynamic range), shifts in $f_\pm$ relative to the applied MW frequency can be linearly mapped to changes in magnetic field, electric field, crystal stress, or temperature.

Apart from the microwave-controllable ground-state spin, the ability to optically initialize and read out the spin population is another critical property that makes the NV center in diamond an excellent quantum sensor. As illustrated in Figure 1.1(b), optical excitation from a pump laser (typically

532 nm) drives the NV electronic spin from the ground-state manifold ($^3A_2$) to the triplet excited state (^3E). The excited NV center can relax back to the ground state through the radiative pathway $^3E \rightarrow {}^3A_2$, emitting red fluorescence in the 637–800 nm range while preserving the spin projection m_s. In addition, the $|m_s = \pm 1\rangle$ levels have access to a spin-selective, non-radiative decay channel through an intersystem crossing (ISC) via the singlet states $^1A_1$ and ^1E, ultimately returning to the $|m_s = 0\rangle$ ground state with a branching ratio of $\sim 30\%$ [10].

As a result, the amount of red fluorescence emitted by the NV center directly reflects the spin-state population, and continuous optical excitation preferentially initializes the NV spin into the bright $|0\rangle$ state. The metastable ^1E state has a lifetime of approximately 200 ns at room temperature [4, 11], while the excited ^3E state has a lifetime of $t_{3E} \approx 13$ ns [12]. The absorption cross section for the $^3A_2 \rightarrow {}^3E$ transition at $\lambda = 532$ nm is $\sigma \approx 3.1 \times 10^{-17}$ cm^2 [13]. These parameters correspond to a saturation intensity of $I_{\text{sat}} \approx hc/\lambda\sigma t_{3E} \approx 0.9$ MW/cm^2, where c is the speed of light.

The ISC is also responsible for the reduced fluorescence of NV centers in the $|m_s = \pm 1\rangle$ sublevels, which emit fewer photons than those in $|m_s = 0\rangle$. The fractional fluorescence difference between these states, known as the fluorescence contrast, can reach $\sim 20\%$ for a single NV center [14] and $\sim 10\%$ for an NV ensemble [15]. In an optically pumped NV-diamond ensemble, the fluorescence intensity therefore reports the relative population in the $|m_s = 0\rangle$ and $|m_s = \pm 1\rangle$ states. A transition driven by a resonant microwave field that transfers population from $|0\rangle$ to $|\pm 1\rangle$ reduces the fluorescence due to increased ISC-mediated decay. This mechanism forms the basis for optical spin readout in NV-diamond-based quantum sensing.

1.2 NV-diamond for Quantum Sensing

Quantum sensing is one of the most promising near-term real-world applications of quantum science and technology. It leverages unique quantum properties, such as superposition, entanglement, and discrete energy levels, to measure physical quantities with precision that can exceed the limits of classical sensors. By encoding external perturbations (e.g., magnetic fields, electric fields, temperature, strain, or rotation) into the quantum state of well-controlled physical systems, quantum sensors achieve exceptional sensitivity and resolution [16]. Modern quantum sensing research builds on decades of advances in atomic physics and magnetic resonance, drawing from foundational technologies such as nuclear magnetic resonance (NMR), atomic clocks, atomic vapor magnetometers, superconducting quantum interference devices (SQUIDs), and solid-state spin defects. As discussed in the previous section, the NV center in diamond has emerged as a leading platform for quantum sensing due to its direct optical spin-state readout, controllable spin dynamics, and ability to operate under ambient conditions. These properties enable non-invasive, high-resolution measurements across a wide range of disciplines, including condensed-matter physics, materials science, biology, chemistry, and electronics.

The NV center in diamond is a versatile quantum sensor capable of detecting magnetic fields, electric fields, temperature, and crystal strain. As shown in Eq. (1.6), the resonant frequencies between the $|0\rangle$ and $|\pm1\rangle$ sublevels of the NV ground state are sensitive to all these perturbations. Magnetic fields induce a differential shift in the $f_\pm$ transition frequencies, whereas temperature, strain, and electric fields introduce common-mode shifts. This distinction enables the magnetic-field contribution to be isolated from other perturbations by independently measuring the $|0\rangle \rightarrow |+1\rangle$ and $|0\rangle \rightarrow |-1\rangle$ transitions, or through a single multi-tone measurement using double-quantum magnetometry, which will be discussed in Chapter 2. In this dissertation, we focus on the use of NV centers in diamond for

sensing magnetic fields.

The diverse range of magnetic sources studied using NV-based magnetometers can be categorized into three regimes according to the characteristic time scale of the signal: static or broadband magnetic fields (DC–100 kHz), narrowband oscillating fields (1 kHz–20 MHz), and high-frequency fields in the gigahertz range. Figure 1.2 summarizes conventional NV magnetometry protocols used to detect each class of magnetic signal.

1.2.1 Static and Broadband Magnetic Sensing Protocols

Continuous-wave optically detected magnetic resonance (CW-ODMR) is the simplest and most robust protocol for sensing broadband magnetic fields. Its technical simplicity has led to widespread adoption throughout the NV community. In CW-ODMR measurements, the NVs are continuously illuminated with a green pump laser while a MW field is simultaneously applied, as illustrated in Figure 1.2. A reduction in NV fluorescence occurs when the MW field is resonant or near-resonant with the $|0\rangle \rightarrow |\pm 1\rangle$ transitions, driving population into the $|\pm 1\rangle$ sublevels before optical pumping returns it to the bright $|0\rangle$ state. By sweeping the frequency of the applied MW field, an ODMR spectrum is obtained, with resonance frequencies that shift in response to external magnetic fields and other perturbations.

The sensitivity of ODMR-based magnetometry depends on both the contrast and the linewidth of the ODMR spectrum [17]. In NV ensembles, magnetic-field gradients, inhomogeneous microwave (MW) driving, and crystal strain all contribute to linewidth broadening. One effective strategy for reducing the ODMR linewidth is to lower the MW driving strength; however, in CW-ODMR, the competing effects of continuous laser excitation and MW driving inherently suppress the achievable

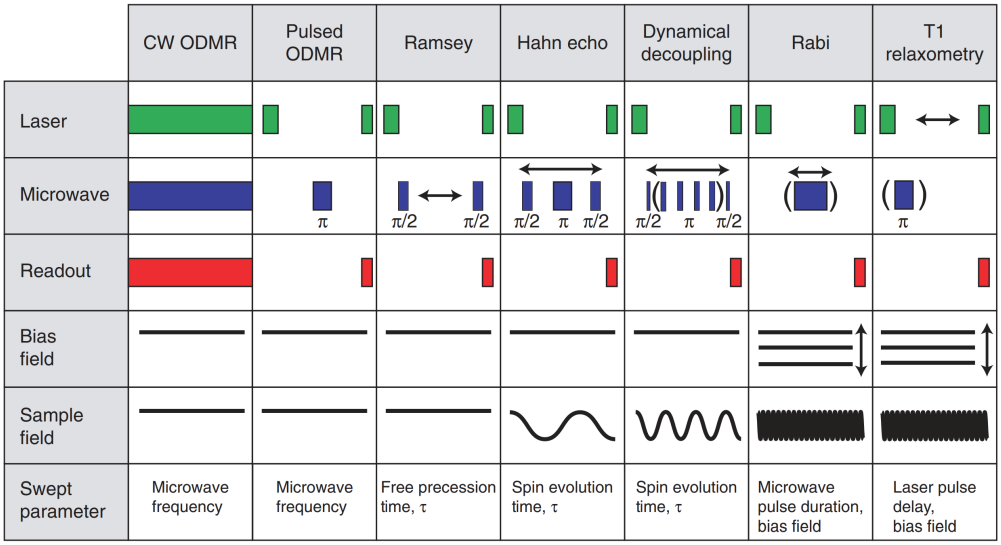


Figure 1.2: NV magnetometry protocols [18]. Schematic of timing and duration of laser pulses, MW pulses, and readout sequences relative to the field being sensed for common NV-diamond protocols. Swept parameters are indicated by arrows. Straight lines for the bias and sample fields indicate static magnetic fields, including the swept static bias field for Rabi and T_1 relaxometry. Sinusoidal curves represent time-dependent sample fields, which are very high frequency for Rabi and T_1 relaxometry.

fluorescence contrast. To overcome this limitation, pulsed-ODMR protocols separate spin initialization, MW control, and spin readout into distinct time windows, as illustrated in Figure 1.2. In a typical pulse sequence, an initial laser pulse polarizes the NV spin into the $|0\rangle$ state, a MW π-pulse transfers population between $|0\rangle$ and $|\pm 1\rangle$, and a final laser pulse performs spin-state readout. This temporal separation reduces power broadening and results in narrower resonance and similar contrast features compared to CW-ODMR. The MW power determines the duration of the π-pulse and must be optimized to balance ODMR linewidth and contrast. Despite improved performance relative to CW-ODMR, the linewidth in pulsed-ODMR still reflects two contributions: the intrinsic T_2^*-limited linewidth and the broadening associated with the finite-duration MW pulse. To optimize the magnetic sensitivity, these two effects are typically made comparable in magnitude [17].

Ramsey-based magnetometry protocols [19] offer superior magnetic sensitivity compared to ODMR techniques by temporally separating the magnetic-field sensing interval from both the optical initialization and MW control pulses. This separation eliminates power broadening effects and enables the use of higher laser intensity and MW field amplitude, increasing the collected fluorescence per measurement cycle. In a typical Ramsey sequence, a green laser pulse polarizes the NV ensemble into the $|m_s = 0\rangle$ state, followed by a resonant $\pi/2$ MW pulse that creates a coherent superposition between two spin sublevels (e.g., $|m_s = 0\rangle$ and $|m_s = +1\rangle$, or the double-quantum $|+1\rangle$ and $|-1\rangle$ states). During the subsequent free precession interval, τ, the MW and laser fields remain off while the superposition evolves under the local magnetic environment and accumulates a dynamic phase $\phi = 2\pi\gamma|B_0 + B_s|\tau$,where γ is the NV gyromagnetic ratio and $|B_0 + B_s|$ is the total field experienced by the NV centers.

After phase accumulation, a second $\pi/2$ pulse maps the dynamic phase onto the population difference of the spin states, which is then measured optically using spin-dependent fluorescence contrast. By sweeping the free precession time, one obtains the characteristic Ramsey fringes, sinusoidal oscillations whose envelope decays over the ensemble dephasing time T_2^*, where $T_2^* \approx 1/(\pi\Gamma)$ for a Lorentzian linewidth Γ. Although mapping out the full Ramsey fringe pattern allows extraction of the resonance frequency via Fourier transform, this procedure is inefficient for magnetometry. Instead, τ is typically fixed near T_2^* to interrogate the fringe at its point of maximum slope, yielding a highly sensitive DC magnetometry curve. Small changes in magnetic field shift the phase and produce a corresponding oscillation in the detected fluorescence. This approach maximizes magnetic sensitivity while preserving a wide dynamic range, since varying τ enables trade-offs between sensitivity and field range. Furthermore, Ramsey magnetometry benefits from compatibility with techniques such as spin-bath driving to mitigate dephasing [20], and can be implemented in the double-quantum (DQ)

basis to enhance immunity to common-mode noise [21]. Overall, Ramsey interferometry provides a robust, power-broadening-free sensing protocol limited fundamentally by the ensemble dephasing time T_2^*.

1.2.2 AC and Narrowband Magnetic Sensing Protocols

For oscillating magnetic fields, Hahn spin echo [22] provides a fundamental sensing scheme. The Hahn echo sequence, illustrated in Figure 1.2, builds directly upon the Ramsey protocol by inserting a π-pulse midway through the free-precession interval to refocus ensemble dephasing. This refocusing cancels phase dispersion arising from static or slowly varying inhomogeneities such as stress gradients or dipolar interactions with the diamond spin bath. As a result, the Hahn echo extends the relevant coherence timescale from the inhomogeneous dephasing time T_2^* to the spin coherence time T_2, which is typically an order of magnitude longer and determined by dynamical fluctuations in the local magnetic environment [23].

In addition to prolonging coherence, the Hahn echo sequence makes the NV sensor selectively sensitive to narrowband, oscillating (AC) magnetic fields. The applied MW π and $\pi/2$ pulses act as a frequency-domain filter with linewidth determined by the filter response function [24]. By choosing appropriate rotation axes for the final $\pi/2$ pulse (e.g., $\{y, -y\}$ or $\{x, -x\}$), the measurement can be configured to be either linearly sensitive to an AC magnetic field amplitude or quadratically sensitive to magnetic noise with zero mean but finite variance. Optimal sensitivity occurs when the total evolution time τ between the $\pi/2$ pulses approaches T_2; however, in conventional Hahn echo magnetometry this condition is typically not satisfied because the evolution time $\tau/2$ must match half the period of the target AC magnetic field.

To improve the AC sensitivity, multiple refocusing pulses can be introduced to extend the effective coherence time and narrow the spectral filter function. This class of sequences, known as dynamical decoupling (Figure 1.2), includes widely used NMR-derived protocols such as CPMG-n and XY8-n, which have been extensively adopted in NV experiments [24]. The Carr–Purcell–Meiboom–Gill (CPMG) protocol generalizes Hahn echo by introducing a train of N equally spaced π-pulses during the free evolution. This sequence enhances dynamical decoupling from environmental noise, extending the coherence time to T_2^{CPMG}, which increases approximately as $N^{2/3}$ in typical NV-diamond environments that assuming the electronic spin bath is the dominant decoherence source [25]. Because the repeated π pulses act as a spectral filter, CPMG is highly sensitive to oscillating magnetic fields with frequencies matched to the pulse spacing, enabling narrowband AC magnetometry with sub-nanotesla sensitivity. Increasing the pulse number sharpens the filter function and shifts the detection window to higher frequencies, making dynamic decoupling a powerful tool for probing spin noise spectra, detecting nanoscale nuclear spins, and enhancing sensitivity to weak AC magnetic signals.

The sensing frequency range of dynamical decoupling sequences is experimentally limited by the maximum achievable amplitude of MW control pulses, typically restricting detection to frequencies below $\sim 20\,\mathrm{MHz}$. To extend this range up to GHz frequency signals, one can employ a quantum frequency mixer (QFM) [26, 27], in which an applied AC bias field mixes a high-frequency target magnetic field down to a MHz-scale signal compatible with dynamical decoupling-based detection. This technique will be discussed in detail in Chapter 4.

A simpler approach is Rabi magnetometry [28, 29], which provides a direct method for sensing magnetic fields oscillating at or near the NV electronic spin transition frequency in the GHz range, thereby complementing the information obtained from CW-ODMR measurements [30]. Following

optical initialization into the $|m_s = 0\rangle$ state, a continuous resonant MW field is applied for a variable duration. When the MW frequency matches the NV transition (e.g., $|m_s = 0\rangle \leftrightarrow |m_s = +1\rangle$), the spin population undergoes coherent Rabi oscillations at a frequency $\Omega_R \propto \sqrt{P_{\mathrm{MW}}}$, where P_{MW} is the power of the applied MW field. Because the Rabi frequency depends on both the local MW magnetic-field amplitude and the detuning from the NV resonance, Rabi measurements enable spatial mapping of MW drivinginhomogeneities, characterization of local magnetic environments, and wide-field imaging without requiring long free-precession intervals.

T_1 relaxometry probes magnetic noise at or near the NV resonance frequency by measuring the longitudinal relaxation time of the NV spin. After optical initialization into the $|m_s = 0\rangle$ state, the NV is allowed to relax in the dark for a time τ before a readout pulse measures the remaining spin polarization. This relaxation process typically follows an exponential decay with characteristic time T_1, which can reach up to several milliseconds at room temperature when dominated by phonon interactions [31]. T_1 can be strongly reduced by magnetic frequency noise or nearby paramagnetic spins with fluctuations at the NV transition frequency (approximately 2.87 GHz). By sweeping the applied bias magnetic field, one can tune the NV transition frequency, thereby probing the spectral density of magnetic noise across a range of frequencies. This makes T_1 relaxometry particularly useful for detecting paramagnetic species, probing high-frequency spin noise, and imaging magnetic nanoparticles or biomolecular spin labels.

1.3 Quantum Diamond Microscope

The Quantum Diamond Microscope (QDM) is a wide-field magnetic imaging platform that leverages ensembles of NV centers in diamond to map magnetic fields with high spatial resolution,

high sensitivity, and real-time acquisition capability. By combining optical excitation, spin-dependent fluorescence readout, and microwave control of the NV ground-state spin manifold, the QDM enables pixel-parallel detection of local magnetic fields across a large field of view. Unlike scanning probe techniques, which acquire data point-by-point, the QDM uses a camera to simultaneously image a thick and dense NV layer embedded beneath the diamond surface, allowing rapid reconstruction of magnetic field maps produced by the sample. The spatial resolution of the QDM is typically at the micron scale, limited primarily by two factors [32]:

1. **Diffraction Limit:** The NV fluorescence wavelength (λ) ranges from 636 to 800 nm. With a free-space objective of numerical aperture (NA) less than 1, the spatial resolution is constrained by diffraction, yielding a resolution limit of approximately $> \frac{\lambda}{2\mathrm{NA}} \approx 0.5\,\mu\mathrm{m}$.

2. **NV Layer Thickness:** To suppress photon shot noise and improve sensitivity, a larger sensing volume of the NV ensemble is desired. Thus, the thickness of the NV layer is typically 1 to 10 $\mu\mathrm{m}$, which further limits spatial resolution to the micron scale.

1.3.1 Basic Components and Design Consideration of QDM

A schematic of a typical QDM setup is shown in Fig. 1.3. The core components of a QDM include a diamond slab containing a dense layer of near-surface NV centers for magnetic sensing; a bias magnetic field, provided either by permanent magnets or Helmholtz coils, to define the NV quantization axis and suppress transverse magnetic noise; an optical pumping laser used to initialize and read out the NV spin state; and a MW delivery structure to generate MW pulses that drive transitions between the NV ground-state spin sublevels. The NV fluorescence is collected and imaged onto a camera using a finite-conjugate wide-field imaging system consisting of a microscope objective,

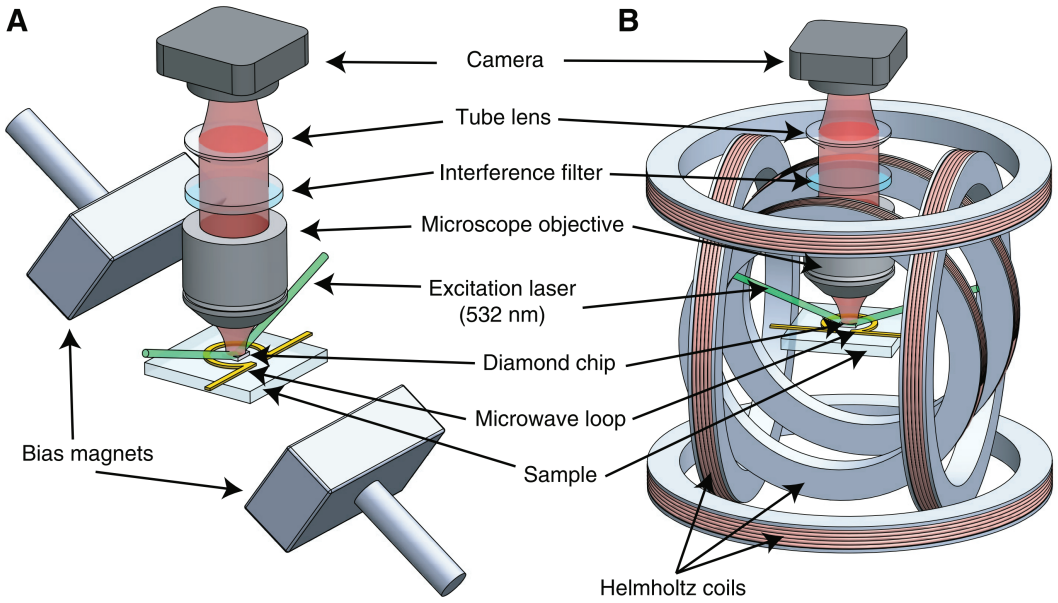


Figure 1.3: Quantum Diamond Microscope (QDM) [18]. Examples of QDM setups using (a) permanent magnets and (b) Helmholtz coils to apply a bias magnetic field. In both configurations, a 532-nm excitation laser illuminates the diamond chip, and optics collect NV fluorescence onto a camera. An interference filter is used to transmit NV fluorescence while blocking scattered excitation light. A planar gold omega-loop, fabricated onto a substrate, is shown delivering microwaves to the diamond chip for NV control.

a tube lens, and appropriate optical filters. Together, these components enable wide-field imaging of magnetic fields across the diamond surface.

The properties of the diamond sensor itself strongly influence the overall performance of the QDM. The NV density determines the available signal and therefore impacts the magnetic sensitivity [17]. However, excessive NV concentration or inhomogeneity in strain and impurity density can broaden spin resonances, leading to shorter spin lifetimes T_2^* and T_2, consequently degrading performance. Additionally, the NV layer thickness should be matched to the sample geometry to maximize signal while minimizing stand-off distance.

The laser illumination system plays a critical role in both NV spin initialization and optical readout. The required optical power scales with the field of view (FOV); typically, high-power green

lasers at 532 nm are used due to their availability and compatibility with NV excitation. Achieving a 500 μm-scale FOV generally requires 5–10 W of optical power. Although fluctuations in laser intensity, on timescales much longer than the NV sensing sequence (μs to tens of μs), can be compensated through signal and reference normalization, long-term laser power drift directly affects the maximum achievable averaging time by degrading the stability of fluorescence contrast. Because the four NV orientations in diamond are crystallographically distinct, the laser polarization has to be chosen carefully. To efficiently excite the NV orientation aligned with the bias magnetic field, the laser polarization should be oriented orthogonal to the bias-field direction to maximize NV optical transition electric dipole coupling. Additionally, ensuring spatially homogeneous illumination across the FOV is essential for achieving uniform sensor response and minimizing spatial variations in initialization efficiency.

The MW delivery system determines the uniformity and stability of NV spin manipulation across the FOV. Amplitude and phase fluctuations in the MW drive introduce noise that degrades magnetic sensitivity, while spatial inhomogeneities in the MW field lead to variations in the NV Rabi frequency across the imaging area. For wide-field QDM imaging, achieving high MW uniformity is therefore a key design requirement. One effective approach to improving MW homogeneity is to increase the diameter of the antenna structure; however, doing so reduces the MW field intensity and consequently lowers the achievable Rabi frequency. In general, QDM operation benefits from higher Rabi frequencies for several reasons: driving all nuclear-spin hyperfine transitions ($\approx$1.5 MHz for $^{15}\mathrm{N}$ and 2.2 MHz for $^{14}\mathrm{N}$), suppressing linewidth broadening caused by crystal strain and bias-field inhomogeneity, and shortening the sensing sequence duration. Thus, the design of the MW delivery system must balance field uniformity with sufficient Rabi strength. These considerations and their implementation in our system are discussed in detail in Chapter 2.

The static bias field B_0 defines the NV quantization axis and sets the energy splitting between

spin sublevels. However, spatial gradients in the bias field produce variations in the local resonance frequency, leading to nonuniform magnetic sensitivity across the measurement region. Careful bias-field engineering using permanent magnets or Helmholtz coils is required to ensure field uniformity.

The optical imaging system also plays a central role in QDM performance. The NA of the objective lens determines both the fluorescence collection efficiency and the optical resolution. The microscope components, including the objective and tube lens, must be chosen to provide the desired field-of-view and magnification while minimizing aberrations.

The camera determines the pixel sampling, dynamic range, and temporal bandwidth of the QDM. Pixel size should oversample the optical diffraction limit to avoid loss of spatial information. Parameters such as frame rate, full-well depth, and pixel count set the maximum achievable magnetic sensitivity for a given experiment. Data-transfer rates and on-board memory also limit the maximum acquisition speed. The camera's quantum efficiency is typically lower than that of photodiodes, affecting the overall photon shot-noise limit.

Finally, the mechanical and magnetic environment surrounding the diamond must be stabilized. The diamond mount, typically sapphire or SiC wafer, should minimize thermal drift and mechanical vibration, both of which can introduce phase noise or image distortions. External magnetic fields, such as the Earth's field or electronic noise, must be suppressed or compensated to prevent unwanted shifts in the NV resonance frequencies.

Together, these considerations highlight the complexity and interdisciplinary nature of QDM design. Optimizing each subsystem is essential to achieving high-quality, wide-field magnetic imaging using NV center ensembles in diamond.

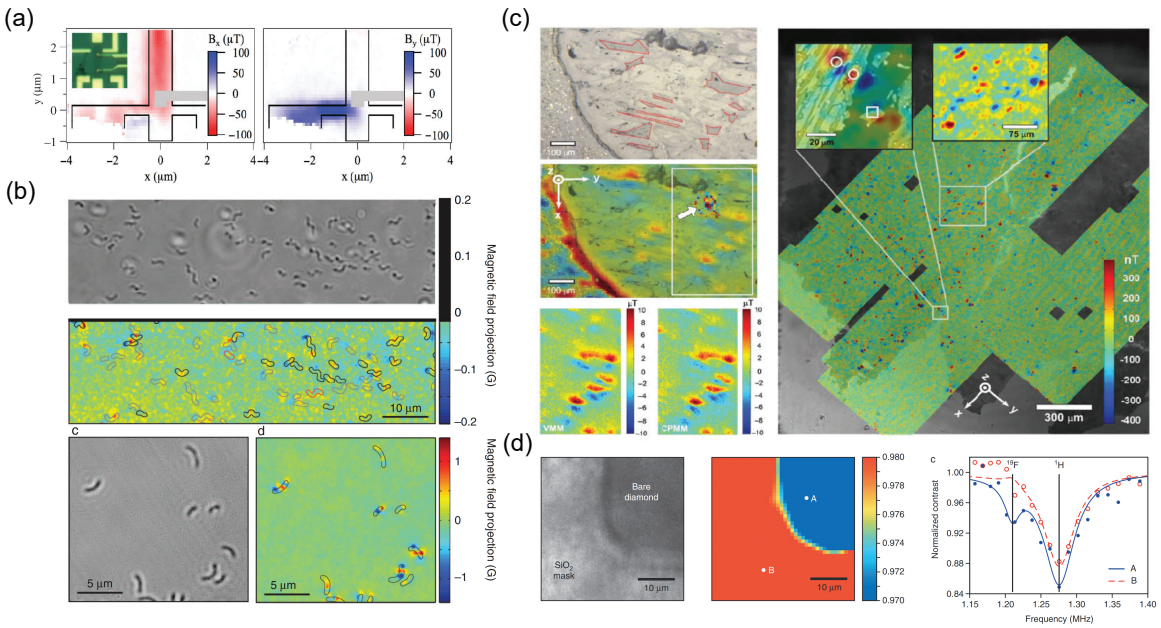


Figure 1.4: QDM applications. (a) Parabolic hydrodynamic current density flow profile in graphene at the Dirac point [33]. (b) Magnetic field image of magnetite intrinsic to MTB bacteria [34]. (c) Remnant magnetization of a geological sample [35]. (d) Spatially-resolved NMR detection of ^{19}F nuclear spins on the diamond surface [36].

1.3.2 Established QDM Applications and Limitations

In the past decade, the QDM has been applied across a diverse range of fields, including fundamental physics [33], bioscience [34], geology [35], integrated circuit analysis [36], and micron-scale NMR detection [37], as shown in Fig. 1.4. These works demonstrate that QDMs can acquire high–spatial resolution magnetic images over a wide range of samples and physical systems. Despite these successes, the previous generation of QDMs exhibits several important limitations.

All demonstrated DC and broadband QDM magnetic imaging techniques rely on ODMR-based sensing. As discussed in the previous section, the sensitivity of ODMR measurements is limited compared to Ramsey-type protocols due to the overlap of the sensing period with MW driving. For

applications involving weak magnetic signals, such as those generated by single neurons or cardiac activity, picoTesla-scale sensitivity is required to obtain magnetic images within reasonable averaging times, which is challenging for ODMR-based QDMs. In addition, although CCD cameras used in earlier QDMs provide low noise and high-quality magnetic images, their slow acquisition rates significantly limit the temporal resolution. This restriction makes it difficult to image rapidly evolving broadband magnetic fields or dynamical processes.

For high-frequency narrowband magnetic imaging, the NMR imaging work by DeVience *et al.* [37] serves as a prototype for Chapter 5 of this dissertation. While their demonstration successfully mapped spatial variations in NMR signals, the use of an optical chopper and a slow CCD camera limited the spectral resolution and sensitivity, preventing adaptation to high-performance methods such as coherently averaged synchronized readout (CASR) [38].

Here, we demonstrate an improved QDM architecture with advancements in camera technology, signal generation, and sensing protocols that enable next-generation quantum magnetic microscopy. On the hardware side, we design and construct a QDM incorporating a high-speed lock-in camera capable of kiloframes-per-second operation, along with an arbitrary waveform generator (AWG) for implementing advanced pulsed quantum sensing protocols. These improvements allow established pulsed NV measurement techniques, previously not demonstrated in a wide-field imaging format, to be applied to QDMs. We demonstrate static and broadband magnetic imaging using Ramsey sequences, narrowband signal imaging via dynamical decoupling, and NMR imaging using the CASR protocol. With enhanced sensitivity and temporal resolution, this next-generation QDM significantly expands the range of detectable signals and physical phenomena, opening new opportunities for scientific discovery and technological applications.

1.4 Organization of this Dissertation

This dissertation is organized to present a progression of advances in quantum magnetic microscopy using NV centers in diamond, beginning with Ramsey-based broadband magnetic imaging, extending to narrowband and wide-frequency-range sensing techniques, and culminating in real-space NMR imaging and industrial applications.

Chapter 2 focuses on broadband magnetic imaging with a QDM, drawing upon the Ramsey-imager framework reported in Ref. [39]. This chapter introduces the principles of sensitive pulsed DC magnetic sensing, including double-quantum four-Ramsey (DQ4R) protocols and spin-bath driving, followed by a detailed experimental implementation of a Ramsey-based wide-field imager. It further presents the design and simulations of the microwave delivery structure used to generate strong and homogeneous Rabi frequencies across the QDM field of view, as well as simulations of the magnetic field patterns produced by a custom-designed micron-scale phantom. These simulations are compared with experimentally measured images, revealing strong agreement between theory and experiment. The chapter concludes with an analysis of sensitivity and spatial resolution, highlighting the advantages of pulsed sensing techniques over conventional ODMR-based approaches.

Chapter 3 extends QDM capabilities to narrowband magnetic imaging, based on the work reported in Ref. [15]. This chapter introduces the operating principles of narrowband magnetometry using dynamical decoupling sequences and demonstrates wide-field XY8 and CASR imaging results. These techniques enable simultaneous imaging of the amplitude, frequency, and phase of oscillatory magnetic fields. The chapter also details the optimization of dynamical decoupling sequences for enhanced AC sensitivity, including the trade-off between sensitivity and spatial noise and a comprehensive analysis of dominant noise sources. Together, these developments significantly improve QDM performance for

applications involving AC magnetic imaging.

Chapter 4 further extends the sensing frequency range of the dynamical-decoupling-based methods introduced in Chapter 3 by employing the QFM-CASR protocol reported in Ref. [27]. This chapter explains how QFM-CASR enables wide-frequency-range magnetic spectroscopy by converting high-frequency signals, spanning from tens of MHz to multiple GHz, into the NV-detectable band, while simultaneously achieving sub-Hz spectral resolution. It presents experimental demonstrations of high-resolution spectroscopy of multi-frequency signals up to 4 GHz, achieving nanotesla-scale noise floors and phase measurement precision below 1°. These results show that QFM-CASR overcomes the intrinsic $\lesssim 20$ MHz bandwidth limitation imposed by MW pulse control in conventional NV-diamond protocols, extending the accessible signal frequency range by more than an order of magnitude. As a result, this technique opens new avenues for radio-frequency and microwave magnetic microscopy, as well as tesla-scale NMR spectroscopy of small samples.

Chapter 5 presents ongoing work on real-space NMR microscopy using a QDM. The chapter begins by discussing the fundamental challenges associated with detecting thermally polarized nuclear spins with NV centers and describes several modifications to our experimental setup designed to overcome these limitations. It then demonstrates CASR-based detection of NMR signals using a photodiode, alongside inductive NMR measurements for validation, and presents preliminary results of spatially resolved NMR imaging and T_2 mapping of liquid samples. The chapter concludes by outlining the future potential of real-space NMR imaging with QDMs and the broader scientific and technological applications such a platform may enable.

Chapter 6 turns to industrial applications of quantum magnetic microscopy, drawing on the author's research internship experience at Toyota Research Institute of North America. This chapter examines low-SWaP (size, weight, and power) considerations essential for deploying quantum sensors

outside the laboratory and describes the development of a compact quantum magnetic camera tailored for electric vehicle battery inspection. The chapter concludes with demonstrations of several industrial use cases, highlighting the practical relevance and translational potential of QDM technology in real-world environments.

Finally, Chapter 7 outlines future research directions for advancing quantum magnetic microscopy. It highlights opportunities to improve DC sensing by mitigating NV-NV interactions, to achieve vector imaging of arbitrary-frequency AC signals, and to extend QDM-based NMR methods toward diffusion imaging. These prospective developments point toward a next generation of QDM platforms capable of probing increasingly complex physical phenomena.

Chapter 2: Ramsey-based Static Magnetic Microscopy

This chapter is primarily based on the work reported in Ref. [39], a project I carried out in collaboration with Jiashen Tangas co-leads on the project. The Ramsey-based QDM was first conceptualized in the Walsworth group with Jennifer Schloss as project lead [40], while the sensing protocol employed in our work builds on the DQ4R scheme developed by Connor Hart and collaborators [21] and the spin-bath driving technique introduced by Erick Bauch and collaborators [20]. Standing on the foundations laid by these outstanding former members of the Walsworth group, Jiashen and I realized the Ramsey imager and demonstrated its capabilities through static magnetic imaging and broadband dynamic imaging of spatial field patterns generated by a micron-scale circuit phantom.

This dissertation chapter focuses largely on my contributions to the project, including the design and simulation of the circuit phantom and microwave delivery structure, implementation of spin-bath driving using an AWG, comparison of simulated and experimentally acquired magnetic images, and a brief analysis of sensitivity and spatial noise. Detailed descriptions of the broadband dynamic imaging results and the denoising procedures used to extract pT-scale signals are presented in the original publication and Jiashen's doctoral dissertation.

2.1 Protocols and Techniques for Ramsey Magnetometry with QDM

2.1.1 Sensitivity of Ramsey Magnetometry with NV Ensembles

As discussed in the previous chapter, Ramsey interferometry is a protocol that extracts small changes in magnetic fields by measuring the dynamical phase accumulated by a quantum superposition state during the free-precession interval. Compared with the conventional ODMR technique, Ramsey

magnetometry separates the sensing period from the spin-state control operations (initialization, MW driving, and readout), leading to improved magnetic-field sensitivity. For Ramsey magnetometry using an NV ensemble in diamond, the photon shot-noise-limited sensitivity is given by [17]:

$$\eta_{shot} = \frac{\hbar}{\Delta m_s g_e \mu_B} \frac{1}{C e^{-(\tau/T_2^*)^p} \sqrt{N}} \frac{\sqrt{t_{I,R} + \tau}}{\tau}, \tag{2.1}$$

where $g_e \approx 2.003$ is the NV center's electronic g-factor, μ_B is the Bohr magneton, and $\hbar$ is the reduced Planck constant. The factor Δm_s denotes the difference between the magnetic sublevels used for sensing; C is the optical measurement contrast at zero free-evolution time ($\tau = 0$); T_2^* is the NV spin dephasing time; and p characterizes the functional form of the Ramsey-envelope decay. The parameter N is the average number of photons collected per measurement, and $t_{I,R}$ represents the combined initialization and readout time in the Ramsey sequence.

The Ramsey sensitivity is optimized when the sensing time τ is approximately equal to the spin dephasing time T_2^* of the NV ensemble. Consequently, for a fixed NV sensing volume and optical pumping power, which together determine the photon number N and the initialization and readout time $t_{I,R}$, extending the spin dephasing time T_2^* is a direct and effective method to improve the Ramsey sensitivity. The NV ensemble dephasing time T_2^* can be expressed as [17]:

$$\begin{aligned} \frac{1}{T_2^*} \approx & \frac{1}{T_2^*\{\text{electronic spin bath}\}} + \frac{1}{T_2^*\{\text{nuclear spin bath}\}} \\ & + \frac{1}{T_2^*\{\text{strain gradients}\}} + \frac{1}{T_2^*\{\text{electric field noise}\}} \\ & + \frac{1}{T_2^*\{\text{magnetic field gradients}\}} + \frac{1}{T_2^*\{\text{temperature variation}\}} \\ & + \frac{1}{T_2^*\{\text{undetermined}\}} + \frac{1}{2T_1}. \end{aligned} \tag{2.2}$$

where the notation $T_2^*\{X\}$ denotes the hypothetical dephasing limit arising solely from mechanism X (in the absence of all other processes). Equation (2.2) assumes that all dephasing mechanisms are independent and that their associated rates add linearly. This linear addition is strictly valid only when each mechanism produces a single-exponential free-induction decay (i.e., a Lorentzian spectral lineshape).

To extend the NV ensemble dephasing time T_2^*, various techniques have been developed to mitigate the individual contributions in Eq. (2.2). Spin-bath driving [20] suppresses dipolar interactions between NV electronic spins and the surrounding electronic spin bath. Carbon-isotope purification during diamond growth reduces the nuclear spin bath arising from naturally abundant $^{13}\mathrm{C}$; in our experiments, we use a diamond with $^{12}\mathrm{C}$ enrichment exceeding 99.995%. Strain gradients, electric-field noise, and temperature variations introduce common-mode shifts to the NV ground-state transition frequencies according to Eq. (1.6). These noise sources can be effectively suppressed using double-quantum (DQ) driving [41], which simultaneously drives both $|0\rangle \leftrightarrow |+1\rangle$ and $|0\rangle \leftrightarrow |-1\rangle$ transitions. Magnetic-field gradients can be minimized by employing a Halbach array or a Helmholtz coil and carefully aligning the applied bias field.

In the following subsections, we describe the implementation of the spin-bath driving technique and DQ sensing protocol in our QDM system and show how they lead to an enhanced T_2^* and improved magnetic-field sensitivity.

2.1.2 Implementation of the Spin-bath Driving Technique

Spin-bath driving [20] is used to decouple dipolar interactions between the NVs and paramagnetic bath spins ($S = 1/2$) in the diamond, including neutral nitrogen $^{15}\mathrm{N}_s^0$ (as we are using ^{15}N-enriched

NV-diamond) and free electrons. A strong, multi-tone radio frequency (RF) drive signal is applied throughout the NV layer to induce rapid Rabi oscillations of the bath spins. The effective dipole moments of these spins are then time-averaged to zero, which reduces their inhomogeneous broadening effect on the NV spin resonance and extends the NV spin dephasing time (T_2^*).

The frequency components of the RF drive need to be resonant with the various bath-spin transitions, which are experimentally determined using NV double electron-electron resonance (DEER) [42] as shown in Figure 2.1(a). To estimate the frequency scanning range for measuring the NV DEER spectrum, we first calculate the expected bath-spin transition frequencies. The free-electron spin transition frequency can be determined from $\gamma_e|\vec{B}|$, where γ_e is the electron gyromagnetic ratio, and $|\vec{B}|$ is the magnitude of the applied bias magnetic field. The transition frequency spectrum for $^{15}\mathrm{N}_s^0$ is calculated using its ground-state Hamiltonian [43]

$$\frac{\hat{H}}{h} = \frac{\mu_B}{h}\vec{B}\cdot\overline{g}\cdot\vec{\hat{S}} + \frac{\mu_N}{h}\vec{B}\cdot\vec{\hat{I}} + \vec{\hat{S}}\cdot\overline{A}\cdot\vec{\hat{I}}, \tag{2.3}$$

where μ_B is Bohr magneton, h is the Planck's constant, $\vec{B} = (B_x, B_y, B_z)$ is the applied bias magnetic field vector, $\overline{g}$ is the electronic g-factor tensor, μ_N is the Bohr magneton, $\vec{\hat{S}} = (\hat{S}_x, \hat{S}_y, \hat{S}_z)$ is the dimensionless electronic spin vector, $\overline{A}$ is the hyperfine tensor, and $\vec{\hat{I}} = (\hat{I}_x, \hat{I}_y, \hat{I}_z)$ is the dimensionless nuclear spin vector. When the z-axis is chosen as one of the four NV crystal axis directions, tensors $\overline{g}$ and $\overline{A}$ are diagonal and defined by

$$\overline{g} = \begin{bmatrix} g_\perp & 0 & 0 \\ 0 & g_\perp & 0 \\ 0 & 0 & g_\parallel \end{bmatrix}, \quad \overline{A} = \begin{bmatrix} A_\perp & 0 & 0 \\ 0 & A_\perp & 0 \\ 0 & 0 & A_\parallel \end{bmatrix}. \tag{2.4}$$

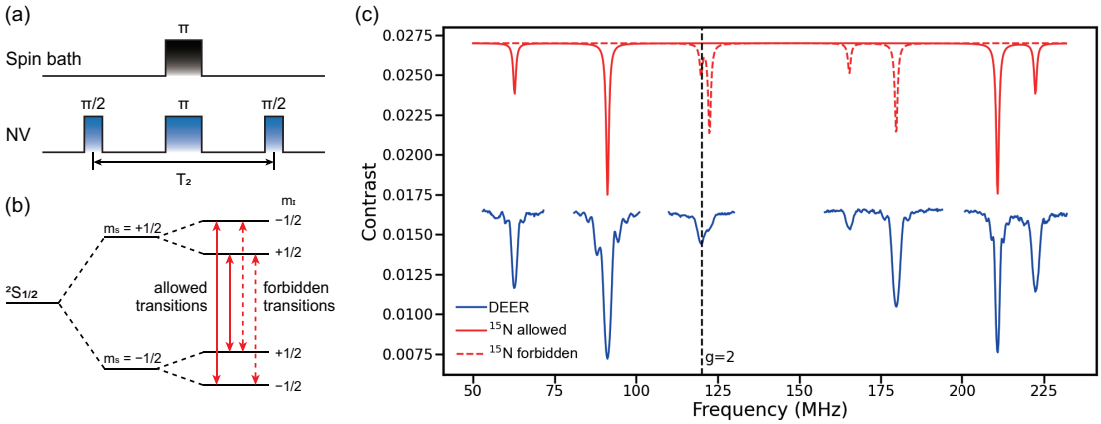


Figure 2.1: (a) NV double electron-electron resonance (DEER) technique for measuring the $^{15}\mathrm{N}_s^0$ and free-electron spin resonance spectrum in the QDM diamond sensor. The total free evolution intervals between the initial and final single-quantum (SQ) $\pi/2$ pulse on the NV spins is chosen to match the ensemble NV spin-echo T_2 for optimal sensitivity to bath-spin resonances. The frequency of the SQ π pulse on the bath spins is swept to measure the NV DEER spectrum by the effect on the NV ensemble fluorescence contrast (see Ref. [20] for details). (b) Energy level diagram of the coupled electron-nuclear spin system in $^{15}\mathrm{N}_s^0$. (c) Simulated $^{15}\mathrm{N}_s^0$ and free-electron ($\mathrm{g} = 2$) spin resonance spectrum (red) overlaid with NV DEER measurement results (blue) and offset vertically for clarity. The simulated resonant frequencies are broadened by a Lorentzian function with linewidth and relative contrast chosen to approximate the measurement data.

where $g_\perp$, $g_{||}$, $A_\perp$, and $A_{||}$ are the gyromagnetic and hyperfine on and off-axis components, respectively. $^{15}\mathrm{N}_s^0$ has $S = 1/2$ and $I = 1/2$, leading to the four eigenstates $|m_S = \pm 1/2, m_I = \pm 1/2\rangle$. The two corresponding dipole-allowed transitions ($\Delta m_S = \pm 1$, $\Delta m_I = 0$, solid arrows), along with the two first-order forbidden transitions ($\Delta m_S = \pm 1$, $\Delta m_I = \pm 1$, dashed arrows) are shown in Figure 2.1(b).

Using $g_\perp = g_{||} = 2$, $A_\perp = -559.7\,\mathrm{MHz}$, $A_{||} = -113.83\,\mathrm{MHz}$, and $|\vec{B}| = 4.278\,\mathrm{mT}$ aligned with an NV axis, we simulate the $^{15}\mathrm{N}_s^0$ resonance spectrum, as shown in Figure 2.1(c). In the experiment, we align the bias magnetic field with one of the four NV orientations, which results in an equal projection onto the remaining three NV axes at an angle of $\theta = 109.5°$. We first solve the Hamiltonian for both on-axis and off-axis $^{15}\mathrm{N}_s^0$ defects and calculate the corresponding eigenvalues. We then

determine the allowed and forbidden transition frequencies by taking pairwise differences between eigenvalues associated with each eigenstate. Finally, we generate Lorentzian peaks with identical linewidths but with a contrast ratio of one to three between the on-axis and off-axis transitions. For a free electron spin with $g = 2$, the resonance frequency is given by $f = g\mu_B|\vec{B}|/h$. The experimentally measured NV DEER spectrum is also shown in Figure 2.1(c), and it agrees well with the simulation.

After calibration of the RF frequency components, the Rabi driving frequencies associated with the dipole-allowed $^{15}N_s^0$ and free-electron transitions are increased to about 2 MHz, limited by the available power of the amplifier. The NV dephasing time T_2^* improves with increasing bath-spin Rabi frequency, and is eventually limited by the next dominant dephasing source (NV-NV interactions). The employed RF loop produces spatially-dependent Rabi driving amplitudes, broadening the distribution of T_2^* as indicated in the Section 2.3.3 of this chapter.

2.1.3 Implementation of the DQ4R Protocol Using a Lock-In Camera

The Ramsey sequence for magnetic imaging utilizes dual-tone MW pulses and a MW-phase alternation scheme to achieve uniform magnetic sensitivity over the field of view [21]. The dual-tone MW pulse generates a double-quantum (DQ) coherence between the $|m_s = +1\rangle$ and $|m_s = -1\rangle$ ground state spin triplet sublevels of the NV center. Compared to using a single-quantum (SQ) coherence between $|m_s = 0\rangle$ and $|m_s = +1\rangle$ or $|m_s = -1\rangle$, the DQ scheme is twice as sensitive to magnetic fields and can isolate magnetic signals from spurious strain and temperature artifacts. However, heterogeneity of MW control fields, diamond strain, and temperature can cause errors in DQ pulses across the NV ensemble and generate a residual SQ coherence. Thus a single DQ Ramsey measurement is still not free from spurious signals unless pulse errors are mitigated. To overcome

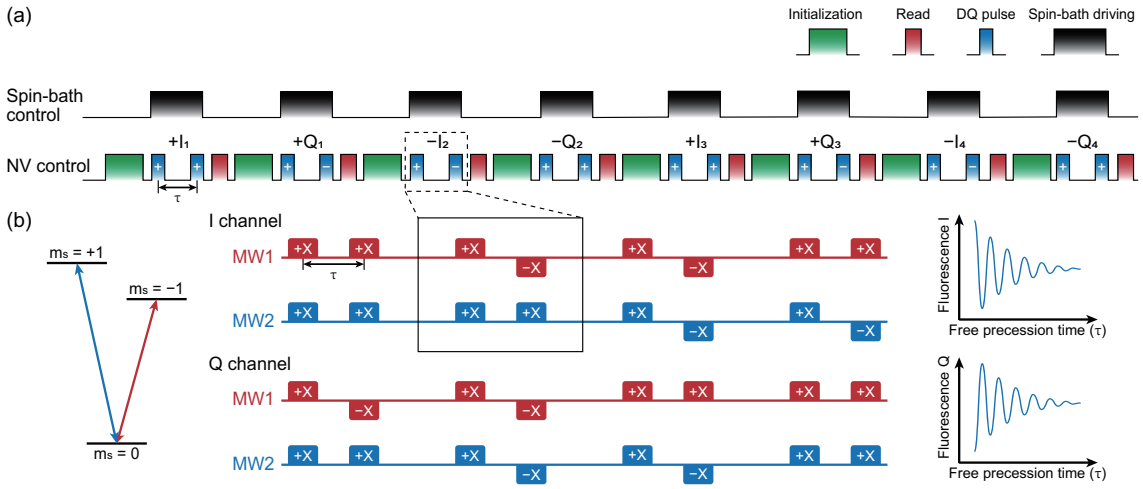


Figure 2.2: (a) Sequence for magnetic imaging using the DQ 4-Ramsey protocol for NV interrogation together with spin-bath driving. The camera internal exposures alternate between the I and Q channel; on-chip circuitry accumulates differential results between two successive measurements in both channels. For example, the output in the I channel using the sequence in (a) will be $S_{I1} - S_{I2} + S_{I3} - S_{I4}$. (b) Left: Dual-tone MW resonant with $|m_s = 0\rangle \leftrightarrow |m_s = +1\rangle$ and $|m_s = 0\rangle \leftrightarrow |m_s = -1\rangle$ NV spin transitions is used to implement DQ pulses. Middle: Phase alternations of individual MW tones in a DQ 4-Ramsey sequence. The $\pm$X directions are defined in the effective Bloch sphere formed by the two NV spin levels $|m_s = 0\rangle$ and $|m_s = +1\rangle$ (or $|m_s = -1\rangle$). The duration of the DQ pulse is the time to change the NV spin state from $|m_s = 0\rangle$ to a superposition state with equal population between $|m_s = +1\rangle$ and $|m_s = -1\rangle$. Right: The permutation of MW-phase alternation in the Q channel results in NV fluorescence dynamics of opposite phase to that of the I channel. Differential results between these two measurements are output to an external frame.

this challenge, the phases of the two MW tones can be alternated across four individual DQ Ramsey measurements (a protocol known as DQ4R [21]). If we denote the fluorescence signals from the i-th measurement as S_i, the phase-alternation scheme generates DQ magnetic signals in S_2 and S_4 that are opposite to S_1 and S_3, while residual SQ signals in the sum $S_1 + S_3$ are also observed in $S_2 + S_4$. A final normalized signal $S_{norm} = S_1 - S_2 + S_3 - S_4$ preserves the DQ component and achieves robustness to pulse errors and magnetic artifacts by eliminating the SQ contributions. In addition, the normalization scheme can be integrated with a lock-in camera to further mitigate laser intensity variation.

Figure 2.2(a) outlines a particular implementation of the DQ 4-Ramsey protocol in conjunction

with spin-bath-driving pulses for magnetic-imaging experiments using the Heliotis heliCam lock-in camera. The NV fluorescence signals from individual DQ Ramsey measurements are stored during the internal exposures of the camera. Additionally, the internal exposures alternate between an in-phase (I) and a quadrature (Q) channel; and every second measurement in the I and Q channel is subtracted from the first measurement through on-chip circuitry. To obtain the normalized signal S_{norm} in the external frame, we implement a MW-phase alternation scheme as shown in Figure 2.2(b). Two DQ 4-Ramsey sequences are both synchronized with the internal exposures on the I and Q channel. The phase permutation in the Q channel is further chosen to generate a signal S^Q_{norm}, with opposite polarity of that in the I channel S^I_{norm}. Finally, an external frame containing S_{norm} is obtained from the differences between S^I_{norm} and S^Q_{norm}.

For all magnetic imaging experiments (including either with and without spin-bath driving, measurements of spatial magnetic noise, and phantom magnetic-field images), the NV fluorescence signal in the camera external frame S_{norm} is converted to magnetic signal using a magnetometry calibration curve. Briefly, with the Ramsey free evolution interval τ fixed, the MW frequency is swept around the NV electronic spin resonances to emulate the change of magnetic field B; the response of S_{norm} is then measured, producing a magnetometry calibration curve. The optimal MW frequency for magnetic measurements is then determined by maximizing the slope dS_{norm}/dB. For DQ magnetometry, the two MWs that are separately resonant with NV electronic spin transitions $|m_s = 0\rangle \leftrightarrow |m_s = +1\rangle$ and $|m_s = 0\rangle \leftrightarrow |m_s = -1\rangle$ are swept differentially (i.e., a detuning of δ is applied to one MW tone while a detuning of $-\delta$ is applied to the second MW tone). The optimal choice of the Ramsey free evolution interval τ is approximately equal to the NV ensemble spin dephasing time T_2^*; however, due to Ramsey fringe beating introduced by the hyperfine splitting of the NV spin resonances, τ is manually adjusted to maximize the median per-pixel magnetic sensitivity η.

2.2 Electromagnetic Design and Simulation of QDM Components

2.2.1 Design and Simulation of the Coplanar Microwave Waveguide

As mentioned in Section 1.3.1, the MW delivery structure in a QDM must generate a strong and homogeneous Rabi drive across the NV ensemble during magnetic imaging. At the same time, heating from the MW antenna is one of the dominant sources of temperature instability in the experiment. In our setup, we designed a 300 nm-thick gold Ω-shaped coplanar waveguide (CPW), fabricated on a SiC wafer, to serve as the MW antenna. The concept of the Ω-loop was originally developed by Matthew Turner and other previous members of the Walsworth group to produce a spatially homogeneous MW driving field. Here, we further improved its performance through several design optimizations and electromagnetic simulations.

We first chose SiC as the substrate material due to its high thermal conductivity and mechanical stability; the available wafer thickness is $330\,\mu\mathrm{m}$. Next, we optimized the transmission performance of the waveguide to enhance the achievable Rabi frequency. Gold was selected as the metal layer for its high electrical conductivity. As shown in Figure 2.3, a U.FL surface-mount connector is used to interface the SMA cable with the CPW, which fixes the required trace width at the waveguide boundary to match the connector geometry.

To minimize reflections at the junction between the MW cable and the CPW, the characteristic impedance of the waveguide must match the $50\,\Omega$ impedance of the MW line. The characteristic impedance of a coplanar waveguide can be approximated by [43]

$$Z_0 \approx \frac{60\pi}{\sqrt{\varepsilon_{\mathrm{eff}}}} \left[\frac{1}{\ln\left(1 + \frac{4h}{\pi s}\left(1 + \frac{s}{w}\right)\right)} \right], \tag{2.5}$$

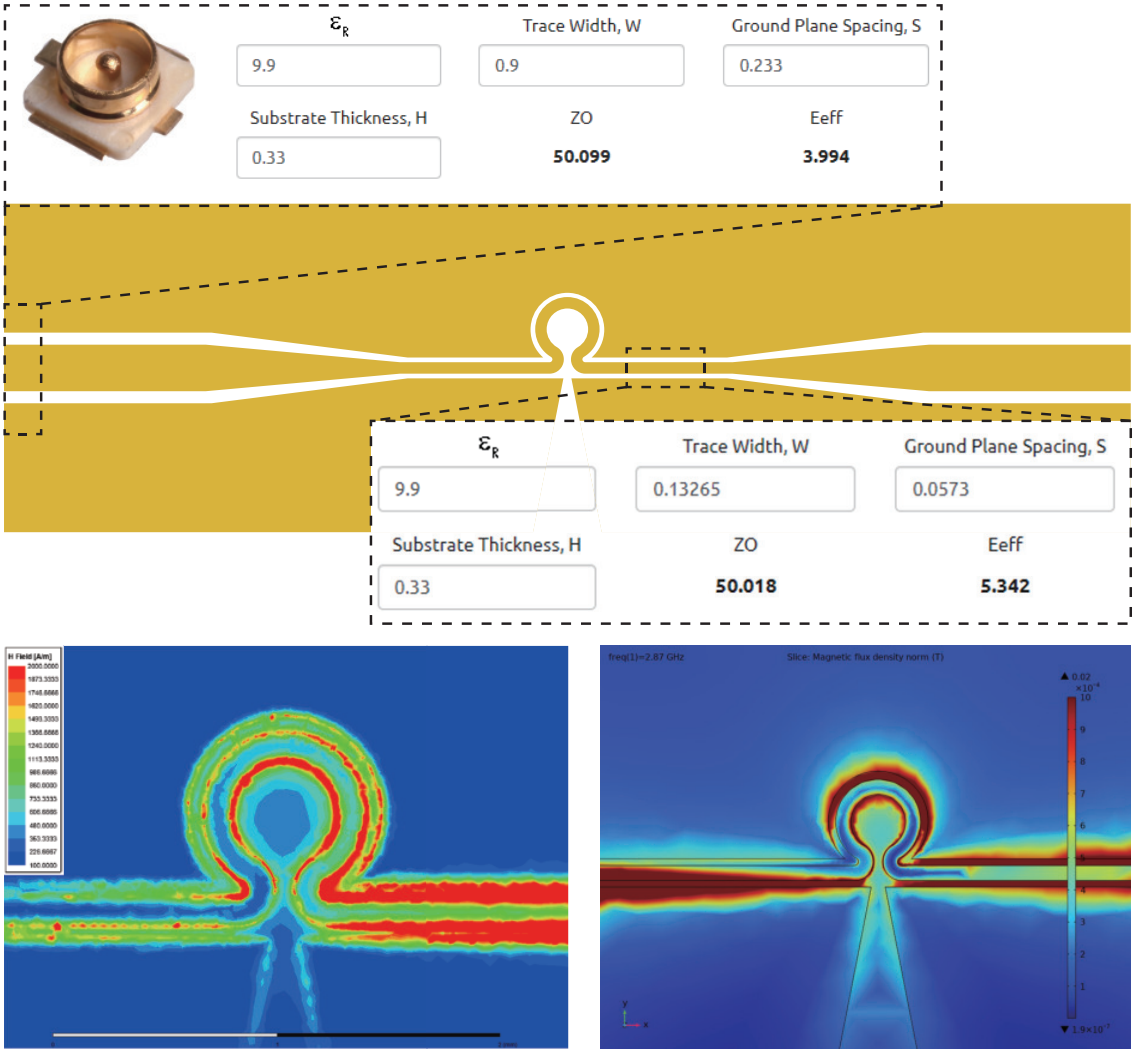


Figure 2.3: Design and simulation of the CPW Ω-loop antenna. The inner diameter of the Ω-shaped structure is $800\,\mu\mathrm{m}$. The trace width at the connector boundary is designed to be $0.9\,\mathrm{mm}$ to match the geometry of the U.FL connector, while the trace width of the antenna loop is $132\,\mu\mathrm{m}$. The gaps between the center trace and the ground planes are optimized to achieve a $50\,\Omega$ impedance match for both regions, thereby minimizing MW reflections. Bottom left: Rabi-homogeneity simulation using Ansys HFSS. The HFSS output is a time-dependent MW magnetic field propagation; here we show a snapshot at zero phase with an input power of 44 dBm at 2.87 GHz. Bottom right: Rabi-field simulation performed using COMSOL Multiphysics, showing the spatial distribution of the magnetic flux density. Both simulations demonstrate a homogeneous Rabi driving region with a diameter of approximately $500\,\mu\mathrm{m}$.

where w is the width of the center conductor, s is the gap between the center conductor and the adjacent ground planes, and h is the substrate thickness measured from the metal layer to the bottom of the dielectric. The substrate has relative permittivity ε_r, and the effective dielectric constant ε_{eff} describes the distribution of electromagnetic fields between the substrate and air. For a sufficiently thick substrate, a common approximation is $\varepsilon_{\text{eff}} \approx (\varepsilon_r + 1)/2$. The resulting value of Z_0 represents the characteristic impedance of the CPW. This empirical expression provides a convenient, high-accuracy approximation without requiring the evaluation of complete elliptic integrals. With all parameters fixed except for the gap s, we determine the required spacing between the center trace and the ground planes at both the connector boundary and the antenna region to achieve the desired $50\,\Omega$ impedance, as shown in Figure 2.3.

After determining the geometry of the CPW design, we imported the structure into finite-element method (FEM) software to simulate the Rabi-field homogeneity. First, using Ansys HFSS with a 44 dBm MW input at 2.87 GHz, we obtained the time-dependent MW magnetic-field propagation produced by the CPW, as shown in Figure 2.3. We then used COMSOL Multiphysics to simulate the corresponding magnetic flux density. Both simulations reveal a homogeneous Rabi-driving region with a diameter of approximately $500\,\mu\text{m}$, which is sufficient for QDM imaging given that the FOV is smaller than this scale. Experimentally, we measured a Rabi frequency of $\sim 7\,\text{MHz}$ under a $\sim 40\,\text{dBm}$ MW input with a standard $50\,\Omega$ termination. In the presence of a phase shifter at the termination, which uses reflected power to enhance the drive amplitude, the Rabi frequency can be further increased to $\sim 12\,\text{MHz}$.

2.2.2 Simulation of the Magnetic Field Generated by the Circuit Phantom

To demonstrate the capability of our QDM to image wide-field magnetic spatial distributions with micron-scale resolution, we designed a circuit phantom that generates a well-defined magnetic-field pattern. The phantom has the shape of a diamondback terrapin, the mascot of the University of Maryland. It consists of a trace with width $\approx 4\,\mu\mathrm{m}$, spans an area of approximately $220 \times 180\,\mu\mathrm{m}^2$, and has a thickness of $\approx 10\,\mathrm{nm}$. To avoid mutual induction between the phantom and the CPW Ω-loop used for MW driving, we fabricated the phantom from palladium, which provides a high resistance of $54.56\,\mathrm{k}\Omega$. The phantom and the Ω-loop are fabricated on the SiC substrate in separate layers. Details of the fabrication process are provided in Appendix A of this dissertation.

We simulate the magnetic features generated by our circuit phantom using the FEM in COMSOL Multiphysics, as shown in Figure 2.4. The simulation is constructed using the *Magnetic Fields, Currents Only* module. We first import the terrapin-shaped design to define the geometry and construct the circuit structure by specifying its thickness and material properties. A surrounding air sphere is added to define the simulation boundary conditions. The circuit is designated as a conducting domain, and an intersection face is selected as the terminal through which we apply a terminal current determined from the experimental voltage and the measured resistance of the phantom. The solver then computes the resulting spatial distribution of the magnetic field generated by the phantom.

Although the simulation provides the spatial magnetic field generated by the phantom, two geometric parameters remain unknown and strongly influence the magnetic image acquired with the NV-diamond sensor: the stand-off distance between the NV layer and the phantom, and the NV-axis orientation relative to the sample. As shown in Figure 2.4, the magnetic features become increasingly blurred and weaker as the distance from the phantom increases. Experimentally, it is challenging to

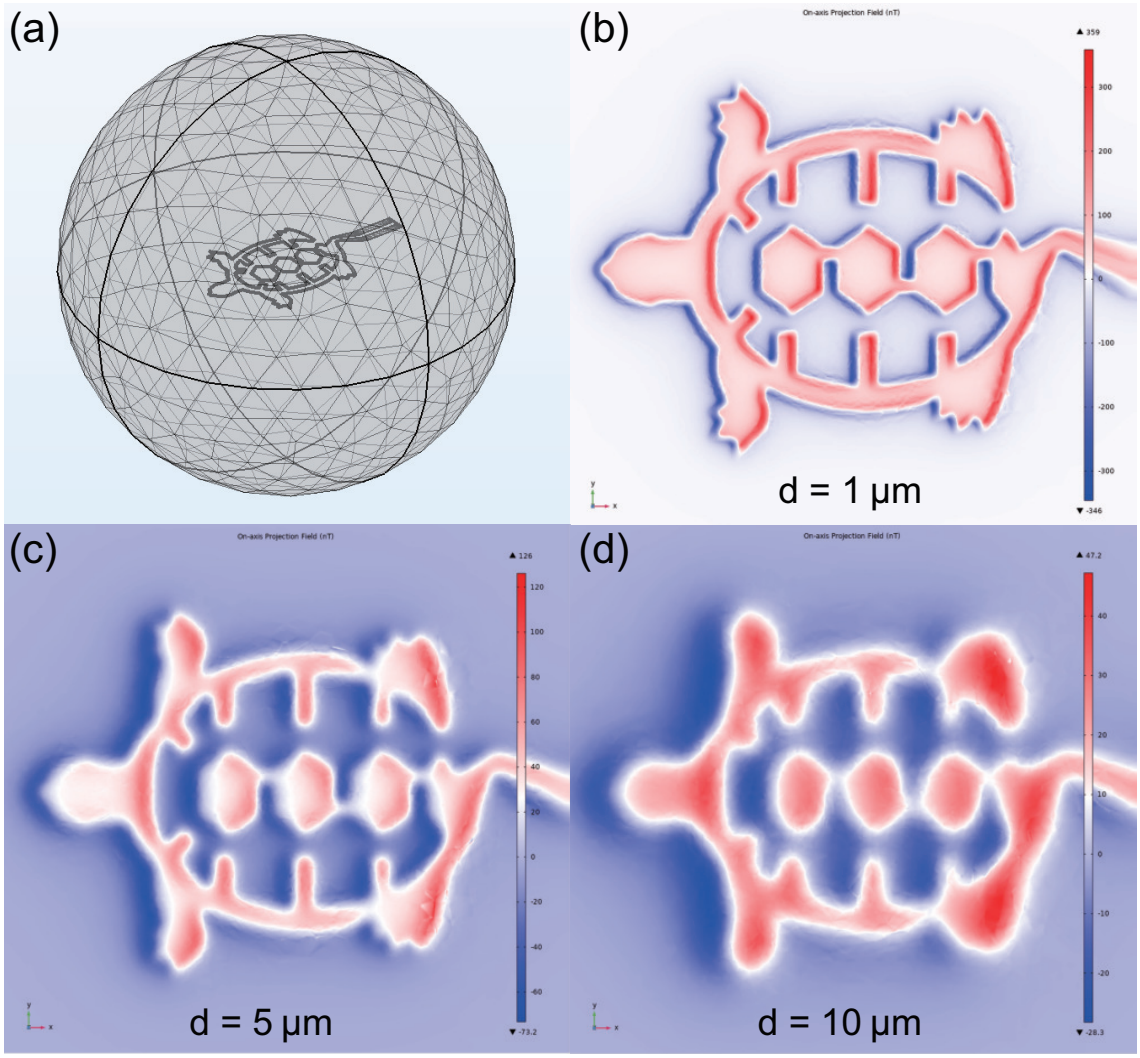


Figure 2.4: Design and simulation of the terrapin-shaped circuit phantom. (a) Geometry construction of the phantom and boundary conditions in COMSOL. (b), (c), and (d) Snapshots of the magnetic-field intensity projected onto one NV axis at stand-off distances of 1, 5, and 10 μm from the phantom.

precisely determine the stand-off distance when gluing the diamond onto the SiC wafer. Furthermore, our diamond contains a $10\,\mu$m-thick NV layer, meaning the measured field represents an average of the magnetic signal over this depth, which adds another layer of complexity when matching simulations to experimental images.

To estimate the stand-off distance, we simulate magnetic-field projections by placing the center of the NV layer at various distances from the phantom and averaging the magnetic field across the NV-layer thickness. This procedure generates a series of candidate magnetic-field images corresponding to different stand-off distances. By comparing these simulated images with the experimentally measured magnetic images (discussed later in this chapter), we determine the stand-off distance in our experiment to be approximately $5\,\mu\mathrm{m}$.

The orientation of the NV axis is much simpler to determine than the stand-off distance. Because we use an NV ensemble in a single-crystal diamond, there are only four possible NV orientations. The diamond used in this work is cut into a square prism with side facets perpendicular to the $[110]$ and $[1\bar{1}0]$ crystal axes. This geometry facilitates alignment of the diamond sensor to the fabricated wire phantom; the diamond is directly mounted onto the silicon carbide wafer that hosts the phantom structure, fixing their relative orientation. All magnetic images in this study correspond to the projection of the phantom's magnetic-field pattern along one of the four NV quantization axes. Figure 2.5 shows the simulated static magnetic-field patterns of the phantom projected along each of the four NV crystal axes. By comparing these simulated patterns with the experimentally acquired magnetic images, we determine that the NV axis used in our measurements corresponds to the $[111]$ crystal orientation.

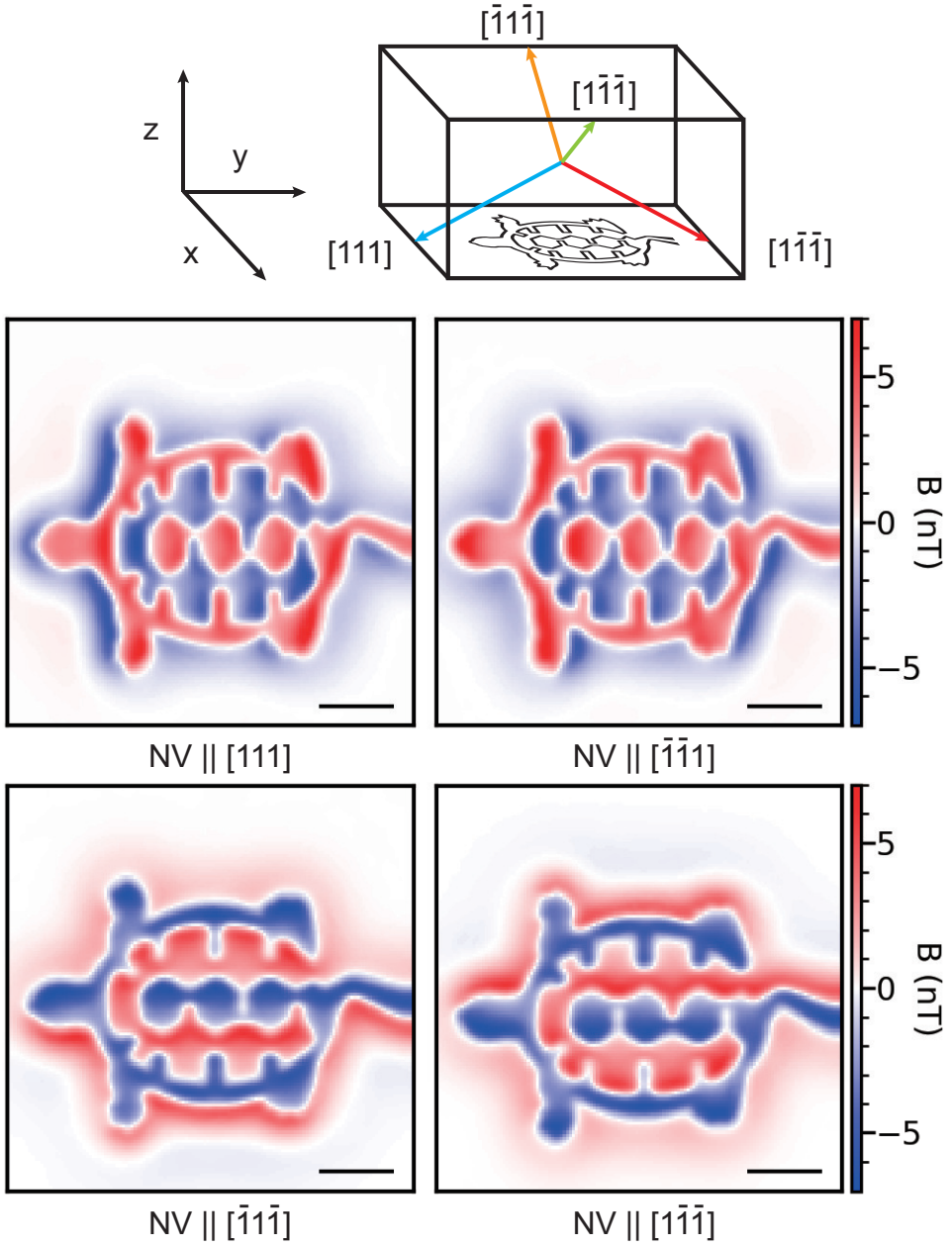


Figure 2.5: Simulated phantom static magnetic-field patterns (bottom four panels) projected along the four NV axes in the diamond crystal (shown schematically in the top panel). In this study, the QDM is configured to image the magnetic field projected along the $[111]$ axis. Simulations include NV-layer averaging over $10\,\mu$m depth and pixel binning. The NV–phantom stand-off distance is $5\,\mu$m.

2.3 Experimental Details and Results

After introducing the key technical components used for Ramsey-based magnetic microscopy, in this section we describe how these elements are integrated into our advanced QDM system to perform the experiments. We present experimental imaging results and show that they agree well with our simulations. In addition, we benchmark the spin dephasing time of the NV ensemble and quantify the DC sensitivity across the FOV, discussing the trade-offs between spatial noise and spatial resolution.

The QDM diamond sensor, shown in Figure 2.6, consists of a $10\,\mu$m-thick, ^{15}N-enriched CVD layer of NV centers ($[\mathrm{N}] = 17\,\mathrm{ppm}$, $>99.995\%$ ^{12}C), grown by Element Six Ltd. on a $2 \times 2 \times 0.5\,\mathrm{mm}^3$ high-purity diamond substrate. Post-growth electron irradiation and annealing increase the NV concentration to approximately 2.4 ppm. Defect concentrations are provided by Element Six Ltd. using the characterization methods described in Ref. [44].

A diode-pumped solid-state laser (Lighthouse Photonics, Sprout-D5W) generates the 532 nm excitation beam. The beam is focused onto an acousto-optic modulator (AOM) (Gooch & Housego, Model 3250-220) by an $f = 500\,\mathrm{mm}$ spherical lens, and the first-order diffracted beam is used for all experiments. Optical pulses for NV initialization and readout are produced by gating the AOM RF driver using microwave switches (Mini-Circuits, ZASWA-2-50DR+) triggered by TTL pulses (SpinCore Technologies, PBESR-PRO-500). The first-order beam is further shaped using an $f = 130\,\mathrm{mm}$ cylindrical lens and an $f = 100\,\mathrm{mm}$ spherical lens to produce an elliptical profile that enters a polished side facet of the diamond. Approximately 2.5 W of optical power enters the diamond and undergoes total internal reflection (TIR) at the NV layer, illuminating an area of about $300 \times 600\,\mu\mathrm{m}^2$.

NV fluorescence is collected by a $20\times$/0.75 NA Nikon objective, filtered by a 647 nm long-pass filter (Semrock), and directed either to a photodiode (Thorlabs, PDA36A2) or to a lock-in camera

(Heliotis, heliCam C3). Photodiode voltages are acquired using a National Instruments DAQ (NI USB-6363).

Dual-tone microwave (MW) pulses for NV spin control are generated using two signal generators with built-in IQ mixers (Stanford Research Systems, SG384), gated by switches and TTL pulses. MW signals are delivered to the NV layer through a fabricated, nominally 300 nm-thick, $800\,\mu$m-wide, gold Ω-shaped coplanar waveguide (shown in Figure 2.6). The palladium wire phantom (shaped as a terrapin) has a trace width of $\approx 4\,\mu$m, spans an area of $220 \times 180\,\mu\mathrm{m}^2$, and has a thickness of ≈ 10 nm. Stimulus voltages from a waveform generator (Keysight 33622A) are applied to the phantom to induce currents and generate magnetic-field patterns. Both the phantom and the MW loop are fabricated on a silicon carbide wafer to provide mechanical rigidity and efficient heat dissipation. The diamond is glued onto the surface of the MW loop, making the minimum possible stand-off between the phantom and the NV layer the MW metal thickness (≈ 300 nm).

Multi-tone resonant RF pulses for spin-bath driving are generated by an AWG (Keysight M8190), gated by switches and TTL pulses, and delivered to the bath spins using a shorted coaxial loop (≈ 1 mm wide) positioned above the MW waveguide.

A bias magnetic field of approximately 4.3 mT is provided by two pairs of temperature-compensated samarium–cobalt ring magnets. This field strength is convenient for our apparatus, but similar QDM performance can be achieved across a broad range of NV resonance frequencies corresponding to fields from millitesla to tesla.

The size of a single camera pixel in the objective focal plane is determined by comparing the known phantom geometry to its optical fluorescence image. Because metallic phantom traces reflect and locally enhance the excitation laser intensity, they produce increased NV fluorescence following the phantom pattern. The resulting NV-layer pixel area is approximately $1.9 \times 1.9\,\mu\mathrm{m}^2$, consistent with

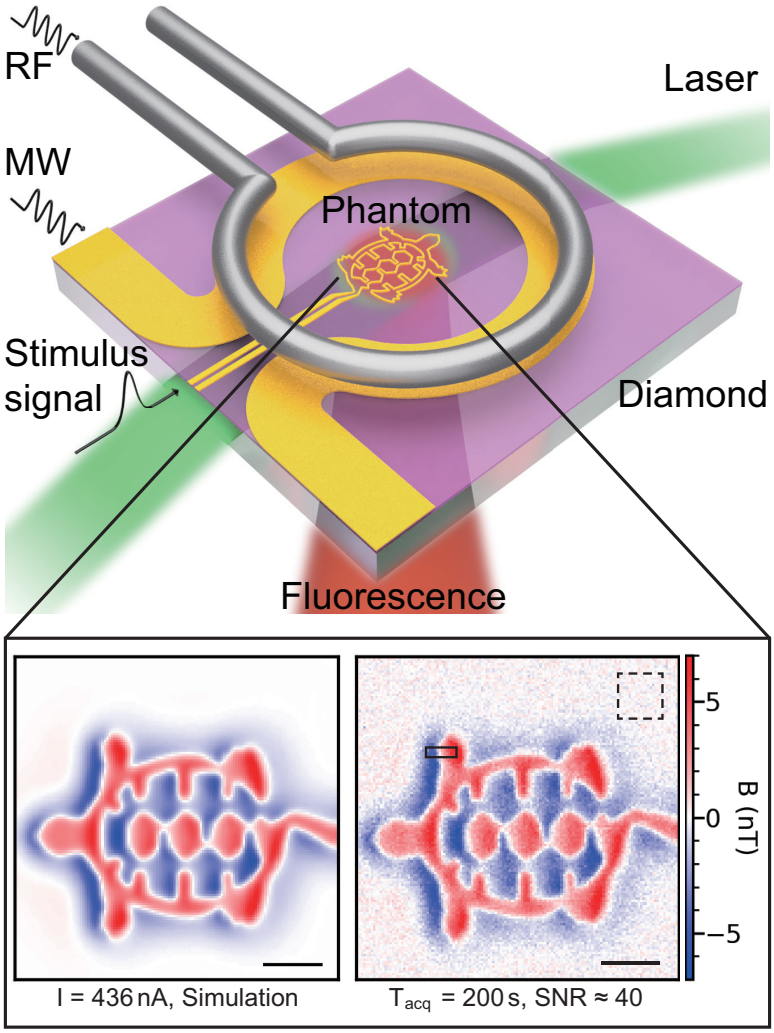


Figure 2.6: Imaging phantom magnetic fields using a QDM. A 532 nm laser excites NV centers in a $10\,\mu$m-thick layer of a diamond chip. A gold Ω-loop delivers microwaves for NV spin control, and NV fluorescence is collected onto a photodiode or high-speed camera (not shown). A bias magnetic field is applied along one NV axis, and an RF coil drives bath spins to extend T_2^*. A driven current in the terrapin-shaped palladium phantom generates the magnetic-field pattern to be imaged. (Zoom-in) Simulated (left) and measured (right) static magnetic-field patterns acquired with the Ramsey-based QDM. The measurement uses a 25 mV excitation (436 nA) and $\sim$200 s averaging. SNR is computed using the peak-to-peak signal (solid box) and spatial noise in a source-free region (dashed box). Simulations include NV-layer averaging over $10\,\mu$m depth and pixel binning ($1.9 \times 1.9\,\mu\mathrm{m}^2$). The NV–phantom stand-off distance is extracted to be $5\,\mu$m.

the expectation from the 20× magnification and the physical camera pixel size ($39.6 \times 39.6\,\mu\mathrm{m}^2$).

The camera supports an internal exposure frequency up to 1 MHz and an external frame rate up to 3.8 kHz. Each external frame accumulates the results of multiple internal exposures. Details on synchronizing the internal exposure cycles with the dual-tone Ramsey sequence are provided in Section 2.1.3. The internal buffer holds up to 500 external frames, and transferring this buffer to a computer takes approximately 5 s. Additional software overhead includes data conversion and saving: about 2 s for static imaging (averaging 500 frames) and about 17 s for dynamic imaging (saving individual frames). This overhead is not included in the acquisition time T_{acq}, but it contributes to the wall-clock time T_{wall}.

2.3.1 Static Magnetic Field Imaging and Comparison with Simulation

We characterize the capability of the Ramsey-based QDM to image static magnetic fields by applying steady currents to the fabricated wire phantom. To suppress common-mode background signals and slow drifts, the polarity of the applied voltage is alternated between successive acquisitions, and differential measurements are performed. As shown in Figure 2.6, a magnetic-field pattern with a peak-to-peak amplitude of approximately 14 nT is obtained by applying a fixed voltage of 25 mV (corresponding to a current of 436 nA) to the phantom and averaging for an acquisition time of $T_{\mathrm{acq}} = 200$ s, resulting in a wall-clock time of $T_{\mathrm{wall}} \approx 21$ min.

To interpret the experimental results and validate the imaging performance, we simulate the expected magnetic-field pattern using finite-element modeling software COMSOL. The simulation calculates the current-density distribution and the resulting magnetic field based on the known geometry of the phantom and the experimentally applied current I. The stand-off distance d_{so} between the

phantom and the NV layer is treated as the only free parameter. By comparing the simulated magnetic-field patterns with the experimentally acquired images, we find the best agreement for a stand-off distance of $d_{\mathrm{so}} \approx 5\,\mu\mathrm{m}$. To realistically reproduce the experimental imaging conditions, the simulated magnetic fields are averaged over a depth of $10\,\mu\mathrm{m}$, corresponding to the thickness of the NV layer, and spatially binned to match the effective camera pixel size of $1.9 \times 1.9\,\mu\mathrm{m}^2$.

We further demonstrate the sensitivity of the Ramsey-based QDM by imaging magnetic fields at the picotesla scale. By applying a voltage of $500\,\mu\mathrm{V}$ (corresponding to a current of 9 nA) to the phantom and averaging for $T_{\mathrm{acq}} = 3600\,\mathrm{s}$ ($T_{\mathrm{wall}} \approx 7\,\mathrm{h}$), we resolve a magnetic-field pattern with a peak-to-peak amplitude of approximately 300 pT and a signal-to-noise ratio of $\mathrm{SNR} \approx 3$. These results are detailed reported in Ref. [39] and in Jiashen's doctoral dissertation.

2.3.2 Dynamic Magnetic Field Imaging

Access to individual frames from the QDM lock-in camera enables imaging of time-dependent magnetic signals. As a demonstration, we apply a 1 s-long broadband voltage waveform, designed to mimic a human cardiac signal, to the circuit phantom, and image the resulting temporal evolution of the magnetic-field patterns.

The camera external frame rate F_s is set to approximately $0.5\,\mathrm{kHz}$, corresponding to a temporal resolution of $\sim$2 ms per frame. This choice balances time resolution with the constraint of the 500-frame on-board buffer [45]. As in the static measurements, a differential measurement protocol is employed by alternating the phantom drive between on and off states across successive frame-set acquisitions. The full experiment is repeated 400 times to improve signal-to-noise ratio through averaging.

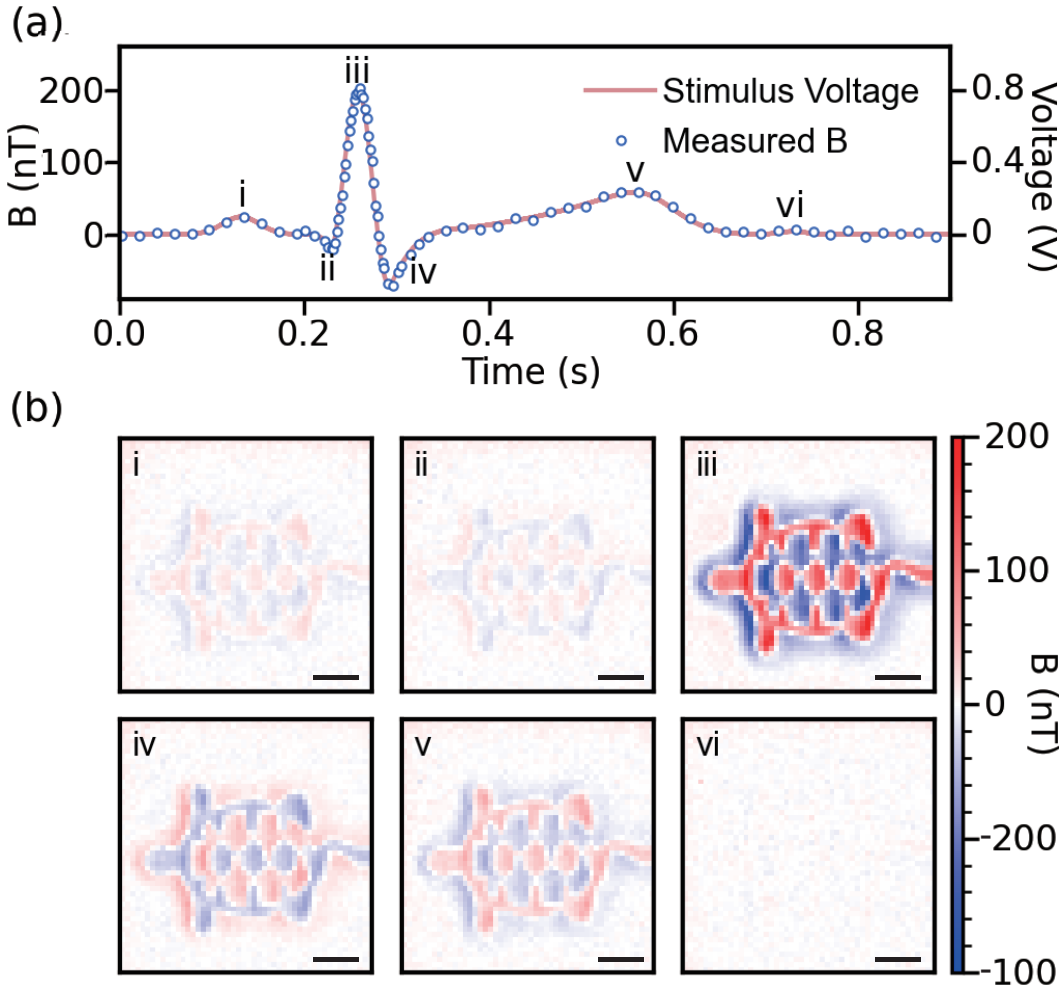


Figure 2.7: Time-resolved imaging of dynamic magnetic fields using the Ramsey-based QDM and a differential measurement protocol. A voltage trace mimicking a broadband cardiac-like signal is applied to the phantom. Magnetic images are acquired with a temporal resolution of $\sim$2 ms and 3×3 pixel binning, and the experiment is repeated 400 times for signal averaging. (a) Temporal evolution of the peak magnetic-field amplitude extracted from the images, overlaid with the applied voltage trace scaled by 274.26 nT/V. The agreement demonstrates faithful waveform reconstruction. (b) Representative magnetic-field images at selected time points indicated in (a). The spatial magnetic noise at time point (vi) is $\sim$3 nT.

The reconstructed dynamic magnetic-field data are shown in Figure 2.7, with 3×3 pixel binning corresponding to an effective spatial resolution of $\lesssim 10\,\mu\mathrm{m}$. Figure 2.7(a) shows the temporal variation of the peak magnetic-field amplitude extracted from each frame, overlaid with the applied voltage waveform. To facilitate direct comparison, the applied voltage trace is converted to magnetic-field units using a calibration factor of 274.26 nT/V, obtained from the static imaging measurements. The close agreement between the applied waveform and the reconstructed magnetic signal demonstrates the ability of the QDM to faithfully capture broadband temporal features, suggesting potential applications such as comparison with electrophysiological measurements (e.g., patch-clamp recordings).

Figure 2.7(b) presents representative magnetic-field images at selected time points corresponding to characteristic features (local extrema) of the applied waveform. As the signal amplitude decreases, the phantom-generated magnetic-field pattern becomes indistinguishable from the background, as seen at time point (vi). This condition is used to estimate the spatial magnetic noise floor, yielding $\sigma_{\mathrm{spatial}} \approx 3\,\mathrm{nT}$.

2.3.3 Spin Dephasing Time and Sensitivity

We benchmark the performance of the Ramsey-based QDM by characterizing the DC magnetic-field sensitivity on a pixel-by-pixel basis across the full field of view. As shown in Eq. (2.1), the photon shot-noise-limited Ramsey sensitivity is directly determined by the NV ensemble spin dephasing time T_2^*. Figure 2.8(a) illustrates the impact of DQ driving on the measured T_2^*.

As discussed in previous sections, crystal strain is one of the dominant contributors to NV ensemble dephasing. This effect is evident in the SQ Ramsey map, where spatial inhomogeneity in T_2^* closely follows strain-related features in the diamond. By contrast, when operating in the DQ

basis and simultaneously addressing the $|m_s = \pm 1\rangle$ states, common-mode shifts arising from strain are largely canceled. This compensation results in a significantly more homogeneous and extended T_2^* across the field of view.

Building on the DQ protocol, the application of spin-bath driving further enhances both the NV ensemble dephasing time and magnetic sensitivity, as shown in Figure 2.8(b). We characterize the performance of the Ramsey-based QDM with and without spin-bath driving by extracting T_2^* and the DC magnetic sensitivity η for each pixel. For these measurements, the remaining limitation to T_2^* arises primarily from dipolar interactions with bath spins. Under these conditions, spin-bath driving effectively suppresses bath-induced dephasing, leading to improved T_2^* and enhanced magnetic sensitivity.

With spin-bath driving enabled, the median per-pixel T_2^* is extended by approximately $1.8\times$ to 2.2(1) μs, approaching the estimated NV–NV interaction limit of 2.5 μs for this sample (Section IV of the Supplementary Material). Correspondingly, the median per-pixel DC magnetic sensitivity improves by approximately $2.4\times$ to 4.1(1) nT/$\sqrt{\text{Hz}}$ without pixel binning. This value is comparable to the combined quantization- and photon-shot-noise-limited sensitivity estimate of 3.2 nT/$\sqrt{\text{Hz}}$, with roughly equal contributions from each noise source.

In the present QDM implementation, the sensitivity nominally improves linearly with increasing T_2^* [17, 20], since the overhead time $t_{I,R} = 7.04\,\mu$s exceeds the optimal sensing time $\tau \approx T_2^*$. In this regime, the sensitivity approximately scales as $\eta_{\text{shot}} \propto \frac{\sqrt{t_{I,R}}}{\tau C}$. The observed improvement in η slightly exceeds the linear scaling expected from the increase in T_2^*. This superlinear behavior is attributed to two additional effects: an observed $\sim 1.2\times$ increase in the spin-state readout contrast C when using spin-bath driving, and discrete choices of the optimal sensing time τ imposed by Ramsey fringe beating due to the hyperfine splitting of the NV spin resonances [21].

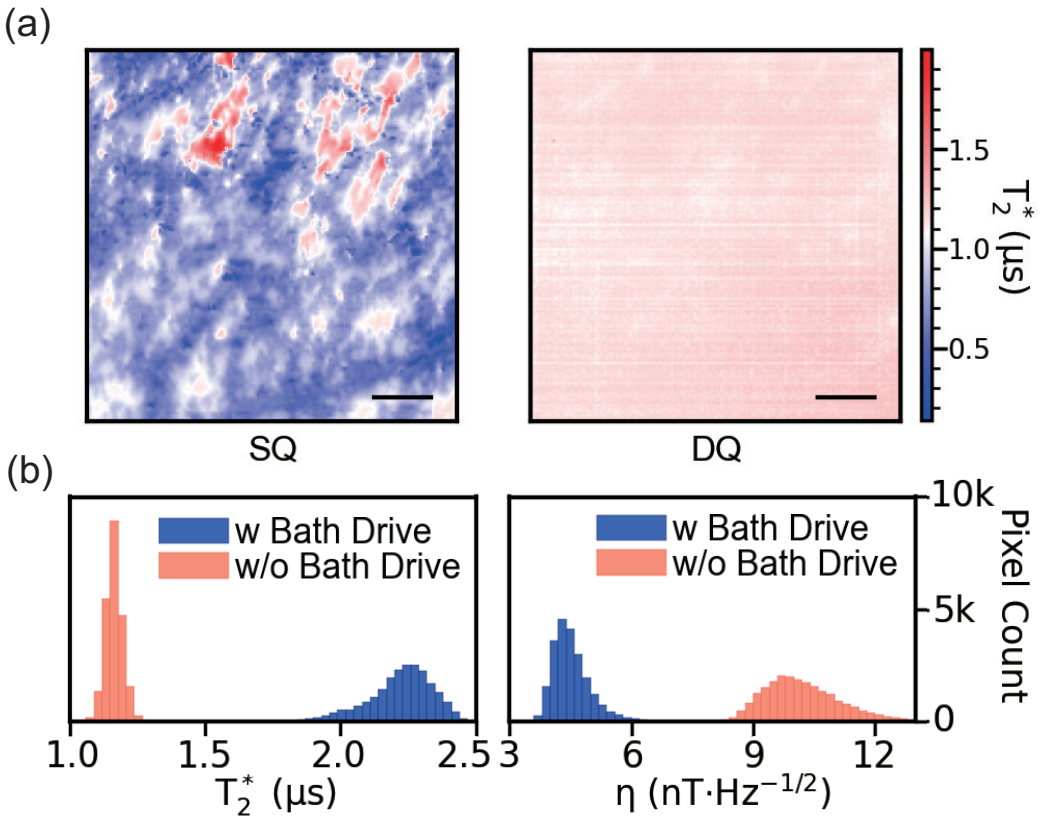


Figure 2.8: (a) QDM maps of the NV ensemble spin dephasing time T_2^* obtained from single-quantum (SQ) and double-quantum (DQ) Ramsey measurements. The SQ T_2^* is limited by heterogeneous strain in the diamond sample. Field of view: $270 \times 270\,\mu\mathrm{m}^2$. Scale bar: $50\,\mu\mathrm{m}$. (b) Median per-pixel T_2^* and DC magnetic sensitivity η measured with and without spin-bath driving. The median T_2^* is 2.2(1) μs and 1.2(1) μs with and without spin-bath driving, respectively. The corresponding median per-pixel sensitivities are 4.1(1) nT/$\sqrt{\mathrm{Hz}}$ and 9.4(1) nT/$\sqrt{\mathrm{Hz}}$.

The reported per-pixel magnetic sensitivity corresponds to the expected magnetic noise after 1 s of signal acquisition. The acquisition time T_{acq} accounts only for the time spent collecting measurement data and excludes the implementation-dependent overhead required to transfer and store data from the 500-frame camera buffer to the host computer. This overhead is included when reporting the wall-clock time T_{wall}.

2.3.4 Spatial Resolution and Spatial Noise

In magnetic imaging, the ability to resolve a signal of interest depends on both the per-pixel magnetic sensitivity and the spatial magnetic noise floor [35]. Following the approach in Ref. [35], we quantify the spatial magnetic noise floor, $\sigma_{\mathrm{spatial}}$, for a given acquisition time by computing the standard deviation of the magnetic-field values across a time-averaged image acquired in the absence of any external signal sources. While uncorrelated spatial noise can be reduced through temporal averaging, spatially correlated noise, particularly when its correlation length is comparable to the spatial scale of the signal of interest, limits the effectiveness of averaging and sets a lower bound on the minimum resolvable magnetic field.

In practice, spatially correlated noise in QDM images can arise from mechanical vibrations, temperature fluctuations, or slow drifts in optical illumination intensity. These effects can induce correlated spatial and temporal variations in the bias magnetic field or the optical readout, thereby degrading the spatial noise performance of the microscope.

For QDM imaging of externally controllable signal sources, such as the circuit phantom used in this work, we mitigate the impact of slowly varying, spatially correlated noise by employing a differential measurement protocol. In this protocol, the current applied to the phantom is modulated

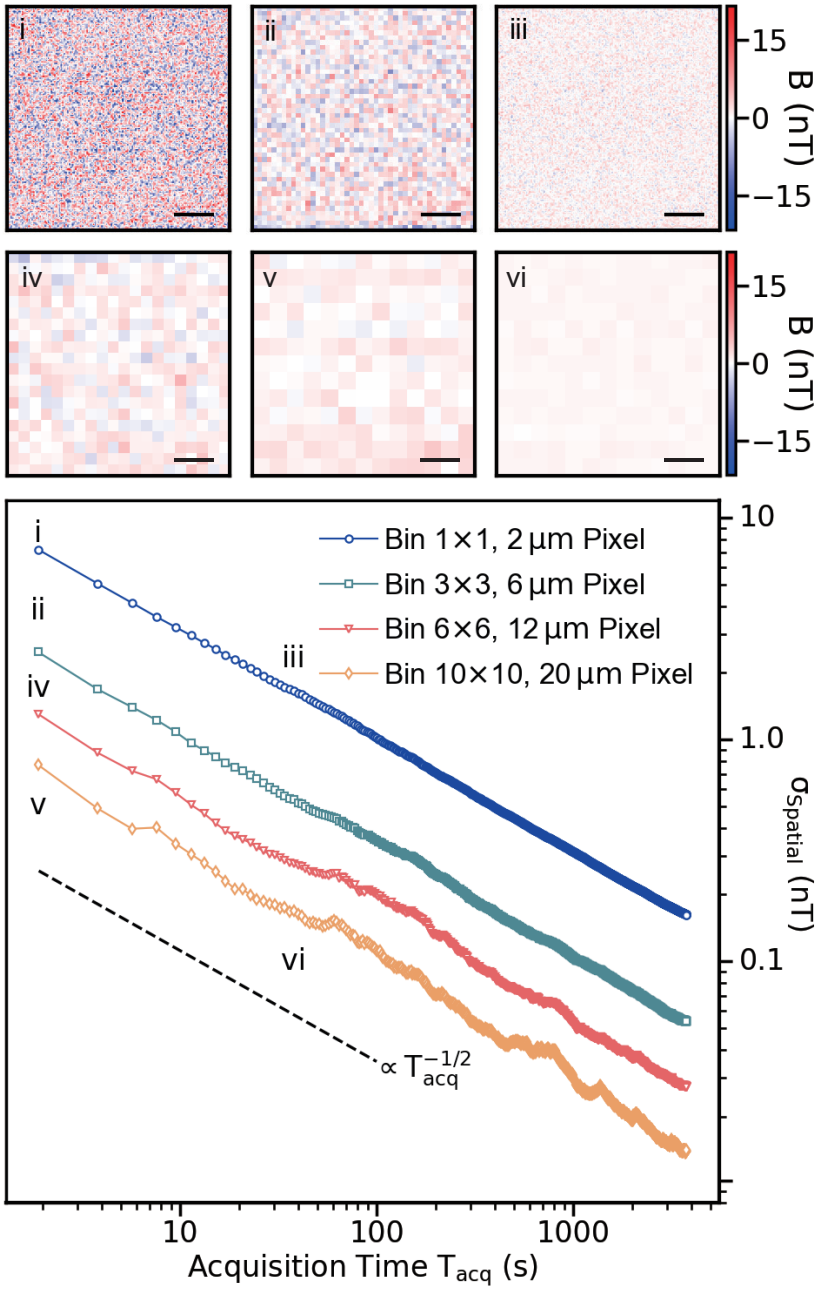


Figure 2.9: Spatial magnetic noise floor measured using the differential measurement protocol. Top: Magnetic noise images acquired with different acquisition times and pixel binning, in the absence of any applied phantom current. The acquisition time includes only the measurement duration and excludes implementation-dependent data transfer and storage overhead. The noise exhibits no significant spatial correlation across the field of view. Field of view: $270 \times 270\,\mu\mathrm{m}^2$. Scale bar: $50\,\mu\mathrm{m}$. Bottom: Spatial magnetic noise floor $\sigma_{\mathrm{spatial}}$ as a function of acquisition time T_{acq} for each pixel binning. The dashed line indicates the expected $\propto T_{\mathrm{acq}}^{-1/2}$ scaling.

either by on/off gating or by polarity reversal between successive acquisitions of 500-frame camera data sets. Because the time required to transfer a full frame set to the host computer is long compared to the internal exposure cycle, this approach effectively suppresses slow drifts and enables long-term averaging. This technique is well suited for studying signals that can be externally controlled, such as those generated by electronic circuits or electrically active biological samples.

For signal sources that cannot be readily modulated, alternative strategies can be employed to suppress spatially correlated noise. These include modulation of the bias magnetic-field polarity, more advanced MW pulse-sequence schemes, or post-processing techniques such as spatial and temporal filtering [9, 46, 47].

As shown in Figure 2.9(b), the spatial distribution of magnetic noise exhibits negligible correlation across the field of view when the differential measurement protocol is used, even for long acquisition times. The resulting spatial magnetic noise floor $\sigma_{\mathrm{spatial}}$ decreases with increasing acquisition time, following the expected $\sigma_{\mathrm{spatial}} \propto T_{\mathrm{acq}}^{-1/2}$ scaling up to approximately $T_{\mathrm{acq}} = 4000\,\mathrm{s}$, corresponding to a wall-clock time of $T_{\mathrm{wall}} \approx 8\,\mathrm{h}$. In addition, averaging over $n_{\mathrm{bin}} \times n_{\mathrm{bin}}$ pixels reduces the spatial noise floor approximately as $\sigma_{\mathrm{spatial}} \propto 1/n_{\mathrm{bin}}$, enabling a trade-off between spatial resolution, magnetic sensitivity, and acquisition time.

Chapter 3: Dynamical-Decoupling-Based AC Magnetic Microscopy

This chapter is primarily based on the work reported in Ref. [15]. Having demonstrated high-resolution, sensitive broadband DC magnetic microscopy in the previous chapters, we now extend the capabilities of the QDM to the detection and imaging of narrowband, high-frequency magnetic fields.

In this work, we integrate a wide-field QDM with a dynamical-decoupling-based narrowband detection protocol and a lock-in camera, enabling spatially resolved imaging of radio-frequency (RF) magnetic field patterns generated by microcoils. The resulting instrument achieves a spectral resolution of approximately 1 Hz while operating at MHz-scale carrier frequencies.

This RF-QDM supports multi-frequency magnetic imaging with a central detection frequency that is readily tunable over the MHz range. Such tunability enables spatial discrimination of both spectrally crowded resonances and well-separated frequency components within a single imaging platform. The present system achieves a spatial resolution of approximately $2\,\mu\mathrm{m}$ over a field of view of $\sim 300 \times 300\,\mu\mathrm{m}^2$, with a per-pixel sensitivity to narrowband magnetic fields of $\sim 1\,\mathrm{nT} \cdot \mathrm{Hz}^{-1/2}$. Through temporal averaging and/or spatial binning, the effective spatial noise floor can be further reduced to the picotesla level.

By simultaneously resolving the amplitude, frequency, and phase of narrowband magnetic fields with micron-scale spatial resolution, the RF-QDM provides a powerful platform for imaging dynamic magnetic phenomena. Potential applications include real-space NMR imaging, AC magnetic susceptibility mapping, impedance tomography, analysis of integrated electronic circuits, and spatially resolved eddy-current-based inspection.

3.1 Protocols and Techniques for AC Magnetometry with QDM

In this section, we describe in detail the dynamical-decoupling-based protocols employed for AC magnetometry with the QDM. Specifically, we discuss the XY8 pulse sequence, the associated magnetic-field sensitivity, and the Coherent Averaged Synchronized Readout (CASR) protocol.

We further explain how these AC sensing protocols are implemented within the wide-field QDM platform, including the integration of microwave pulse control, optical readout, and camera-based detection. Together, these techniques enable spatially resolved, narrowband magnetic-field imaging with high sensitivity and spectral resolution.

3.1.1 Dynamical Decoupling Sequences for AC Sensing

As mentioned in Sec. 1.2.1, the Hahn echo protocol [22] (also referred to as the spin-echo sequence), shown in Figure 1.2, represents the most fundamental form of dynamical decoupling. This sequence builds upon the Ramsey protocol by inserting a central MW π pulse, which refocuses inhomogeneous dephasing of the NV^- spin ensemble arising from static or slowly varying noise sources. As a result, the decay of spin coherence measured using Hahn echo sequence is characterized by the coherence time T_2, which is typically one to two orders of magnitude longer than the Ramsey dephasing time T_2^* in NV ensemble measurements.

In addition to suppressing dephasing from static magnetic fields, the refocusing π pulse renders the Hahn echo sequence intrinsically sensitive to oscillating magnetic fields. In particular, the sequence exhibits maximum sensitivity to AC magnetic fields with a period T_B that matches the total spin interrogation time τ of the pulse sequence. This property forms the basis of dynamical-decoupling-based AC magnetometry.

More advanced dynamical decoupling sequences, such as CPMG-n and XY8-n, are constructed by extending the Hahn echo sequence through the application of multiple microwave π pulses with appropriate phase modulation. By applying π pulses at a repetition rate of $1/(2T_B)$, these multipulse sequences serve two key functions: (i) they further extend the NV^- spin coherence time T_2 by more effectively decoupling the spins from environmental magnetic noise, and (ii) they increase the total interrogation time during which the NV^- spins coherently accumulate phase from an oscillating magnetic field.

The dynamical-decoupling-based AC sensing protocol begins with an optical initialization pulse that polarizes the electronic spin state of each NV center in the ensemble into $|m_s = 0\rangle$. A subsequent MW $\pi/2$ pulse prepares each NV in a coherent superposition of the $|m_s = 0\rangle$ and $|m_s = 1\rangle$ states, enabling phase accumulation in the presence of an oscillating magnetic field. The AC magnetic signal to be detected is modeled as $B_{\mathrm{AC}}(t) = B_z \cos(2\pi f_s t + \phi_0)$, where B_z is the projection of the magnetic-field amplitude along the NV axis, f_s is the signal frequency, and ϕ_0 is the relative phase between the applied AC field and the dynamical decoupling pulse sequence.

Following the initial $\pi/2$ pulse, a sequence of N_π MW π pulses is applied, with each pulse separated by a free precession interval $\tau = 1/(2f_s)$. Under these conditions, the accumulated dynamical phase for each NV center is given by

$$\theta(B_z, \phi_0) = \frac{g\mu_B N_\pi B_z}{\pi\hbar f_s} \cos\phi_0, \tag{3.1}$$

where $g \approx 2$ is the Landé g-factor, μ_B is the Bohr magneton, and $\hbar$ is the reduced Planck constant.

By introducing a relative $\pi/2$ phase shift between the initial and final MW $\pi/2$ pulses, the accumulated phase is mapped onto the NV population difference, yielding a fluorescence readout

signal

$$\begin{aligned} S(B_z, \phi_0) &= S_0 + S_a \sin(\theta) \\ &= S_0 + S_a \sin(\kappa B_z \cos\phi_0)\,, \end{aligned} \tag{3.2}$$

where S_0 denotes the fluorescence offset, S_a is the oscillation amplitude of the fluorescence signal, and $\kappa = g\mu_B N_\pi/(\pi\hbar f_s)$ is a proportionality constant. The fluorescence levels corresponding to projection onto the $|m_s = 0\rangle$ and $|m_s = 1\rangle$ states are given by $S_0 \pm S_a$, respectively.

3.1.2 Coherent Averaged Synchronized Readout (CASR)

Coherent Averaged Synchronized Readout (CASR) [38] is a detection protocol developed by David Glenn, Dominick Bucher, and other collaborators in the Walsworth group for the measurement of narrowband magnetic signals with ultrahigh spectral resolution, particularly for NMR spectroscopy. CASR provides the spectral selectivity required for NMR by coherently averaging synchronized NV magnetometry measurements over long interrogation times.

The CASR protocol, illustrated in Figure 3.1, consists of repeated NV sensing pulse sequences interleaved with projective NV spin-state readout, all synchronized to a stable external clock. In the regime of weak coupling between the NV ensemble and the signal source, the measurement back-action on the sample spins is negligible and does not induce significant dephasing. Under these conditions, the detector linewidth is limited primarily by technical factors, such as magnetic-field gradients in the bias field B_0 and the stability of the timing reference. Crucially, because the NV sensor detects the thermal spin polarization of the sample, the phase of the signal can be made identical across successive measurements by applying an initial $\pi/2$ pulse to the nuclear spins at time $t = 0$. This enables coherent signal averaging, which provides a substantially improved sensitivity scaling

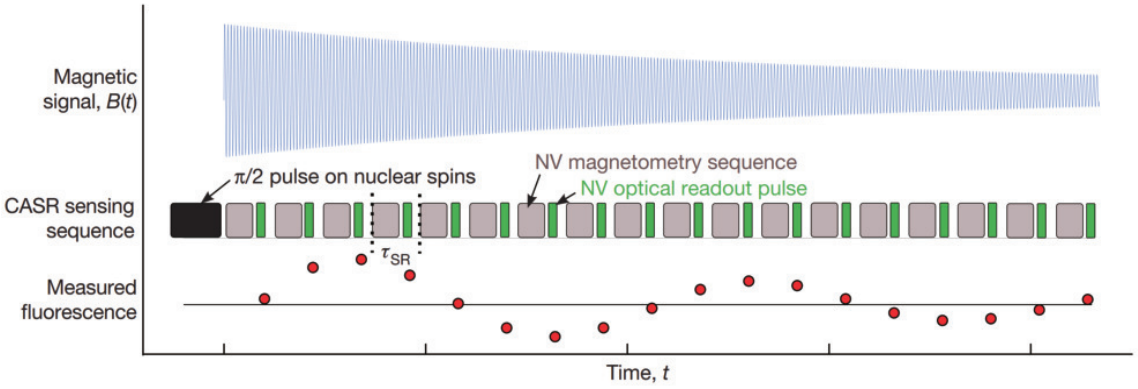


Figure 3.1: [38] Numerical simulation of CASR detection of an NMR free nuclear precession (FNP) signal. The top panel shows the oscillating magnetic field $B(t)$ produced by the precession of thermally polarized nuclear spins (blue) at frequency f. The middle panel illustrates the CASR protocol: a $\pi/2$ pulse (black box) applied to the nuclear spins at time $t = 0$ initiates spin precession with a well-defined phase, enabling coherent signal averaging. The protocol then consists of repeated blocks of identical NV AC magnetometry pulse sequences with central frequency f_0 (gray boxes), interleaved with optical NV spin-state readouts (green boxes). These blocks are repeated with a synchronized readout cycle period τ_{SR}. The bottom panel shows the NV fluorescence signal over successive CASR readouts, which oscillates at the aliased frequency $\delta f = f - f_0$.

compared to incoherent averaging schemes. In this work, CASR is used to detect synthetic AC magnetic fields generated by microcoils; therefore, the initial nuclear $\pi/2$ pulse is not included. The application of CASR to NMR detection is discussed in detail in Chapter 5.

In the CASR protocol, the phase of the detected signal varies in time due to the oscillatory nature of the magnetic field. Accordingly, Eq. (3.2) can be generalized to include an explicit time dependence:

$$\begin{aligned} S(t, B_z, \phi_0) &= S_0 + S_a \sin[\kappa B_z \cos(2\pi f_s t + \phi_0)] \\ &= S_0 + 2S_a \sum_{n=0}^{\infty} (-1)^n J_{2n+1}(\kappa B_z) \cos[(2n+1)(2\pi f_s t + \phi_0)] \,, \end{aligned} \tag{3.3}$$

where $J_n(x)$ is the nth-order Bessel function of the first kind and f_s is the signal carrier frequency.

Taking the Fourier transform of Eq. (3.3) yields the CASR spectrum

$$\begin{aligned} S(f, B_z, \phi_0) = \sqrt{2\pi}\Bigg\{ & S_0\delta(f) + 2\pi S_a \sum_{n=0}^{\infty}(-1)^n J_{2n+1}(\kappa B_z) \\ & \times \left[e^{-i\phi_0}\delta(f-(2n+1)f_s) + e^{i\phi_0}\delta(f+(2n+1)f_s)\right] \Bigg\} \\ = S_{\mathrm{DC}} + S_{\mathrm{Real}} + & iS_{\mathrm{Imag}}, \end{aligned} \tag{3.4}$$

where $\delta(f)$ is the Dirac delta function. The DC component is given by $S_{\mathrm{DC}} = \sqrt{2\pi}S_0\delta(f)$, while the real and imaginary components are

$$\begin{aligned} S_{\mathrm{Real}}(f, B_z, \phi_0) = & (2\pi)^{3/2} S_a \cos(\phi_0) \sum_{n=0}^{\infty}(-1)^n J_{2n+1}(\kappa B_z) \\ & \times \left[\delta(f+(2n+1)f_s) + \delta(f-(2n+1)f_s)\right], \\ S_{\mathrm{Imag}}(f, B_z, \phi_0) = & (2\pi)^{3/2} S_a \sin(\phi_0) \sum_{n=0}^{\infty}(-1)^n J_{2n+1}(\kappa B_z) \\ & \times \left[\delta(f+(2n+1)f_s) - \delta(f-(2n+1)f_s)\right]. \end{aligned} \tag{3.5}$$

In the RF-QDM CASR experiments, we employ an XY8-8 sequence to image RF magnetic field patterns with peak amplitudes $B_{z,\max} \approx 40\,\mathrm{nT}$, corresponding to $\kappa B_{z,\max} \approx 0.8$. In the regime $\kappa B_z < 1$, higher-order Bessel terms are negligible. Retaining only the first-order term and considering the positive-frequency component, the real and imaginary parts simplify to

$$\begin{aligned} S^{+}_{\mathrm{Real}}(f, B_z, \phi_0) = & (2\pi)^{3/2} S_a \cos(\phi_0) J_1(\kappa B_z)\delta(f-f_s), \\ S^{+}_{\mathrm{Imag}}(f, B_z, \phi_0) = & -(2\pi)^{3/2} S_a \sin(\phi_0) J_1(\kappa B_z)\delta(f-f_s). \end{aligned} \tag{3.6}$$

In CASR imaging, the temporal separation between successive measurements is $t_m = N_d t_{\mathrm{Seq}}$,

where t_{Seq} is the duration of a single pulse sequence and N_d is the number of sequences per camera demodulation cycle. The effective sampling rate is therefore $f_{\mathrm{SR}} = 1/t_m$, yielding a detection bandwidth of $f_{\mathrm{SR}}/2$ according to the Nyquist–Shannon sampling theorem. The measured alias frequency is

$$f_a = |f_s - m f_{\mathrm{SR}}|,$$

where m is the integer closest to f_s/f_{SR}. The detected signal components for each image pixel are thus

$$\begin{aligned} S^{+}_{\mathrm{Real,m}}(f, B_z, \phi_0) &= (2\pi)^{3/2} S_a \cos(\phi_0) J_1(\kappa B_z) \delta(f - f_a), \\ S^{+}_{\mathrm{Imag,m}}(f, B_z, \phi_0) &= -(2\pi)^{3/2} S_a \sin(\phi_0) J_1(\kappa B_z) \delta(f - f_a). \end{aligned} \tag{3.7}$$

Defining the signal amplitude to have the same sign as the real component, the FFT amplitude spectrum is

$$\begin{aligned} S^{+}_{\mathrm{Amp,m}}(f, B_z) &= \frac{S^{+}_{\mathrm{Real,m}}}{|S^{+}_{\mathrm{Real,m}}|} \sqrt{\left(S^{+}_{\mathrm{Real,m}}\right)^2 + \left(S^{+}_{\mathrm{Imag,m}}\right)^2} \\ &= (2\pi)^{3/2} S_a J_1(\kappa B_z) \delta(f - f_a). \end{aligned} \tag{3.8}$$

Integrating the spectral peak yields the CASR signal amplitude

$$S_{\mathrm{CASR}}(B_z) = \int_{f_a - \Delta f}^{f_a + \Delta f} S^{+}_{\mathrm{Amp,m}}(f, B_z)\, df = (2\pi)^{3/2} S_a J_1(\kappa B_z), \tag{3.9}$$

where the half linewidth is $\Delta f \approx 1\,\mathrm{Hz}$ in our experiments, such that $S_{\mathrm{CASR}} \approx S^{+}_{\mathrm{Amp,m}}$. For $\kappa B_z < 1$, $J_1(\kappa B_z)$ is approximately linear, yielding $S_{\mathrm{CASR}} \propto B_z$. Additionally, Signal phase is constructed from the real and imaginary Fourier components as

$$\phi_0 = \arctan\left(-\frac{S^{+}_{\mathrm{Imag,m}}}{S^{+}_{\mathrm{Real,m}}}\right). \tag{3.10}$$

3.1.3 Implementation of XY8 AC Magnetometry with a Lock-In Camera

In this work, we employ the same lock-in camera used for DC magnetic microscopy in Chapter 2. As a result, the dynamical decoupling pulse sequences must be adapted to the camera's internal demodulation scheme. For each imaging pixel, the local RF magnetic field generated by the microcoils is measured using an XY8-n sequence, in which the net phase accumulated by the NV electronic spin due to the oscillating magnetic field is mapped onto a population difference between the ground-state spin levels by a final $\pi/2$ pulse prior to optical readout.

Four distinct XY8-n pulse sequences, comprising a single demodulation cycle, are interwoven with the exposures of the lock-in camera, as shown in Figure 3.2. The corresponding NV fluorescence signals acquired during these exposures are denoted as S_1, S_2, S_3, and S_4. By appropriately controlling the phase of the final $\pi/2$ pulse, the readout contrast is maximized while broadband laser intensity noise is suppressed through in-pixel lock-in demodulation.

For each demodulation cycle and for every pixel, the camera generates an in-phase (I) signal by analog subtraction of the third exposure from the first, and a quadrature (Q) signal by subtraction of the fourth exposure from the second. The accumulated difference signals over N_d demodulation cycles are digitized to produce external I and Q frames, which are stored in the camera's on-board memory buffer. Because the I and Q frame pairs contain equivalent information due to the specific phase alternation pattern employed, they are summed to form a single external frame after transfer to the host computer. Consequently, each external frame is composed of $2N_d$ internal camera frames.

For an applied RF test signal

$$B_{\mathrm{RF}}(t) = B_z \cos(2\pi f_s t + \phi_0), \tag{3.11}$$

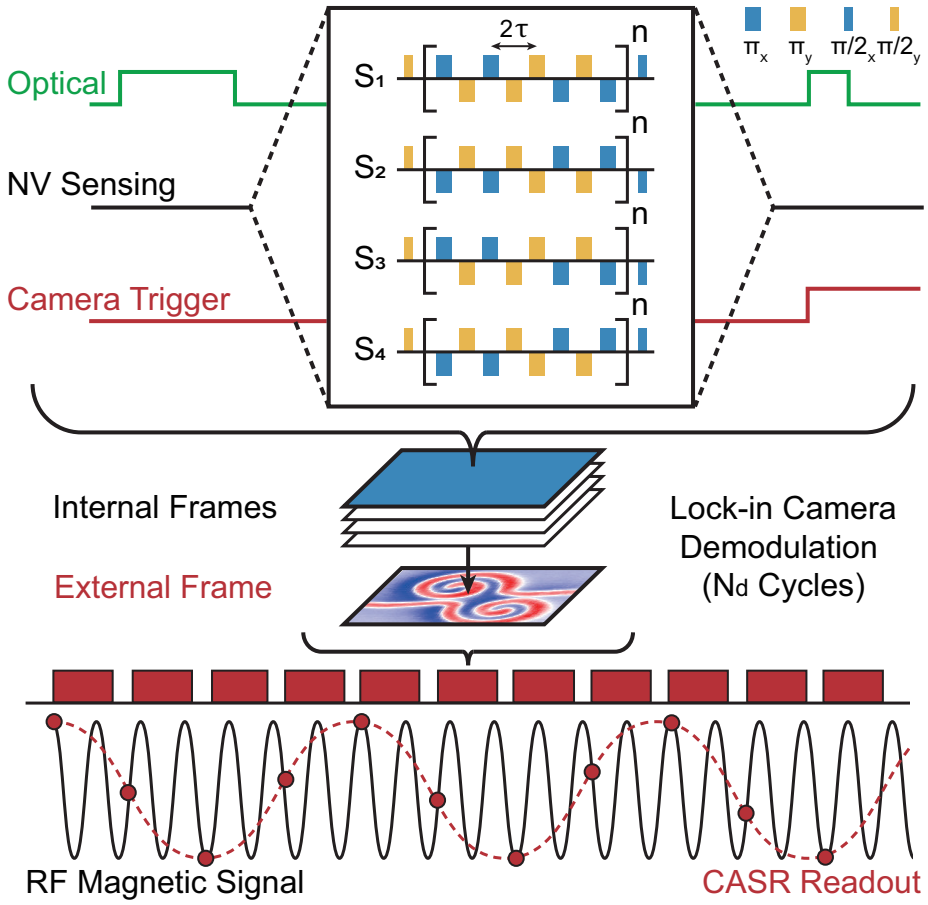


Figure 3.2: RF magnetic field imaging protocol with a lock-in camera. Within one camera demodulation cycle, four exposures occur, with phase-modulated XY8-n sequences applied to NV spins to generate internal I & Q frames. After N_d cycles (i.e., $2N_d$ total internal frames), an external frame of the RF magnetic field image is obtained. The CASR protocol comprises interspersed blocks of single external frame measurements (red boxes) with a frame rate of f_{SR}. The RF magnetic signal (black curve) with frequency f_s is sampled via CASR readout (red dashed curve) at an alias frequency $f_s - m f_{\mathrm{SR}}$, where m is the integer closest to f_s / f_{SR}.

where B_z is the projection of the RF magnetic field amplitude along the NV axis, f_s is the oscillation frequency, and ϕ_0 is the phase offset, the readout signal for each pixel in an external frame can be written as

$$\begin{aligned} S &= N_d[(S_1 - S_3) - (S_2 - S_4)] \\ &= 4N_d S_a \sin(\kappa B_z \cos\phi_0), \end{aligned} \tag{3.12}$$

Here, S_a is the fluorescence signal amplitude, $\kappa = 2\gamma N_\pi / f_s$ is a proportionality constant, $\gamma = 2\pi \times 28.024\,\mathrm{GHz/T}$ is the NV electronic gyromagnetic ratio [4], and N_π is the number of π pulses in the XY8-n sequence. For a small magnetic-field variation ΔB_z, the corresponding change in fluorescence signal is $\Delta S = 4N_d S_a \kappa \Delta B_z$. By calibrating the magnetometry slope for each pixel, quantitative RF magnetic field images can be extracted from the fluorescence images, as described in the following sections.

To simultaneously image the amplitude, frequency, and phase of RF magnetic field patterns with high spectral resolution ($\sim 1\,\mathrm{Hz}$), we employ the CASR protocol [38]. Consecutive external frames from the lock-in camera (Figure 3.2) provide time-resolved NV fluorescence signals sampled at a rate f_{SR} equal to the external frame rate. For each pixel, this produces a time-domain oscillatory signal corresponding to the RF magnetic field.

Applying a Fast Fourier Transform (FFT) to the time-domain signal yields a CASR spectrum for each pixel, centered at the alias frequency $f_s - m f_{\mathrm{SR}}$, where m is the integer closest to f_s / f_{SR}. The peak amplitude of the CASR signal is given by

$$S_{\mathrm{CASR}} = 4N_d (2\pi)^{\frac{3}{2}} S_a J_1(\kappa B_z), \tag{3.13}$$

where $J_1(x)$ is the first-order Bessel function as described in the previous subsection. In the

experiments presented here, we ensure that $\kappa B_z < 1$, such that $J_1(\kappa B_z)$ is well approximated by a linear function, resulting in $S_{\mathrm{CASR}} \propto B_z$.

3.2 Experimental Details and Calibrations

3.2.1 Experimental Setup and Device Fabrication

Two side-polished diamond samples are used in this work. One sample contains a $10\,\mu\mathrm{m}$-thick ^{15}N-enriched CVD layer of NV centers ($[\mathrm{N}] = 17\,\mathrm{ppm}$, $> 99.99\%$ ^{12}C), grown by Element Six Ltd. on a $2 \times 2 \times 0.5\,\mathrm{mm}^3$ high-purity diamond substrate, as shown in Figure 3.3(a). Post-growth electron irradiation and annealing were used to increase the NV concentration to approximately $2.7\,\mathrm{ppm}$. The second diamond sample contains a $1.7\,\mu\mathrm{m}$-thick NV layer with otherwise identical properties.

A diode-pumped solid-state laser (Lighthouse Photonics, Sprout-H) provides continuous-wave 532 nm excitation. The laser beam is focused onto an acousto-optic modulator (AOM; Gooch & Housego, Model 3250-220) using a spherical convex lens with focal length $f = 500\,\mathrm{mm}$, and the first-order diffracted beam is used for all experiments. Optical pulses for NV spin initialization and readout are generated by gating the AOM RF drive with a fast RF switch (Mini-Circuits, ZASWA-2-50DR+), controlled by transistor–transistor logic (TTL) pulses from the marker channel of an arbitrary waveform generator (AWG; Zurich Instruments, SHFSG).

After the AOM, the beam is shaped by a cylindrical convex lens ($f = 130\,\mathrm{mm}$) and a spherical convex lens ($f = 100\,\mathrm{mm}$) to produce an elliptical beam profile incident on a polished side surface of the diamond. Approximately $2.5\,\mathrm{W}$ of laser power enters the diamond and undergoes total internal reflection at the surface containing the NV layer, illuminating an area of approximately $400 \times 600\,\mu\mathrm{m}^2$. NV fluorescence (photoluminescence, PL) is collected using a $20\times$/0.75 NA Nikon objective and

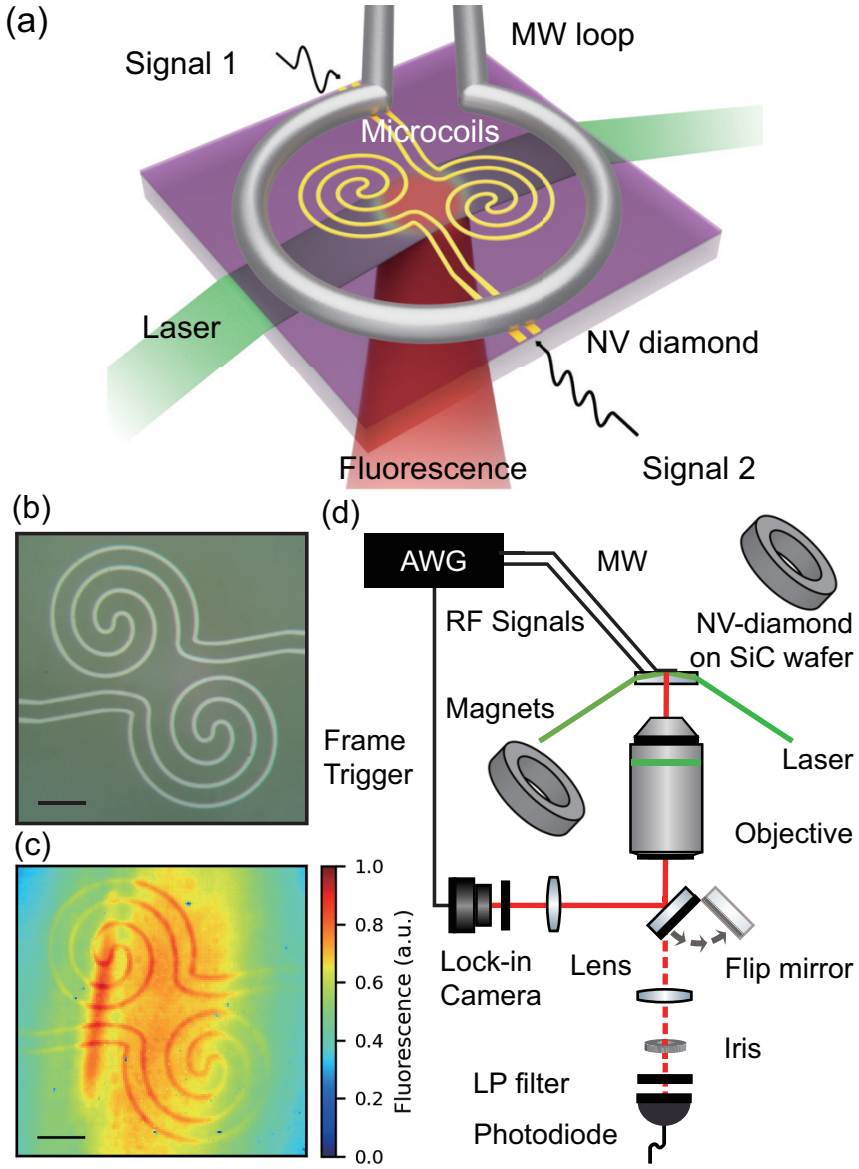


Figure 3.3: (a) Wide-field imaging of near-field patterns of narrowband magnetic fields using a QDM operated under ambient conditions. RF test signals are applied to microcoils to generate distinct magnetic field patterns across the NV-diamond surface. Laser and MW fields are used for NV electronic spin manipulation, with spin-state population readout via spin-dependent fluorescence. (b) Optical image of the spiral-shaped microcoils positioned at a stand-off distance of approximately $10\,\mu\mathrm{m}$ from the NV layer. All scale bars correspond to $50\,\mu\mathrm{m}$. (c) NV fluorescence image under CW laser excitation, illustrating the relative illumination profile (beam shape) across the FOV. The normalized fluorescence is proportional to the detected photon count. (d) Experimental apparatus. A flip mirror directs NV fluorescence to either a photodiode or a lock-in camera. An AWG provides MW pulses for NV spin control, RF signals for the microcoils, and synchronized frame triggers for camera exposure using its internal oscillator. A Sic wafer serves as a mechanical mount and thermal heat sink for the MW loop, microcoils, and NV-diamond chip. An RF test coil (not shown) is used for AC magnetometry calibration.

filtered by a 647 nm long-pass filter (Semrock) before detection with either a photodiode (Thorlabs, PDA36A2) or a lock-in camera (Heliotis, heliCam C3). Photodiode signals are recorded using a data acquisition system (National Instruments, NI USB6259).

Microwave pulses for NV spin manipulation are generated by a signal channel of the same AWG. A fabricated 300 nm-thick gold Ω-shaped coplanar waveguide, with an inner diameter of $800\,\mu\mathrm{m}$, delivers MW fields to the NV ensemble, producing a spatially homogeneous Rabi frequency across the FOV. Spiral-shaped palladium microcoils are fabricated to generate spatially structured RF magnetic fields. These microcoils have a trace width of $5\,\mu\mathrm{m}$, span an area of $280 \times 300\,\mu\mathrm{m}^2$, and have a thickness of 10 nm (Figure 3.3(b)). Palladium is chosen for its relatively high resistivity compared to gold, which minimizes mutual inductive coupling between the microcoils and the MW loop and thereby preserves MW control fidelity.

The microcoils and MW loop are fabricated on a SiC wafer, which provides both mechanical support and efficient heat dissipation. The diamond is glued to the MW loop with an estimated stand-off distance of approximately $10\,\mu\mathrm{m}$. RF magnetic field patterns are generated by applying multi-frequency voltage waveforms from additional AWG channels to the microcoils, inducing controlled RF currents. An RF test coil, wound from 22 American Wire Gauge wire with 14 turns and a diameter of $50\,\mathrm{mm}$, is positioned above the SiC wafer to generate calibration signals for AC magnetometry. A static bias magnetic field of approximately $22\,\mathrm{mT}$ is provided by four pairs of temperature-compensated samarium–cobalt ring magnets, which offer improved field homogeneity compared to cylindrical magnets.

The effective pixel size in the object plane is determined using the known dimensions of the microcoils and optical images acquired via NV fluorescence. Metallic microcoil traces locally reflect the excitation laser, increasing the illumination intensity and producing enhanced NV fluorescence

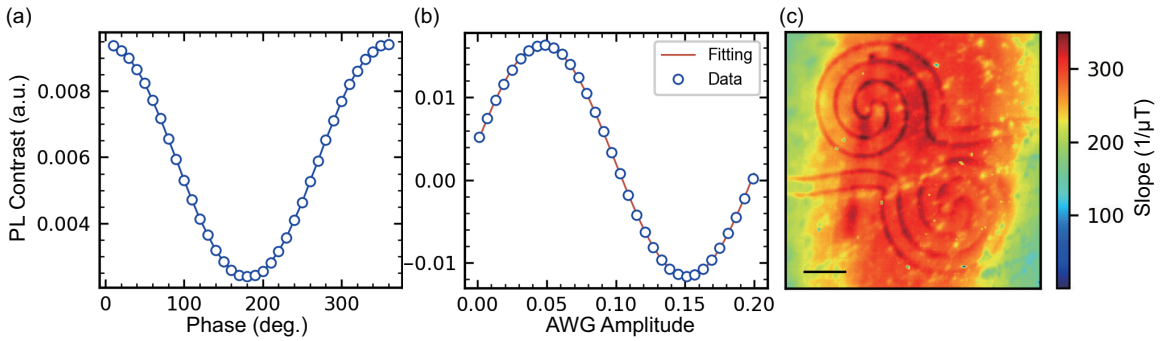


Figure 3.4: Example calibration measurements of the RF-QDM for dynamical-decoupling-based AC magnetometry, performed using photodiode detection (laser beam illumination diameter $\approx 50\,\mu\mathrm{m}$) and wide-field imaging with the lock-in camera. (a) Phase sweep of photodiode-based AC magnetometry used to determine the initial phase of a nominally in-phase AC magnetic field ($f_s = 1\,\mathrm{MHz}$) applied with the RF test coil. (b) Photodiode AC magnetometry curve showing the relative NV photoluminescence contrast measured using the XY8-8 sequence, in good agreement with a sinusoidal fit. (c) Imaged spatial distribution of the zero-crossing slope of the AC magnetometry curve, which exhibits spatial variation due to the laser illumination profile on the NV layer (see Figure 3.3(c)). The scale bar corresponds to $50\,\mu\mathrm{m}$.

that outlines the phantom structure (Figure 3.3(c)). Each camera pixel corresponds to an area of approximately $2 \times 2\,\mu\mathrm{m}^2$ in the focal plane, consistent with estimates based on the $20\times$ objective magnification and the physical pixel size of $39.6 \times 39.6\,\mu\mathrm{m}^2$ specified by the camera manufacturer. A schematic overview of the complete experimental apparatus is shown in Figure 3.3(d).

3.2.2 Calibration of AC Magnetometry

We calibrate the AC magnetometry performance of the RF-QDM as follows. First, we adjust the phase ϕ_0 of a low-amplitude AC test signal ($f_s = 1\,\mathrm{MHz}$) applied to the RF test coil by setting the arbitrary waveform generator (AWG) output amplitude to 0.01, corresponding to $11.25\,\mathrm{mV_{pp}}$ across the coil. AC magnetometry measurements are then performed using photodiode detection of the NV fluorescence under a laser beam illumination diameter of approximately $50\,\mu\mathrm{m}$.

In the small-signal regime, the NV photoluminescence contrast is approximated by

$$S(\phi_0) = S_0 + S_a \kappa B_z \cos\phi_0. \tag{3.14}$$

By sweeping the phase offset ϕ_0, we determine the effective phase of the applied AC magnetic field as measured by the dynamical decoupling sequence from the value of ϕ_0 that maximizes the fluorescence contrast. As shown in Figure 3.4(a), the experimentally determined phase offset is small, on the order of 1°.

With the phase fixed at $\phi_0 = 0$, we sweep the AWG output amplitude to vary B_z over a range comparable to that encountered in microcoil imaging experiments, yielding the AC magnetometry curve shown in Figure 3.4(b). By fitting this curve with a sinusoidal function, we extract the AWG amplitude change $A_{2\pi}$ corresponding to a 2π phase accumulation by the NV spins ($\theta = 2\pi$).

Using Eq. (3.1), the AC magnetic field amplitude required for a 2π phase accumulation is

$$B_{2\pi} = \frac{2\pi^2 f_s \hbar}{g\mu_B N_\pi}. \tag{3.15}$$

The calibration factor converting AWG output amplitude to AC magnetic field amplitude is then calculated as $C = B_{2\pi}/A_{2\pi}$. The derivative of the magnetometry curve at the zero-crossing point provides the slope of the NV fluorescence signal with respect to AWG output amplitude, $\Delta S/\Delta A$. For AC magnetic sensing, the corresponding magnetic-field slope is

$$\frac{\Delta S}{\Delta B_z} = C\frac{\Delta S}{\Delta A}. \tag{3.16}$$

In the imaging modality, this calibration procedure is performed independently for each pixel.

The resulting spatial distribution of the zero-crossing slope, which is primarily determined by the laser illumination profile on the NV layer, is shown in Figure 3.4(c). Once an NV fluorescence image is acquired, the in-phase AC magnetic field image is reconstructed using the pre-calibrated zero-crossing slope for each pixel.

3.3 Experimental Results

3.3.1 In-Phase RF Magnetic Imaging

To characterize the performance of the RF-QDM, we first image narrowband magnetic fields with known phase. Two AC signals at 1 MHz and 0.8 MHz, each with a peak amplitude of $6.6\,\mu$A, are applied simultaneously to two separate microcoils on the NV–diamond surface as shown in Figure 3.1(a). We align the XY8-8 sensing sequence in phase with the 1 MHz signal by setting the π-pulse spacing to $\tau_1 = 0.5\,\mu$s and sweeping the test-signal phase to maximize the detected contrast. After a 1.2 s acquisition (200 camera external frames), we obtain an RF magnetic field amplitude image with a peak-to-peak variation of approximately 130 nT, revealing the near-field pattern generated exclusively by the upper microcoil with an SNR of ~ 50 as shown in Figure 3.5(b).

By adjusting the π-pulse spacing to $\tau_2 = 0.625\,\mu$s, the XY8-8 sequence is synchronized to the 0.8 MHz signal, enabling selective imaging of the magnetic field pattern produced solely by the lower microcoil. The RF-QDM yields clean near-field images at either frequency with no measurable cross-talk between the simultaneously applied signals, as the two frequencies are separated by more than the narrowband filter function of the sensing sequence (Figure 3.5(c)). The center frequency of the filter function is readily tunable via the pulse spacing τ, while the detection bandwidth is set by the number of repetitions n in the XY8-n sequence [48]. For the present demonstration, using

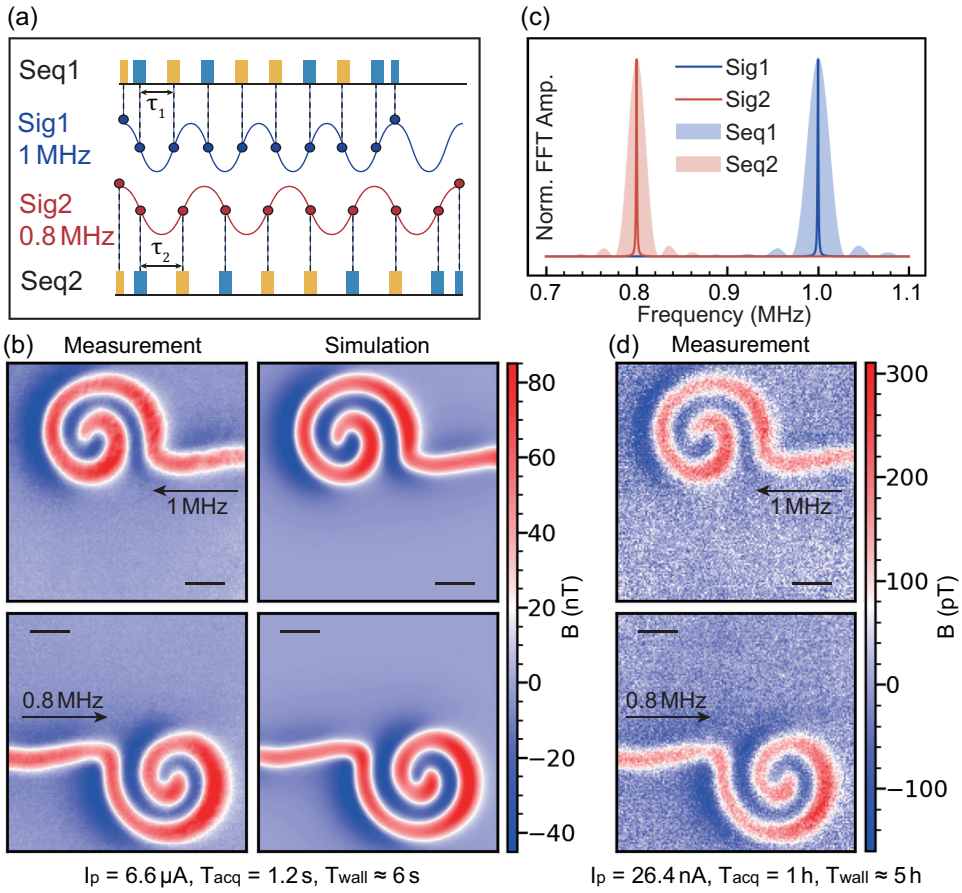


Figure 3.5: RF-QDM imaging of narrowband, multi-frequency magnetic fields using a dynamical-decoupling (XY8-8) protocol. (a) Simultaneous application of 1 MHz (Sig1) and 0.8 MHz (Sig2) AC currents to two microcoils on the NV–diamond surface; selective detection is achieved by tuning the π-pulse spacing τ. (b) Measured (left) and simulated (right) RF magnetic field images for peak currents of $6.6\,\mu$A, with SNR ≈ 50 after 1.2 s averaging per frequency. (c) FFT spectra of the applied signals and corresponding XY8-8 filter functions, illustrating spectral selectivity. (d) Sub-nanotesla RF magnetic imaging with peak currents of $26.4\,$nA, yielding SNR ≈ 15 after 1 hour averaging per frequency. All scale bars are $50\,\mu$m. Colorbars are not centered at zero due to asymmetry in the projection onto the sensing NV axis.

an XY8-8 sequence at frequencies near 1 MHz, the filter-function bandwidth is approximately 30 kHz. These results demonstrate micron-scale spatial discrimination of spectrally well-separated narrowband signals using the RF-QDM.

In Figure 3.5(b), the measured RF magnetic field distributions are compared with numerical simulations. Using the same method as described in Sec. 2.2.2, we compute the three-dimensional magnetic field generated by a static current of $6.6\,\mu\mathrm{A}$ constrained to the spiral microcoil geometry using finite-element software. The simulated field is averaged at a stand-off distance of $10\,\mu\mathrm{m}$ over a $10\,\mu\mathrm{m}$-thick NV layer and projected onto the sensing NV orientation. The resulting simulated images show good agreement with the experimental measurements.

To further illustrate the sensitivity and stability of the RF-QDM, we reduce the peak amplitudes of both test signals to $26.4\,\mathrm{nA}$. After an acquisition time of 3600 s per signal frequency, we obtain images of the in-phase narrowband magnetic field generated by each microcoil with a peak-to-peak variation of approximately 500 pT and an SNR of ~ 15 as shown in Figure 3.5(d). We note that a machine-learning approach has recently been applied to the inverse problem of reconstructing current distributions from QDM magnetic field images [49].

3.3.2 Simultaneous Amplitude and Phase Imaging

Next, we implement the CASR protocol in the RF-QDM to simultaneously image the amplitude and phase of multi-frequency RF magnetic fields with a spectral resolution of approximately 1 Hz, as shown in Figure 3.6. For these demonstration measurements, we apply a dual-tone current $I_1 = I_p \cos[2\pi(f_0 + f_1)t + \theta_1] + I_p \cos[2\pi(f_0 + f_3)t + \theta_3]$ to the lower microcoil, and a single-tone current $I_2 = I_p \cos[2\pi(f_0 + f_2)t + \theta_2]$ to the upper microcoil. Here, the carrier frequency is $f_0 = 1\,\mathrm{MHz}$;

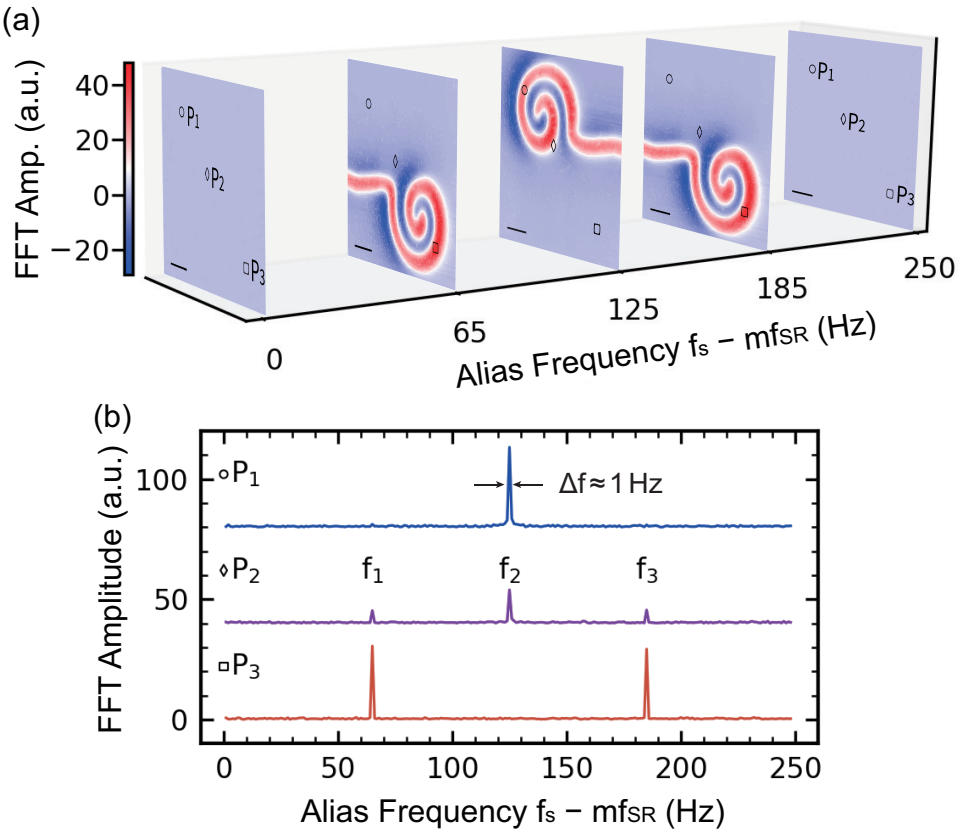


Figure 3.6: RF-QDM imaging of arbitrary phase, multi-frequency magnetic fields using the CASR protocol. As described in the text, a single tone alternating current (1 MHz + 125 Hz) is applied to the upper microcoil; and a two tone current (1 MHz + 65 Hz and 1 MHz + 185 Hz) is simultaneously applied to the lower microcoil. Both currents have peak amplitude $I_p = 3.3\,\mu$A. The phases of each signal frequency component (tone) are arbitrary but fixed during the measurements. Total image acquisition time is 200 s. (a) CASR images of RF magnetic field amplitudes at each signal frequency component, as well as at alias frequencies (1 Hz and 250 Hz) far from any signal tone. The imaged arbitrary phase magnetic field amplitudes have SNR of approximately 70 (calculated with the same method as Figure 3.5(b) for each signal frequency component, and exhibit good agreement with images of in-phase signals shown in Figure 3.5(b). The colorbar is not centered around zero because of asymmetry in the projection of the RF magnetic field amplitude on the sensing NV axis. (b) CASR spectra (FFT) of three test pixels $\mathrm{P}_{1,2,3}$ with positions labeled in (a). Peaks corresponding to three frequency components $f_{1,2,3}$ are clearly illustrated in the spectra, with peak heights proportional to the RF magnetic field amplitude. Linewidths of all spectral peaks $\approx$ 1 Hz. Amplitude offsets are added to the spectra of $\mathrm{P}_{1,2}$ for a better visualization. All scale bars in (a) correspond to 50 μm.

the offset frequencies are $f_{1,2,3} = 65\,\mathrm{Hz}$, $125\,\mathrm{Hz}$, and $185\,\mathrm{Hz}$; and $\theta_{1,2,3}$ are fixed but arbitrary phase offsets.

The peak current amplitude is $I_p = 3.3\,\mu\mathrm{A}$, corresponding to an estimated peak RF magnetic field amplitude below $40\,\mathrm{nT}$, ensuring operation within the linear response regime of the measurement. The lock-in camera frame rate is set to $f_{\mathrm{SR}} = 500\,\mathrm{Hz}$ with eight demodulation cycles per external frame. After 1 s of data acquisition, a time series of NV fluorescence images is obtained, sampling the RF magnetic field at the CASR alias frequencies. This measurement is repeated 100 times to reduce the noise floor, after which a FFT is applied to the time-dependent fluorescence signal of each pixel.

The CASR amplitude images for each frequency component are extracted by normalizing the FFT amplitudes to the steady-state NV fluorescence intensity for each pixel, as described in Sec. 3.1.2.

To illustrate CASR amplitude imaging, three representative pixels are selected (Figure 3.6(a,b)). Pixel P_1, located near the upper microcoil, exhibits a single frequency peak at f_2 in its CASR spectrum. Pixel P_3, located near the lower microcoil, shows two frequency components corresponding to f_1 and f_3. The intermediate pixel P_2, positioned between the two microcoils, exhibits contributions from both sources with reduced amplitude. In all cases, the linewidth of the CASR spectral peaks is approximately $\Delta f \approx 1\,\mathrm{Hz}$.

From the CASR spectra of each pixel, magnetic field amplitude images are reconstructed for each frequency within the measurement bandwidth. Example amplitude images at frequencies $f_{1,2,3}$ are shown in Figure 3.6(a), revealing RF magnetic field patterns consistent with the in-phase imaging and simulations presented earlier.

In addition to amplitude imaging, CASR enables simultaneous phase imaging of the RF magnetic field at each frequency component. The measured phases $\phi_{1,2,3}$ depend on the phases of the applied currents $\theta_{1,2,3}$, the impedance of the microcoils, and fixed timing offsets between the current drive

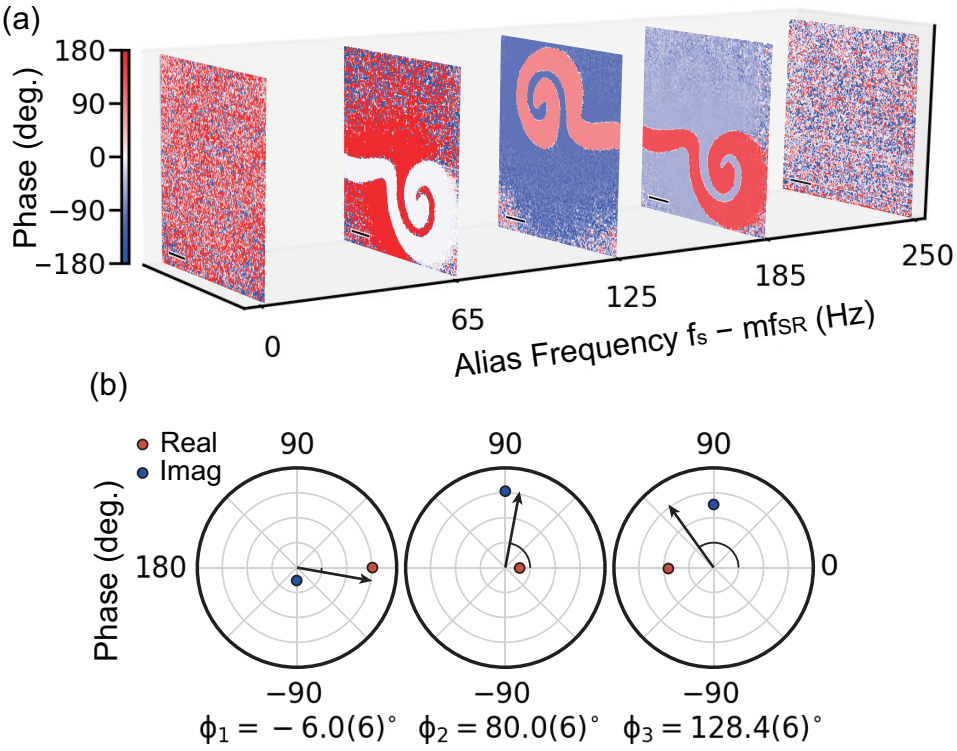


Figure 3.7: CASR phase imaging of multi-frequency RF magnetic fields. (a) CASR images of RF magnetic field phases at each signal frequency component, as well as at alias frequencies far from any signal tone (1 Hz and 250 Hz). Noisy phase distributions in no-signal regions are attributed to the ratio of near-zero real and imaginary amplitudes of the CASR FFT. (b) Polar plots illustrate the phases of each signal frequency component, derived from CASR measurements. ϕ_1 and ϕ_3 are determined from the real and imaginary parts of the FFT of pixel P_3; and ϕ_2 is determined from P_1. Red and blue dots represent the real and imaginary amplitudes of the associated FFT spectra, respectively, while black arrows indicate the absolute value of the amplitude as shown in Figure 3.6(a). Grids are depicted as circles with a step size equivalent to the radius of 10 arbitrary units of FFT amplitude. All scale bars in (a) correspond to 50 μm.

and CASR sensing sequence. These parameters remain constant during the measurement, resulting in stable but arbitrary phase distributions across the field of view.

The CASR amplitude is obtained from the root mean square of the real and imaginary FFT components, while the phase is extracted from their ratio. Using this approach, we determine the phases $\phi_{1,2,3}$ with an accuracy of approximately $0.6°$, estimated from the noise floor in Figure 3.6(b). Repeating this analysis for each pixel yields spatially resolved phase images at each frequency step of the CASR spectrum, as shown in Figure 3.7(a).

CASR imaging data are acquired at a frame rate of 500 Hz over a 1 s acquisition window. To improve the SNR, a 1 s background measurement (with no RF signal applied to the microcoils) is performed after each CASR acquisition with signal applied, and this sequence is repeated 100 times for signal averaging. During each acquisition cycle, the camera stores 500 external frames in its internal memory buffer, transfers the data to the host computer, and then clears the buffer before the next iteration. Consequently, the total acquisition time is 200 s; however, due to data transfer overhead, the total wall time of the experiment is approximately 30 min.

Although the raw data volume is large (approximately 17 GB), background subtraction and averaging yield a time-domain CASR data set for each pixel in the form of a $150 \times 150 \times 500$ matrix, corresponding to a reduced data size of about 80 MB. The computational time required to perform the Fourier transform for all pixels across the field of view is approximately 0.4 s.

The current generation of Heliotes lock-in cameras cannot read out and write data simultaneously. Measurement data are temporarily stored in an internal memory buffer; once the buffer approaches capacity, the experiment is paused while the data are transferred to the host computer and the buffer is cleared, a process that takes approximately 5 s. This limitation could be mitigated by using cameras capable of streaming data directly to the host computer, which would improve the throughput and

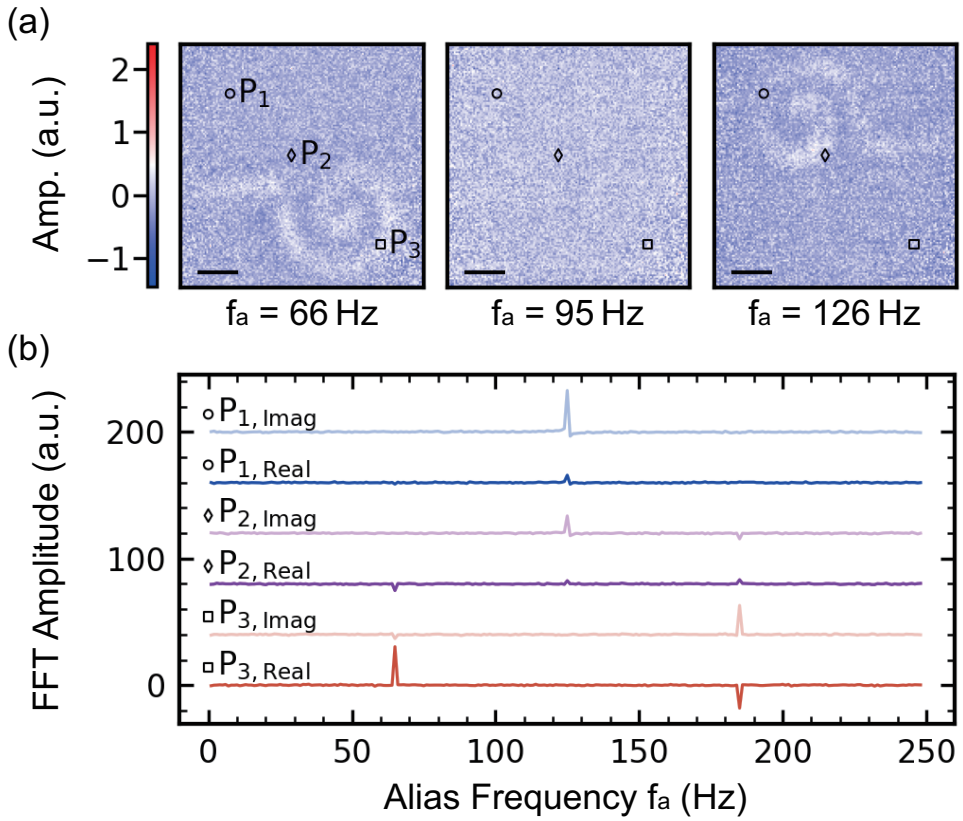


Figure 3.8: CASR imaging at detuned alias frequencies. (a) CASR amplitude images acquired under the same conditions as Figure 3.6, shown at alias frequencies of 66 Hz and 126 Hz (detuned by 1 Hz from the applied tones at 65 Hz and 125 Hz, respectively), and at an intermediate alias frequency of 95 Hz. All scale bars correspond to $50\,\mu\mathrm{m}$. The colorbar is not centered at zero due to asymmetry in the projection of the RF magnetic field onto the sensing NV axis. (b) Real and imaginary components of the CASR spectrum as a function of alias frequency for three representative pixels, $\mathrm{P}_{1,2,3}$, whose locations are indicated in (a). Peaks corresponding to the applied signal tones are illustrated in the phase-offset polar plot of Figure 3.7(b).

practicality of RF-QDM measurements.

In Figure 3.6, CASR amplitude images are shown at the applied RF signal frequencies as well as at alias frequencies far from any signal tone. Figure 3.8(a) provides complementary CASR amplitude images acquired under identical experimental conditions at alias frequencies detuned by 1 Hz from the applied tones at 65 Hz and 125 Hz, and at an intermediate alias frequency of 95 Hz. The color scale in Figure 3.8(a) is reduced by a factor of 20 relative to Figure 3.6 to highlight the weak residual signal amplitudes observed when the detection frequency is detuned by as little as 1 Hz.

Figure 3.8(b) shows the positive-frequency real component, $S^{+}_{\mathrm{Real,m}}$, and the negative imaginary component, $-S^{+}_{\mathrm{Imag,m}}$, of the CASR spectrum as a function of alias frequency for the three representative pixels $\mathrm{P}_{1,2,3}$. These results complement the polar representation in Figure 3.7(b), which summarizes the phase offsets and peak amplitudes of the real and imaginary CASR components for each applied signal tone.

The phase uncertainty in the CASR measurements is estimated as

$$\delta\phi = \arcsin\left(\frac{\sigma_1}{S_{\mathrm{CASR}}(f_2)}\right) \approx 0.6^{\circ}, \tag{3.17}$$

where σ_1 is the noise floor of the CASR spectrum for pixel P_1 as shown in Figure 3.7(b), and $S_{\mathrm{CASR}}(f_2)$ is the CASR amplitude at the alias frequency corresponding to $f_2 = 125\,\mathrm{Hz}$.

3.4 Performance of the RF-QDM

3.4.1 Spatial Resolution and Frequency Range

To further illustrate the $\sim 2\,\mu\mathrm{m}$ spatial resolution and the wide, tunable frequency range of the RF-QDM, we perform measurements under the same conditions as those described in Figure 3.5(b), except that a diamond with a $1.7\,\mu\mathrm{m}$-thick near-surface NV layer is used. We first apply a 1 MHz AC signal with peak current $I_p = 6.6\,\mu\mathrm{A}$ to the upper microcoil on the NV–diamond surface. After a 1.2 s acquisition (200 camera external frames), we obtain an RF magnetic field amplitude image with a peak-to-peak variation of approximately 300 nT, revealing the near-field pattern generated by the microcoil with an SNR of ~ 53, in good agreement with numerical simulations as shown in Figure 3.9.

The simulations are performed following the same approach described in Sec. 2.2.2, by calculating the three-dimensional magnetic field produced by the microcoil, averaging the field at a $7\,\mu\mathrm{m}$ stand-off distance over the NV layer thickness, and projecting the result onto the sensing NV orientation.

As discussed in Sec. 3.3.1, the central detection frequency of the dynamical decoupling sequence is readily tunable over the MHz range by adjusting the spacing between π pulses. The maximum sequence duration, limited by the NV ensemble spin coherence time T_2, determines the lower bound of the detectable signal frequency f_s. For the XY8-8 sequence used here, we measure $T_2 \approx 60\,\mu\mathrm{s}$ as shown in Figure 3.10, which corresponds to a maximum pulse spacing of $\tau \approx 1\,\mu\mathrm{s}$ and thus a minimum detectable frequency of $f_s \approx 0.5\,\mathrm{MHz}$. As a demonstration, we image the RF magnetic field generated by a 0.5 MHz AC signal applied to the upper microcoil with the same peak current of $6.6\,\mu\mathrm{A}$ as shown in Figure 3.9. Although the spatial pattern remains consistent with the 1 MHz measurement and simulations, the SNR decreases to approximately 34 due to increased NV fluorescence decay

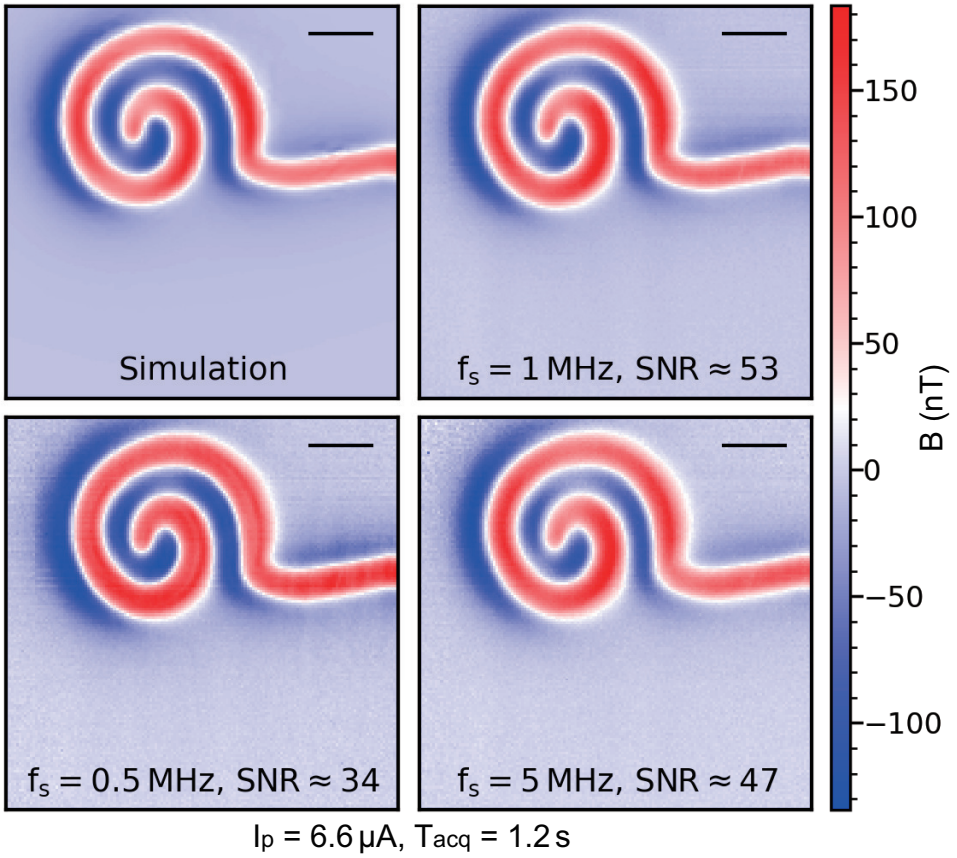


Figure 3.9: RF-QDM imaging of narrowband magnetic fields with known phase using a dynamical-decoupling (XY8-8) protocol and a $1.7\,\mu$m-thick NV layer. Alternating currents at 1 MHz, 0.5 MHz, and 5 MHz with peak amplitude $I_p = 6.6\,\mu$A are applied to the upper microcoil in separate experiments. After 1.2 s of averaging per frequency, the images exhibit SNRs of approximately 50, 34, and 47, respectively, calculated using the same method as in Figure 3.5(b). The imaged RF magnetic field patterns are consistent over an order of magnitude in signal frequency and agree with numerical simulations of a DC current of $6.6\,\mu$A. All scale bars correspond to $50\,\mu$m. The colorbar is not centered at zero due to asymmetry in the projection of the RF magnetic field onto the sensing NV axis.

during the longer sensing time.

To image even lower-frequency narrowband signals, a spin-echo sequence may be employed [50]. For the diamonds used in the present work, this corresponds to a maximum pulse spacing of $\tau = T_{2,\mathrm{Hahn}} \approx 10\,\mu\mathrm{s}$, indicating that the RF-QDM is capable of detecting narrowband signals down to approximately 50 kHz, albeit with reduced sensitivity.

The upper detection frequency limit of the dynamical decoupling sequence is set by the duration of the π pulses, which is determined by the achievable NV Rabi frequency under microwave driving. In the current RF-QDM implementation, the on-chip Ω-shaped coplanar waveguide produces a Rabi frequency of approximately 6.4 MHz at the maximum microwave amplifier output power (~ 50 dBm). Because the pulse spacing τ must exceed the π-pulse duration, the maximum detection frequency is therefore below 6.4 MHz. As a demonstration, we image a 5 MHz RF magnetic field pattern with $I_p = 6.6\,\mu\mathrm{A}$, achieving an SNR of approximately 47, comparable to the 1 MHz results.

Increasing the maximum detectable frequency could be achieved by reducing the diameter of the microwave antenna to enhance the Rabi frequency; however, this would degrade microwave field homogeneity, which is detrimental for wide-field imaging. Alternatively, microwave resonators can be used to achieve stronger driving fields, but at the cost of fixing the detection frequency and reducing experimental flexibility. To enable imaging of higher-frequency signals, spanning from $\sim 10\,\mathrm{MHz}$ into the GHz regime without these limitations, we employ a quantum frequency-mixing protocol with the RF-QDM [26], which is discussed in the following chapter.

3.4.2 AC Magnetic Sensitivity Optimization

For AC magnetic field measurements using NV centers and dynamical decoupling sequences, the magnetic sensitivity limited by photon shot noise and spin-projection noise is approximately given by [17]

$$\eta_{\mathrm{AC}} = \frac{\pi}{2\Delta m_s \gamma} \frac{1}{C e^{-(t_{\mathrm{S}}/T_2)^p} \sqrt{N}} \frac{\sqrt{t_{\mathrm{I,R}} + t_{\mathrm{S}}}}{t_{\mathrm{S}}}, \tag{3.18}$$

where $\Delta m_s = 1$ corresponds to the spin-state difference used for sensing, C is the optical readout contrast at zero sensing time, T_2 is the NV spin coherence time, p characterizes the coherence decay envelope [23], N is the average photon number collected per measurement, and $t_{\mathrm{I,R}}$ is the combined initialization and readout time.

The coherence time measured with dynamical decoupling sequences follows a power-law dependence on the number of π pulses [51], $T_2(N_\pi) = T_2(1) N_\pi^s$, where the exponent s is determined by the noise spectrum of the surrounding spin bath and typically exhibits sublinear behavior [25]. For an AC signal at frequency f_s, the sensing time scales linearly with pulse number as $t_{\mathrm{S}} = 2N_\pi / f_s$. After experimental determination of C, N, and $t_{\mathrm{I,R}}$, the optimal number of π pulses that minimizes the AC sensitivity is [17]

$$N_{\pi,\mathrm{opt}} = \left[\frac{(2 f_s T_2(1))^p}{2p(1-s)} \right]^{\frac{1}{p(1-s)}}. \tag{3.19}$$

Using photodiode measurements with the $10\,\mu\mathrm{m}$ NV layer diamond, we determine a spatially averaged value of $T_2(1) = 10\,\mu\mathrm{s}$ from a Hahn spin-echo measurement and $p = 1.3$. Fitting the coherence time as a function of pulse number yields $s = 0.44(1)$ as shown in Figure 3.10(a), inset. For a signal frequency of $f_s = 1\,\mathrm{MHz}$, Eq. (3.19) predicts an optimal sequence length of approximately XY8-16.

In wide-field RF-QDM imaging using the lock-in camera, however, camera quantization noise must also be considered. For a fixed number of demodulation cycles, camera noise increases with sensing sequence length, as discussed in Sec 3.4.3. Taking both photon shot noise and camera noise into account, the optimal sensing sequence is therefore shorter than XY8-16.

To experimentally determine the optimal sequence length, including camera noise, we vary the number of XY8 repetitions and measure the AC magnetic sensitivity of each pixel across the field of view. The per-pixel sensitivity is calculated as $\eta = \delta B\sqrt{T_{\mathrm{acq}}}$, where δB is the minimum detectable magnetic field corresponding to $\mathrm{SNR} = 1$ after an acquisition time T_{acq}. For a camera operating at an external frame rate f_{SR}, the per-pixel sensitivity is given by

$$\eta = \frac{\sigma_{\mathrm{pxl}}}{\sqrt{f_{\mathrm{SR}}}}, \tag{3.20}$$

where σ_{pxl} is the standard deviation of the magnetic field signal at that pixel across all recorded frames.

Using 500 frames acquired at $f_{\mathrm{SR}} = 1/[4N_d(t_{\mathrm{I,R}} + t_{\mathrm{S}})]$ with $N_d = 34$, $t_{\mathrm{I,R}} = 26\,\mu\mathrm{s}$, $t_{\mathrm{S}} = N_\pi/(2f_s)$, and $f_s = 1\,\mathrm{MHz}$, we find that the XY8-8 sequence provides the optimal performance. The resulting median per-pixel AC magnetic sensitivity is $0.93(1)\,\mathrm{nT{\cdot}Hz^{-1/2}}$.

Given a sensing voxel volume of $40\,\mu\mathrm{m}^3$, this corresponds to a volume-normalized AC sensitivity of $5.88\,\mathrm{nT{\cdot}Hz^{-1/2}} \cdot \mu\mathrm{m}^{3/2}$, comparable to state-of-the-art photodiode-based XY8 AC magnetometry using NV ensembles [52]. An analogous optimization performed with the $1.7\,\mu\mathrm{m}$-thick NV layer diamond yields a median per-pixel sensitivity of $2.56(1)\,\mathrm{nT{\cdot}Hz^{-1/2}}$ and a volume-normalized sensitivity of $6.68\,\mathrm{nT{\cdot}Hz^{-1/2}} \cdot \mu\mathrm{m}^{3/2}$ as shown in Figure 3.10(b). The reduced performance is attributed to increased camera quantization noise due to the lower NV fluorescence rate in the thinner NV layer.

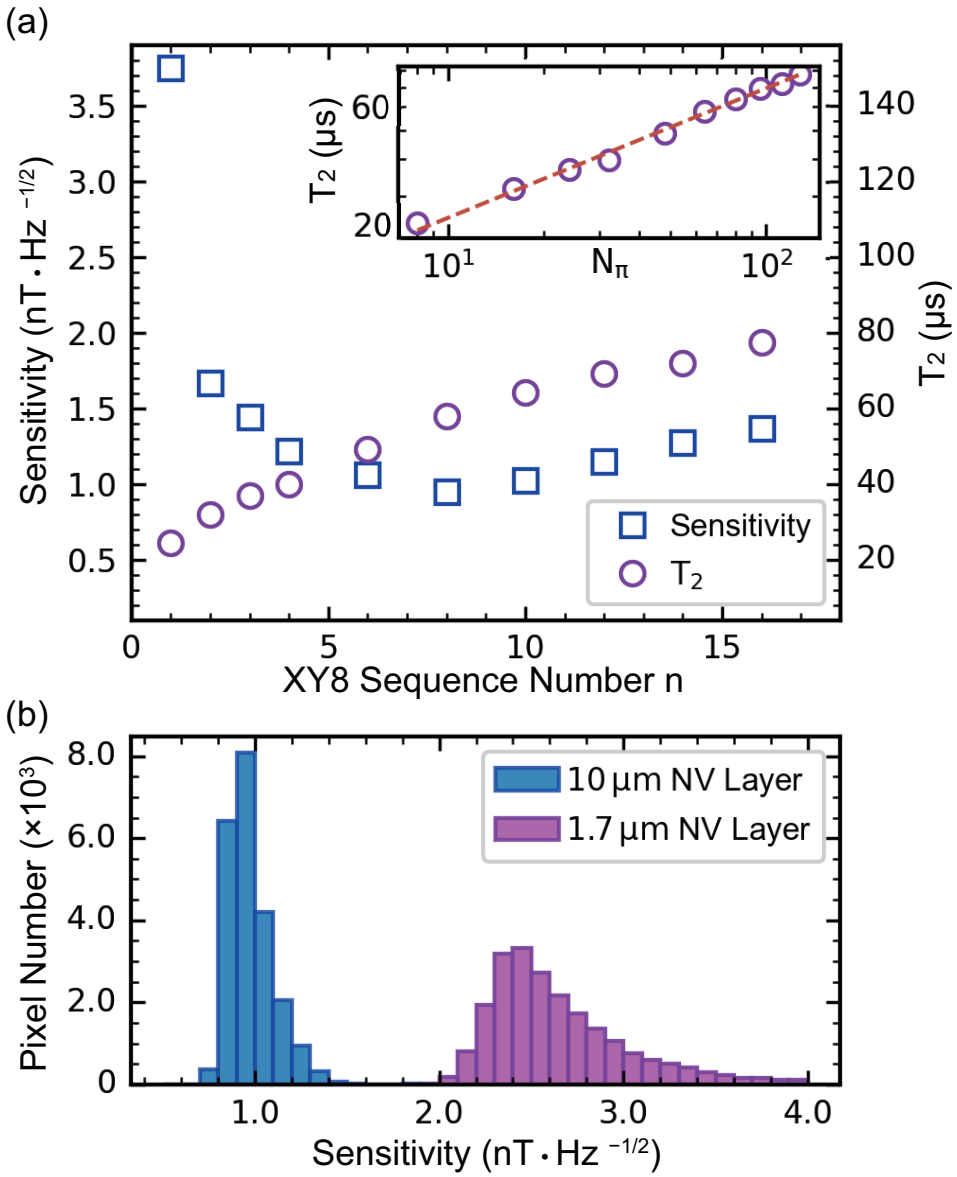


Figure 3.10: (a) Optimization of AC magnetic sensitivity as a function of XY8 sequence number, measured using photodiode detection with a $10\,\mu$m-thick NV layer diamond. Increasing the XY8-n sequence length extends the NV spin coherence time T_2. The optimal median single-pixel sensitivity across the field of view is achieved with the XY8-8 sequence. The inset shows a power-law fit of the measured coherence time T_2 versus the number of π pulses, $N_\pi = 8n$, yielding a fitted exponent $s = 0.44(1)$. (b) RF-QDM imaging using the lock-in camera with a 1 MHz signal applied via the RF test coil. Histogram of the single-pixel AC magnetic sensitivity across the field of view using the XY8-8 sequence. The median sensitivity is $0.93(1)\,\text{nT}\cdot\text{Hz}^{-1/2}$ for the $10\,\mu$m-thick NV layer diamond and $2.56(1)\,\text{nT}\cdot\text{Hz}^{-1/2}$ for the $1.7\,\mu$m-thick NV layer diamond.

3.4.3 Noise Source Analysis

For the RF-QDM measurements presented here, photon shot noise and camera quantization noise are the dominant limitations to AC magnetic sensitivity. We estimate the shot-noise-limited sensitivity using Eq. (3.18). Photodiode measurements with a $50\,\mu\mathrm{m}$ laser illumination diameter yield typical ensemble-averaged parameters for the $10\,\mu\mathrm{m}$ NV layer diamond of $C \approx 3\%$, $T_2 = 58\,\mu\mathrm{s}$, and $p = 1.3$. With $t_{\mathrm{I,R}} = 26\,\mu\mathrm{s}$, $t_{\mathrm{S}} = 32\,\mu\mathrm{s}$ for an XY8-8 sequence, and an estimated photon number of $N \approx 4\times10^4$ per pixel [39], the shot-noise-limited sensitivity at $f_s = 1\,\mathrm{MHz}$ is $\eta_{\mathrm{shot}} \approx 0.3\,\mathrm{nT{\cdot}Hz^{-1/2}}$.

The quantization noise of the Heliotis lock-in camera, which includes electronic and digitization noise, depends on the number of demodulation cycles N_d and can be expressed in device units (DU) as [45]

$$\sigma_{\mathrm{quant}} = \sqrt{0.81 + 0.16N_d}. \tag{3.21}$$

Using the median zero-crossing slope of the AC magnetometry curves across the FOV, $\overline{\Delta S/\Delta B_z} = 258\,\mathrm{DU}/\mu\mathrm{T}$, the corresponding quantization-noise-limited sensitivity is

$$\eta_{\mathrm{quant}} = \frac{\sigma_{\mathrm{quant}}}{\overline{\Delta S/\Delta B_z}\sqrt{f_{\mathrm{SR}}}}, \tag{3.22}$$

yielding $\eta_{\mathrm{quant}} \approx 0.86\,\mathrm{nT{\cdot}Hz^{-1/2}}$.

Combining photon shot noise and camera quantization noise in quadrature gives a total estimated sensitivity of $\eta_{\mathrm{est}} = 0.91\,\mathrm{nT{\cdot}Hz^{-1/2}}$, in agreement with the measured value of $0.93(1)\,\mathrm{nT{\cdot}Hz^{-1/2}}$. For the present RF-QDM, the overall sensitivity is therefore limited primarily by the lock-in camera. Improving sensitivity will require increasing NV fluorescence intensity, spin-state readout contrast, and coherence time T_2, as well as diamond engineering to enable higher laser intensities without

contrast degradation due to charge-state conversion [53].

Finally, we note that wide-field NV sensing using SPAD arrays offers high temporal resolution and single-photon counting capability [54], but is best suited for ultrathin NV layers ($< 100\,\mathrm{nm}$) with very low photon counts per pixel, and therefore provides lower per-pixel magnetic sensitivity than camera-based RF-QDM systems.

3.4.4 Spatial Noise and Spatial Resolution

In addition to per-pixel magnetic sensitivity, spatial noise—arising from pixel-to-pixel camera variance and spatial inhomogeneity in the diamond crystal (e.g., strain and NV density variations)—is a critical metric for evaluating RF-QDM performance. To quantify spatial noise, we perform single-frame measurements with no RF magnetic signal applied. For a given narrowband detection frequency, the spatial magnetic noise floor, $\sigma_{\mathrm{Spatial}}$, is defined as the standard deviation of the measured in-phase magnetic field amplitude across all pixels within the FOV.

During magnetic imaging, a fundamental trade-off exists between spatial resolution and spatial noise. One effective strategy to suppress spatial noise is spatial binning, in which neighboring pixels are grouped to form larger "super pixels." This approach reduces the spatial noise at the cost of coarser spatial resolution. For applications that do not require the highest spatial resolution, spatial averaging can therefore be used in place of extended temporal averaging, enabling shorter acquisition times while maintaining comparable SNR.

We demonstrate this approach using 5×5 pixel binning, corresponding to a super-pixel size of $10\,\mu\mathrm{m}$. With no RF signal applied to the microcoils, we observe that $\sigma_{\mathrm{Spatial}} \propto T_{\mathrm{acq}}^{-1/2}$ for both $2\,\mu\mathrm{m}$ single-pixel resolution and $10\,\mu\mathrm{m}$ super-pixel resolution at a 1 MHz detection frequency (Figure 3.11(a)),

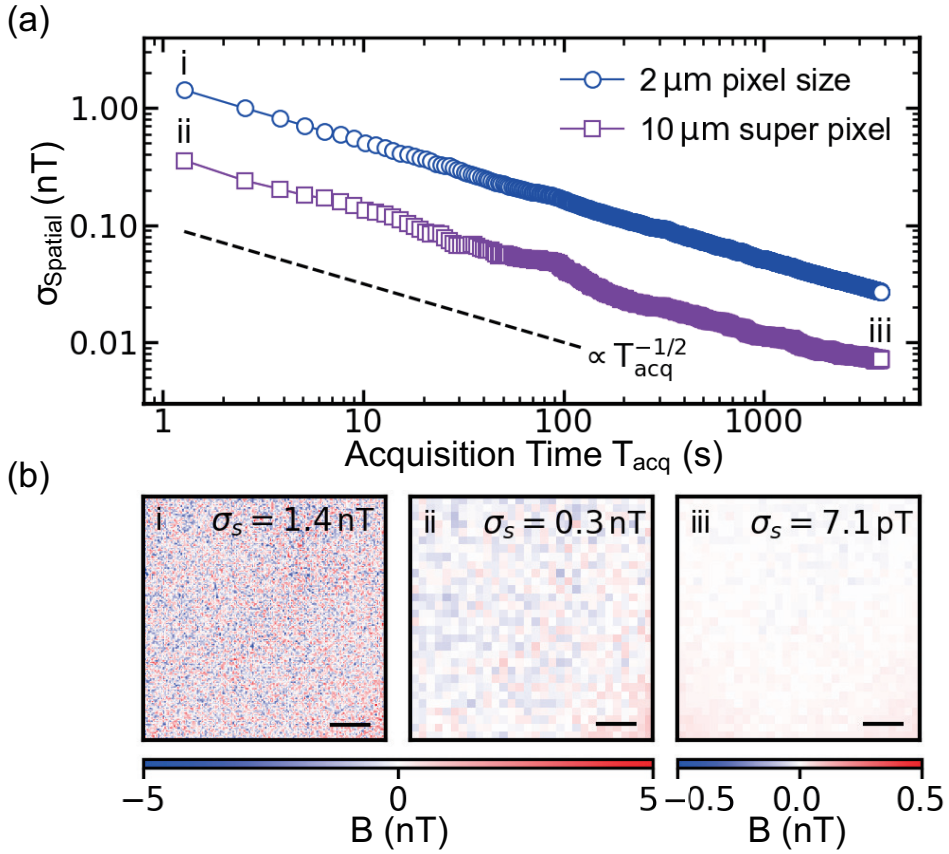


Figure 3.11: Suppression of spatial noise in RF-QDM magnetic images through temporal and spatial averaging. (a) Measured spatial magnetic noise floor, $\sigma_{\mathrm{Spatial}}$, with no RF signal applied to the microcoils and a 1 MHz detection frequency, shown as a function of data acquisition time T_{acq} for $2\,\mu$m single-pixel resolution and $10\,\mu$m (binned) super-pixel resolution. The dashed black line indicates the expected scaling $\sigma_{\mathrm{Spatial}} \propto T_{\mathrm{acq}}^{-1/2}$ as a guide to the eye. (b) Example RF-QDM images of the magnetic noise background and corresponding values of $\sigma_{\mathrm{Spatial}}$: (i) $2\,\mu$m single-pixel resolution with $T_{\mathrm{acq}} = 1.2\,\mathrm{s}$; (ii) $10\,\mu$m super-pixel resolution with $T_{\mathrm{acq}} = 1.2\,\mathrm{s}$; and (iii) $10\,\mu$m super-pixel resolution with $T_{\mathrm{acq}} = 3600\,\mathrm{s}$. All scale bars correspond to $50\,\mu$m. The magnetic noise is spatially uncorrelated. Comparisons between (i) and (ii) illustrate spatial averaging, while comparisons between (ii) and (iii) demonstrate temporal averaging. The lock-in camera frame rate is identical for all measurements.

where T_{acq} is the total data acquisition time. This scaling indicates that the RF-QDM spatial magnetic noise can be effectively suppressed through temporal averaging out to hour-long timescales.

Notably, the spatial noise floor obtained with $10\,\mu\mathrm{m}$ super-pixel resolution after a single $1.2\,\mathrm{s}$ acquisition is comparable to that achieved by averaging multiple frames over $30\,\mathrm{s}$ at $2\,\mu\mathrm{m}$ single-pixel resolution. With $10\,\mu\mathrm{m}$ super-pixel resolution and a 1 hour acquisition time, the spatial noise background can be reduced to $7.1(1)\,\mathrm{pT}$ as shown in Figure 3.11(b). Under these conditions, the median per-pixel narrowband magnetic sensitivity is also improved to $0.18(1)\,\mathrm{nT}\cdot\mathrm{Hz}^{-1/2}$.

3.5 Potential Applications of the RF-QDM

A primary application of the RF-QDM is micron-scale real-space NMR imaging. The Hz-scale spectral resolution demonstrated here enables spatially resolved identification of chemical shifts and scalar (J) couplings, key spectral fingerprints of molecular structure, across samples on the diamond surface [38]. Such capability is critical for NMR applications in chemistry, life sciences, and materials research.

Based on previous NV-NMR studies [38, 55], we estimate that a spatial noise floor of $\sim 50\,\mathrm{pT}$ is required to resolve micron-scale NMR images with $\mathrm{SNR} > 1$ for thermally polarized samples in a bias magnetic field of $\sim 0.1\,\mathrm{T}$. When dynamic nuclear polarization (DNP) is employed, this threshold relaxes to approximately $10\,\mathrm{nT}$. Given the current RF-QDM performance, an acquisition time of $\sim 40\,\mathrm{s}$ is sufficient to surpass the thermal-polarization threshold at a spatial resolution of $10\,\mu\mathrm{m}$, while DNP would enable imaging within $\sim 30\,\mathrm{ms}$ at $2\,\mu\mathrm{m}$ spatial resolution as shown in Figure 3.11(a). Other hyperpolarization techniques can provide even higher nuclear spin polarization [56], though typically at lower bias magnetic fields.

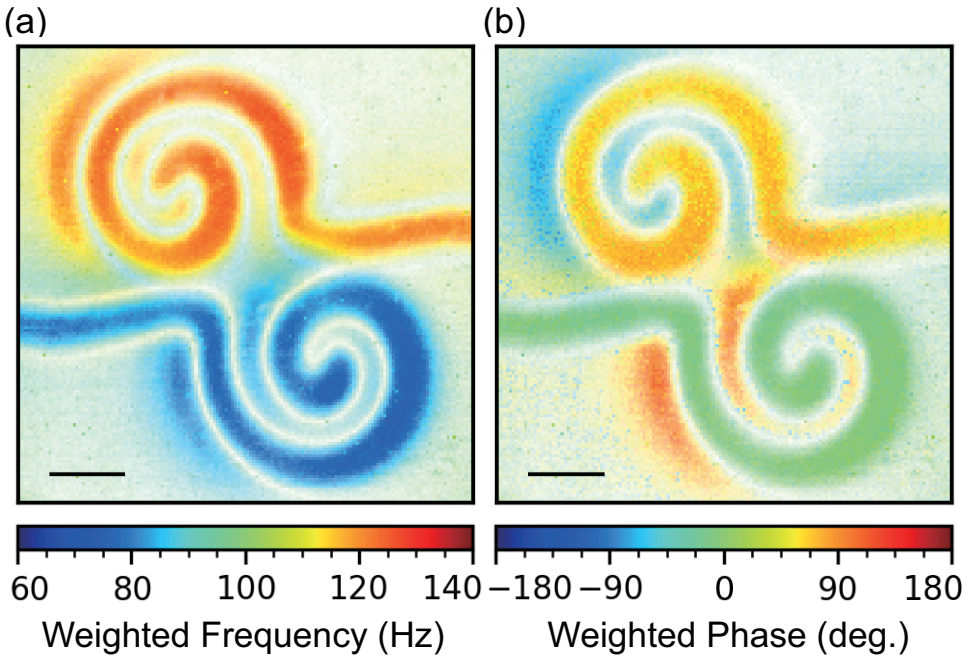


Figure 3.12: CASR imaging of weighted frequency and phase of RF magnetic signals generated by two microcoils under the same experimental conditions as Figure 3.6. (a) Weighted frequency image, defined as $f_w = \int f\, S_{\mathrm{CASR}}\, df / \int S_{\mathrm{CASR}}\, df$. A transparency mask based on the integrated CASR amplitude suppresses no-signal regions. The colorbar indicates the frequency integration range, which includes f_1 and f_2 but excludes f_3, revealing the near-field spatial distributions of the selected frequency components. (b) Weighted phase image, defined as $\phi_w = \int \phi\, S_{\mathrm{CASR}}\, df / \int S_{\mathrm{CASR}}\, df$, using the same mask and integration range as in (a). The spatial distributions of $\phi_1 = -6^\circ$ and $\phi_2 = 80^\circ$ are clearly resolved. The $\sim 180^\circ$ phase reversal outside each spiral arises from the opposite direction of the RF magnetic field generated by the microcoils. All scale bars correspond to $50\,\mu\mathrm{m}$.

With the millisecond-scale temporal resolution provided by the lock-in camera, the RF-QDM may enable real-time imaging of NMR dynamics in micron-scale samples, including chemical processes in living systems at the cellular scale and samples integrated within microfluidic platforms [57]. To illustrate the ability of the RF-QDM to spatially discriminate spectrally crowded narrowband signals, such as those encountered in NMR, we present CASR images of weighted frequency and phase for two microcoils whose signals differ by only 60 Hz around a 1 MHz carrier frequency as shown in Figure 3.12. The near-field RF magnetic patterns from the two microcoils are clearly distinguished at the micron scale based on their frequency and phase. Similar weighted-frequency and weighted-phase NV-NMR images could enable spatially resolved monitoring of chemical composition and concentration in complex samples.

Although the RF signal amplitudes are held constant in the present experiments, the RF-QDM protocols are compatible with signals exhibiting temporal decay envelopes, such as free-induction decay (FID) in NMR. In this case, the decay envelope manifests as a finite linewidth in the CASR spectrum at each pixel, providing spatially resolved information on both signal frequency and linewidth. This capability opens a path toward real-space NV-NMR spectroscopy of micron-scale samples with spatially varying nuclear spin densities and local environments. Further improvements in lock-in camera frame rate and data handling capacity will directly translate into enhanced sensing bandwidth and spectral resolution for such applications.

Beyond NMR, the RF-QDM offers a range of additional applications. Prior work has demonstrated single-channel AC susceptibility measurements of two-dimensional magnetic materials using NV centers and XY8 sequences [58]. The RF-QDM extends this capability to wide-field, micron-scale imaging of AC susceptibility, enabling spatially resolved characterization of magnetic materials. The RF-QDM is also well suited for imaging inductive eddy currents in conductors [59]. By simultaneously

measuring the amplitude and phase of the induced RF magnetic fields, the RF-QDM can provide higher spatial resolution and sensitivity than conventional eddy-current inspection techniques.

For integrated circuits and other micron-scale electronic devices, RF-QDM imaging may support failure analysis [60, 61] and hardware Trojan detection [62]. Mapping magnetic field activity across a range of operating frequencies can provide complementary insight to static magnetic imaging [36, 63]. In addition, the RF-QDM may be applied to impedance tomography in biological systems [64]. Unlike invasive electrode-based approaches that provide only sparse measurements, the RF-QDM offers a noninvasive method for directly imaging the amplitude and phase of modulated currents with full spatial coverage across the field of view.

In summary, we demonstrate a lock-in-camera-based quantum diamond microscope capable of narrowband RF magnetic field imaging with $\sim 1\,\mathrm{Hz}$ spectral resolution under ambient conditions. The RF-QDM achieves per-pixel sensitivities of $\sim 1\,\mathrm{nT}\cdot\mathrm{Hz}^{-1/2}$ with $\sim 2\,\mu\mathrm{m}$ spatial resolution over a $300 \times 300\,\mu\mathrm{m}^2$ field of view. Through temporal averaging and spatial binning, the spatial noise floor can be reduced to the picotesla scale, approaching the levels required for real-space NV-NMR imaging of thermally polarized samples. By simultaneously imaging the amplitude, frequency, and phase of RF magnetic fields, the RF-QDM provides a versatile platform for applications including NMR spectroscopy, AC susceptibility mapping, eddy-current inspection, electronic circuit analysis, and impedance tomography.

For the results presented here, the RF magnetic field images correspond to the projection of the field onto a single NV orientation. Because diamond hosts four crystallographic NV orientations, the RF-QDM can in principle be extended to full vector RF magnetic field imaging [65], enabling correction of image artifacts arising from spatial variations in field direction. The current implementation is limited to signal frequencies below $\sim 10\,\mathrm{MHz}$ by constraints on the achievable NV Rabi frequency.

Future improvements in microwave delivery, as well as using quantum frequency-mixing protocols [26], will enable imaging of higher-frequency signals extending from tens of megahertz into the gigahertz regime.

Finally, the RF-QDM is compatible with advanced narrowband sensing protocols that offer improved sensitivity relative to XY8, such as DROID-60 [66, 67] and quantum-logic-enhanced repetitive readout [52]. Although these protocols introduce additional complexity and longer sensing times, advances in lock-in camera technology and data processing are expected to mitigate current limitations and further enhance RF-QDM performance for narrowband magnetic field imaging.

Chapter 4: High-Resolution and Wide-Frequency-Range Magnetic Spectroscopy

In the previous chapter, the CASR method was implemented in our QDM, enabling simultaneous imaging of the amplitude, frequency, and phase of narrowband oscillating magnetic fields. These results showed strong overall performance, including single-pixel magnetic sensitivity at the nanotesla level, Hz-scale spectral resolution, and micron-scale spatial resolution.

However, most narrowband NV-diamond magnetic sensing protocols including CASR rely on pulsed dynamical decoupling sequences [22, 68]. As a result, the detectable signal frequency range is typically limited to below $\sim 20\,\mathrm{MHz}$, constrained by the amplitude and timing requirements of MW control pulses used to manipulate NV electronic spins [15, 52, 66]. Continuous dynamical decoupling techniques, such as spin-lock Rabi protocols, can extend the sensing bandwidth to approximately $85\,\mathrm{MHz}$ [69, 70], but generally suffer from reduced sensitivity compared to pulsed techniques and remain limited by the achievable MW driving strength. Other approaches, including Rabi magnetometry [28, 29], enable narrowband sensing with low spectral resolution (on the order of kHz) over a frequency range extending up to $\sim 300\,\mathrm{MHz}$ from the NV spin transition frequencies (near $3\,\mathrm{GHz}$ at low bias magnetic fields). However, these methods are not well suited for intermediate signal frequencies ($\sim 100\,\mathrm{MHz}$ to $2\,\mathrm{GHz}$) or for higher-frequency signals ($> 4\,\mathrm{GHz}$) unless a strong DC bias magnetic field (on the order of $0.1\,\mathrm{T}$) is applied to tune the NV spin resonances.

Recently, a quantum frequency mixing (QFM) effect was proposed to overcome these limitations by converting narrowband magnetic signals from otherwise inaccessible frequency regimes into the optimal detection band of NV sensing protocols. A proof-of-principle experimental demonstration achieved detection of a $150\,\mathrm{MHz}$ test signal with a spectral resolution of approximately $10\,\mathrm{kHz}$ [26]. Subsequently, QFM-based Rabi magnetometry was extended to wide-field NV ensemble imaging

with comparable spectral resolution [71]. As summarized below, the QFM approach exploits the nonlinear response of the NV electronic spin system to both a target RF magnetic signal (at an arbitrary frequency) and a strong applied AC bias field that is detuned from the target signal by $\sim 1\,\mathrm{MHz}$. This interaction produces an effective magnetic signal at the difference frequency between the target and bias fields, thereby "mixing down" the signal into a frequency range that is well matched to NV-based detection protocols.

In this chapter, we demonstrate a QFM-based magnetic spectroscopy protocol that operates over a wide signal frequency range spanning from $10\,\mathrm{MHz}$ to $4\,\mathrm{GHz}$ and can be integrated with CASR to achieve sub-Hz spectral resolution, nanotesla-level noise floors, and precise phase measurements with errors below 1°. We begin by characterizing the narrowband magnetic sensitivity of the combined QFM–CASR protocol across this broad frequency range, showing good agreement between experimental measurements and theoretical estimates. We then highlight the protocol's wide-frequency capability and high spectral resolution by measuring multi-frequency spectra at $0.6\,\mathrm{GHz}$, $2.4\,\mathrm{GHz}$, and $4\,\mathrm{GHz}$, resolving fine spectral features separated by as little as $1\,\mathrm{Hz}$. Finally, we demonstrate phase-sensitive detection by measuring the phase of a $2.4\,\mathrm{GHz}$ signal with a standard deviation of 0.4°. Compared to previous demonstrations of QFM-based magnetometry [26, 71], the QFM–CASR approach presented here extends the accessible signal frequency range by more than an order of magnitude and improves the achievable spectral resolution by over four orders of magnitude. As noted in the thesis introduction, this chapter recapitulates material published in [27]. This peer-reviewed journal article also contains additional technical details, e.g., about the experimental setup, not included in the present chapter.

4.1 QFM-CASR Spectroscopy Protocol

To enable high-resolution detection of magnetic signals over a broad frequency range, we employ a QFM protocol that down-converts a target RF signal of arbitrary frequency into the optimal detection band of NV-based narrowband sensing schemes. This approach is conceptually analogous to classical frequency mixing [72], where nonlinear circuit elements generate sum and difference frequency components. In the quantum case, the nonlinear response arises from the driven NV electronic spin system, which can be described within a multi-mode Floquet framework.

4.1.1 Rotating Frame Hamiltonian Approximation in the Floquet Picture

Following the analysis of the QFM effect introduced in [26], we model the NV electronic spin ground state as a two-level Hamiltonian H_0 simplified to include only one resonant transition from $m_s = 0$ to $m_s = +1$ or $m_s = -1$ with transition frequency ω_0:

$$H_0 = \frac{\omega_0}{2}\sigma_z. \tag{4.1}$$

The interaction Hamiltonian representing the effect of both an AC bias field and target RF signal field, denoted H_b and H_s respectively, is given by:

$$H_{int} = H_b + H_s. \tag{4.2}$$

We consider the case where both the AC bias field and signal field are far detuned from the NV spin transition ω_0 and linearly polarized transverse to the NV $\hat{z}$ axis, e.g., linearly polarized in $\hat{x}$, so that the

relevant bias and signal Hamiltonians are given by:

$$H_{b,s} = \Omega_{b,s} \cos(\omega_{b,s} + \phi_{b,s})\sigma_x, \tag{4.3}$$

where $\Omega_{b,s}$ and $\omega_{b,s}$ are the amplitude and frequency of the bias or signal fields, respectively. The total Hamiltonian of the system in the laboratory frame is:

$$H = \frac{\omega_0}{2}\sigma_z + \Omega_s \cos(\omega_s + \phi_s)\sigma_x + \Omega_b \cos(\omega_b + \phi_b)\sigma_x. \tag{4.4}$$

We then transform into a rotating frame described by the frequency ω_0 with the unitary $U = e^{-i(\omega_0 t/2)\sigma_z}$, such that the Hamiltonian in the rotating frame is given by:

$$\tilde{H} = U^\dagger H U + i\frac{\partial U^\dagger}{\partial t}U. \tag{4.5}$$

See Figure 4.1(b). Since $U^\dagger H_0 U + i(\partial U^\dagger/\partial t)U = 0$, $\tilde{H} = U^\dagger H_{int} U$. Applying the rotating frame transformation to the AC bias field and signal field Hamiltonians, we obtain:

$$\tilde{H}_{b,s} = U^\dagger H_{b,s} U = \frac{\Omega_{b,s}}{2}(e^{i(\omega_{b,s}t+\phi_{b,s})} + e^{-i(\omega_{b,s}t+\phi_{b,s})})(e^{i\omega_0 t}\sigma_+ + e^{-i\omega_0 t}\sigma_-). \tag{4.6}$$

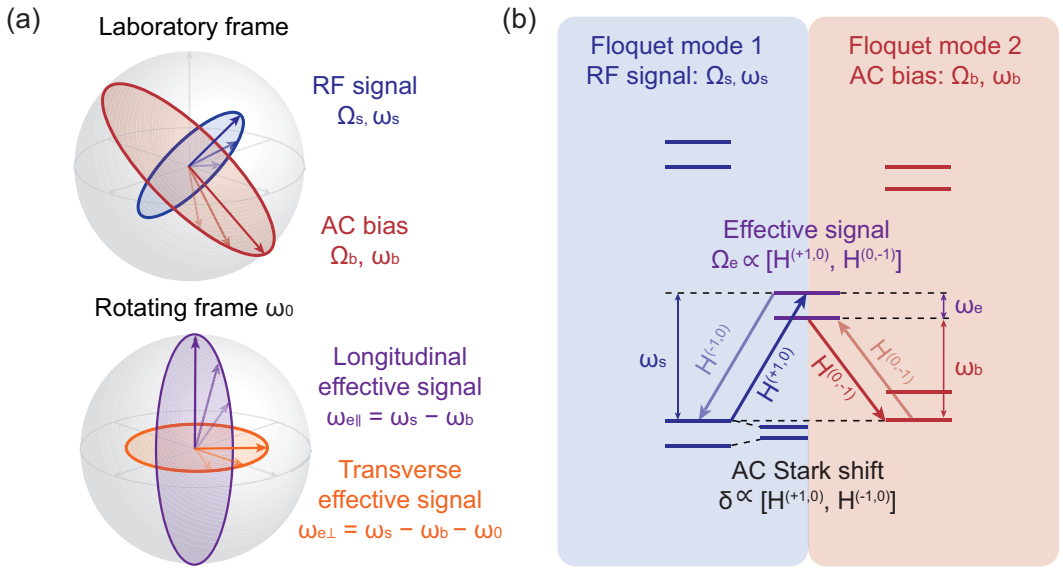


Figure 4.1: (a) Bloch sphere visualization of the AC bias, target RF signal, and effective signal fields in both the laboratory and rotating frames, illustrating the general case. In the present work, the XY8 sequence is primarily sensitive to the longitudinal effective signal; and the RF signal and AC bias fields are linearly polarized and generated by the same coil, and hence are colinear in the laboratory frame. Thus, we consider only the x-component of the RF signal and AC bias fields, which contribute to the longitudinal effective signal, to simplify the Hamiltonian model. (b) Simplified schematic of quantum frequency mixer dynamics, including the effective signal amplitude Ω_e and AC Stark shift δ mediated by virtual Floquet modes.

The total system Hamiltonian in the rotating frame, $\tilde{H} = \tilde{H}_b + \tilde{H}_s$, is then given by:

$$\begin{aligned}\tilde{H} = &\frac{\Omega_b}{2}\left(\cos\left([\omega_b-\omega_0]t+\phi_b\right)\sigma_x + \sin\left([\omega_b-\omega_0]t+\phi_b\right)\sigma_y\right)\\ &+\frac{\Omega_b}{2}\left(\cos\left([\omega_b+\omega_0]t+\phi_b\right)\sigma_x - \sin\left([\omega_b+\omega_0]t+\phi_b\right)\sigma_y\right)\\ &+\frac{\Omega_s}{2}\left(\cos\left([\omega_s-\omega_0]t+\phi_s\right)\sigma_x + \sin\left([\omega_s-\omega_0]t+\phi_s\right)\sigma_y\right)\\ &+\frac{\Omega_s}{2}\left(\cos\left([\omega_s+\omega_0]t+\phi_s\right)\sigma_x - \sin\left([\omega_s+\omega_0]t+\phi_s\right)\sigma_y\right).\end{aligned} \tag{4.7}$$

This Hamiltonian describes a four-mode Floquet problem, with frequency modes $(\omega_b - \omega_0)$, $(\omega_b + \omega_0)$, $(\omega_s - \omega_0)$, $(\omega_s + \omega_0)$. To simplify the analysis for the regime relevant to our experiment, we first consider the two-mode Floquet problem; see Figure 4.1(c). For a time-dependent Hamiltonian

$H(t)$ with two uncoupled frequency modes ω_1 and ω_2 of evolution amplitudes Ω_1 and Ω_2, the Fourier expansion is given by:

$$H(t) = \sum_{n=-\infty}^{\infty} \sum_{k=-\infty}^{\infty} H^{(n,k)} e^{in\omega_1 t} e^{ik\omega_2 t}. \tag{4.8}$$

We can write $H(t)$ as a Floquet Hamiltonian H_F in the Floquet space, using the ladder operators $F_{n,k}^{\omega_{1,2}}$ and the number operator F_z:

$$H_F = \sum_{n=-\infty}^{\infty} \sum_{k=-\infty}^{\infty} \left(H^{(n,k)} \otimes F_n^{\omega_1} \otimes F_k^{\omega_2} + \omega_1 I \otimes F_z^{\omega_1} \otimes I + \omega_2 I \otimes I \otimes F_z^{\omega_2} \right). \tag{4.9}$$

We then approximately diagonalize H_F by transforming with unitary $U = e^S$ for Hermitian operator S, and apply the Baker–Campbell–Hausdorff (BCH) expansion for the infinitesimal case:

$$\tilde{H}_F = e^S H_F e^{-S} = H_F + [S, H_F] + \frac{1}{2}[S, [S, H_F]] + ... \tag{4.10}$$

With an appropriate choice of S, the off-diagonal terms can be made to cancel to first order; and the second order term can be simplified so that transformation back to the Hilbert space yields the second order term [26]:

$$H_2^{(m,h)} = -\frac{1}{2} \sum_{n,k} \frac{[H^{(m-n,h-k)}, H^{(n,k)}]}{n\omega_1 + k\omega_2}. \tag{4.11}$$

As the fast-oscillating terms quickly average to zero, we consider only the cases where the integer pairs (m, h) satisfy $m\omega_1 + h\omega_2 \ll \omega_3$, for $\omega_3 \in \{n\omega_1 + k\omega_2 \,|\, n, k \in \mathbb{Z},\ n\omega_1 + k\omega_2 \neq 0,\ H^{(n,k)} \neq 0\}$. When the amplitudes $\Omega_1, \Omega_2 \ll \omega_1, \omega_2$, the system dynamics are then well approximated by a single

effective Hamiltonian given by:

$$H(t) = \frac{1}{2}\left(\frac{1}{\omega_1} - \frac{1}{\omega_2}\right)[H_1, H_2]e^{i(\omega_1+\omega_2)t}. \tag{4.12}$$

We now apply the above analysis to the four-mode Floquet problem assuming $\Omega_b, \Omega_s \ll \omega_b, \omega_s$ so that we can truncate at second order. The resulting Hamiltonian includes all possible sums and differences of the four frequency modes $(\omega_b - \omega_0)$, $(\omega_b + \omega_0)$, $(\omega_s - \omega_0)$, $(\omega_s + \omega_0)$. However, we also assume $|\omega_s - \omega_b| \ll (\omega_b + \omega_s), \omega_0$ and make the rotating wave approximation to neglect fast oscillating terms. Thus, only the $|\omega_s - \omega_b|$ and DC terms survive in the effective Hamiltonian:

$$\begin{aligned}\tilde{H}_e = -\left(\frac{\omega_0}{\omega_b^2 - \omega_0^2} + \frac{\omega_0}{\omega_s^2 - \omega_0^2}\right)\frac{\Omega_b\Omega_s}{2}\frac{e^{i[(\omega_s-\omega_b)t+(\phi_s-\phi_b)]} + e^{-i[(\omega_s-\omega_b)t+(\phi_s-\phi_b)]}}{2}\sigma_z \\ + \left(-\frac{\Omega_b^2\omega_0}{2(\omega_b^2 - \omega_0^2)} - \frac{\Omega_s^2\omega_0}{2(\omega_s^2 - \omega_0^2)}\right)\sigma_z.\end{aligned} \tag{4.13}$$

We define the effective signal at frequency $\omega_e = \omega_s - \omega_b$, with phase $\phi_e = \phi_s - \phi_b$, effective amplitude Ω_e, and AC Stark shift δ:

$$\Omega_e = \frac{\Omega_b\Omega_s}{2}\left(\frac{\omega_0}{\omega_b^2 - \omega_0^2} + \frac{\omega_0}{\omega_s^2 - \omega_0^2}\right), \tag{4.14}$$

$$\delta = \left(-\frac{\Omega_b^2\omega_0}{\omega_b^2 - \omega_0^2} - \frac{\Omega_s^2\omega_0}{\omega_s^2 - \omega_0^2}\right). \tag{4.15}$$

The effective interaction Hamiltonian in the rotating frame is that of an applied longitudinal field with amplitude Ω_e at frequency ω_e:

$$\tilde{H}_e = \frac{\delta}{2}\sigma_z + \Omega_e \cos(\omega_e t + \phi_e)\sigma_z. \tag{4.16}$$

We note the asymptotic behavior of Ω_e tends towards $\frac{\Omega_b\Omega_s}{\omega_0}$ in the low frequency limit for ω_s and ω_b

and towards $\frac{\Omega_b \Omega_s \omega_0}{\omega_s^2}$ in the ultra-high frequency limit, assuming $\omega_b \approx \omega_s$.

We also note that driving an NV electronic spin transition with a strong field $\Omega_0 \cos(\omega_0 t)\sigma_x$, as part of a dynamical decoupling sensing protocol (XY8-6 in this work), induces a Bloch-Siegert shift of the effective signal frequency given by $\frac{\Omega_0}{8\omega_0}$ [26]. Since the NV resonance frequency ω_0 is typically on the order of GHz, while the microwave field amplitude Ω_0 is on the order of MHz, this static shift is much smaller than the CASR detection bandwidth employed in this work and hence has insignificant effect on calibration of the QFM-CASR protocol.

4.1.2 QFM-CASR Experimental Design and Signal Processing

In our experiment, an ensemble of NV centers in diamond serves simultaneously as the quantum frequency mixer and the magnetic field sensor. A target RF magnetic field at frequency ω_s and a strong AC bias field at frequency ω_b are applied through the same coil as shown in Figure 4.2(a). The bias field frequency is chosen such that the difference frequency $\omega_e = \omega_s - \omega_b$ lies within the sensitive bandwidth of a pulsed dynamical decoupling sequence. As derived in the previous subsection, the combined action of the two off-resonant fields produces an effective longitudinal magnetic field in the rotating frame, described by the approximate Hamiltonian

$$\tilde{H}_e \approx \frac{\delta}{2}\sigma_z + \Omega_e \cos(\omega_e t + \phi_e)\sigma_z, \tag{4.17}$$

where δ is an AC Stark shift, $\phi_e = \phi_s - \phi_b$ is the effective signal phase, and the effective signal amplitude is

$$\Omega_e = \frac{\Omega_s \Omega_b}{2}\left(\frac{\omega_0}{\omega_s^2 - \omega_0^2} + \frac{\omega_0}{\omega_b^2 - \omega_0^2}\right). \tag{4.18}$$

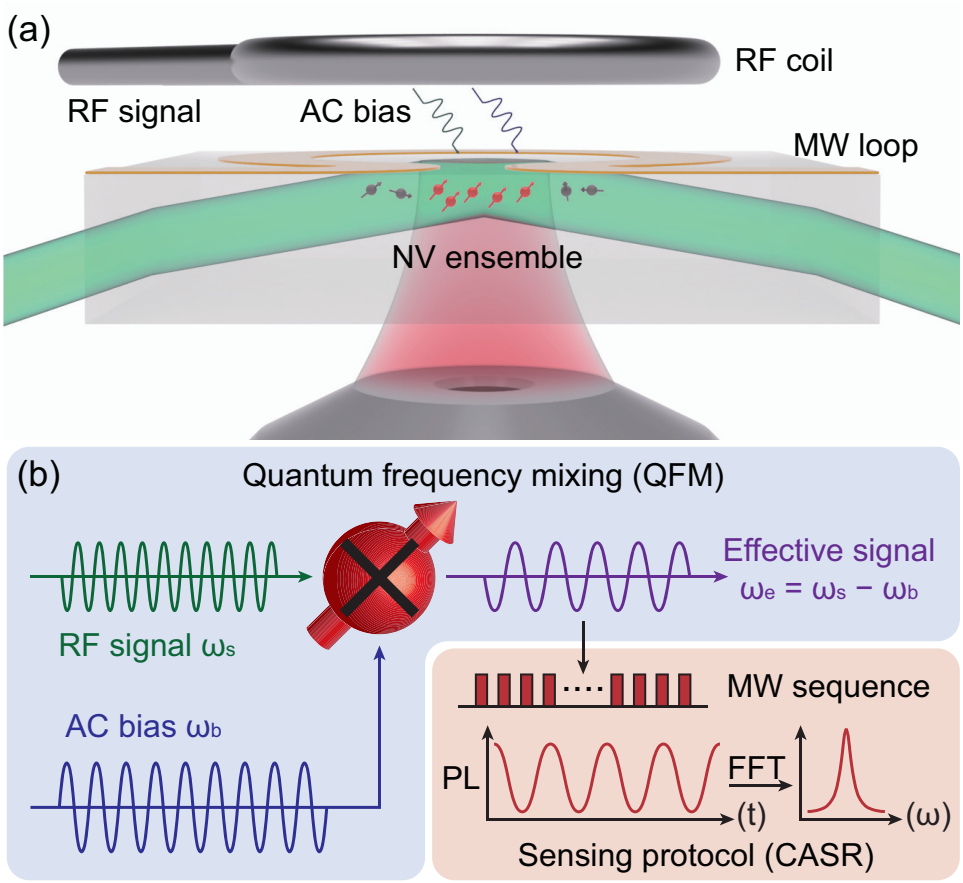


Figure 4.2: (a) Wide-frequency-range RF magnetic sensing using an NV ensemble in diamond. The NV electronic spin state is initialized and read out optically, while MW control pulses are applied via an on-chip MW loop. A target RF signal and a strong AC bias field are applied through the same coil. QFM between these fields generates an effective signal within the optimal detection band (~ 1 MHz) of narrowband NV sensing protocols. (b) Integration of QFM with the CASR protocol. The target signal at frequency ω_s is mixed with an AC bias field at frequency ω_b, producing an effective longitudinal signal at $\omega_e = \omega_s - \omega_b$. The CASR protocol samples the resulting NV PL at a rate ω_{SR}, yielding an aliased signal at ω_a and enabling sub-Hz spectral resolution after Fourier analysis.

Because $\Omega_b \ll |\omega_{s,b} \pm \omega_0|$ in the experimental regime, the mixed-down signal amplitude Ω_e is substantially smaller than the original target signal amplitude Ω_s.

To sensitively detect this weak effective signal, we integrate the QFM scheme with the CASR protocol [38] as shown in Figure 4.2(b). CASR consists of repeated, phase-synchronized blocks of identical dynamical decoupling sequences (XY8-k in this work), interleaved with optical readout of the NV photoluminescence (PL) at a fixed sampling rate ω_{SR}. The resulting time-domain PL signal encodes the oscillation of the effective longitudinal field generated by QFM.

For the experimental parameters used here, the normalized time-domain QFM-CASR signal can be approximated as [15]

$$S(t) = \frac{1}{2}\left[1 + \sin\left(\frac{4\pi N\Omega_e}{\omega_e}\cos(\omega_e t + \phi_e)\right)\right], \tag{4.19}$$

where N is the total number of π pulses in each sensing sequence ($N = 48$ for the XY8-6 protocol used in this experiment). Applying a Fast Fourier Transform (FFT) to the discretely sampled CASR signal yields a frequency-domain spectrum centered at the alias frequency

$$\omega_a = |\omega_e - n\omega_{\mathrm{SR}}|, \tag{4.20}$$

with peak amplitude

$$S_{\mathrm{CASR}} \propto J_1\left(\frac{4\pi N\Omega_e}{\omega_e}\right), \tag{4.21}$$

where $J_1(x)$ is the first-order Bessel function and n is the integer closest to $\omega_e/\omega_{\mathrm{SR}}$. Under the operating conditions of this experiment, higher-order Bessel contributions are negligible (see details in Section 3.1.2).

We ensure $\Omega_e \ll \omega_e$ so that the first-order Bessel function is well approximated by a linear response, yielding $S_{\mathrm{CASR}} \propto \Omega_e$. By calibrating the CASR response using a known reference signal, the effective amplitude Ω_e can be extracted directly from the measured spectrum. Because the AC bias field frequency and amplitude are independently known and held constant, this calibration enables quantitative determination of the target signal's frequency, amplitude, and phase over a wide frequency range.

4.2 Sensitivity Assessment Across a Wide Signal Frequency Range

We first demonstrate the wide target-signal frequency range accessible with the QFM–CASR protocol (10 MHz to 4 GHz) and characterize the corresponding narrowband magnetic sensitivity. Figure 4.3 summarizes the measured and estimated sensitivities, and provides additional details on sensitivity calibration, error bars, and bias-field polarization.

All measurements are performed using a micron-scale 2.7 ppm NV ensemble near the surface of a CVD diamond substrate. We implement CASR using XY8-k sequences as the sensing blocks to improve robustness against pulse errors [73]. In these experiments, we optimize sensitivity for an effective (mixed-down) signal frequency $\omega_e = (2\pi)\,1$ MHz by setting the π-pulse spacing to $\tau = 0.5\,\mu$s and choosing $k = 6$ [18, 52]. The XY8-6 sensitivity for a 1 MHz test signal is calibrated to be $\eta_0 = 102(1)\,\mathrm{pT}\cdot\mathrm{Hz}^{-1/2}$ using the method described in Section 3.4.2

Using the QFM relation for the effective signal amplitude [Eq. (4.18)], the expected sensitivity to a target signal at frequency ω_s can be estimated as

$$\eta_s = \eta_0 \frac{\Omega_s}{\Omega_e}, \tag{4.22}$$

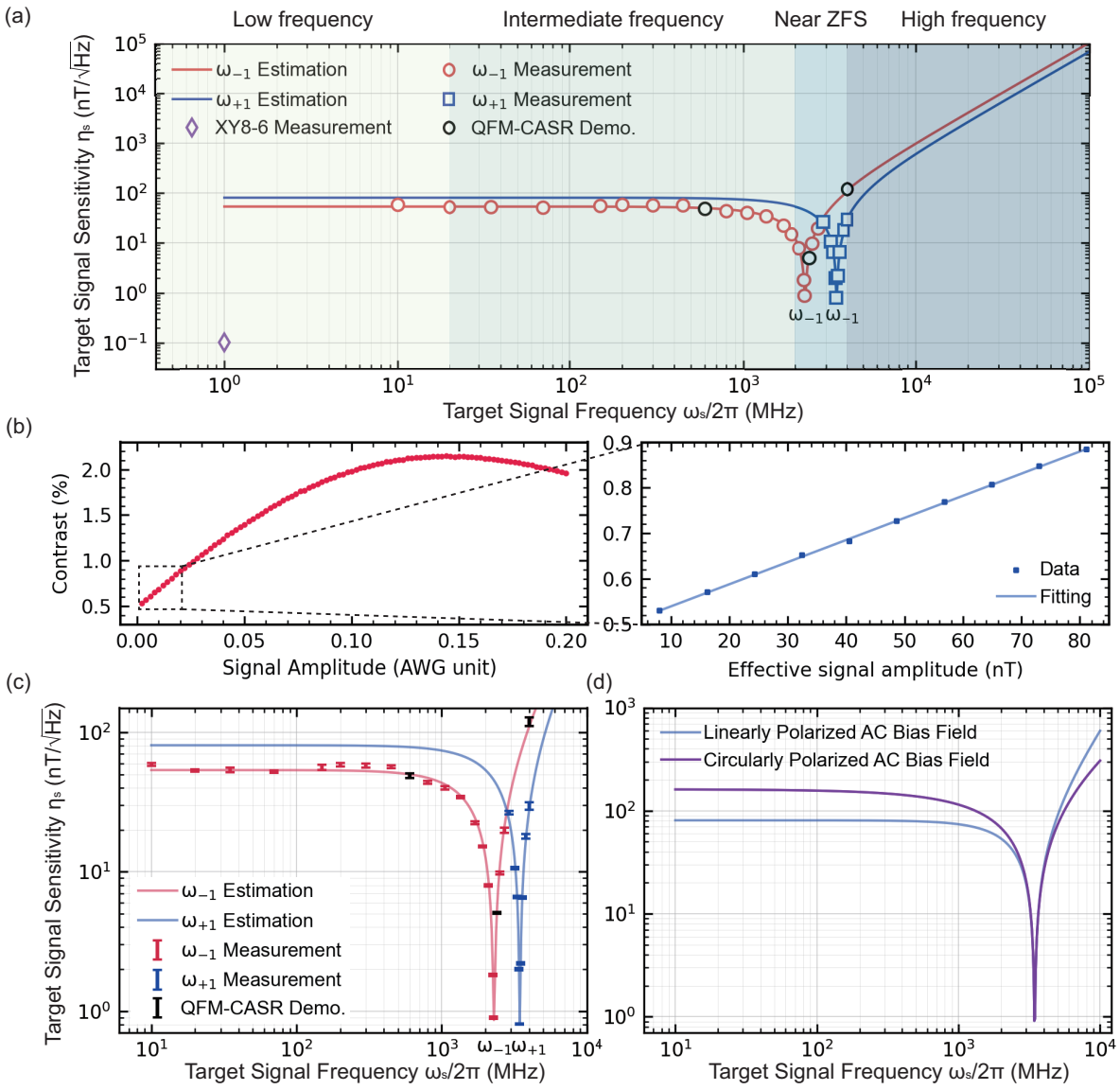


Figure 4.3: QFM–CASR sensitivity across a wide target signal frequency range. (a) Estimated and measured QFM–CASR narrowband magnetic sensitivity for target signal frequencies from 10 MHz to 4 GHz. The AC bias field is detuned by 1 MHz from the target signal and has a fixed amplitude $\Omega_b = (2\pi)4.3$ MHz. Red and blue curves show estimated sensitivities based on the measured XY8-6 sensitivity at 1 MHz (purple diamond) and Eq. (4.18), for MW pulses resonant with the NV spin transitions at $\omega_{-1} = (2\pi)2.29$ GHz and $\omega_{+1} = (2\pi)3.45$ GHz, respectively. Circles and squares indicate experimentally measured sensitivities at selected target frequencies. Black circles ("QFM–CASR Demo.") correspond to frequencies used in the sub-Hz spectral resolution demonstrations shown in Figure 4.4. (b) Example sensitivity calibration measurement for a target signal at 2.4 GHz with an effective (mixed-down) signal frequency near 1 MHz. (c) Same data as in (a), shown with error bars derived from the standard deviation of 10 independent sensitivity measurements at each target frequency. (d) Comparison of estimated sensitivities for linearly polarized (blue) and circularly polarized (purple) AC bias fields, evaluated for the NV spin transition at ω_{+1}. Circular polarization provides a modest sensitivity enhancement for $\omega_s > \omega_{+1}$.

evaluated for the two cases in which the applied MW control pulses are resonant with the NV spin transitions at $\omega_{\pm1}$ (solid curves in Figure 4.3). For $\omega_s \ll \omega_{\pm1}$, the estimated target-signal sensitivity is approximately frequency independent, with $\eta_{s,-1} \approx 55\,\mathrm{nT}\cdot\mathrm{Hz}^{-1/2}$ and $\eta_{s,+1} \approx 80\,\mathrm{nT}\cdot\mathrm{Hz}^{-1/2}$ for our experimental parameters. The sensitivity improves as ω_s approaches the NV resonance while remaining in the far-detuned QFM regime (detuning > 20 MHz in our experiment) [26]. For $\omega_s > \omega_{\pm1}$, the estimated sensitivity rapidly degrades because the effective signal strength decreases strongly at high frequencies (see Eq. (4.18)).

Experimentally, we characterize QFM-CASR sensitivity using a procedure analogous to the XY8-6 sensitivity measurement described in Section 3.4.2. At each target signal frequency, we measure the 1-second standard deviation of the NV PL, calibrate the effective-signal magnetometry slope to obtain η_e, and convert to the target-signal sensitivity η_s using Eq. (4.18). We repeat this measurement 10 times at each frequency to obtain the mean value and the standard deviation, which sets the error bars shown in Figure 4.3(c). Across all target frequencies, the average fractional uncertainty is $\overline{\sigma/\eta_s} \approx 2.7\%$. The measured values of η_s agree well with the estimates in Figure 4.3.

4.2.1 AC bias-field calibration and target-signal amplitude control

Because $\Omega_e \propto \Omega_s\Omega_b$ [Eq. (4.18)], accurate calibration of the AC bias-field amplitude is essential for quantitative sensitivity measurements. We first measure the reflection coefficient S_{11} of the RF coil and find it to be approximately flat across the frequencies of interest. Using a spectrum analyzer (Signal Hound USB-SA44B), we monitor the RF amplifier output power and adjust the input power to the RF coil to ensure consistent delivered power across frequency.

We calibrate the AC bias-field amplitude by tuning the drive frequency to the NV resonance

$\omega_0 = \omega_{-1}$, driving NV Rabi oscillations, and extracting the Rabi frequency Ω_0. We then record the corresponding amplifier output power. Assuming that the coil response is sufficiently similar between ω_0 and a given bias frequency ω_b, we assign $\Omega_b = \Omega_0$ for equal delivered power. We evaluate the validity of this assumption experimentally in Section. 4.4. For the sensitivity measurements reported here, we use this procedure to maintain a constant bias-field amplitude Ω_b across all ω_b.

Because the target RF signal and AC bias field are generated by the same RF chain (AWG, amplifier, and RF loop) and differ in frequency by only ~ 1 MHz, the same power-calibration procedure also ensures that the target-signal amplitude is constant (for a given input setting) across the measured frequency range.

4.2.2 Example sensitivity calibration and polarization considerations

Figure 4.3(b) shows an example sensitivity calibration for a target signal at 2.4 GHz with an effective signal near 1 MHz. After setting the effective signal to be in-phase with XY8-6 (i.e., $\phi_s - \phi_b = 0$), we measure the AC magnetometry curve of the effective signal by sweeping the AWG output amplitude A (thereby sweeping Ω_s) while holding ϕ_s, ϕ_b, and Ω_b fixed. We identify the first turning point $A_{\pi/2}$ at which the NVs accumulate a $\pi/2$ dynamical phase; for this example, $A_{\pi/2} = 0.144$ AWG units. The effective-field amplitude corresponding to a $\pi/2$ phase is

$$B_{\pi/2} = \frac{\hbar\pi^2}{2g\mu_B N} = 0.58\,\mu\mathrm{T}, \tag{4.23}$$

yielding a calibration factor $B_{\pi/2}/A_{\pi/2} = 4.06\,\mu\mathrm{T}/\text{AWG unit}$. A linear fit to the near-zero region of the magnetometry curve gives a contrast slope $s = 4.86 \times 10^{-5}\,\mathrm{nT}^{-1}$. We then acquire 1 s of QFM–CASR data with no applied target signal to measure the contrast noise $\sigma = 4.57 \times 10^{-6}$, yielding an

effective-signal sensitivity

$$\eta_e = \frac{\sigma}{s}\sqrt{t} = 0.094\,\mathrm{nT}\cdot\mathrm{Hz}^{-1/2}, \tag{4.24}$$

and a corresponding target-signal sensitivity $\eta_s = 4.87\,\mathrm{nT}\cdot\mathrm{Hz}^{-1/2}$.

The small residual discrepancies between measured and estimated sensitivities are attributed primarily to frequency-dependent coil response: although S_{11} is approximately flat from 10 MHz to 4 GHz, it exhibits variations at the $\sim 10\%$ level.

Finally, Figure 4.3(d) compares estimated sensitivities for a linearly polarized AC bias field (used in all measurements here) and a circularly polarized AC bias field (not implemented experimentally). For a circularly polarized bias field and a linearly polarized target signal, the effective amplitude is [26]

$$\Omega_e = \frac{\Omega_b\Omega_s}{4}\left(\frac{1}{\omega_b-\omega_0}+\frac{1}{\omega_s-\omega_0}\right). \tag{4.25}$$

Linearly polarized bias fields provide better sensitivity for target signals below resonance ($\omega_s < \omega_0$), whereas circular polarization is optimal for signals above resonance ($\omega_s > \omega_0$). For NV resonance frequencies comparable to those used here (DC bias fields ~ 10 mT), a circularly polarized bias field is expected to yield an approximately twofold sensitivity improvement at a 10 GHz target frequency.

4.3 Demonstration and Performance of QFM-CASR Spectroscopy

4.3.1 Detection of Multi-frequency RF Signals with Hz-scale Spectral Resolution

We next experimentally demonstrate the capability of the QFM-CASR protocol to perform magnetic spectroscopy of multi-frequency RF signals with sub-Hz spectral resolution across a wide frequency range, as shown in Figure 4.4.

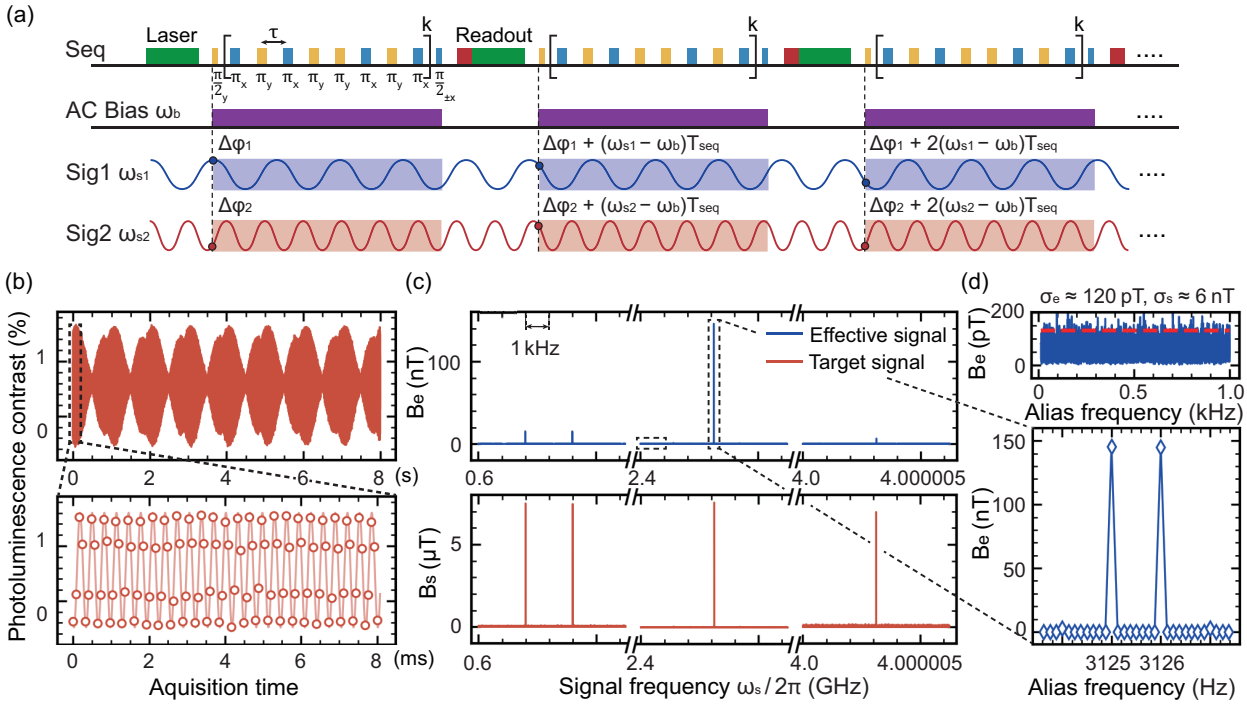


Figure 4.4: Demonstration of QFM-CASR spectroscopy of multi-frequency RF signals with sub-Hz spectral resolution over a wide frequency range. (a) QFM-CASR measurement protocol applied to a target signal consisting of two frequency components within the detection bandwidth. In a synchronized sequence of measurement periods, the NV electronic spin ensemble is initialized and read out using 532 nm laser pulses (green). A $\pi/2$ microwave pulse along the y-axis prepares the NV spin in a magnetically sensitive superposition state, followed by an XY8-k sequence ($k = 6$) resonant with a 1 MHz effective signal. A final $\pi/2$ pulse along the x or $-x$ axis projects the longitudinal spin state as signal or reference, followed by photoluminescence (PL) readout (red). During each measurement period, an AC bias field (violet) is applied to mix the two target signal frequencies, ω_{s1} and ω_{s2}, into an effective signal within the optimal detection band of the XY8-k sequence via quantum frequency mixing. (b) Time-domain QFM-CASR measurement of the two-tone target signal. A 1 Hz beating between the two signal components is clearly visible in the upper panel, while the lower zoomed-in panel resolves the higher-frequency oscillation near the CASR alias frequency ($\approx$ 3 kHz). (c) QFM-CASR spectra obtained from FFTs of the time-domain measurements over a wide frequency range. Center: spectrum near 2.4 GHz derived from the data in (b) after DC offset removal. Left and right: spectra near 0.6 and 4 GHz, respectively. The measured effective signal amplitudes are consistent with the frequency-dependent sensitivity of the QFM-CASR protocol (black circles in Figure 4.3). (d) Top: effective-signal noise floor with a standard deviation $\sigma_e \approx 120$ pT, corresponding to $\sigma_s \approx 6$ nT for a target signal near 2.4 GHz. Bottom: zoomed-in spectrum demonstrating sub-Hz resolution, clearly resolving the two target signal peaks at ω_{a1} and ω_{a2}.

A target signal near the 2.4 GHz communication band is applied, consisting of two frequency components: $\omega_{s1} = (2\pi)(2.4\,\mathrm{GHz} + 3.125\,\mathrm{kHz})$ and $\omega_{s2} = \omega_{s1} + (2\pi)1\,\mathrm{Hz}$, each with a nominal amplitude $\Omega_s = (2\pi)0.21\,\mathrm{MHz}$ ($B_s = 7.5\,\mu\mathrm{T}$).

To generate effective signals near 1 MHz, resonant with the XY8-6 sensing sequence (with π-pulse spacing $\tau = 0.5\,\mu\mathrm{s}$), we apply an AC bias field with frequency $\omega_b = (2\pi)2.399\,\mathrm{GHz}$ and amplitude $\Omega_b = (2\pi)4.3\,\mathrm{MHz}$ ($B_b = 153.4\,\mu\mathrm{T}$). The NV resonance frequency (using the $|0\rangle$ and $|-1\rangle$ states) is $\omega_{-1} = (2\pi)2.29\,\mathrm{GHz}$, corresponding to a DC bias magnetic field of 20.7 mT.

For each acquisition step in the QFM-CASR protocol (Figure 4.4(a)), the total sequence duration is $T_{\mathrm{seq}} = 80\,\mu\mathrm{s}$, yielding a CASR sampling rate of $\omega_{\mathrm{SR}} = (2\pi)12.5\,\mathrm{kHz}$. Based on Eq. (4.18), quantum frequency mixing reduces the effective signal amplitude by a factor of approximately 50 relative to the target signal. Because $\Omega_s \ll \Omega_b$, higher-order mixing terms are negligible, suppressing cross-talk between signal tones.

We perform a series of 10^5 QFM-CASR measurements, corresponding to 8 s of time-domain NV PL contrast data (Figure 4.4(b)). The upper panel clearly shows 1 Hz beating between the two signal components, while a zoomed-in view of the first 8 ms reveals fast oscillations at the alias frequency $\omega_a \approx (2\pi)3\,\mathrm{kHz}$. An FFT of the time-domain data yields QFM-CASR spectra with high signal-to-noise ratio for both effective and target signals, as shown in the center panel of Figure 4.4(c).

To demonstrate the wide operational frequency range of the protocol, we perform additional measurements near 0.6 GHz ($\omega_b = (2\pi)0.599\,\mathrm{GHz}$, $\omega_{s3} = (2\pi)(0.6\,\mathrm{GHz}+2\,\mathrm{kHz})$, $\omega_{s4} = (2\pi)(0.6\,\mathrm{GHz}+4\,\mathrm{kHz})$) and near 4 GHz ($\omega_b = (2\pi)3.999\,\mathrm{GHz}$, $\omega_{s5} = (2\pi)(4\,\mathrm{GHz} + 3.125\,\mathrm{kHz})$), using the same nominal target signal amplitude. These results are shown in the left and right panels of Figure 4.4(c). As expected from Eq. (4.18), the effective signal amplitude varies with target frequency, consistent with the frequency-dependent sensitivity summarized in Figure 4.3.

Figure 4.4(d) shows a zoomed-in view of the effective signal near 2.4 GHz, clearly resolving the two frequency components $\omega_{a1} = (2\pi)3125\,\mathrm{Hz}$ and $\omega_{a2} = (2\pi)3126\,\mathrm{Hz}$ with sub-Hz spectral resolution. The upper panel highlights the spectral noise floor, with an effective signal standard deviation of $\sigma_e \approx 120\,\mathrm{pT}$, comparable to the AC sensitivity of the XY8-6 sequence at 1 MHz. This corresponds to a target signal uncertainty of $\sigma_s \approx 6\,\mathrm{nT}$, consistent with the QFM-CASR sensitivity at 2.4 GHz shown in Figure 4.3.

4.3.2 Precise Phase Measurement of RF Signals

We further demonstrate that the QFM-CASR technique enables precise phase measurements of RF signals over a wide frequency range. Applying an FFT to the time-domain NV PL signal yields a complex frequency-domain response proportional to $\delta(\omega - \omega_e)e^{-i\phi_e}$ (see Eq. (4.19). The effective signal phase ϕ_e can therefore be extracted from the real and imaginary components of the QFM-CASR spectrum, as illustrated in Figure 4.5(a). With the AC bias phase ϕ_b controlled and known, the target signal phase is obtained directly as $\phi_s = \phi_b + \phi_e$.

In a demonstration experiment, we apply an AC bias field with $\phi_b = 0$ at $\omega_b = (2\pi)2.4\,\mathrm{GHz}$ and sweep the target signal phase ϕ_s for $\omega_s = (2\pi)2.401\,\mathrm{GHz}$. At each phase value, time-domain QFM-CASR data are acquired and transformed via FFT to obtain the corresponding spectrum. A full 360° phase sweep with a step size of 1° is performed, yielding the absolute, real, and imaginary components shown in Figure 4.5(b). Each phase point is acquired over 1 s without averaging.

The magnitude of the QFM-CASR spectrum, proportional to Ω_e, remains constant across the phase sweep, while the real and imaginary components oscillate sinusoidally with a relative $\pi/2$ phase shift. From their ratio, we determine the measured phase ϕ_s' and compute the phase error $\Delta\phi = \phi_s' - \phi_s$.

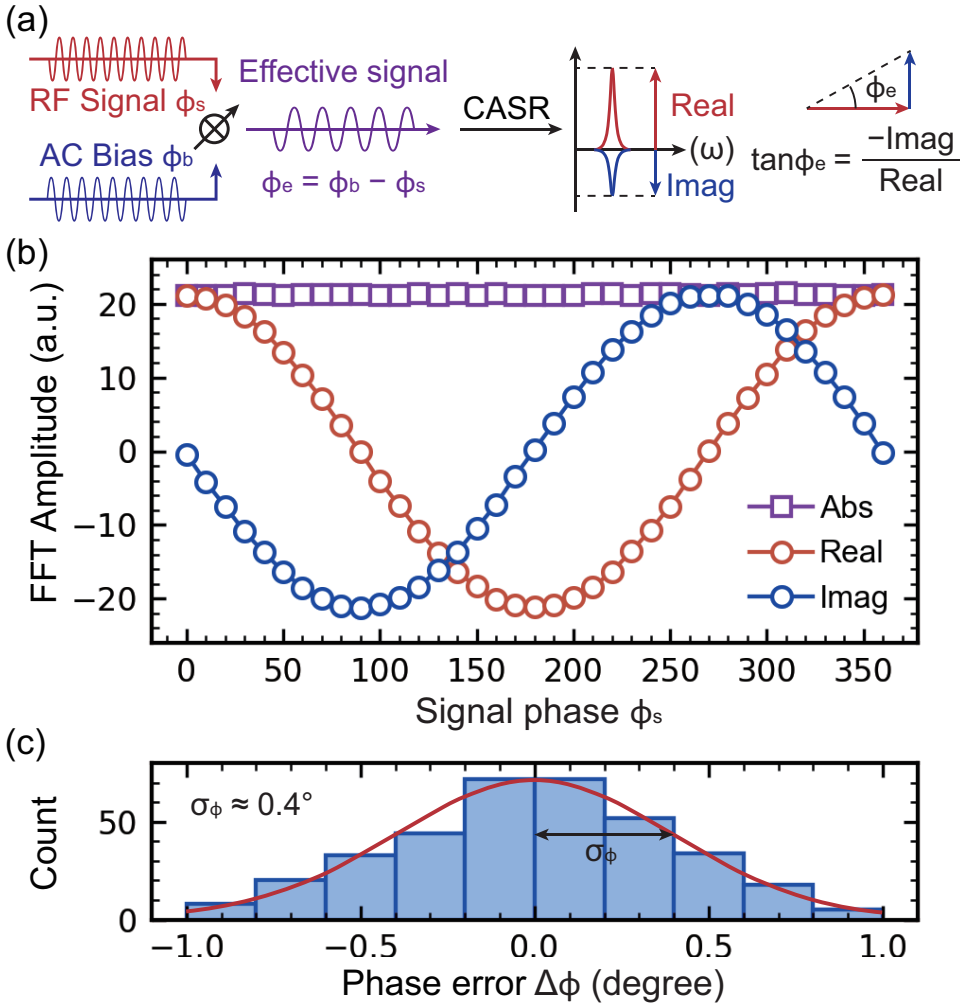


Figure 4.5: Precise phase measurement using QFM-CASR. (a) The effective signal generated through quantum frequency mixing has a phase ϕ_e equal to the difference between the target signal phase ϕ_s and the AC bias phase ϕ_b. By analyzing the real and imaginary components of the QFM-CASR spectrum, ϕ_e can be extracted. With ϕ_b known and controlled, the target phase is obtained as $\phi_s = \phi_e + \phi_b$. (b) Experimental demonstration with $\omega_b = (2\pi)2.4\,\mathrm{GHz}$ and $\omega_s = (2\pi)2.401\,\mathrm{GHz}$. While keeping $\phi_b = 0$, ϕ_s is swept over $360°$ in $1°$ steps. The real, imaginary, and absolute values of the QFM-CASR spectrum are shown for every 10 phase steps. (c) Histogram of the phase error between measured and applied phases. The distribution is Gaussian with standard deviation $\sigma_\phi \approx 0.4°$.

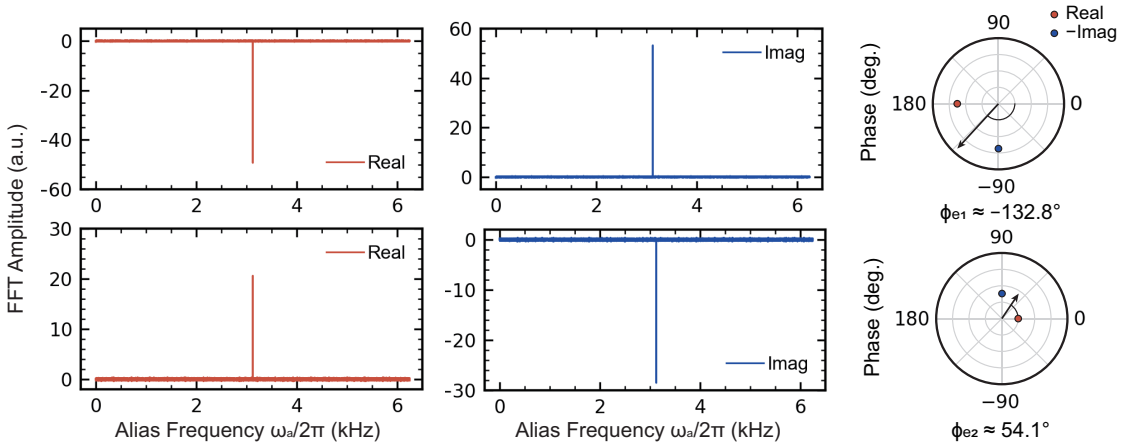


Figure 4.6: Precise QFM-CASR phase measurements of target signals near 666 MHz (top) and 4 GHz (bottom). For the experiment near 666 MHz. For the experiment near 4 GHz, the same $\Omega_{b,s}$ is applied as for the 666 MHz experiment, with $\omega_s = (2\pi)(4\,\mathrm{GHz} + 3.125\,\mathrm{kHz})$ and $\omega_b = (2\pi)3.999\,\mathrm{GHz}$. Real (red) and imaginary (blue) components of the QFM-CASR spectra are displayed, as generated from FFT of time-domain QFM-CASR data (NV PL measurements). Polar plots illustrate the phases of each effective signal, as derived from QFM-CASR measurements. Red and blue dots represent the real and imaginary amplitudes of the associated QFM-CASR spectra, respectively, while black arrows indicate the absolute value of the amplitude. Grids are shown as circles with a radial step size equivalent to 20 arbitrary units of FFT amplitude.

The resulting distribution (Figure 4.5(c)) is approximately Gaussian with standard deviation $\sigma_\phi \approx 0.4°$. Although the effective signal amplitude is reduced by quantum frequency mixing, the achieved phase precision remains high.

This approach can be extended to phase measurements of RF signals across the full detection bandwidth of the QFM-CASR protocol. We also demonstrate precise QFM-CASR phase measurement near two additional frequencies, $666\,\mathrm{MHz}$ and $4\,\mathrm{GHz}$. We use AC bias phases $\phi_{b1} = \phi_{b2} = 0$ at both frequencies; and applied target signal phases $\phi_{s1} = -133°$ at 666 MHz and $\phi_{s2} = 54°$ at 4 GHz.

The phase of the effective signal ϕ_e is determined from the ratio of the real and imaginary components of the QFM-CASR spectrum (see Figure 4.6). The experimental target signal phase ϕ'_s is then extracted via the relationship $\phi'_s = \phi_e + \phi_b$. From our measurements, we determine $\phi'_{s1} \approx -132.8°$ and $\phi'_{s2} \approx 54.1°$, in good agreement with the applied target signal phases.

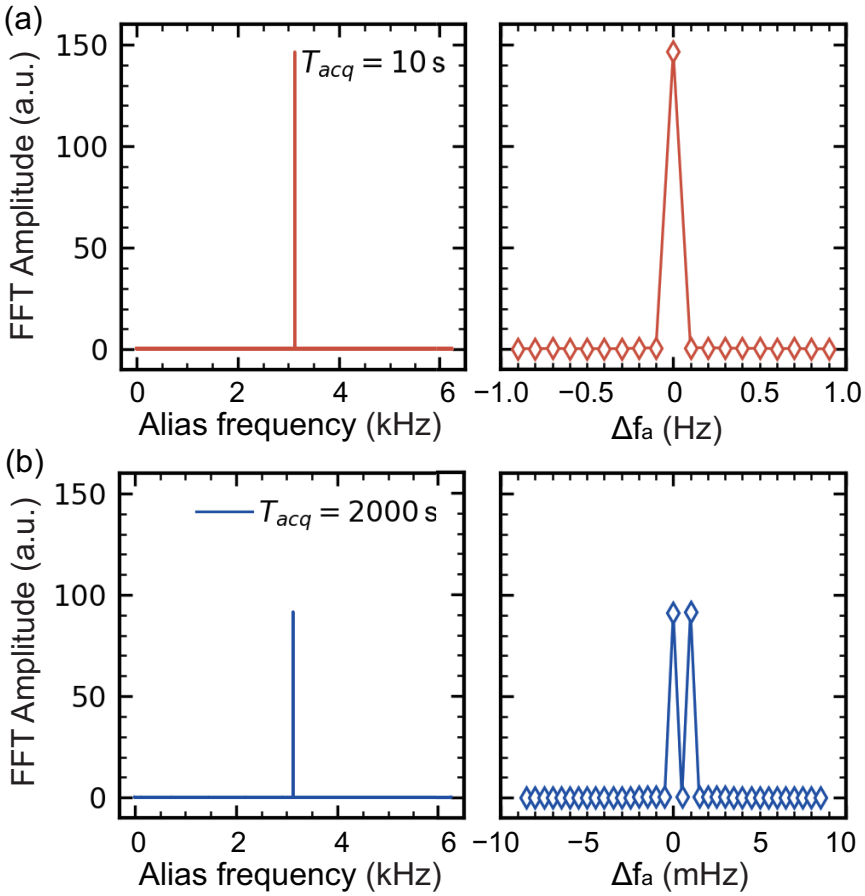


Figure 4.7: Demonstration of sub-Hz QFM-CASR spectral resolution using two test signals near 2.4 GHz $+3.125$ kHz with a frequency separation of 1 mHz. (a) For an acquisition time $t_{\mathrm{acq}} = 10$ s, the frequency resolution is $\delta f \approx 100$ mHz, and the two signals are not resolved, appearing as a single peak in the FFT of the QFM-CASR time-domain data. (b) For $t_{\mathrm{acq}} = 2000$ s, corresponding to $\delta f \approx 0.5$ mHz, the two signals are clearly resolved, demonstrating a 1 mHz frequency separation.

4.3.3 Demonstration of Sub-Hz Spectral Resolution

In spectroscopy, the achievable frequency resolution is approximately $\delta f \approx 1/t_{\mathrm{acq}}$, where t_{acq} is the total acquisition time of the time-domain signal, which in this work corresponds to the NV PL readout. In Section 4.3.1 we demonstrated QFM-CASR measurements with an acquisition time of 8 s, which is already sufficient to achieve sub-Hz spectral resolution. Here, we present additional measurements that explicitly verify and extend this capability.

In principle, the spectral resolution of the QFM-CASR protocol can be made arbitrarily high, as t_{acq} is not fundamentally limited by the NV spin coherence time [38]. To experimentally demonstrate millihertz-level resolution, we apply two target signals at frequencies $f_{s1} = 2.4\,\mathrm{GHz} + 3.125\,\mathrm{kHz}$ and $f_{s2} = f_{s1} + 1\,\mathrm{mHz}$, together with an AC bias field at $f_b = 2.399\,\mathrm{GHz}$. The resulting QFM-CASR spectra are shown in Figure 4.7.

We first perform measurements with an acquisition time of $t_{\mathrm{acq}} = 10\,\mathrm{s}$, yielding a frequency resolution of $\delta f \approx 100\,\mathrm{mHz}$. As shown in Figure 4.7(a), the FFT of the QFM-CASR time-domain data exhibits a single spectral peak, indicating that the two signals cannot be resolved at this resolution, as expected. We then increase the acquisition time to $t_{\mathrm{acq}} = 2000\,\mathrm{s}$. Under these conditions, the two signals separated by 1 mHz are clearly resolved, corresponding to an effective spectral resolution of approximately 0.5 mHz, as shown in Figure 4.7(b).

In practice, the maximum usable acquisition time is limited by slow systematic drifts of the experimental apparatus, which occur on timescales of tens of hours. Nevertheless, these results demonstrate that the QFM-CASR protocol can achieve sub-millihertz spectral resolution, which is more than sufficient for a wide range of prospective sensing and spectroscopy applications.

4.4 Effective Signal Validation with Rabi and DEER-Rabi

In the previous sections, we assumed that the amplitude of the applied AC bias field is constant and independent of frequency, ensured experimentally by maintaining a fixed RF amplifier output power across the relevant frequency range. Here, we experimentally validate this assumption in two frequency regimes where the RF field amplitudes can be measured directly, without relying on QFM.

Specifically, near the lower NV spin transition ($\omega_0 = \omega_{-1}$), we directly measure both the

signal and bias field amplitudes via the induced NV Rabi nutation frequency. Near the electron-spin-resonance (ESR) transition of paramagnetic nitrogen impurities (P1 centers) at $\sim 666\,\mathrm{MHz}$, we independently measure the RF field amplitudes using a DEER-Rabi protocol. The principles of spin-bath driving, DEER spectroscopy, and P1 spin structure are discussed in detail in Section 2.1.2 and are only briefly summarized here.

Finally, we verify Eq. (4.18) by comparing the effective signal field amplitude B_e measured using a QFM-XY8-6 AC magnetometry protocol with the effective field B'_e calculated from independently measured signal and bias field amplitudes obtained via NV Rabi and DEER-Rabi measurements.

We first perform QFM-XY8-6 AC magnetometry measurements near 2.4 GHz and independently calibrate the RF signal and bias field amplitudes using NV Rabi oscillations at the NV resonance frequency $\omega_{-1} \approx 2.29\,\mathrm{GHz}$. Applying a signal field at 2.4 GHz together with an AC bias field at 2.399 GHz produces an effective signal near 1 MHz. By sweeping the AWG output amplitude of the signal field while maintaining a constant bias amplitude, we obtain the QFM-XY8-6 AC magnetometry curve shown in Figure 4.8(a).

The AWG output amplitude corresponding to a $\pi/2$ phase accumulation is identified from the maximum of the magnetometry curve. This phase accumulation corresponds to an effective field amplitude $B_{\pi/2} = 0.58\,\mu\mathrm{T}$ same as Eq. (4.23), where $g \approx 2$ is the NV electron g-factor, $N = 48$ is the number of π pulses in the XY8-6 sequence, and the uncertainty arises from sinusoidal fitting of the magnetometry curve.

To independently measure the RF field amplitudes, we calibrate the RF amplifier output powers at the signal and bias frequencies using a spectrum analyzer, as described in the previous section. The calibrated RF powers are then applied individually at ω_{-1} to induce NV Rabi oscillations, yielding $\Omega_b = (2\pi)4.310(6)\,\mathrm{MHz}$ and $\Omega_s = (2\pi)0.841(2)\,\mathrm{MHz}$, as shown in Figure 4.8(b). Substituting

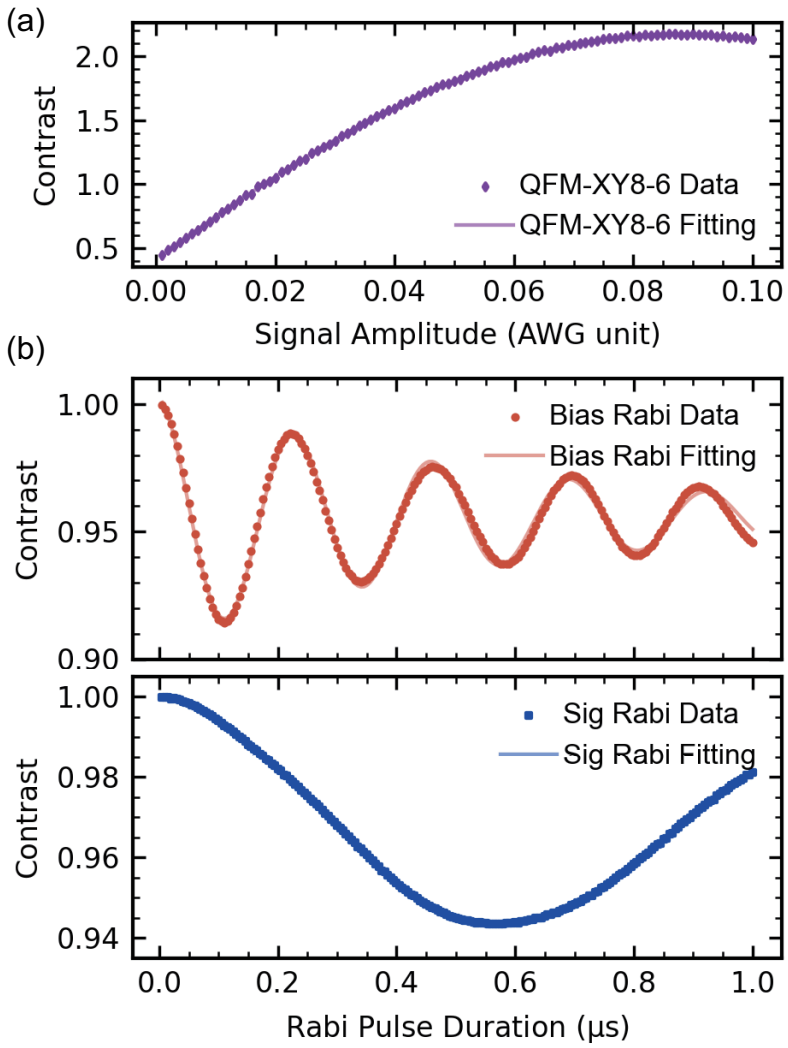


Figure 4.8: (a) QFM-XY8-6 AC magnetometry curve for the effective field at 1 MHz, obtained by varying the target signal amplitude while holding the AC bias field amplitude constant. The signal and bias frequencies are 2.4 GHz and 2.399 GHz, respectively. The maximum of the curve corresponds to a $\pi/2$ phase accumulation of the NV spin due to the effective field, yielding an effective field amplitude of $0.58(1)\,\mu\mathrm{T}$. (b) NV Rabi oscillation measurements used to determine the RF amplitudes of the AC bias field, $\Omega_b = (2\pi)4.310(6)$ MHz (upper panel), and the signal field, $\Omega_s = (2\pi)0.841(2)$ MHz (lower panel).

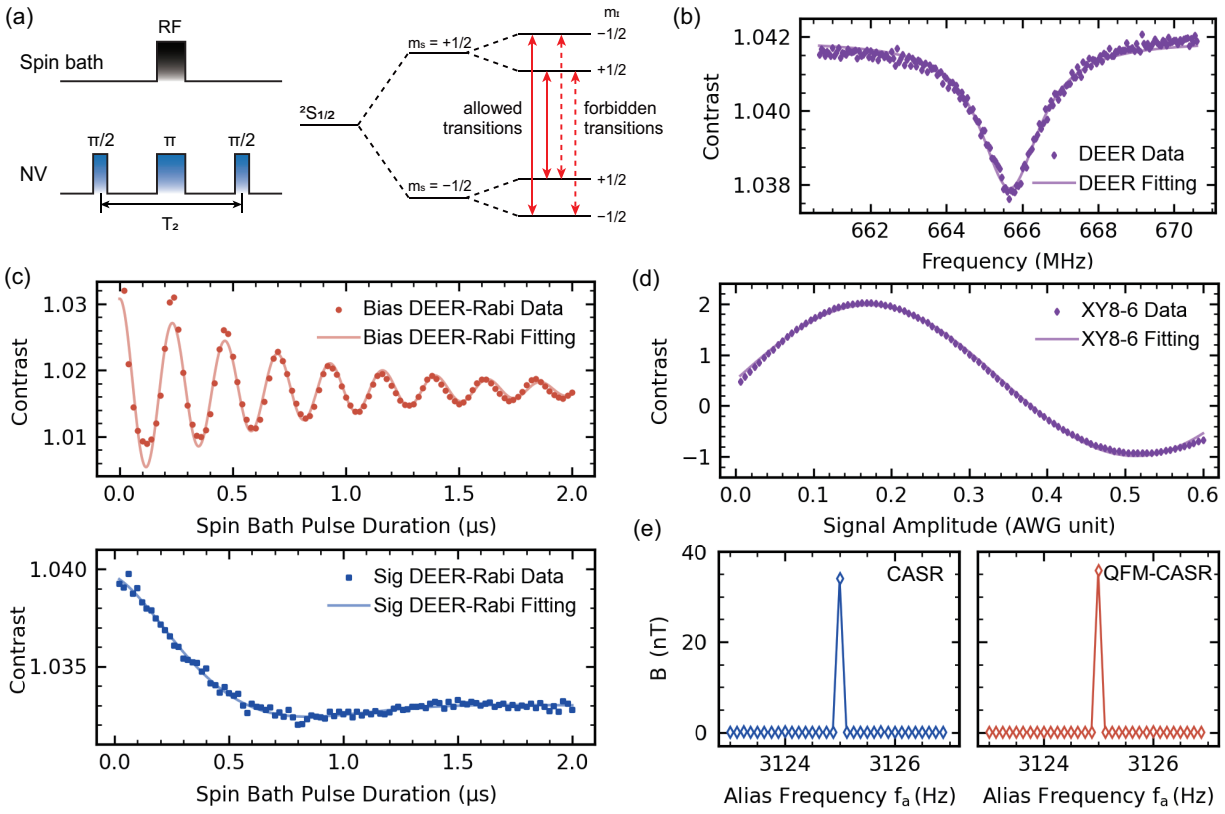


Figure 4.9: (a) DEER pulse sequence used to probe P1 center spin dynamics during an NV Hahn-echo measurement. (b) DEER spectrum measured by sweeping the RF frequency around the on-axis P1 transition near 666 MHz. (c) DEER-Rabi oscillations obtained by sweeping the duration of the spin-bath RF pulse using either the AC bias field (red) or the signal field (blue). (d) Non-QFM XY8-6 AC magnetometry measurement of a 1 MHz test signal used to calibrate RF field amplitude versus AWG output amplitude. (e) (left) CASR (non-QFM) spectrum of a $1\,\mathrm{MHz} + 3.125\,\mathrm{kHz}$ test signal. (right) QFM-CASR spectrum of the effective signal generated using signal and bias fields near 666 MHz.

these values into Eq. (4.18) gives a calculated effective field amplitude $B'_e \approx 0.57\,\mu\mathrm{T}$. The $\sim 2\%$ discrepancy between the measured (B_e) and calculated (B'_e) values is consistent with the uncertainty in identifying the $\pi/2$ phase point in the magnetometry curve. No significant contribution is observed from potential frequency-dependent variations in RF amplitude between 2.29 GHz and 2.4 GHz.

We next perform an analogous validation using DEER-Rabi magnetometry near the P1 ESR frequency. The DEER technique and the electronic structure of ^{15}N P1 centers are described in Section 2.1.2. Briefly, a near-resonant RF pulse applied to the spin bath during an NV Hahn-echo

sequence partially inverts the bath spins, leading to a measurable reduction in NV coherence. Sweeping the RF pulse duration produces a DEER-Rabi oscillation, whose frequency directly yields the applied RF field amplitude.

Using DEER spectroscopy, we identify the on-axis P1 resonance frequency $f_{\mathrm{P1}} = 665.67(1)\,\mathrm{MHz}$ (Figure 4.9(b)), in good agreement with the calculated value. Sweeping the duration of an RF pulse applied at this frequency produces DEER-Rabi oscillations for both the AC bias field and the target signal field. As shown in Figure 4.9(c), we obtain DEER-Rabi frequencies of $4.30(1)\,\mathrm{MHz}$ for the bias field and $0.56(3)\,\mathrm{MHz}$ for the signal field. The bias-field amplitude agrees well with the value obtained via NV Rabi measurements, while the signal-field amplitude exhibits a $\sim 30\%$ systematic discrepancy, attributable to increased uncertainty when calibrating weak RF fields using DEER-Rabi. Notably, QFM-CASR sensitivity calibration requires a constant bias-field amplitude as a function of frequency, but does not require maintaining a constant target signal amplitude across all frequencies.

We then perform QFM-CASR measurements using a signal field at $666\,\mathrm{MHz} + 3.125\,\mathrm{kHz}$ and an AC bias field at 665 MHz, with amplitudes determined from DEER-Rabi. The resulting QFM-CASR spectrum is shown in Figure 4.9(e). To calibrate the effective signal amplitude, we first perform a non-QFM XY8-6 AC magnetometry measurement using a 1 MHz test signal, yielding a calibration factor of $B/A = 341(1)\,\mathrm{nT}$ per AWG output amplitude. Applying this calibration to the CASR spectrum of a $1\,\mathrm{MHz} + 3.125\,\mathrm{kHz}$ test signal gives a signal amplitude of $34.1(1)\,\mathrm{nT}$. Using the same calibration, we determine the QFM-CASR effective signal amplitude to be $B_e = 37.4(1)\,\mathrm{nT}$.

Using Eq. (4.18) and the independently measured DEER-Rabi amplitudes near 666 MHz, we calculate $B'_e \approx 40\,\mathrm{nT}$. The $\sim 8\%$ discrepancy between B_e and B'_e is attributed to uncertainty in the DEER-Rabi calibration of the weak signal field. As expected, the effective field amplitude near 666 MHz is approximately two orders of magnitude smaller than that obtained near 2.4 GHz, consistent

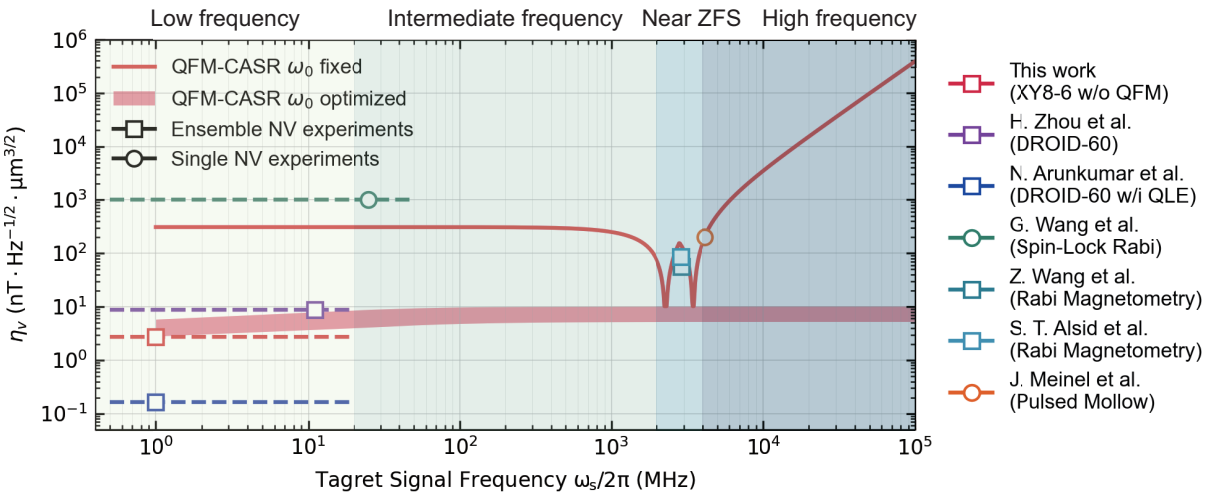


Figure 4.10: Comparison of narrowband (AC) volume-normalized sensitivity and applicable signal frequency range for state-of-the-art NV-diamond experiments, including the present QFM-CASR results (solid red line, fixed ω_0) and optimized QFM-CASR performance (red band). For non-QFM techniques, the marker indicates the reported sensitivity at the demonstrated signal frequency, while the dashed line indicates the approximate operational frequency range. All non-QFM techniques exhibit frequency-dependent AC sensitivity, typically degrading away from the reported operating point [17].

with the frequency dependence of the QFM response far from the NV resonances.

4.5 Performance Comparison, Optimization, and Applications of QFM-CASR

4.5.1 Comparison of NV-Diamond AC Sensing Techniques

Figure 4.10 provides a consolidated comparison of the narrowband AC sensitivity and signal frequency range of the QFM-CASR protocol with state-of-the-art NV-diamond AC sensing techniques, including both NV ensemble and single-NV experiments [28, 29, 52, 66, 69, 74]. To facilitate comparison across experiments with widely varying sensing volumes, we report the volume-normalized sensitivity $\eta_v = \eta\sqrt{V}$. For single-NV measurements, we assume an effective sensing volume of $V = 1\,\mu\mathrm{m}^3$.

The sensitivity of QFM-CASR depends on both the intrinsic AC sensitivity of the underlying

dynamical decoupling sequence and the quantum frequency mixing factor (Eq. (4.18)). The solid red line in Figure 4.10 corresponds to the experimentally realized QFM-CASR sensitivity in this work, with fixed DC bias field and NV resonance frequency. The red band indicates an optimized QFM-CASR performance envelope, estimated by assuming: (i) tunability of the DC bias field to place the NV resonance near the target signal frequency while maintaining the far-detuned QFM condition $|\omega_0 - \omega_b| > \Omega_{b,\max}$; and (ii) application of a strong AC bias field with $\Omega_{b,\max} = (2\pi)20\,\text{MHz}$.

At low signal frequencies ($< 20\,\text{MHz}$), conventional dynamical decoupling techniques such as XY8 and DROID-60 provide substantially higher sensitivity than QFM-CASR. Although applying a large DC bias field ($\sim 95\,\text{mT}$) can improve QFM-CASR sensitivity in this regime by tuning the NV resonance closer to the signal frequency, such large fields significantly increase experimental complexity. As a result, non-QFM dynamical decoupling techniques remain preferable for low-frequency AC sensing.

Near the NV zero-field splitting (ZFS, 2.87 GHz), QFM-CASR achieves sensitivity comparable to Rabi-based magnetometry and heterodyne detection techniques, while offering substantially higher spectral resolution. In contrast to these methods, which require the signal frequency to lie within a few MHz of the NV resonance, QFM-CASR provides access to a much broader signal frequency range without requiring large changes to the DC bias field.

In the intermediate frequency regime (20 MHz–2 GHz) and at higher frequencies ($> 4\,\text{GHz}$), QFM-CASR uniquely enables sensitive, narrowband NV-diamond measurements with sub-Hz spectral resolution. Other AC sensing techniques become impractical in these regimes due to limitations on achievable Rabi frequencies, pulse durations, or bias magnetic fields. Thus, QFM-CASR fills a previously inaccessible region of the NV-diamond sensing parameter space.

4.5.2 QFM-CASR Performance Limitations, Trade-Offs, and Optimization

The performance of QFM-CASR is governed by four key metrics: accessible signal frequency range, sensitivity, detection bandwidth, and spectral resolution.

In this work, we experimentally demonstrate QFM-CASR spectroscopy over a signal frequency range approaching 4 GHz, more than an order of magnitude broader than conventional NV AC sensing techniques. This range is presently limited by the bandwidth of the RF amplifier, rather than by any fundamental constraint of the QFM-CASR protocol. At large detunings between the signal frequency and the NV resonance, the effective signal amplitude decreases rapidly, leading to reduced sensitivity (Figure 4.10). This limitation can be mitigated by increasing the DC bias field to shift the NV resonance closer to the signal frequency or by increasing the AC bias field amplitude.

The sensitivity of QFM-CASR reflects a trade-off between frequency range and signal strength. While quantum frequency mixing dramatically extends the detectable signal frequency range and enables sub-Hz spectral resolution, it reduces the effective signal amplitude relative to conventional AC sensing. Sensitivity can be optimized by employing strong AC bias fields and tuning the NV resonance frequency toward the signal of interest, subject to experimental constraints on field stability and heating.

The QFM-CASR detection bandwidth is approximately $1/(2T_{\mathrm{seq}})$, where T_{seq} is the duration of the measurement sequence. Increasing sensitivity by using longer dynamical decoupling sequences (e.g., XY8-6) necessarily reduces the detection bandwidth. Conversely, reducing T_{seq} broadens the detection bandwidth but decreases sensitivity due to reduced phase accumulation and readout contrast. Thus, QFM-CASR bandwidth and sensitivity must be optimized jointly for a given application.

The spectral resolution of QFM-CASR is determined by the inverse of the total measurement

time and is not limited by NV spin coherence, owing to repeated spin reinitialization [38]. As demonstrated in Sec. 4.3.3, achieving sub-Hz and even millihertz spectral resolution is straightforward in practice. In realistic applications, the ultimate resolution is instead set by instrumental drift or by the intrinsic linewidth of the signal being measured, such as the NMR linewidth of a sample [38, 55, 56].

4.5.3 QFM-CASR Applications and Outlook

The QFM-CASR protocol is uniquely suited for applications requiring narrowband, high-resolution magnetic spectroscopy over a wide frequency range. At low frequencies, conventional dynamical decoupling techniques remain superior in sensitivity. However, at higher frequencies ($> 20\,\mathrm{MHz}$), QFM-CASR provides capabilities that are otherwise inaccessible with NV-diamond sensors.

Near the NV ZFS, QFM-CASR offers sensitivity comparable to Rabi-based and heterodyne techniques while providing substantially greater spectral resolution and signal frequency flexibility. In the intermediate and high-frequency regimes (20 MHz–2 GHz and $> 4\,\mathrm{GHz}$), QFM-CASR is currently the only demonstrated approach for sensitive, sub-Hz-resolution NV spectroscopy of narrowband signals.

Although the present experiments are limited to $\sim 4\,\mathrm{GHz}$ by amplifier bandwidth, there is no fundamental upper limit on the QFM-CASR signal frequency (see Supplementary Note IX). Several approaches could further enhance performance, including increasing the AC bias field amplitude, employing circularly polarized bias fields to enhance effective signal strength [26], and incorporating quantum logic–assisted sensing schemes for operation under tesla-scale bias fields [52].

In summary, QFM-CASR enables narrowband NV-diamond magnetic spectroscopy over an

unprecedented frequency range. The protocol extends the detectable signal frequency range by more than an order of magnitude relative to conventional AC sensing techniques while achieving sub-Hz spectral resolution. We demonstrate multi-frequency spectroscopy, precise phase measurement, and sensitivity down to 120 pT for the effective field across frequencies spanning 600 MHz to 4 GHz. Combined with the wide-field capabilities of the quantum diamond microscope [15, 39], QFM-CASR opens a pathway toward spatially resolved imaging of arbitrary-frequency vector magnetic fields with micron-scale spatial resolution, sub-Hz spectral resolution, and sub-millisecond temporal resolution.

Chapter 5: Real-Space Nuclear Magnetic Resonance Microscopy

In Chapters 3 and 4, we introduced narrowband AC quantum magnetic microscopy using a QDM and photodiode, respectively; and discussed the potential for imaging RF magnetic fields in real space. One particularly compelling application of this capability is nuclear magnetic resonance (NMR) microscopy, which enables chemically specific and noninvasive probing of matter through nuclear spin dynamics.

Nuclear magnetic resonance has been studied for over seven decades since its first experimental demonstrations in the late 1940s [75, 76]. Today, NMR and magnetic resonance imaging (MRI) are mature and widely commercialized technologies, with broad applications spanning chemical analysis, materials science, structural biology, and medical diagnostics [77–79]. Conventional NMR and MRI systems rely on inductive detection using macroscopic RF coils and encode spatial information through magnetic field gradients. While highly successful at the centimeter-to-millimeter scale, these approaches fundamentally limit spatial resolution and sensitivity for microscale and nanoscale samples [78, 80], making them unsuitable for applications such as single-cell NMR spectroscopy or microscale chemical imaging.

Quantum sensors such as NV centers in diamond provide an alternative paradigm for NMR detection. By directly measuring magnetic fields generated by nuclear spin ensembles via optically detected spin resonance, NV-based sensors circumvent the inductive detection limit and offer sensitivity that does not degrade with miniaturization [1, 16]. Over the past decade, NV-NMR techniques have advanced rapidly; a detailed discussion of their development and representative demonstrations is provided in Sec. 5.1.1.

As discussed in Chapter 3, the RF-QDM developed in this work is capable of simultaneously

imaging the amplitude, frequency, and phase of AC magnetic fields with nanotesla-level per-pixel sensitivity and sub-hertz spectral resolution. These capabilities naturally extend to real-space NMR microscopy, where the NMR signal is detected directly as a local RF magnetic field rather than through frequency-encoded gradients. Such an approach enables wide-field, real-space imaging of NMR signals with spatial resolution determined by the optical imaging system, rather than by magnetic field gradients.

In this chapter, we first review the challenges and historical development of NV-NMR detection, with emphasis on the transition from nanoscale spectroscopy to real-space imaging. We then present the experimental design of our NMR-QDM platform and demonstrate preliminary results of real-space NMR microscopy. Finally, we discuss potential application domains for this technique, including microscale chemical analysis and biological sensing, and outline pathways to improve the current QDM architecture to achieve enhanced sensitivity, spatial resolution, and spectral fidelity for NMR imaging.

5.1 Detection of NMR Signals with NV Centers in Diamond

5.1.1 Development of NV-NMR

Over the past decade, NV centers in diamond have emerged as powerful quantum sensors for NMR detection at the micron- and nanoscale, extending in some cases to the detection of individual nuclear spins. NV-NMR offers a fundamentally different detection paradigm compared to conventional inductive NMR, enabled by several unique attributes of the NV center:

1. **Nanoscale Proximity:** Near-surface NV centers can be positioned within a few nanometers of the sample, greatly enhancing magnetic coupling to nuclear spins.

2. **High Magnetic Sensitivity:** Nuclear Larmor frequencies typically lie in the MHz range, well matched to NV-based AC magnetometry protocols that provide high magnetic field sensitivity.

3. **Optical Readout and Imaging:** The NV spin state can be initialized and read out optically, enabling both single-defect detection and wide-field imaging using NV ensembles.

These properties allow NV-NMR spectroscopy to combine high magnetic sensitivity with high spatial resolution.

Figure 5.1 summarizes key milestones in the development of NV-NMR. The field was initiated by pioneering demonstrations from Mamin *et al.* [81] and Staudacher *et al.* [82], who independently reported detection of statistically polarized nuclear spin signals from nanoscale samples using single NV centers located a few nanometers beneath the diamond surface. These experiments established the feasibility of ambient-condition, nanoscale NMR detection.

Subsequent work pushed the sensitivity limits toward detection of individual nuclear spins. Notably, Lovchinsky *et al.* [83] demonstrated magnetic resonance detection of nuclear spins associated with a single protein molecule using a single NV center. Parallel advances focused on improving spectral resolution. Glenn *et al.* [38] introduced the CASR protocol, enabling high-resolution NV-NMR spectroscopy beyond the NV spin coherence time.

Beyond nanoscale detection, NV ensembles have enabled NMR imaging with wide FOV and micrometer-scale spatial resolution. Such developments have opened new opportunities for surface-sensitive NMR [84] and microfluidic on-chip spectroscopy [85], enable 2D applications in sensing and microscopic chemical analysis.

These advances collectively establish NV-diamond platforms as versatile tools for NMR detection across multiple length scales, motivating the development of real-space NMR microscopy using wide-

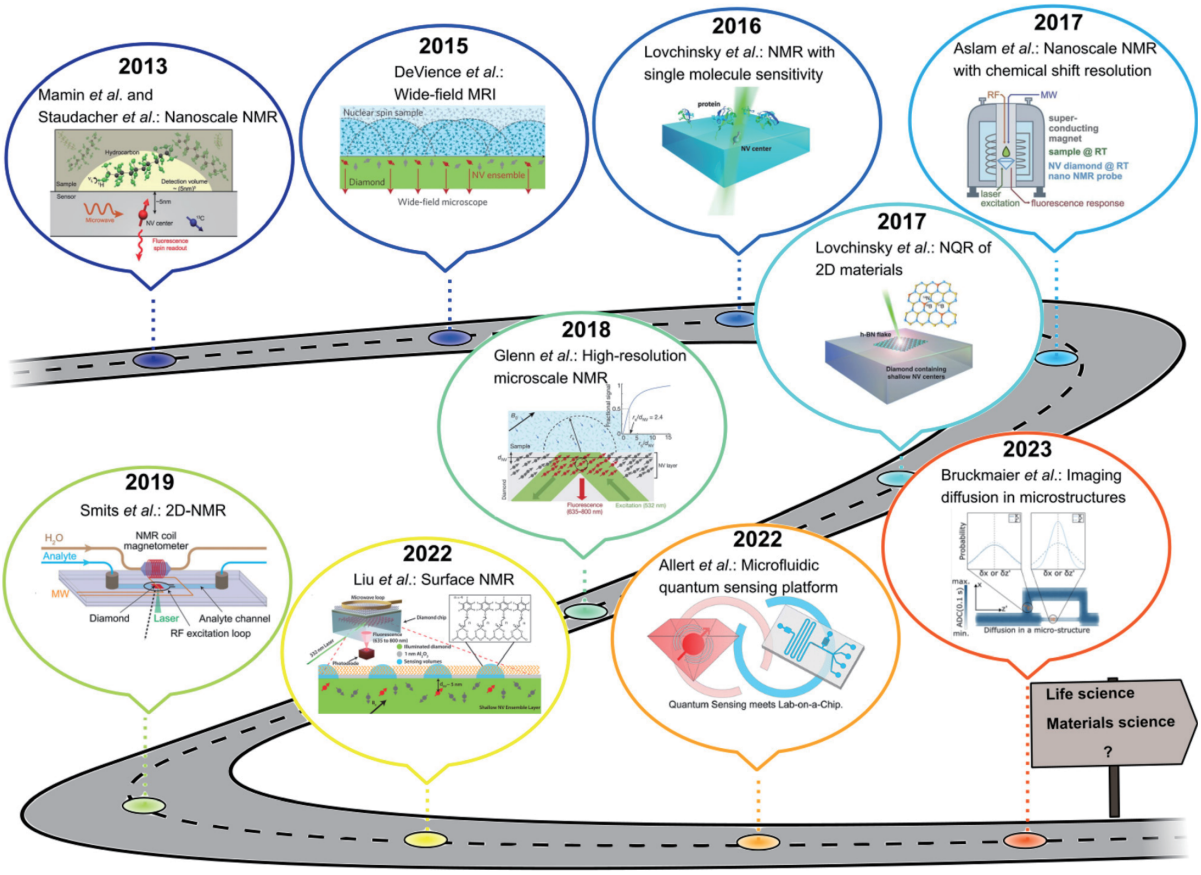


Figure 5.1: Timeline of NV-NMR development, adapted from Ref. [86], highlighting major experimental milestones.

field quantum diamond microscopes.

5.1.2 Challenges Toward NMR Imaging

In Chapter 3, we demonstrated the capability of the RF-QDM to simultaneously image the amplitude and phase of multi-frequency RF signals generated by microcoils using the CASR protocol. However, extending this capability to NMR imaging presents substantially greater challenges. These arise primarily from two factors: the extremely weak amplitude of thermally polarized NMR signals and the intrinsic spectral complexity of real NMR signals.

The dominant challenge is the weak magnetic field generated by Larmor-precessing nuclear

spins. For the bias magnetic field used in the present setup ($B_0 = 40\,\mathrm{mT}$, provided by a SmCo ring permanent magnet), we estimate the NMR magnetic signal amplitude produced by thermally polarized protons in a sample and measured at a test point within the NV ensemble sensor.

The magnetic field generated by the nuclear spin ensemble can be obtained by integrating the dipolar magnetic field over the sample volume. Projecting this field onto the NV quantization axis yields [38]

$$\mathbf{B} \cdot \hat{n}_{NV} = \frac{\mu_0 \rho_{\text{th}}}{4\pi} \int \frac{1}{r^3} \left[3(\hat{r} \cdot \mathbf{m}(t))(\hat{r} \cdot \hat{n}_{NV}) - (\mathbf{m}(t) \cdot \hat{n}_{NV})\right] dV, \tag{5.1}$$

where ρ_{th} is the thermally polarized proton density, $\hat{r}$ is the unit vector from the NV sensing point to an infinitesimal sample element, $\hat{n}_{NV}$ is the NV axis, and $\mathbf{m}(t)$ is the time-dependent nuclear magnetization vector.

Separating the magnitude and direction of the proton magnetic moment allows the dimensional factors to be collected into a prefactor,

$$\mathbf{B} \cdot \hat{n}_{NV} = C \int \frac{1}{r^3} \left[3(\hat{r} \cdot \hat{m}(t))(\hat{r} \cdot \hat{n}_{NV}) - (\hat{m}(t) \cdot \hat{n}_{NV})\right] dV, \tag{5.2}$$

where the prefactor

$$C = \frac{\mu_0 \gamma_p}{4\pi} \rho_{\text{Tot}} \left[1 - \exp\left(-\frac{2\gamma_p B_0}{k_B T}\right)\right] \approx \frac{\mu_0 \gamma_p^2 \rho_{\text{Tot}} B_0}{2\pi k_B T} \tag{5.3}$$

sets the overall scale of the NMR magnetic field. Here ρ_{Tot} is the total proton density (taken as pure water), γ_p is the proton gyromagnetic ratio, k_B is the Boltzmann constant, and T is temperature.

For $B_0 = 40\,\mathrm{mT}$ and $T = 300\,\mathrm{K}$, we obtain $C \approx 25.6\,\mathrm{pT}$. Evaluating the dimensionless geometric integral in Eq. (5.2) for a hemispherical sample geometry on the diamond surface yields a

factor $G \sim 1.4$, resulting in an estimated NMR signal amplitude of $B_{\mathrm{NMR}} \approx 40\,\mathrm{pT}$. This picotesla-scale signal is approximately three orders of magnitude smaller than the RF fields imaged with high signal-to-noise ratio in Chapter 3. Since magnetic noise floor scales as square root of averaging times, achieving comparable SNR would require an averaging time roughly 10^6 times longer, which is experimentally impractical under the present conditions.

In addition to its weak amplitude, the NMR signal is intrinsically more complex than the single-frequency, constant-amplitude RF fields demonstrated previously. Real samples exhibit frequency broadening due to magnetic field inhomogeneity across the sample volume, chemical shift dispersion, and nuclear spin decoherence. The signal envelope decays with the nuclear transverse relaxation time, and spatial variations in B_0 lead to position-dependent resonance frequencies.

Therefore, realizing real-space NMR imaging requires both improvements in magnetic sensitivity and enhanced control over magnetic field homogeneity and spectral stability. Modifications to the current QDM architecture and experimental protocol are required to address these challenges, as discussed in the following sections.

5.1.3 Overhauser Dynamic Nuclear Polarization

A direct approach to overcoming the weak amplitude of NMR signals is to enhance the nuclear spin polarization. One of the most effective methods for achieving this is Overhauser dynamic nuclear polarization (DNP) [55], which transfers spin polarization from electron spins to nearby nuclear spins.

Figure 5.2(a) illustrates the implementation of Overhauser DNP in an NV-NMR spectrometer, as demonstrated by Bucher *et al.* In this approach, thermal polarization of electron spins associated with dissolved molecular radicals is transferred to the nuclei in the sample, significantly increasing the

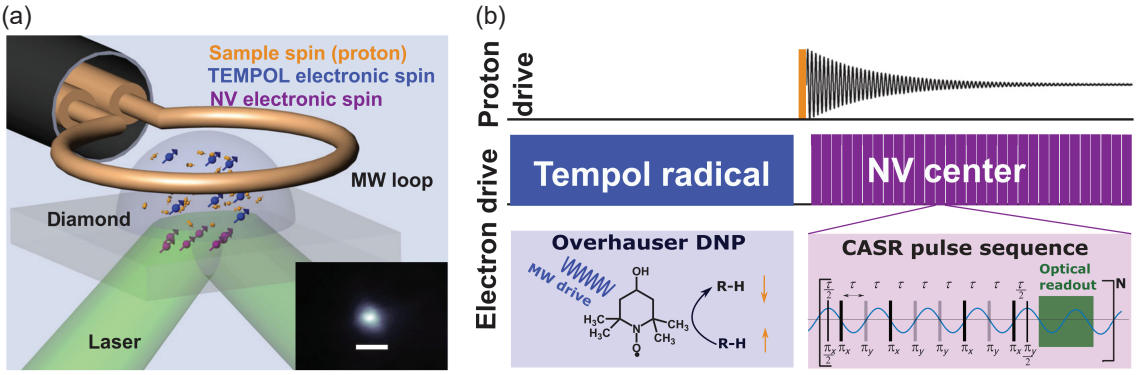


Figure 5.2: NV-NMR spectroscopy with integrated hyperpolarization [55]. (a) Experimental schematic: A microwave loop antenna drives both NV centers (purple) and TEMPOL electron spins (blue). Hyperpolarized NMR signals from nuclear spins in the sample (orange) are detected via NV ensemble fluorescence. Inset: The sensing area is defined by the laser spot on the diamond (scale bar: $30\,\mu$m). (b) Pulse sequence for hyperpolarized NV-NMR. Left: Overhauser DNP, where continuous microwave driving saturates the TEMPOL electron spin transition, enabling polarization transfer to nearby protons. Right: Detection of the proton FNP signal using the CASR protocol with synchronized dynamical decoupling sequences.

nuclear spin polarization. In particular, the stable radical TEMPOL (4-hydroxy-TEMPO) is dissolved in the liquid sample to serve as the polarization agent.

The pulse sequence for DNP-enhanced NV-NMR is shown in Figure 5.2(b). In the first stage of the sequence ($\sim$ 300 ms), a continuous microwave drive is applied to the electron spins of the TEMPOL radicals, inducing polarization transfer to nearby proton spins via the Overhauser effect. In the second stage ($\sim$ 200 ms), a $\pi/2$ pulse is applied to the hyperpolarized protons, initiating free nuclear precession (FNP). The resulting NMR signal is then detected by the NV sensor using the CASR protocol.

The efficiency of DNP-enhanced NV-NMR was first evaluated using a deionized water sample, as shown in Figure 5.3. TEMPOL radicals were dissolved at a concentration of 20 mM, and experiments were performed with a DNP Rabi frequency of 10 MHz. A control measurement with no DNP drive was also conducted under otherwise identical conditions. The CASR-detected NMR spectra show an

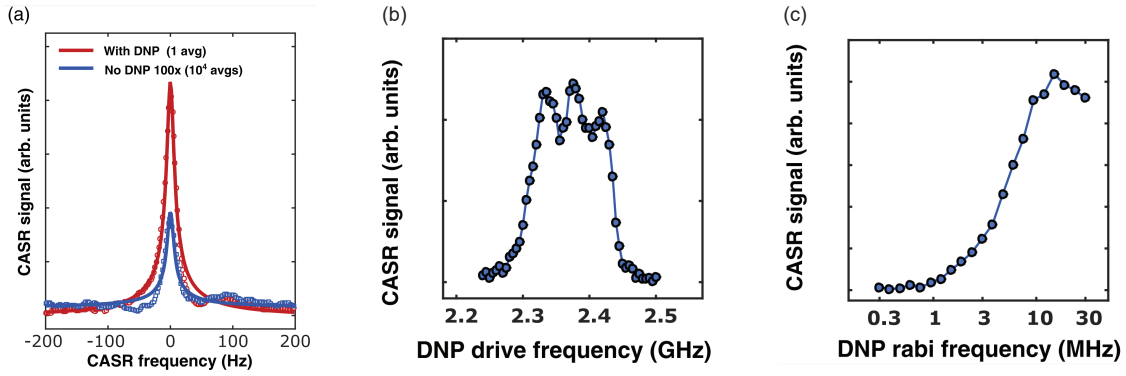


Figure 5.3: Hyperpolarization-enhanced NV NMR of water [55]. (a) Comparison of NV NMR spectra from pure water with DNP (red circles, single spectrum) and without DNP (blue circles, 10^4 spectra averaged), using a CASR pulse sequence. Line shape fits (solid lines) indicate a DNP signal enhancement factor of 230, achieving a proton number sensitivity of 10 pmol/Hz$^{1/2}$ for a signal-to-noise ratio (SNR) of 3. (b) CASR-detected signal magnitude from a pure water sample as a function of DNP drive frequency. The observed triplet structure results from hyperfine coupling between the electron and ^{14}N nuclear spins in the TEMPOL radical. (c) CASR-detected signal magnitude from pure water as a function of DNP drive power, expressed in units of the electron Rabi frequency. The maximum DNP signal enhancement occurs at a drive Rabi frequency of approximately 10 MHz.

enhancement of approximately 230 times with DNP, in good agreement with theoretical expectations for Overhauser DNP at low magnetic fields.

Optimizing the polarization transfer efficiency is essential for maximizing the hyperpolarized NMR signal. This was achieved by measuring the peak CASR-detected FNP signal amplitude while varying the DNP drive frequency and Rabi frequency. As shown in Figure 5.3(b), sweeping the DNP drive frequency reveals a triplet structure, which arises from the ^{14}N hyperfine splitting of the TEMPOL electron spin. Figure 5.3(c) shows that the signal enhancement increases with Rabi frequency and reaches a maximum near 10 MHz, beyond which it saturates, likely due to microwave power limitations and sample heating.

The presence of TEMPOL radicals shortens the proton spin-lattice relaxation time to $T_1 \approx 150$ ms, which is well matched to the timescale of the NV-NMR detection sequence. Reducing the

TEMPOL concentration can increase T_1, at the cost of a modest reduction in polarization enhancement. Over several days of measurements, no significant degradation of the TEMPOL concentration was observed, indicating negligible photobleaching under the experimental conditions.

While Overhauser DNP is a robust and well-established technique for NV-NMR, adapting it to wide-field QDM-based NMR imaging introduces additional challenges. In contrast to confocal NV setups, wide-field imaging requires a larger microwave loop to ensure a spatially homogeneous Rabi field across the field of view. This requirement reduces the maximum achievable Rabi frequency due to limitations in microwave power delivery and field uniformity. In our current QDM implementation, the achievable Rabi frequency is limited to $\sim 6\,\text{MHz}$, compared to the $\sim 10\,\text{MHz}$ optimal value reported in prior Overhauser DNP studies. This reduction in drive strength is expected to decrease the efficiency of polarization transfer. The details of the experimental implementation using a separate DNP coil are described in the following section.

5.2 Experimental Setup for QDM-NMR

At the initial planning stage, this project appeared relatively straightforward. Building upon the RF-QDM platform developed in Chapter 3, where CASR imaging of synthetic RF signals generated by microcoils was demonstrated, the primary anticipated modifications were the introduction of a liquid NMR sample and implementation of DNP. However, in practice, the experiment proved significantly more challenging than expected. Key issues, including bias magnetic field inhomogeneity, suboptimal sample composition, and insufficient DNP efficiency, initially prevented observation of any detectable NMR signal. Substantial iteration was undertaken over the course of approximately one year to overcome these limitations and achieve reliable NMR detection. This section describes the finalized

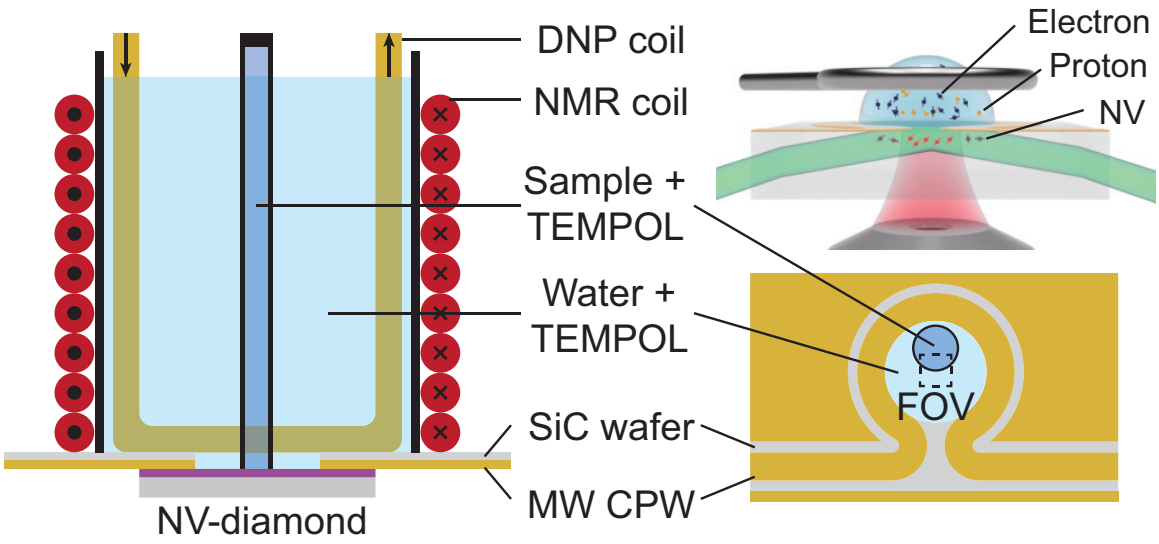


Figure 5.4: Schematic of the integrated QDM-NMR experimental platform. Left: Cross-sectional view of the setup. A liquid sample containing water and dissolved TEMPOL radicals is held in a plastic tube mounted directly above the NV-diamond sensor. A slot is fabricated in the SiC wafer at the center of the Ω-shaped CPW to enable close proximity between the NV sensing layer and the sample. A multi-turn copper coil (red) surrounding the tube provides RF excitation for nuclear spin manipulation (NMR coil) as well as inductive NMR signal detection; while a separate microwave coil (yellow) delivers high-power driving for Overhauser DNP. Top right: Conceptual illustration of the sensing mechanism. Electron spins in TEMPOL radicals transfer polarization to nearby proton spins via DNP, and the resulting nuclear magnetic resonance signal is detected by the NV ensemble. Bottom right: Bottom view of the Ω-shaped CPW structure defining the microwave delivery region and the optical FOV of the QDM system. A capillary tube can be inserted into the sample volume to introduce spatially varying samples for microscopic NMR imaging.

QDM-NMR experimental configuration.

5.2.1 Integrated Inductive NMR and NV-NMR

Compared to conventional inductive NMR, NV-NMR offers microscopic spatial resolution. However, due to the much smaller sensing volume, the detected NV-NMR signal is significantly weaker than that obtained via inductive detection. Therefore, incorporating inductive NMR detection is highly beneficial during the early stages of the experiment, enabling rapid identification of the resonance

frequency and optimization of nuclear driving and DNP parameters.

A key modification to the QDM-NMR system is the integration of inductive NMR detection with NV-based sensing. As illustrated in Figure 5.4, we employ the same NV-diamond sensor and Ω-shaped coplanar waveguide (CPW) for microwave delivery as used in previous chapters. To enable direct contact between the NV sensing layer and the liquid sample, a slot is laser-cut at the center of the Ω loop in the SiC substrate. On the top side of the chip, a 6 mm-diameter plastic tube is attached to serve as a container for the liquid sample (water with dissolved TEMPOL radicals).

A copper wire wound into a 14-turn coil around the tube is used to drive the nuclear spins and for inductive NMR signal detection. This coil is tuned to the proton Larmor frequency (~ 1.69 MHz at a bias field of 39.7 mT, quality factor $Q \approx 180$) using an L-C resonant circuit. For DNP driving, we employ a rectangular coaxial microwave coil, rather than using the NV microwave antenna as in Ref. [55]. This configuration enables stronger microwave drive amplitudes and ensures that the microwave field is oriented perpendicular to the bias magnetic field, improving coupling to the electron spin dipoles and enhancing DNP efficiency.

To enable spatially resolved NMR imaging, a capillary tube (diameter < 1 mm) containing a different sample can be inserted into the larger tube, creating spatial contrast in the microscopic NMR images.

The electronic instrumentation and signal routing are shown in Figure 5.5. We use the same arbitrary waveform generator (Zurich Instruments SHFSG), lock-in camera (Heliotes heliCam C3), and data acquisition system (NI USB-6259) as in the RF-QDM setup. To improve optical readout signal-to-noise ratio, the photodiode is replaced with a balanced detector (Thorlabs PDB210A), which suppresses laser intensity noise.

The computer-controlled AWG serves as the central timing unit, generating microwave pulses for

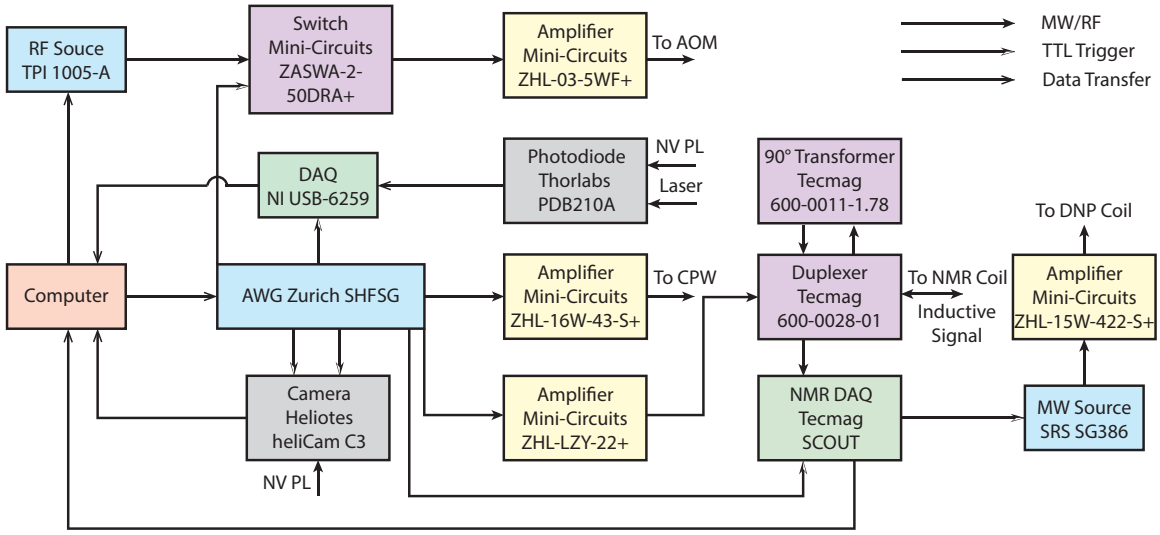


Figure 5.5: Block diagram of the electronic control and signal routing for the integrated QDM-NMR system. The computer-controlled AWG serves as the central timing and control unit, generating MW pulses for NV spin manipulation and RF signals for nuclear spin excitation, while providing TTL triggers to synchronize all subsystems. NV PL is detected either by a balanced photodiode for high-sensitivity measurements or by a wide-field lock-in camera for spatial imaging. The photodiode signal is digitized by a DAQ system. For inductive NMR detection, the signal from the NMR coil is routed through a duplexer and a 90° transformer to separate the weak inductive signal from the strong RF drive, and is then recorded by the NMR DAQ. The duplexer protects the receiver while enabling simultaneous RF excitation and signal acquisition. Microwave excitation for DNP is generated by an independent MW source and amplified, providing higher output power than the AWG-based path. Additional RF and MW signals are amplified using amplifiers before being delivered to the CPW, NMR coil, or DNP coil. Arrows indicate signal flow for MW/RF delivery, TTL triggering, and data acquisition, illustrating the fully synchronized operation of NV-based sensing and inductive NMR detection.

NV control and RF pulses for nuclear spin manipulation. It also provides TTL triggers to synchronize the data acquisition system, camera, and inductive NMR DAQ (Tecmag SCOUT). A duplexer and a 90° phase shifter are used to separate the strong RF drive from the weak inductive NMR signal, protecting the NMR receiver.

Microwave signals for DNP are generated by a separate microwave source (SRS SG386), triggered by the NMR spectrometer. Compared to AWG-based generation, this approach provides higher microwave power, enabling more efficient polarization transfer.

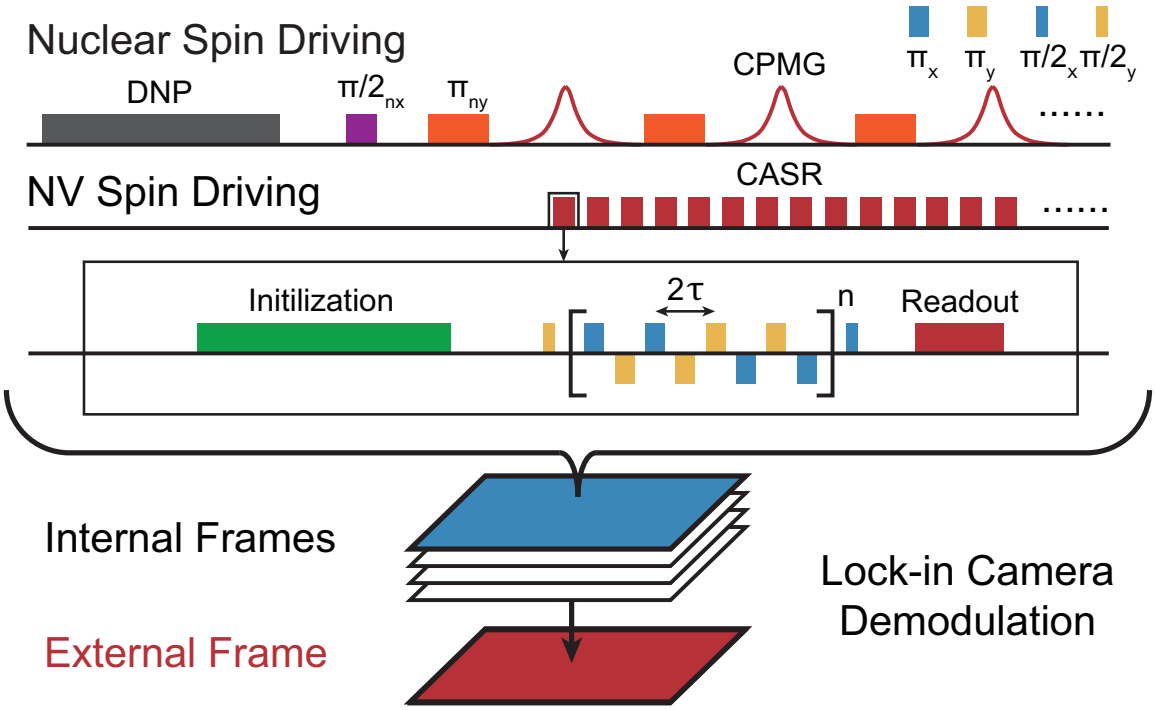


Figure 5.6: Schematic of the nuclear CPMG sequence synchronized with NV-CASR detection and lock-in camera demodulation. Top: Nuclear spin control sequence. Following an initial Overhauser DNP polarization period, a $\pi/2$ pulse initializes nuclear spin coherence, followed by a train of π pulses with alternating phase (CPMG) to generate a series of spin echoes. This sequence extends the effective signal duration from the dephasing time T_2^* to the longer coherence time T_2. Middle: NV spin control using the CASR protocol. Repeated blocks of dynamical decoupling sequences (XY8-n) are synchronized to the nuclear spin evolution, enabling detection of the NMR signal. Bottom: Lock-in camera demodulation. Multiple internal frames are acquired during each camera exposure and combined to form a single external frame contains the time domain signal. This demodulation process extracts the oscillating NMR signal while suppressing static background contributions.

With this integrated setup, simultaneous inductive NMR detection and NV-based sensing with both photodiode-based and wide-field imaging can be performed.

5.2.2 Nuclear CPMG Sequence with Lock-in Camera Demodulation

As discussed in previous sections, in addition to their weak amplitude, NMR signals exhibit shorter dephasing times and broader linewidths compared to the synthetic RF signals demonstrated

in Chapter 3. These challenges are further exacerbated when using a lock-in camera for wide-field imaging. Due to the demodulation process, the camera operates at a relatively low effective sampling rate, resulting in a limited spectral window. For the configuration used in Chapter 3, the spectral window is approximately 250 Hz, which is comparable to the linewidth of the NMR signal and therefore insufficient for robust spectral discrimination. Moreover, the low sampling rate leads to inadequate temporal sampling of rapidly decaying signals such as free induction decay (FID) or spin-echo signals, where the nuclear T_2^* is on the order of a few milliseconds.

To address these limitations, we implement a nuclear Carr–Purcell–Meiboom–Gill (CPMG) sequence synchronized with NV-based CASR detection and lock-in camera demodulation, as illustrated in Figure 5.6. In the NMR imaging experiment, nuclear spins are first hyperpolarized via Overhauser DNP using TEMPOL radicals dissolved in the liquid (water) sample (TEMPOL concentration $\approx$ 30 mM) during a long polarization period ($\sim$ 200 ms). Following polarization, a $\pi/2$ pulse is applied to initiate nuclear spin precession, followed by a train of π pulses with alternating phase to generate a series of spin echoes.

While each individual spin-echo envelope decays with the dephasing time $T_2^* \sim 5$ ms, the overall echo train decays with the much longer coherence time $T_2 \sim 100$ ms. This effectively extends the duration of the detectable NMR signal, allowing sufficient temporal sampling within the limited frame rate of the lock-in camera.

To further improve detection, we employ a phase-cycled readout protocol. The nuclear CPMG sequence is repeated with phases of $0°$, $90°$, $180°$, and $270°$, yielding four measurements corresponding to $\pm X$ and $\pm Y$ components. The complex signal is then reconstructed as $S = X - (-X) + i\,[Y - (-Y)]$, which suppresses common-mode (DC) background signals and effectively doubles the usable spectral window.

NV signal detection is performed using the CASR protocol described in Chapter 3, with a modified π-pulse spacing of $\tau = 0.3\,\mu$s to match the target NMR frequency of $\sim 1.69\,$MHz. The lock-in camera is synchronized to the NMR signal through a double-aliasing scheme, optimized as described in Appendix A.

5.3 QDM-NMR Experimental Results

In this section, we present the experimental results of the QDM-NMR system. We begin with inductive NMR measurements, which are used to identify the NMR resonance frequency and optimize the RF and DNP pulse parameters. We then demonstrate NV-NMR detection using photodiode readout to measure nuclear CPMG signals and compare the extracted T_2 with inductive measurements. Finally, for wide-field imaging, we employ a synthetic signal with a temporal profile similar to the measured nuclear CPMG signal but with higher amplitude, enabling proof-of-principle QDM imaging within a practical acquisition time.

5.3.1 Inductive NMR Measurement for Pulse Optimization

Compared to NV-based detection, inductive NMR probes a much larger sample volume and therefore produces a significantly stronger signal. This enables rapid optimization of experimental parameters with high SNR and minimal averaging time.

In the current setup (Figure 5.4), both the NMR coil and the DNP coil uniformly drive the entire sample volume within the NMR tube. This configuration allows efficient optimization of both the nuclear RF pulses and the DNP parameters using inductive detection.

For DNP calibration, a single spin-echo is used instead of a full CPMG train. Figure 5.7(a)

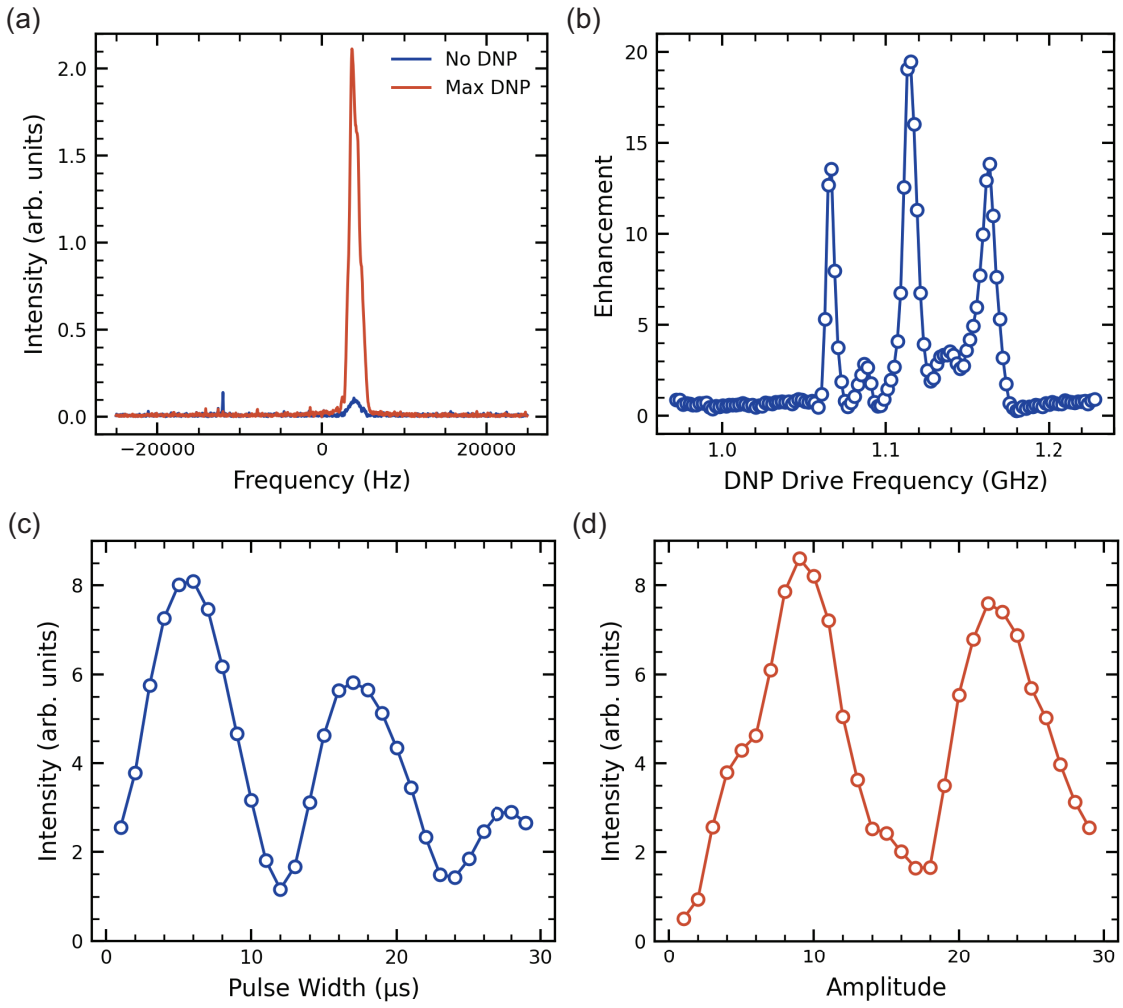


Figure 5.7: Inductive NMR measurements used for optimization of DNP and nuclear RF pulses. (a) Inductive ^{1}H NMR spectra of deionized water with (red) and without (blue) Overhauser DNP, showing an enhancement of approximately 20$\times$ in signal amplitude under optimized DNP conditions. (b) NMR signal enhancement as a function of DNP drive frequency. The observed triplet structure arises from hyperfine coupling between the electron spin and the ^{14}N nuclear spin in the TEMPOL radical, with the optimal DNP frequency identified near 1.116 GHz. (c) Nuclear Rabi oscillation obtained by sweeping the RF pulse duration at fixed amplitude, used to determine the optimal π-pulse duration. (d) Nuclear Rabi oscillation obtained by sweeping the RF pulse amplitude at fixed duration, used to determine the optimal RF drive amplitude.

shows example measured inductive NMR spectra with and without Overhauser DNP. With an RF drive at $f_{\mathrm{RF}} = 1.6914\,\mathrm{MHz}$ applied to the NMR coil, the detected NMR signal appears at 1.6951 MHz, corresponding to a frequency offset of approximately 3.7 kHz. Although this resonance frequency may differ slightly from the NV-detected signal due to local magnetic field variations, it provides a reliable reference for subsequent NV-NMR measurements.

With DNP applied, the inductive NMR signal amplitude is enhanced by approximately a factor of 20 compared to the thermally polarized signal. This enhancement is lower than that reported in Ref. [55], primarily due to the broader NMR linewidth in our system. The increased linewidth arises from magnetic field gradients introduced by the permanent ring magnet and the larger sample volume used in this experiment.

To optimize the DNP drive, we sweep the microwave frequency and measure the resulting inductive NMR signal amplitude, as shown in Figure 5.7(b). A characteristic triplet structure is observed, originating from hyperfine coupling between the electron spin and the ^{14}N nuclear spin in the TEMPOL radical. The optimal DNP frequency is identified at approximately 1.116 GHz, corresponding to the maximum signal enhancement.

For power optimization, the system operates in the non-saturated regime, and the DNP drive amplitude is set to the maximum available output of the microwave source (9 dBm). While higher microwave power could further improve polarization transfer efficiency, it may introduce sample heating or hardware limitations.

With the DNP parameters optimized, we proceed to calibrate the nuclear RF pulses using nuclear Rabi measurements. As shown in Figure 5.7(c), the RF pulse duration is first optimized by fixing the amplitude (10 AWG units) and sweeping the pulse length, yielding an optimal π-pulse duration of 6 μs. Subsequently, the pulse amplitude is optimized by fixing the duration at 6 μs and sweeping the

drive amplitude, as shown in Figure 5.7(d).

5.3.2 Simultaneous NV and Inductive Nuclear CPMG Measurements

After calibrating the RF and DNP pulses for nuclear spin manipulation, we perform a nuclear CPMG-25 experiment, as shown in Figure 5.6, with simultaneous inductive and NV-NMR acquisition. The measurements are averaged 1000 times to improve signal-to-noise ratio. The spacing between consecutive nuclear π pulses is 4 ms, resulting in a total signal duration of approximately 100 ms.

The time-domain results are shown in Figure 5.8(a) for inductive NMR and Figure 5.8(b) for NV-NMR. A sequence of 25 individual spin-echo envelopes is clearly resolved in both datasets, separated by the strong nuclear π pulses. To improve visualization of the spin-echo signals, the large-amplitude π pulses are removed by applying an amplitude threshold, as shown in Figure 5.8.

The NV-NMR and inductive NMR signals exhibit good temporal alignment, confirming consistent detection of the same nuclear spin dynamics. Each individual spin-echo envelope decays with the nuclear dephasing time T_2^*, on the order of a few milliseconds. The NV-NMR signal is noisier than the inductive signal due to the smaller sensing volume; however, it exhibits a longer apparent T_2^*, which we attribute to reduced magnetic field gradients over the localized NV sensing region.

The peak amplitudes of the spin-echo envelopes decay over time according to the nuclear spin coherence time T_2. However, direct extraction of T_2 from the time-domain peak amplitudes is unreliable due to noise in the measured signals. To improve the robustness of the analysis, we employ two alternative methods.

In the first method, each individual spin echo is first isolated and transformed into the frequency domain via FFT. Excluding the first spin echo, which exhibits a distorted envelope, we analyze the

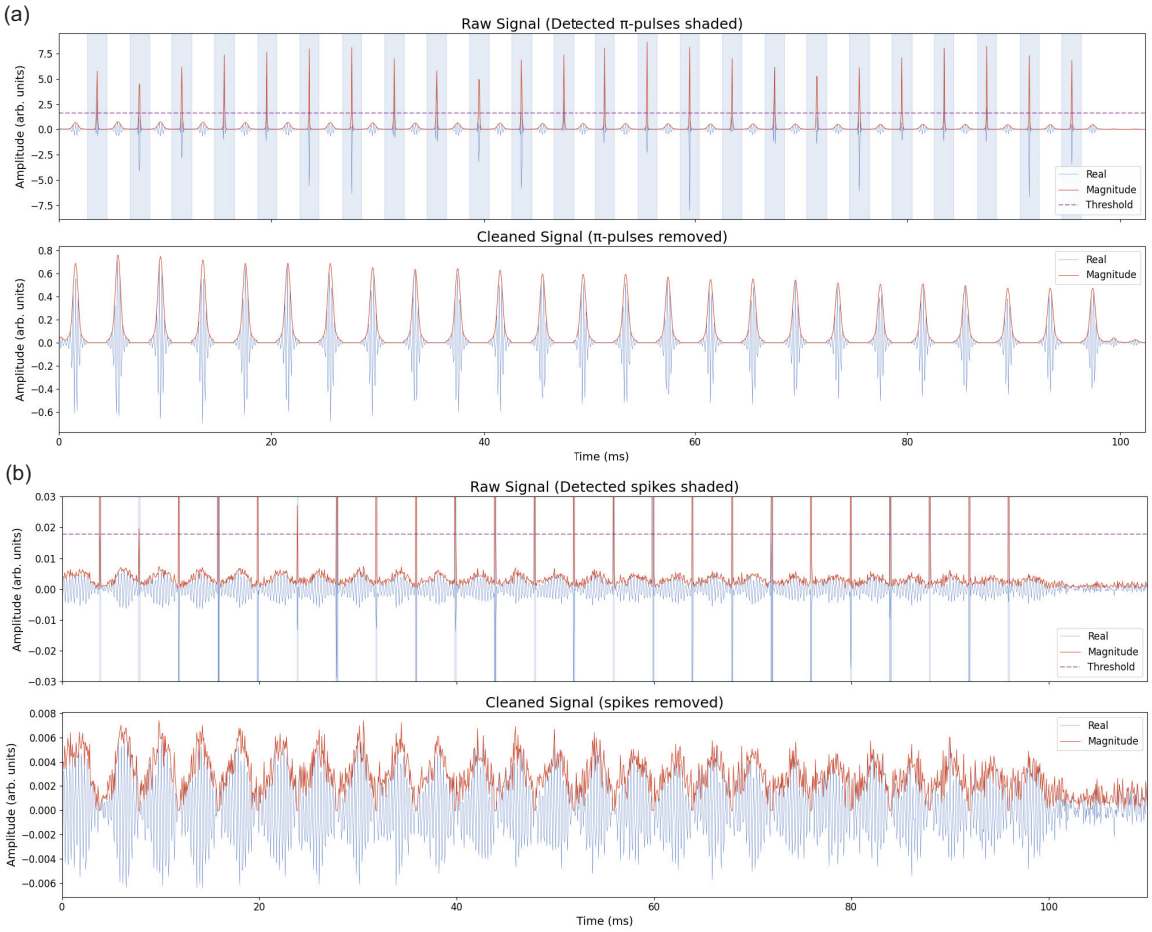


Figure 5.8: Time-domain nuclear CPMG-25 signals measured simultaneously using inductive ^{1}H NMR and NV-based detection of deionized water with Overhauser DNP. (a) Inductive NMR signal. Top: Raw signal with high-amplitude nuclear π pulses shaded; a threshold is used to identify these pulses. Bottom: Cleaned signal after removing the π-pulse contributions, revealing 25 spin-echo envelopes separated by 4 ms. (b) NV-NMR signal measured via photodiode readout. Top: Raw signal with detected spikes (corresponding to nuclear π pulses) shaded. Bottom: Cleaned signal after spike removal, showing the corresponding spin-echo train. The inductive and NV-NMR signals exhibit clear temporal alignment, confirming consistent detection of the same nuclear spin dynamics. Each spin-echo envelope decays with the nuclear dephasing time T_2^*, while the envelope peaks decrease over time according to the coherence time T_2. The NV-NMR signal shows higher noise but captures the same echo structure, demonstrating its capability for time-resolved NMR detection with microscopic sensing volume.

second spin echo as a representative example. The resulting spectrum (Figure 5.9(a)) shows a clear alias peak near 3.25 kHz with a linewidth of approximately 300 Hz.

In our experiment, the CASR sequence length is $T_{\mathrm{seq}} = 32.5\,\mu$s, corresponding to an effective sampling rate

$$f_s = \frac{1}{2T_{\mathrm{seq}}} \approx 15.38\,\mathrm{kHz}. \tag{5.4}$$

The detected alias frequency f_a is related to the true signal frequency f_0 by

$$f_a = |f_0 - n f_s|\,. \tag{5.5}$$

Using the inductive NMR measurement as a reference ($f_0 \approx 1.69\,\mathrm{MHz}$), we estimate

$$n \approx \frac{f_0}{f_s} \approx 110, \tag{5.6}$$

which yields

$$f_0 = 110 f_s \pm f_a. \tag{5.7}$$

Substituting the measured values gives two possible solutions:

$$\begin{aligned} f_0 &= 1{,}692{,}307.7 - 3{,}250 = 1{,}689{,}057.7\ \mathrm{Hz}, \\ f_0' &= 1{,}692{,}307.7 + 3{,}250 = 1{,}695{,}557.7\ \mathrm{Hz}. \end{aligned} \tag{5.8}$$

Comparing with the inductive NMR result, the correct solution is identified as

$$f_0 \approx 1.689\ \mathrm{MHz}. \tag{5.9}$$

The peak amplitude of the FFT spectrum can be used to estimate the NV-NMR signal amplitude in magnetic field units. From a calibration measurement, a 32 nT test signal with the same acquisition time and sampling rate yields a CASR spectral amplitude of 0.3, providing a conversion factor between spectral amplitude and magnetic field. Applying this calibration, the NV-NMR signal amplitude of the second spin echo is estimated to be $\sim 3.6\,\mathrm{nT}$ as shown in Figure 5.9(b).

For a more accurate determination of the signal magnitude, we compute the amplitude spectral density (ASD) and power spectral density (PSD), defined as

$$\mathrm{ASD} = \frac{\mathrm{FFT}}{\sqrt{f_s/N}}, \quad \mathrm{PSD} = |\mathrm{ASD}|^2, \tag{5.10}$$

where f_s is the sampling rate and N is the number of samples. The NMR signal amplitude is then obtained from

$$B = \sqrt{\int \mathrm{PSD}\, df} = 4.46\,\mathrm{nT}. \tag{5.11}$$

This measured amplitude is approximately two orders of magnitude larger than the expected thermal signal estimated in Eq. (5.3), indicating a DNP enhancement of $\sim 100\times$, consistent with Ref. [55].

Finally, the peak amplitude of the FFT spectrum for each spin echo decays over time according to the nuclear spin coherence time T_2. Fitting this decay yields T_2, as shown in Figure 5.10(a,c).

In the second method, we directly integrate the time-domain signal within each spin-echo window and fit the resulting amplitudes to extract T_2, as shown in Figure 5.10(b,d). Both methods provide more reliable estimates of T_2 compared to direct peak extraction.

We apply the same analysis to the inductive NMR data for comparison. Both techniques yield

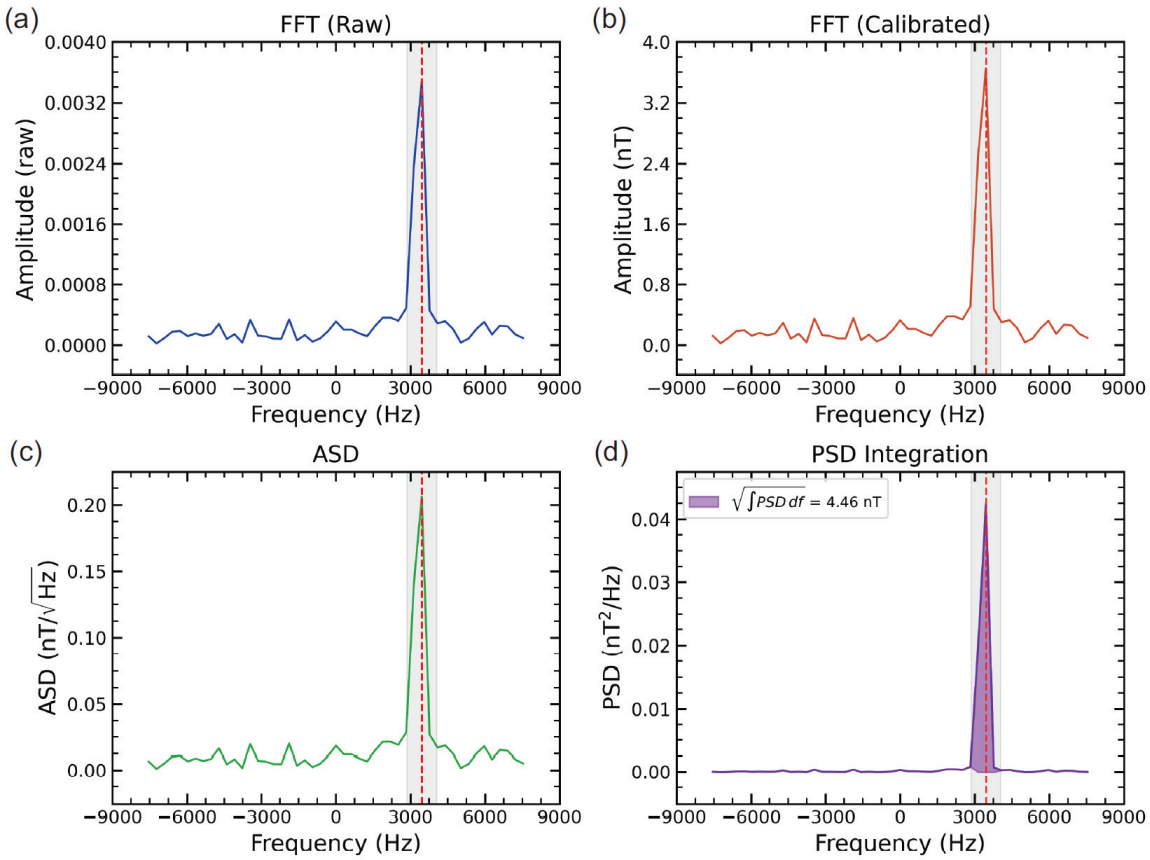


Figure 5.9: Frequency-domain analysis of a single NV-NMR spin-echo signal. (a) Raw FFT spectrum showing a clear alias peak near $f_a \approx 3.25\,\text{kHz}$ (red dashed line), with the shaded region indicating the integration window. (b) Calibrated FFT spectrum converted to magnetic field units using a reference measurement, yielding a peak amplitude on the order of a few nT. (c) Amplitude spectral density (ASD), obtained by normalizing the FFT to the measurement bandwidth, highlighting the signal-to-noise characteristics. (d) Power spectral density (PSD) and integration over the signal bandwidth (shaded region), yielding a total magnetic field amplitude of $\sqrt{\int \text{PSD}\, df} = 4.46\,\text{nT}$. The extracted signal amplitude significantly exceeds the thermally polarized expectation, indicating $\sim 100\times$ enhancement due to Overhauser DNP.

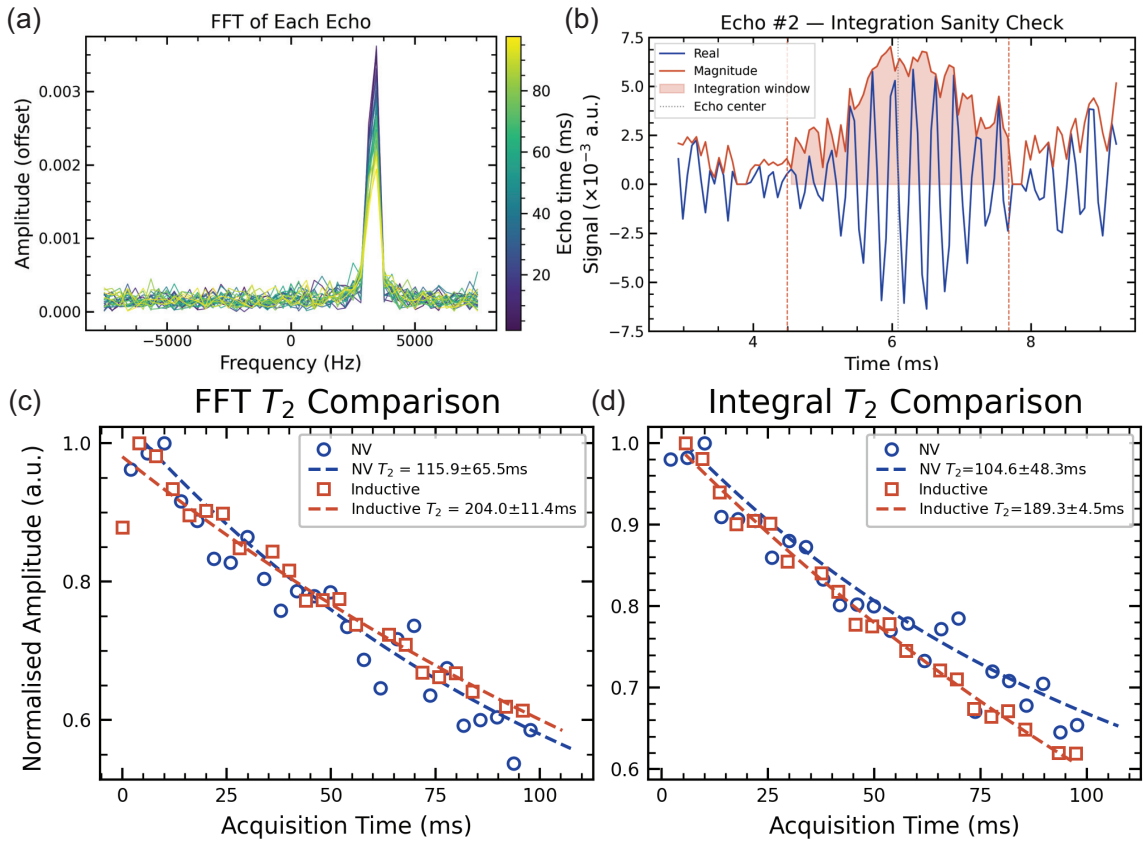


Figure 5.10: Analysis of nuclear spin (^{1}H) coherence time T_2 from simultaneous NV-NMR and inductive NMR measurements using the CPMG-25 sequence for deionized water with Overhauser DNP. (a) FFT spectra of individual NV-NMR spin echoes, vertically offset and color-coded by echo time. A clear alias peak near 3.25 kHz is observed for all echoes, with the peak amplitude gradually decreasing due to nuclear spin decoherence. (b) Example integration window used for time-domain analysis of the second spin echo. The shaded region indicates the integration range centered between nuclear π pulses. (c) Comparison of T_2 extracted from the FFT peak amplitudes of each spin echo for NV-NMR and inductive NMR measurements. Dashed lines are exponential fits. (d) Comparison of T_2 obtained from time-domain integration of each spin echo. Both analysis methods yield similar coherence times, with the NV-NMR data exhibiting larger fitting uncertainty due to lower signal-to-noise ratio. The shorter NV-NMR T_2 compared with the inductive measurement is attributed to diffusion and magnetic-field gradients near the diamond surface.

similar coherence times of $T_2 \sim 200\,\text{ms}$. The T_2 obtained from NV-NMR is slightly shorter than that from inductive detection, which we attribute to enhanced molecular diffusion near the diamond surface. Additionally, the NV-NMR data exhibit larger fitting uncertainty due to the lower signal amplitude and higher noise level.

5.3.3 Proof-of-Principle CPMG-Shaped Signal Imaging

Compared to photodiode-based detection, wide-field imaging using a lock-in camera suffers from higher readout noise, lower effective sampling rate, and longer data transfer times. As a result, achieving a comparable SNR for NV-NMR signals with the camera is currently challenging. Given that the NV-NMR signal characteristics are already established from photodiode measurements, we instead perform a proof-of-principle QDM-CASR imaging experiment using a synthetic, spatially-varying signal with a CPMG-like temporal profile but significantly higher amplitude.

In this experiment, we employ two RF test signals. The first is a constant-amplitude AC signal at frequency $f_0 = 1.6890528\,\text{MHz}$, generated by the large NMR coil (and thus modest spatial variation in NMR signal amplitude), which serves as a background reference. The second signal is generated using the spiral microcoil described in Chapter 3 and is designed to mimic the temporal structure of a nuclear CPMG signal. Specifically, it consists of an exponentially decaying envelope with $T_2 = 200\,\text{ms}$, modulated by a periodic Lorentzian envelope with a period of 4 ms and a linewidth of 2 ms. This signal has a carrier frequency of $f_s = 1.6900528\,\text{MHz}$.

The lock-in camera configuration is optimized following the procedure described in Appendix A. The sequence length for one demodulation cycle is $97.1\,\mu\text{s}$, corresponding to an effective sampling rate of $f_s^{\text{cam}} = 1/(4T_{\text{demod}}) \approx 2.57\,\text{kHz}$. Under this configuration, the two signals are detected at aliased

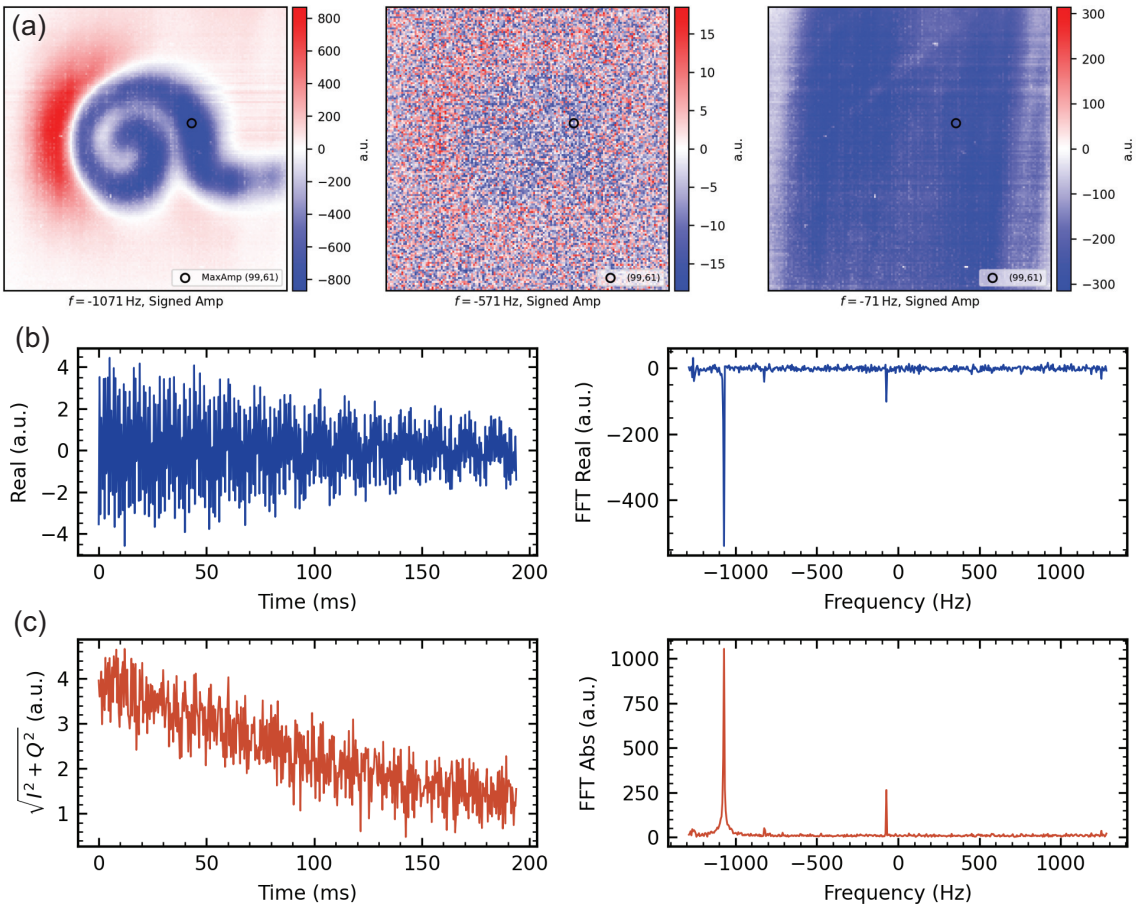


Figure 5.11: Proof-of-principle imaging of a CPMG-shaped synthetic signal using QDM-CASR. (a) Spatial maps of the signed FFT amplitude at three frequencies: the signal frequency $f_{as} = -1071\,\text{Hz}$ (left), an off-resonant frequency $f = -571\,\text{Hz}$ (middle), and the reference/background frequency $f_{a0} = -71\,\text{Hz}$ (right). The signal map at f_{as} clearly resolves the spiral microcoil pattern, while the off-resonant map shows only noise and the background map reflects the spatial profile of the large NMR coil and illumination inhomogeneity. The circled pixel (99,61) indicates the location of maximum signal amplitude used for further analysis. (b) Time-domain CASR signal (left) and corresponding FFT real component (right) for the selected pixel. The signal exhibits an exponentially decaying envelope in time and a distinct spectral peak at f_{as} in the frequency domain. (c) Magnitude of the complex CASR signal $\sqrt{I^2+Q^2}$ (left) and corresponding FFT amplitude spectrum (right). The spectrum shows a dominant peak at f_{as} and a smaller peak at f_{a0}, corresponding to the synthetic signal and reference background, respectively.

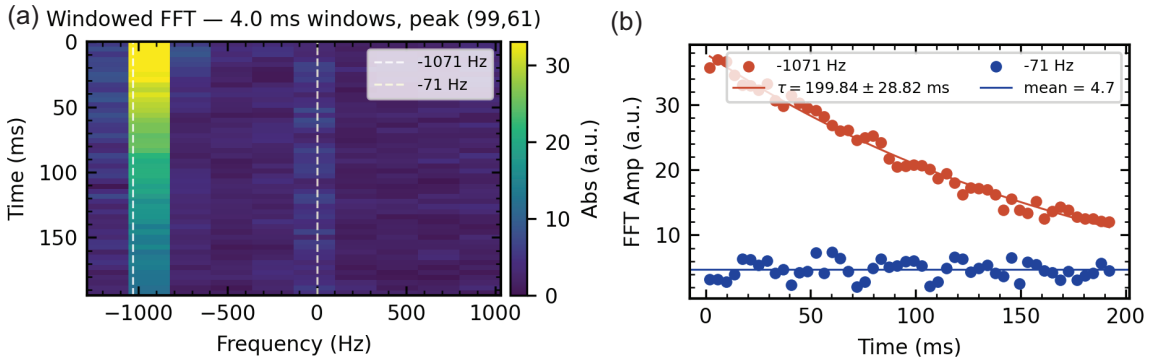


Figure 5.12: Time-resolved spectral analysis of the CPMG-shaped synthetic signal using windowed FFT. (a) Spectrogram obtained by applying FFT to successive 4 ms time windows of the CASR signal at the pixel of maximum amplitude (99,61). The dominant signal component at $f_{as} = -1071$ Hz (left dashed line) exhibits a clear exponential decay over time, while the reference/background component at $f_{a0} = -71$ Hz (right dashed line) remains approximately constant. (b) Temporal evolution of the FFT peak amplitudes extracted from (a). The signal component at f_{as} (red) is fit to an exponential decay, yielding $T_2 = 199.84 \pm 28.82$ ms, consistent with the programmed decay constant of the synthetic signal. The reference component at f_{a0} (blue) shows no decay and remains constant within noise, confirming its origin as a steady background field.

frequencies of $f_{a0} = -71$ Hz and $f_{as} = -1071$ Hz, respectively.

Example CPMG-shaped test signal imaging results after 100 averages are shown in Figure 5.11(a). As in Chapter 3, we define the sign of the image amplitude according to the real component of the FFT spectrum. The image clearly reveals a spatially structured signal at f_{as}, a near-uniform background at f_{a0} generated by the large NMR coil, and broadband noise between these two frequencies.

To further illustrate the signal characteristics, we select the pixel with the maximum amplitude at $(99, 61)$ and analyze its time-domain and frequency-domain CASR signals, including both the real component and absolute amplitude, as shown in Figure 5.11(b,c). In the time domain, the signal exhibits the expected exponential decay profile. In the frequency domain, distinct peaks corresponding to the signal (f_{as}) and reference (f_{a0}) are clearly resolved.

To demonstrate spatially resolved T_2 extraction, we perform decay analysis following the same method used in Figure 5.10. The time-domain signal is segmented into 4 ms windows, and an FFT is

applied to each segment. As shown in Figure 5.12, line cuts at f_{as} and f_{a0} reveal two components: an exponentially decaying signal at f_{as} and a constant-amplitude background at f_{a0}. Fitting the decay yields $T_2 = 199.84$ ms, in excellent agreement with the programmed value of 200 ms.

The signed FFT amplitude images in Figure 5.11(a) capture the qualitative spatial features of the field, but do not directly represent the magnetic field in physical units. For example, the image at f_{a0} exhibits a horizontal Gaussian profile, which originates from the spatial variation of laser illumination intensity rather than the magnetic field generated by the NMR coil.

To correct for this effect, we perform a calibration measurement using the NMR coil, following a procedure similar to that in Figure 3.4. As shown in Figure 5.13, we sweep the AWG amplitude to obtain AC magnetometry curves for each pixel and extract a calibration factor map proportional to the local magnetic field response. A spatial gradient is observed in this map due to the field of view not being centered within the NMR coil.

Using this calibration map, we convert the FFT amplitudes into magnetic field units according to

$$B = \frac{A(f_{as})}{A(f_{a0})} \cdot 0.003 \cdot C, \tag{5.12}$$

where $A(f)$ denotes the FFT amplitude at frequency f, 0.003 is the applied AWG amplitude, and C is the calibration factor. The resulting magnetic field images are shown in Figure 5.13(c).

The CPMG-like signal generated by the microcoil has an amplitude on the order of 100 nT, while the background field from the NMR coil corresponds to $0.003\times$ the values shown in Figure 5.13(b). The horizontal stripe artifacts observed in the magnetic field image are attributed to saturation of the CMOS sensor in the camera; when a pixel saturates, it introduces an offset across the entire readout line.

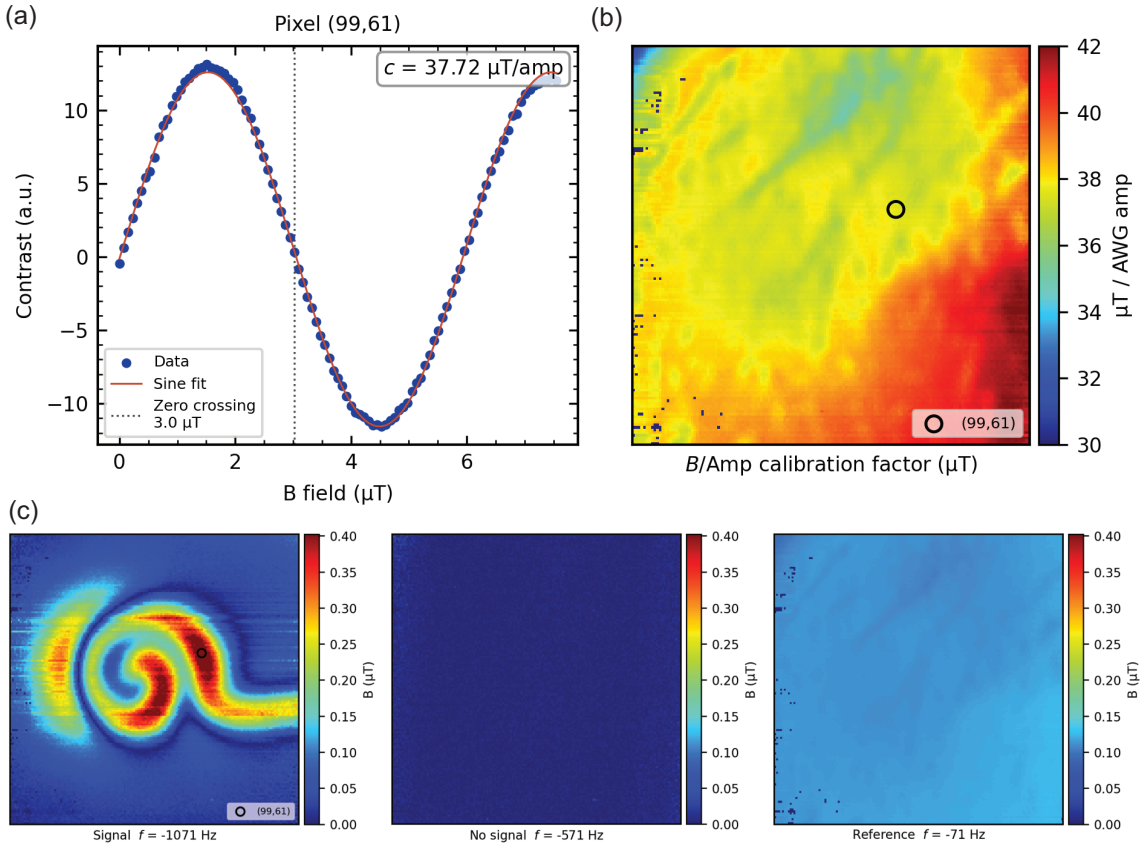


Figure 5.13: Magnetic-field calibration and quantitative imaging of the CPMG-shaped synthetic signal. (a) Pixel-wise AC magnetometry calibration at the selected pixel (99,61). The NV fluorescence contrast is measured as a function of applied RF magnetic field amplitude and fit to a sinusoid, yielding a calibration factor $C = 37.72\,\mu\mathrm{T/amp}$. The vertical dashed line indicates the operating point used in the experiment. (b) Spatial map of the calibration factor (B/Amp) across the field of view, reflecting the spatial variation of the RF magnetic field generated by the NMR coil and the relative positioning of the sample within the coil. The circled pixel indicates the location used for calibration in (a). (c) Reconstructed magnetic-field amplitude images obtained by applying the calibration map to the FFT amplitudes. Left: signal component at $f_{as} = -1071\,\mathrm{Hz}$, clearly resolving the spiral microcoil pattern with peak amplitudes on the order of $100\,\mathrm{nT}$. Middle: off-resonant frequency ($f = -571\,\mathrm{Hz}$), showing noise-limited background. Right: reference component at $f_{a0} = -71\,\mathrm{Hz}$, corresponding to the spatial distribution of the background field generated by the large NMR coil. Horizontal artifacts arise from partial saturation of the CMOS sensor during acquisition.

It is important to note that the synthetic signal used in this proof-of-principle experiment is approximately two orders of magnitude stronger than the NV-NMR signal measured using the photodiode. Substantial technical improvements are therefore still required to realize real-space NMR imaging. Potential advancements include improving bias magnetic field homogeneity to reduce NMR linewidth, enhancing DNP efficiency to increase signal amplitude, and optimizing camera sensitivity.

One practical approach for improving imaging sensitivity is pixel binning, which increases the SNR at the expense of spatial resolution. As shown in Figure 5.14, we measure the CASR noise floor using 1000 successive averages and evaluate the sensitivity under different binning conditions. Based on these results, we estimate that an NMR image with SNR ~ 10 could be achieved with a spatial resolution of approximately $8\,\mu$m (corresponding to 4×4 pixel binning) using 1000 averages, requiring a total acquisition time of approximately 6 h.

5.4 Next Steps for QDM-NMR Applications

Having demonstrated that the QDM-NMR system can spatially resolve CPMG-like signals, including their coherence time T_2 and frequency, using microcoil-generated test signals, the next natural step is to extend this capability to real NMR samples. In particular, we aim to image proton (^{1}H) NMR signals from water and other liquid samples, such as glycerol, which has a higher viscosity than water. The difference in molecular dynamics between these samples is expected to produce measurable spatial variations in nuclear spin coherence time T_2, providing a clear demonstration of contrast in QDM-NMR imaging.

As a simple proof-of-principle experiment for generating spatial T_2 contrast, micron-scale glass beads (diameter ~ 10–$50\,\mu$m) can be introduced into the sample region. When placed within the slot,

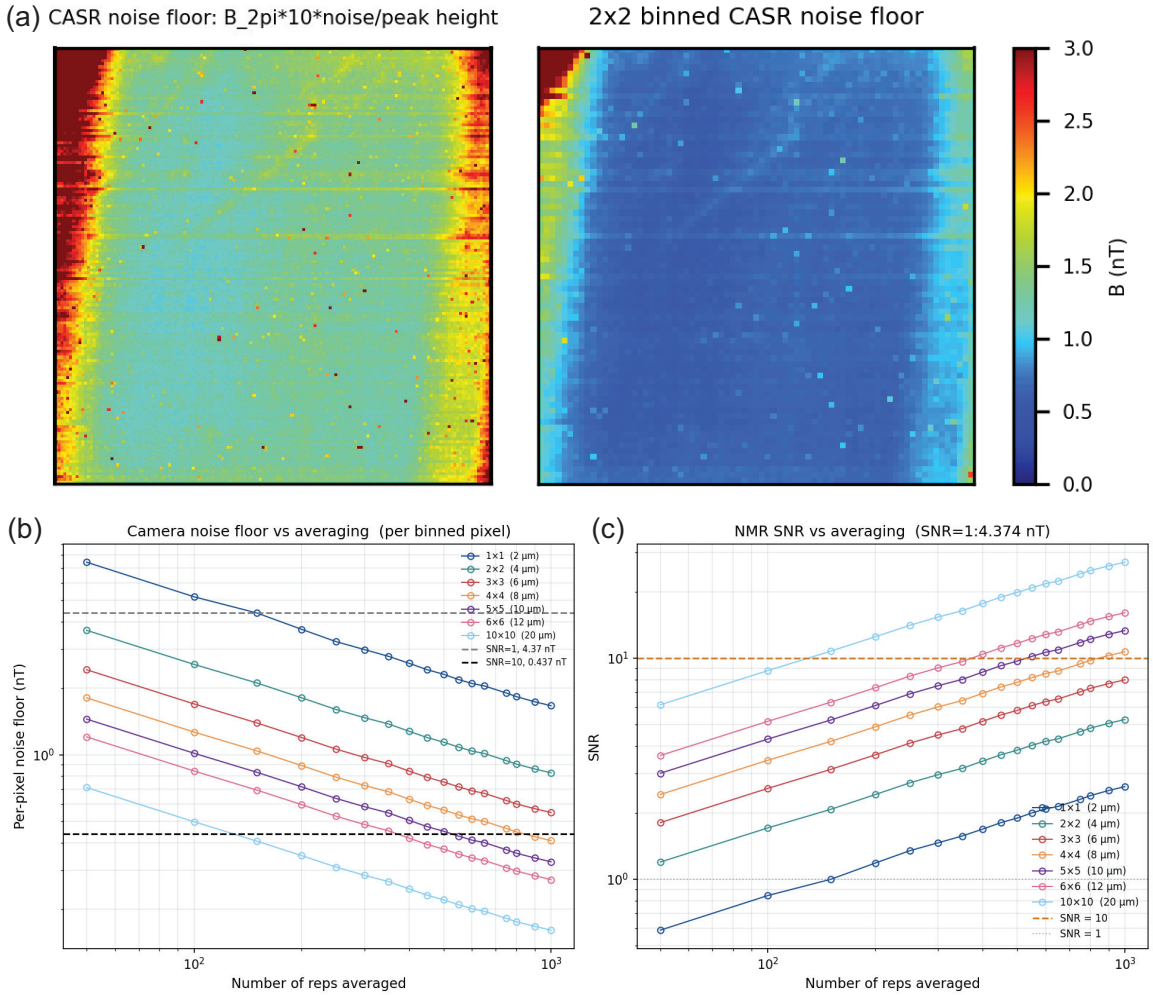


Figure 5.14: SNR improvement through pixel binning and averaging for QDM-NMR imaging. (a) Spatial maps of the measured CASR noise floor after 1000 averages for the original image resolution (left) and after 2×2 pixel binning (right). Pixel binning reduces the effective per-pixel noise level. (b) Estimated per-pixel magnetic noise floor as a function of the number of averaged measurements for different pixel binning conditions. Curves are shown for binning factors from 1×1 (2 μm spatial resolution) to 10×10 (20 μm spatial resolution). The dashed lines indicate estimated signal amplitudes of 4.37 nT and 0.437 nT, corresponding to SNR = 1 and SNR = 10. (c) Estimated QDM-NMR SNR as a function of averaging number for different binning conditions. The dashed line indicates SNR = 10. Based on these estimates, an NMR image with SNR ~ 10 can be achieved at approximately $8\,\mu$m spatial resolution (4×4 binning) with 1000 averages, corresponding to a total acquisition time of approximately 6 h.

these beads locally perturb molecular diffusion and magnetic field homogeneity, leading to spatially varying nuclear spin dephasing. As a result, a spatial map of T_2 can be generated in the surrounding water, providing a straightforward and controllable test of QDM-NMR imaging performance.

These experiments can be implemented using the configuration illustrated in Figure 5.4. Such measurements require long acquisition times to achieve sufficient SNR, making system stability a critical factor. In particular, stability of the bias magnetic field, microwave and RF sources, and optical readout must be maintained over extended averaging periods.

Beyond these proof-of-principle demonstrations, we plan to apply the QDM-NMR platform to address practical challenges in chemical analysis and biological systems. In the following subsections, we outline potential applications in soft materials and biological environments, where spatially resolved NMR measurements at the microscale could provide unique insights.

5.4.1 Potential QDM-NMR Applications in Hydrogels

Hydrogels provide an attractive and experimentally accessible platform for QDM-NMR imaging due to their high water content, tunable structure, and compatibility with surface-based sensing. In particular, polyethylene glycol (PEG)-based hydrogels can be readily fabricated *in situ* under mild conditions, allowing direct formation on the diamond surface. This minimizes the stand-off distance between the sample and the NV sensing layer, which is critical for maximizing magnetic sensitivity.

An additional advantage of hydrogel systems is their compatibility with DNP. During the gelation process, paramagnetic radicals such as TEMPOL can be incorporated into the polymer network, enabling Overhauser DNP to enhance nuclear spin polarization. This provides a practical route to overcoming the intrinsically weak NMR signal amplitude discussed in previous sections.

Figure 5.15 shows the formation and structural properties of PEG-based hydrogels. Crosslinked networks are formed via thiol–ene chemistry between PEG precursors, resulting in a homogeneous gel under conventional conditions. However, under certain synthesis conditions, gel–gel phase separation (GGPS) can occur, producing coexisting dense and dilute polymer regions.

Such structural heterogeneity is particularly important for NMR imaging. Variations in polymer density and water mobility directly influence nuclear spin relaxation and diffusion, leading to spatially dependent coherence times. Dense polymer regions typically exhibit reduced molecular mobility and shorter T_2, while dilute regions maintain longer coherence times. As a result, hydrogels naturally generate intrinsic contrast mechanisms for QDM-NMR imaging.

These properties make hydrogels an ideal testbed for demonstrating spatially resolved NMR measurements with the QDM. By mapping the spatial variation of the NMR signal decay, it becomes possible to visualize internal structures such as phase boundaries, diffusion gradients, and mechanical heterogeneity. Furthermore, the ability to engineer hydrogel composition and structure provides a controllable platform for benchmarking QDM-NMR performance and optimizing imaging protocols.

Overall, hydrogels combine ease of fabrication, compatibility with hyperpolarization techniques, and tunable spatial heterogeneity, making them a promising system for advancing QDM-NMR toward practical applications in soft matter and biological imaging.

5.4.2 Potential QDM-NMR Applications in Bio-systems

In this work, we present a methodology for applying QDM wide-field imaging to detect NMR signals in real space. Our initial objective is to demonstrate NMR imaging of simple liquid systems. However, this represents only a first step toward more complex and biologically relevant applications.

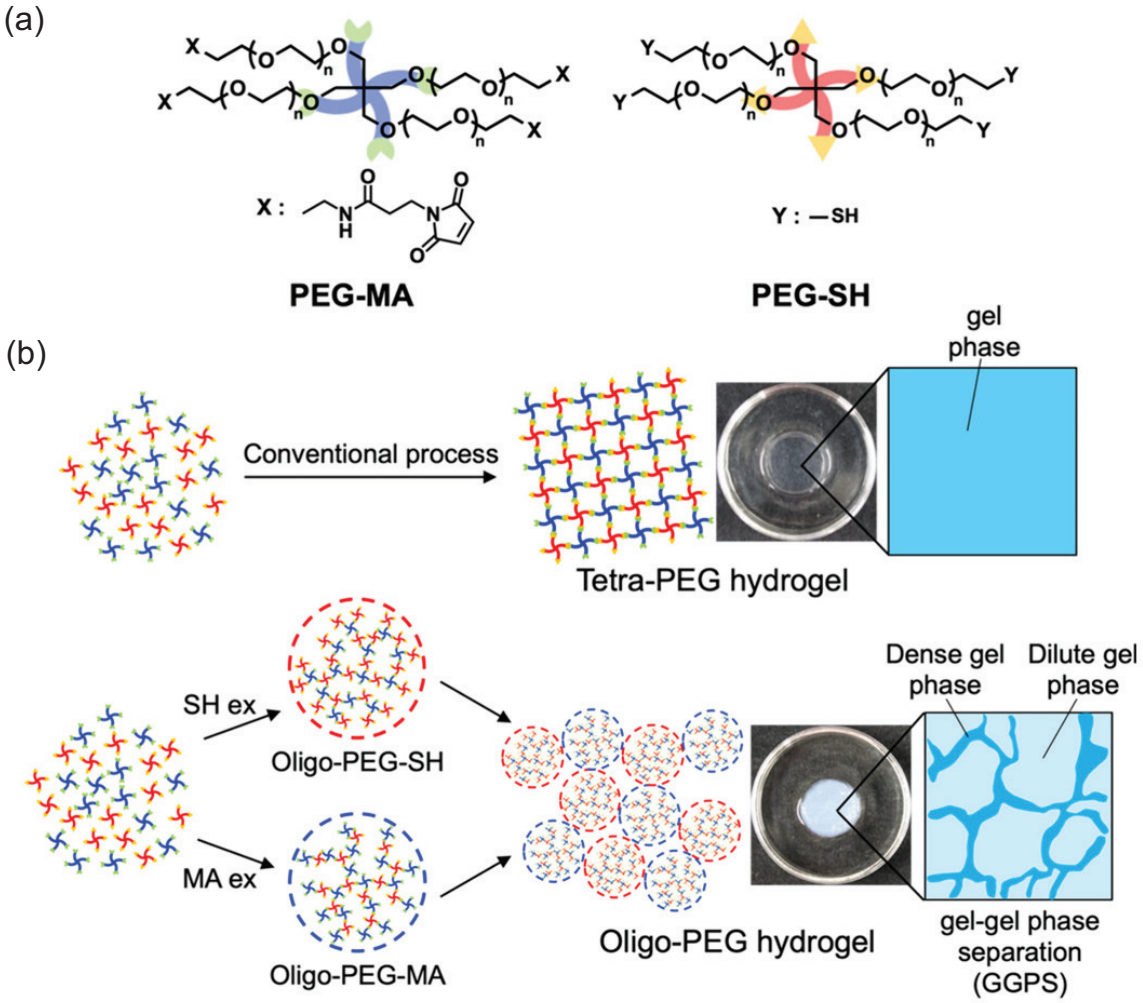


Figure 5.15: Adapted from Ref. [87]. PEG-based hydrogel formation and structural heterogeneity relevant to QDM-NMR imaging. (a) Schematic of PEG precursor molecules (PEG-MA and PEG-SH) used to form crosslinked hydrogel networks. (b) Comparison between homogeneous hydrogel formation (top) and gel–gel phase separation (GGPS, bottom), where dense and dilute polymer domains coexist. These structural variations lead to spatial differences in molecular diffusion and local viscosity, which can produce spatial contrast in nuclear spin coherence time T_2.

To guide the development of QDM-based NMR imaging, we identify several key criteria for suitable bio-systems:

1. **Scientific Relevance**: The target system should be broadly meaningful, avoiding overly specialized cases, and ideally represent a class of biologically or chemically important materials.

2. **Robustness and Stability**: QDM measurements require prolonged laser illumination and extended averaging times. Therefore, the system must tolerate continuous optical and microwave exposure over hours without degradation.

3. **Quasi-2D Geometry**: Since the NMR signal strength decreases rapidly with stand-off distance, the sample should be confined close to the diamond surface. Systems with thickness $\lesssim 10\,\mu\mathrm{m}$ are preferred.

4. **Micron-Scale Spatial Features**: The system should exhibit intrinsic spatial structure at the ~ 10–$100\,\mu\mathrm{m}$ scale, enabling meaningful contrast within the QDM field of view.

5. **Detectable NMR Signal**: The system must produce sufficiently strong and spatially localized NMR signals, potentially requiring signal averaging but remaining within practical limits.

These criteria provide a framework for identifying candidate systems for QDM-based NMR imaging.

One particularly suitable class of systems is biofilms, which are structured communities of microorganisms (e.g., bacteria, algae, and fungi) embedded within a hydrated extracellular polymeric substance (EPS) matrix [88]. More than 90% of microorganisms in natural environments exist in biofilms, spanning a wide range of environments from aquatic ecosystems to medical devices [89–92].

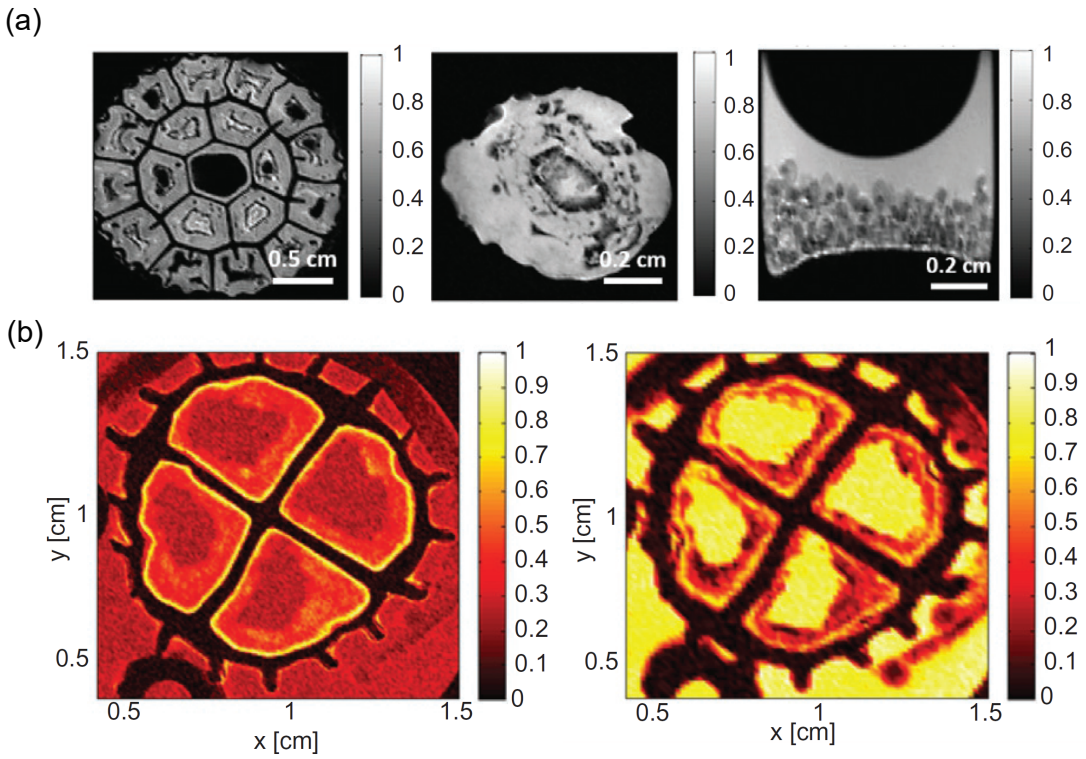


Figure 5.16: MRI of various biofilm geometries [94, 95]. (a) MRI visualization of different biofilm structures: autotrophic biofilm (left), granulated biofilm (middle), and granulated biofilms of varying sizes (right). (b) T_1-weighted (left) and T_2-weighted (right) MRI contrast revealing internal heterogeneity in a heterotrophic biofilm.

Their inherent structural complexity and environmental adaptability make biofilms both scientifically significant and challenging to characterize using conventional imaging techniques.

Understanding biofilm structure and its response to environmental factors is a central research topic. Conventional imaging techniques such as optical microscopy, confocal laser scanning microscopy (CLSM), and electron microscopy have provided valuable insights, but often require staining, invasive preparation, or non-physiological conditions [93].

Magnetic resonance imaging (MRI) provides a non-invasive approach to probing biofilm structure and composition. It enables imaging at spatial resolutions down to $\sim 50\,\mu\mathrm{m}$ and allows measurement of transport processes and chemical environments [96]. Because biofilms typically contain up to 95% water, the ^{1}H NMR signal is dominant. Relaxation parameters, particularly T_1 and T_2, play a central

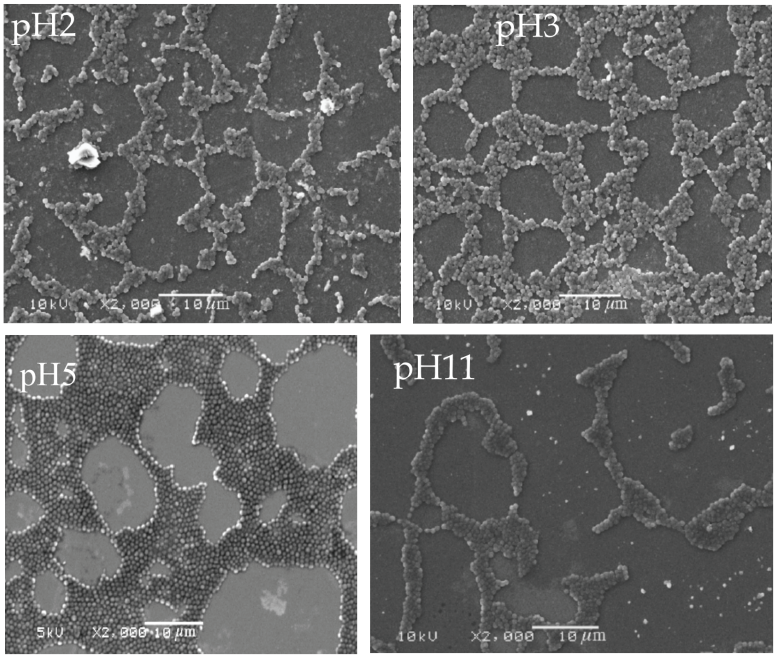


Figure 5.17: SEM images of *Staphylococcus aureus* biofilms adhered to glass under different pH conditions [97].

role in generating MRI contrast.

Despite these advantages, conventional MRI is limited to millimeter- or tens-of-micron-scale resolution. In contrast, QDM-based NV-NMR offers the potential for micron-scale, real-space imaging, enabling investigation of biofilm structure at near-cellular resolution.

A promising candidate system is *Staphylococcus aureus* biofilms. As shown in Figure 5.17, SEM studies reveal strong structural dependence on environmental conditions such as pH. By growing biofilms directly on the diamond surface, QDM-NMR could enable spatially resolved imaging of these structural variations through differences in nuclear spin relaxation, providing a new, non-invasive modality for studying biofilm organization.

Another promising candidate is *Spirogyra*, a filamentous green alga composed of long chains of cylindrical cells. Each cell features a characteristic helical chloroplast, along with a large central vacuole and a nucleus suspended within the cytoplasm. This well-defined and highly ordered cellular

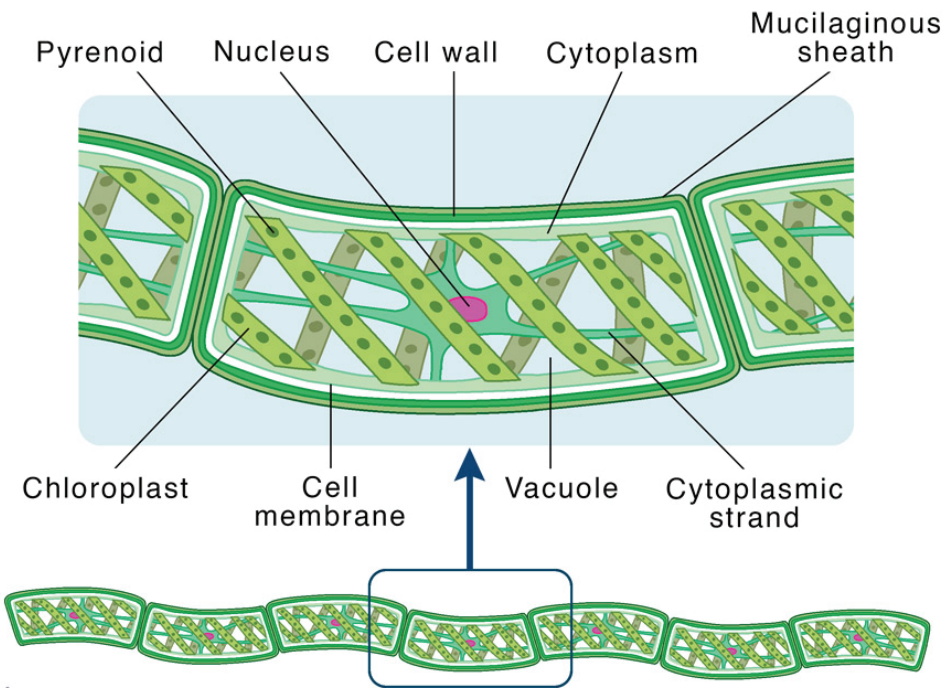


Figure 5.18: Structural diagram of Spirogyra cells, illustrating the characteristic helical chloroplast morphology.

geometry makes *Spirogyra* an attractive model system for spatially resolved imaging.

Although extensively studied using optical microscopy, Spirogyra remains an excellent candidate for demonstrating NMR-based imaging. Optical methods primarily provide structural information and often require labeling, while electron microscopy requires vacuum conditions that prevent *in vivo* observation.

Early work by Ciobanu *et al.* demonstrated 3D MRI imaging of Spirogyra using inductive NMR techniques [98], as shown in Figure 5.19. However, the spatial resolution was insufficient to resolve sub-cellular features such as the spiral chloroplast.

QDM-based NV-NMR has the potential to overcome this limitation by providing micron-scale spatial resolution combined with chemical sensitivity. In addition to structural imaging, NMR contrast can reveal information about molecular composition and dynamics, offering a richer understanding of

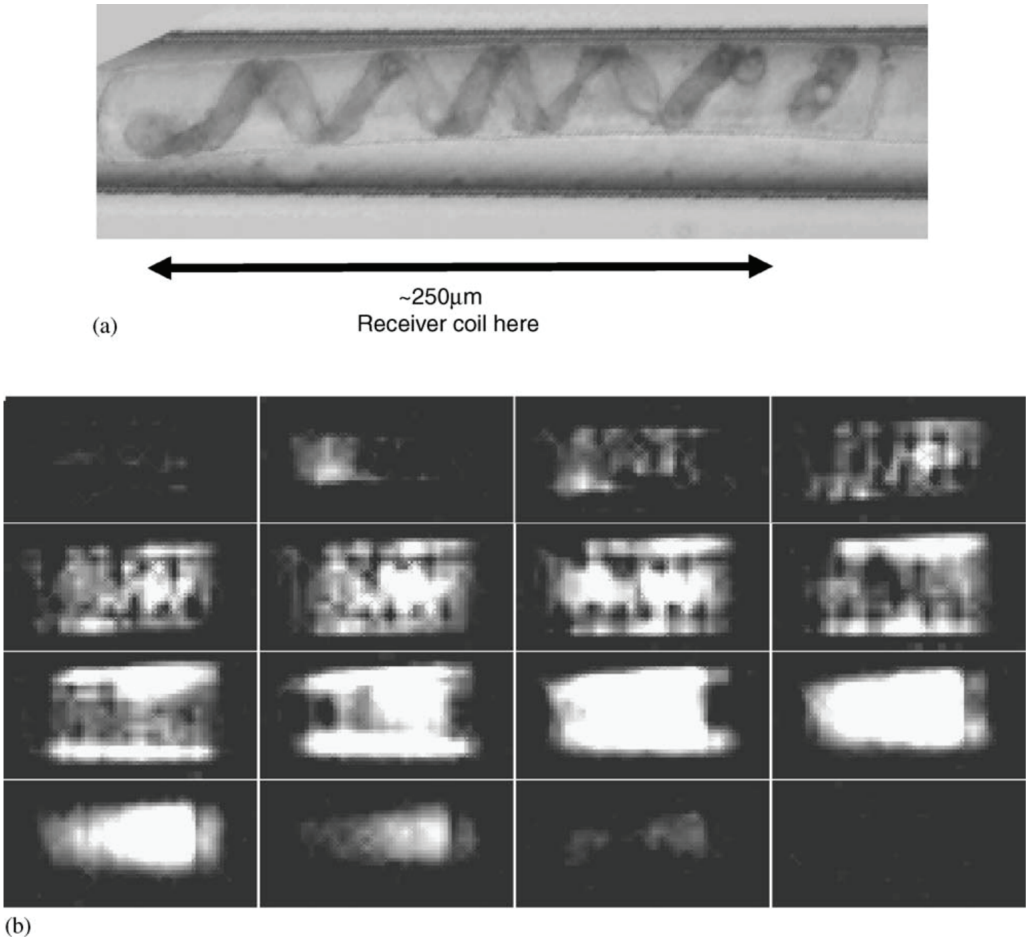


Figure 5.19: 3D MRI of a single Spirogyra cell [98]. (a) Optical image of the sample. (b) Corresponding MRI reconstruction showing overall cell morphology.

cellular processes such as photosynthesis and metabolite transport.

Overall, Spirogyra represents a well-defined biological system in which QDM-NMR could demonstrate simultaneous structural and functional imaging at the microscale.

Chapter 6: Quantum Magnetic Microscopy for Industrial Applications

In the previous chapters, we presented the development of state-of-the-art quantum magnetic microscopy systems in laboratory environments, demonstrating high-performance DC and AC magnetic imaging using NV centers in diamond. Benefiting from room-temperature operation, excellent chemical stability, and optical readout compatibility, NV-diamond sensors have emerged as a promising platform for real-world applications.

After more than a decade of rapid development, NV-based quantum sensing is transitioning from laboratory research toward commercialization and industrial deployment. This chapter discusses key considerations for this transition, with a focus on system miniaturization, robustness, and application-driven design, based on insights gained during my internship at Toyota Research Institute North America.

6.1 Development of Compact NV-diamond Magnetic Sensors

6.1.1 Industrial Requirements and Low-SWaP Constraints

Unlike academic research, which primarily focuses on optimizing performance such as sensitivity and spatial resolution, industrial applications impose additional constraints on system size, weight, and power (SWaP), as well as robustness, cost, and ease of integration.

The QDM system used in the previous chapters exemplifies a laboratory-scale platform: it occupies a volume on the order of $\sim 2\ \mathrm{m}^3$, incorporates more than $50\ \mathrm{kg}$ of optical and electronic components (excluding the optical table), and requires high power consumption (e.g., $\sim 5\ \mathrm{W}$ laser power and $\sim 16\ \mathrm{W}$ microwave amplification). Such specifications are incompatible with most industrial

Table 6.1: Comparison of magnetometer technologies.

Feature	NV	SERF	VMR
Sensitivity	pT–nT/$\sqrt{\text{Hz}}$	fT/$\sqrt{\text{Hz}}$	nT–μT/$\sqrt{\text{Hz}}$
Spatial resolution	10 nm–μm	mm	mm
Operating temperature	Cryogenic to > 600 K	Room temp	Room temp
Magnetic field range	0 to >T	Near zero	$\sim$100 mT
Size/portability	Developing	Compact	Chip-scale
Imaging capability	Yes (2D/scan)	No	No
Mechanical robustness	Very high	Lower	High
Cost	Moderate	High	Low

deployment scenarios, particularly in automotive, portable sensing, or in-line inspection applications.

Therefore, the development of compact, low-SWaP NV-diamond magnetometers is a critical step toward practical implementation. However, miniaturization introduces significant trade-offs, particularly between sensitivity, spatial resolution, and system complexity.

6.1.2 Comparison with Alternative Magnetometer Technologies

To evaluate the industrial viability of NV-based sensors, it is instructive to compare them with other compact magnetometer technologies like spin-exchange relaxation-free (SERF) magnetometers and vector magnetoresistance (VMR) sensors as summarized in Table 6.1.

Competing technologies may outperform NV sensors in specific regimes. For example, SERF and SQUID magnetometers achieve superior sensitivity in shielded environments, while VMR sensors provide cost-effective, compact solutions for industrial and automotive applications where moderate sensitivity is sufficient.

However, NV-diamond magnetometers offer several unique advantages, including operation at room (and even elevated) temperature without the need for cryogenics, micron- to nanoscale spatial

resolution, compatibility with biological and chemically active environments, vector sensing, and the capability for wide-field, two-dimensional magnetic imaging. Consequently, NV-diamond sensors are particularly well suited for applications requiring short stand-off distances ($\sim \mu$m), high spatial resolution, and spatially resolved magnetic field mapping, whereas VMR-based sensors are often more competitive for bulk sensing scenarios where compactness and cost are the primary considerations.

6.1.3 Examples of Low-SWaP NV Magnetometers

Recently, significant progress has been made toward compact NV-diamond devices through various integration strategies as shown in Figure 6.1.

Early efforts demonstrated CMOS-integrated NV magnetometers with on-chip photodiodes and microwave generation, achieving millimeter-scale form factors and low power consumption (~ 0.5 W), but suffering from low ODMR contrast ($< 1\%$) and limited sensitivity ($\sim 32\ \mu\mathrm{T}/\sqrt{\mathrm{Hz}}$) due to reliance on free-space optical excitation [99].

Fiber-integrated approaches introduced compact sensor heads incorporating GRIN lenses, balanced photodetection, and resonant microwave structures, achieving sensitivities on the order of $344\ \mathrm{pT}/\sqrt{\mathrm{Hz}}$. However, embedding the diamond within the sensor head increases stand-off distance and limits spatial resolution, reducing the advantages over conventional magnetometers [100].

More recent developments have focused on PCB-level integration, where optical excitation, readout, microwave delivery, and signal processing are implemented on compact electronic platforms. While such systems significantly reduce size, limitations remain in signal processing (e.g., absence of lock-in detection) and long-term robustness due to laser stability issues [101].

Fully integrated LED-based systems further reduce complexity by replacing laser sources with

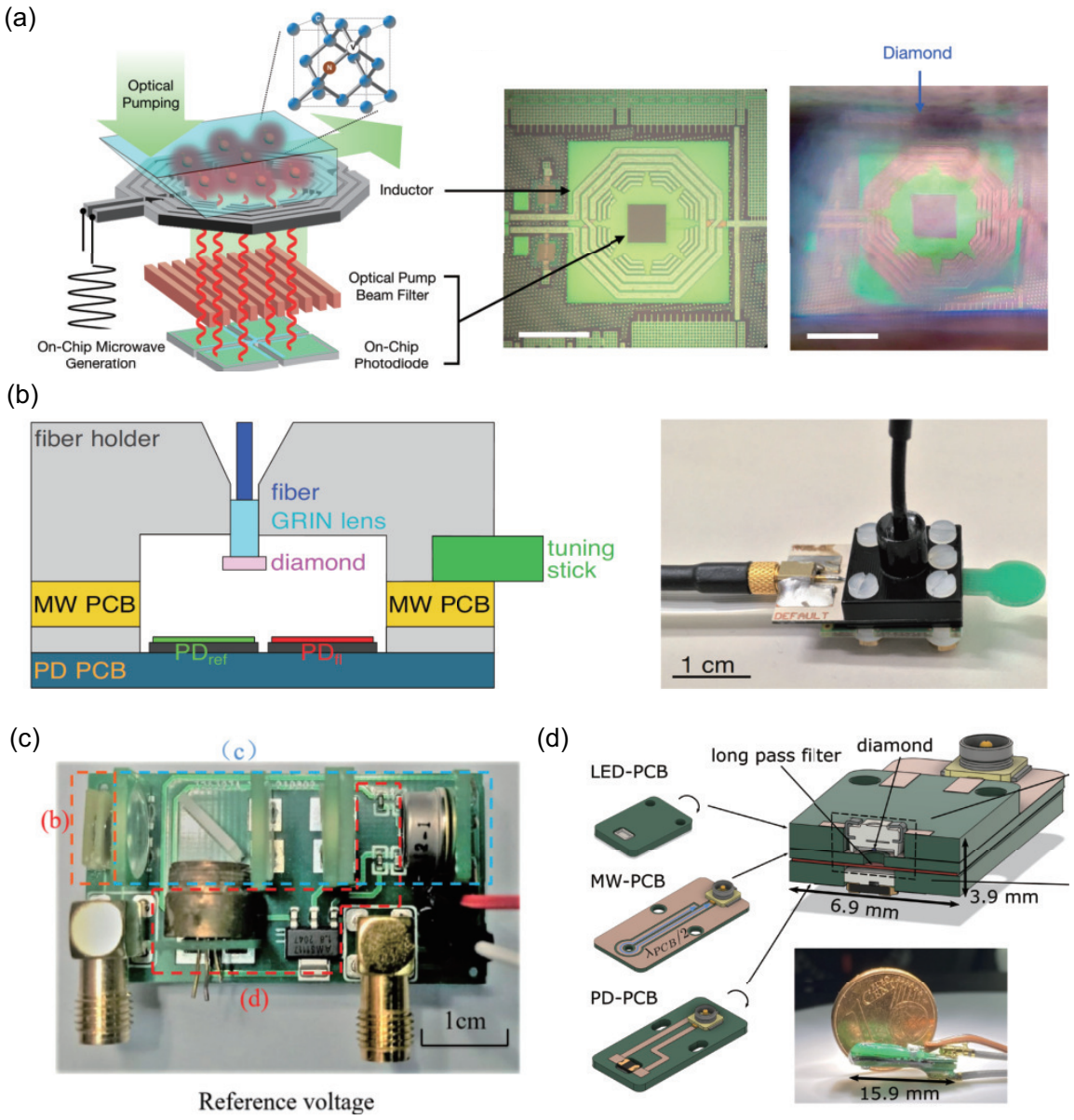


Figure 6.1: Representative compact NV-diamond magnetometer implementations. (a) CMOS-integrated device with on-chip photodiode and microwave generation [99]. (b) Fiber-integrated sensor with compact optical and microwave components [100]. (c) PCB-level integrated system combining optical excitation, microwave delivery, and signal processing [101]. (d) Fully integrated LED-based device with compact sensor head architecture [102].

LEDs and integrating photodiodes and microwave antennas within stacked PCB architectures. These devices achieve compact form factors with sensitivities around $28.3\ \mathrm{nT}/\sqrt{\mathrm{Hz}}$, but similarly suffer from reduced imaging capability due to increased sensor stand-off distance [102].

6.1.4 Design Considerations for Industrial QDM Systems

The transition from laboratory-scale QDM systems to compact industrial devices introduces several fundamental challenges. First, miniaturization reduces optical collection efficiency, microwave field uniformity, available excitation power, all of which degrade ODMR contrast and sensitivity. Second, efficient collection of NV photoluminescence becomes increasingly difficult in compact geometries. Techniques such as side-collection and total internal reflection (TIR) lens designs have been proposed to improve photon collection efficiency without increasing system size. Third, noise management becomes more challenging as electronics are integrated closer to the sensing volume. Thermal noise, electromagnetic interference, and electronic cross-talk can significantly limit performance. Finally, compact packaging often increases the stand-off distance between the diamond and the sample, introducing a fundamental trade-off between spatial resolution and system integration.

To optimize NV-based sensors under SWaP constraints, a hierarchical design approach is required. At the first-order level, intrinsic sensitivity should be maximized under power and size limitations by optimizing NV concentration, optical excitation efficiency, and microwave delivery. At the second-order level, system noise contributions must be minimized by careful engineering of thermal management, electromagnetic shielding, and system layout, including the relative placement of the diamond sensor and electronic components. At the system level, industrial deployment requires balancing sensitivity, spatial resolution, SWaP, cost, and manufacturability. These trade-offs ultimately determine the suitability

of NV-based sensors for specific applications.

6.2 Development of a Compact Quantum Magnetic Camera

As discussed in Section 6.1.3, existing compact, low-SWaP NV sensors suffer from several limitations, including low optical collection efficiency, poor thermal dissipation, and increased stand-off distance to the sample, all of which restrict their applicability to high-resolution imaging. In this section, we present the design of a compact quantum magnetic camera [103], which can be regarded as a miniaturized implementation of the QDM system. We describe the illumination module, imaging module, and the multilayer packaging architecture of the device.

6.2.1 Components of the camera

The components of the compact quantum magnetic camera are illustrated in Figure 6.2. A 532 nm laser ($\sim$100 mW) is coupled into the system via an optical fiber connected to a triplet fiber collimator (Thorlabs TC06FC-532). The collimated beam is redirected vertically and passes through a cylindrical lens (Edmund Optics #47-764) with an effective focal length of 20 mm, which compresses the beam along one dimension to achieve high-intensity illumination at the diamond surface.

The shaped beam is then directed onto the side surface of the diamond at an incident angle of 23.4°. Inside the diamond, the beam undergoes total internal reflection (TIR), illuminating an approximately $1\,\mathrm{mm} \times 1\,\mathrm{mm}$ region near the surface.

As shown in Figure 6.2(a), the NV-diamond is mounted on a thermally conductive wafer at the top layer of the device. Under optical excitation, the NV spin ensemble emits spin-state-dependent fluorescence (i.e., photoluminescence) that encodes the local magnetic field. This fluorescence is

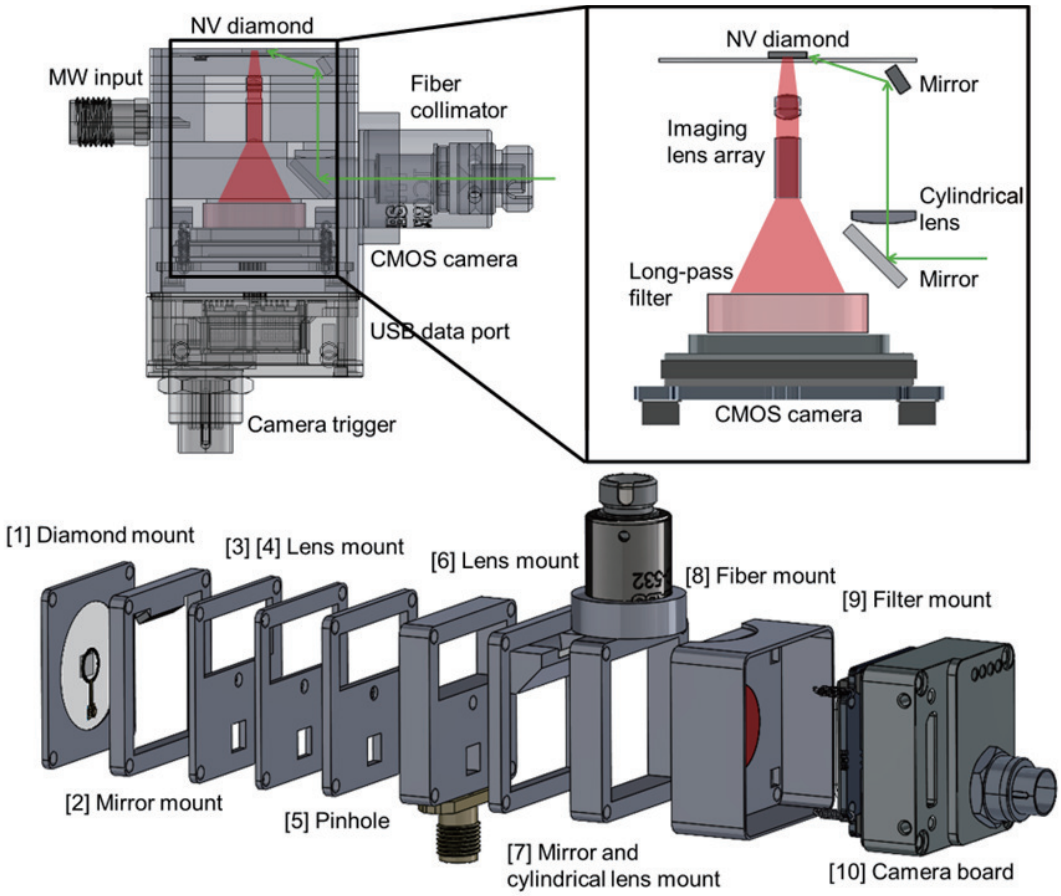


Figure 6.2: Design of the compact quantum magnetic camera. (a) Cross-sectional view of the assembled device and optical layout. A fiber-coupled laser is collimated and shaped by a cylindrical lens, then directed via mirrors to illuminate the NV diamond from the side. The resulting spin-dependent fluorescence is collected by an imaging lens array, filtered, and detected by an on-chip CMOS camera. Microwave (MW) excitation is delivered through an integrated input port. (b) Exploded view of the device showing the ten-layer modular architecture, including the diamond mount **[1]**, mirror mount **[2]**, imaging lens mounts **[3]**, **[4]**, **[6]**, pinhole **[5]**, cylindrical lens and mirror mount **[7]**, fiber mount **[8]**, filter mount **[9]**, and CMOS camera board **[10]**.

collected by a triplet imaging lens array and projected onto an on-chip CMOS camera (XIMEA MC023CG-SY-BRD) based on the SONY IMX174 sensor (active area $11\,\mathrm{mm} \times 7.1\,\mathrm{mm}$). The same sensor is used in the Basler acA1920-155um camera, which has been widely adopted in previous NV imaging studies [33, 36]. The imaging system is designed with a magnification of $7\times$ and optimized to correct third-order aberrations, enabling high-fidelity imaging across the full field of view. A long-pass optical filter (Semrock VLP02-633-12.5) is placed in front of the sensor to suppress residual pump laser light and reduce background noise.

MW control of the spin ensemble is provided by a delivery structure (e.g., stripline, loop antenna, or coplanar waveguide) fabricated on the diamond mounting wafer. A U.FL connector links this structure to an external SMA port. Compared to PCB-based MW delivery, the thermally conductive wafer provides improved heat dissipation for both optical and MW-induced heating. Figure 6.2(b) illustrates the 10-layer architecture of the device:

[1] Quantum diamond, thermally conductive wafer, and MW delivery structure. An optional cover layer can suppress ambient light but slightly increases stand-off distance.

[2] Mirror for adjusting the laser incident angle.

[3], [4], [6] Mounts for the triplet imaging lens array.

[5] Pinhole (0.65 mm diameter) for image quality enhancement.

[7] Mount for cylindrical lens and steering mirror.

[8] Fiber collimator mount.

[9] Long-pass filter mount.

[10] CMOS camera board, connected via stretch springs for fine focus adjustment.

Although optimized for a FOV and magnification, the system is adaptable. For example, centimeter-scale imaging can be achieved by adding an orthogonal cylindrical lens in Layer **[7]** to expand the beam in the second dimension, while re-optimizing the imaging optics (Layers **[3]–[6]**) for lower magnification.

The platform is also compatible with alternative quantum materials beyond bulk NV diamond, including nanodiamond, hBN, SiC, and GaN. In such cases, the excitation wavelength and incident angle can be adjusted via Layer **[2]** to account for material-dependent refractive indices. Furthermore, the triplet lens system may be replaced by a metasurface for enhanced integration, the fiber input (Layer **[8]**) may be replaced by a laser diode, and the CMOS sensor (Layer **[10]**) may be substituted with a SPAD array or lock-in camera for advanced detection schemes.

6.2.2 Design and Simulation of the Illumination Module

A key feature of this design is side illumination of the diamond, enabling both high-intensity excitation and minimal stand-off distance between the sensor and sample. This allows direct contact with the sample surface, which is critical for near-field magnetic imaging with high spatial resolution.

Figure 6.3 shows the optical design and simulation results obtained using the Physical Optics Propagation (POP) method in Zemax OpticStudio. The input beam is modeled as a collimated Gaussian beam with a $1/e^2$ waist diameter of 1.1 mm at position **[1]**.

After passing through the cylindrical lens (f = 20 mm), the beam is compressed along one axis and enters a $3\,\mathrm{mm} \times 3\,\mathrm{mm} \times 0.5\,\mathrm{mm}$ diamond at position **[2]** with a 23.4° incident angle. At the FOV edge (position **[3]**), the vertical waist is reduced to 45.3 μm while maintaining the horizontal width. At

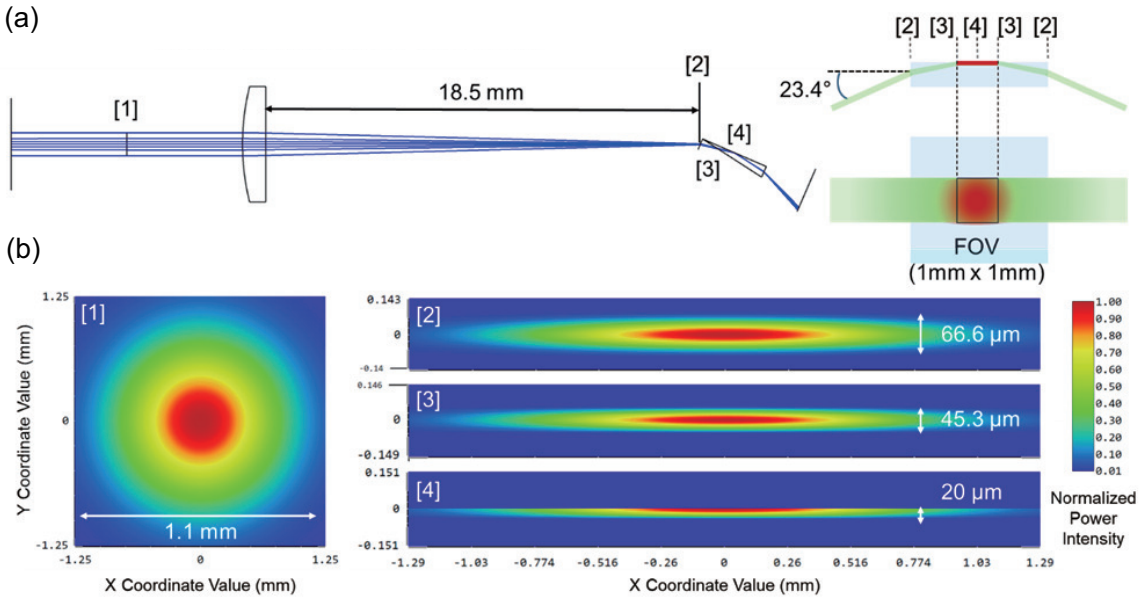


Figure 6.3: Design and simulation of the side-illumination module. (a) Optical layout of the illumination path. A collimated Gaussian beam from the fiber output **[1]** is compressed by a cylindrical lens and directed into the diamond at position **[2]** with an incident angle of 23.4°. The beam propagates along the diamond via TIR, illuminating the target FOV of $1\,\mathrm{mm} \times 1\,\mathrm{mm}$. (b) Simulated normalized power intensity distributions at key propagation positions **[1]–[4]** using the POP method. The beam is progressively compressed along the vertical direction, with a waist reduced from 1.1 mm at the input to 66.6 μm and 45.3 μm near the diamond entry, and further confined to a $\sim$20 μm-thick layer at the sensing surface, enabling efficient and localized excitation of NV centers.

the center of the FOV (position **[4]**), the beam undergoes TIR and illuminates a $\sim$20 μm-thick surface layer.

This configuration provides uniform, high-intensity excitation over a $\sim 1\,\mathrm{mm} \times 1\,\mathrm{mm}$ area. The simulation confirms efficient optical confinement, minimal loss, and enhanced power density at the sensing layer, leading to improved fluorescence contrast and magnetic sensitivity.

6.2.3 Design and Simulation of the Imaging Module

The imaging system was designed and optimized using ray-tracing simulations in Zemax. The NV fluorescence spectrum was approximated using six discrete wavelengths (18.6% at 651 nm, 15.1%

at 664 nm, 27.7% at 682 nm, 14.7% at 699 nm, 12.0% at 720 nm, and 11.9% at 744 nm), based on the eight-wavelength model reported in Ref. [104], with minor spectral components ($< 3\%$) neglected for computational efficiency, as shown in Figure 6.4(a).

The object field was defined as a $\sqrt{2}$ mm diameter, corresponding to the diagonal of a $1\,\mathrm{mm} \times 1\,\mathrm{mm}$ FOV. Three representative field points (center, mid-field, and edge) were selected for optimization. The total system length was constrained to < 25 mm, with a minimum element spacing and component thickness of 0.5 mm to ensure practical manufacturability. A fixed magnification of $7\times$ was chosen to fully utilize the CMOS sensor area.

A triplet lens configuration was adopted to correct primary aberrations. The optimization variables included surface curvatures, inter-element spacing, lens thicknesses, and material selection. Under the constraints of fixed magnification, compact system size, and fabrication limits, Zemax optimization was performed to minimize the wavefront error at the image plane. The final optical design consists of a convex–concave lens, a convex–convex lens, a pinhole, and a thick convex–concave lens, as illustrated in Figure 6.4(b).

The simulated performance of the imaging system is presented in Figure 6.5. The wavefront error remains below 0.4 waves across all fields and wavelengths, and below 0.3 waves for the sampled field points, indicating high optical fidelity.

The modulation transfer function (MTF) was evaluated relative to the sensor Nyquist frequency (89.29 cycles/mm for 5.6 μm pixels), corresponding to 12.8 cycles/mm in object space with a $7\times$ magnification. The system maintains an MTF greater than 0.5 at this frequency across all fields, demonstrating strong contrast preservation.

The Seidel aberration analysis further confirms that residual third-order aberrations, including spherical aberration, coma, astigmatism, and field curvature, as well as chromatic aberrations are well

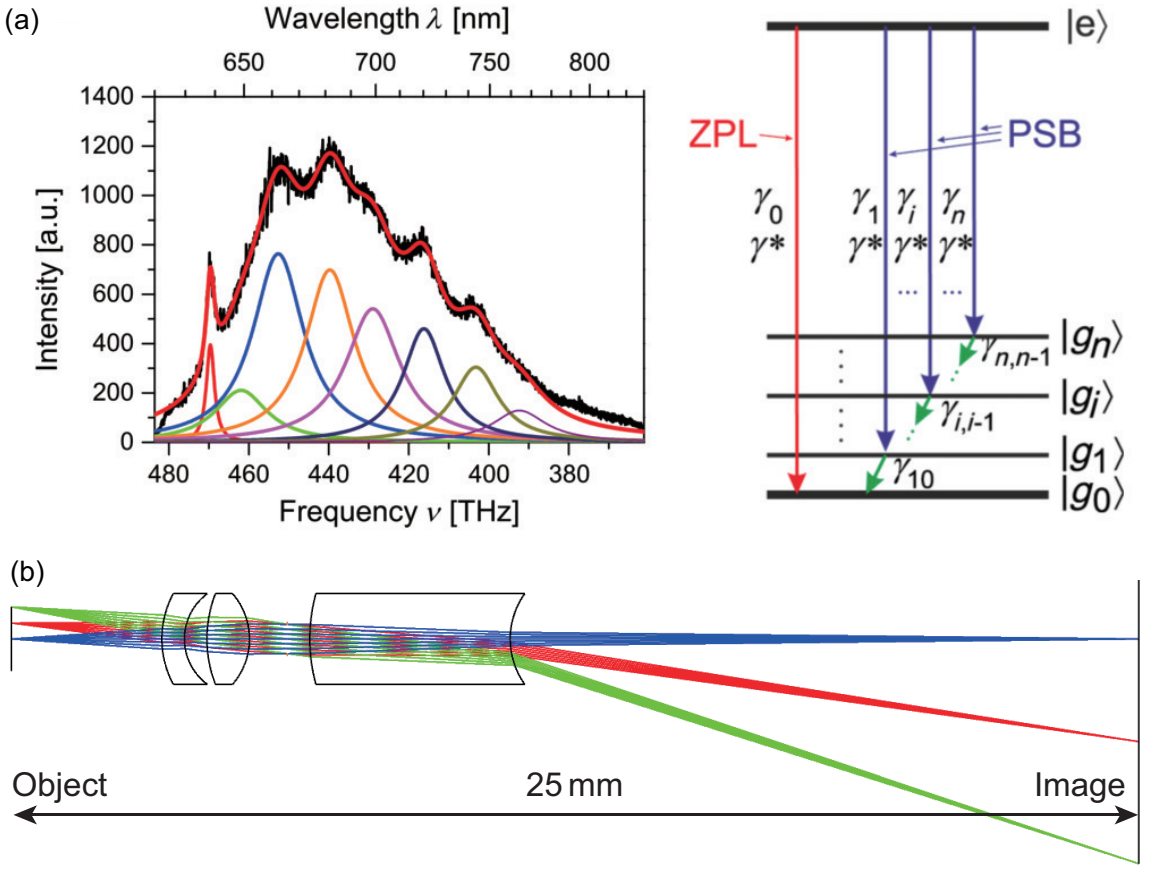


Figure 6.4: (a) Adapt from Ref. [104]. Room-temperature emission spectrum of a single NV center in a nanodiamond, fitted with eight Lorentzian components. The zero-phonon line (ZPL) and phonon sideband (PSB) contributions are illustrated, along with a simplified energy-level model including multiple vibronic ground states $|g_i\rangle$ and an excited state $|e\rangle$. Spectral broadening arises from spontaneous emission, pure dephasing, and phonon-assisted transitions. (b) Optical design of the finite-conjugate imaging system. Ray traces for three representative field positions (center, mid-field, and edge, shown in blue, red, and green, respectively) over a total system length of 25 mm.

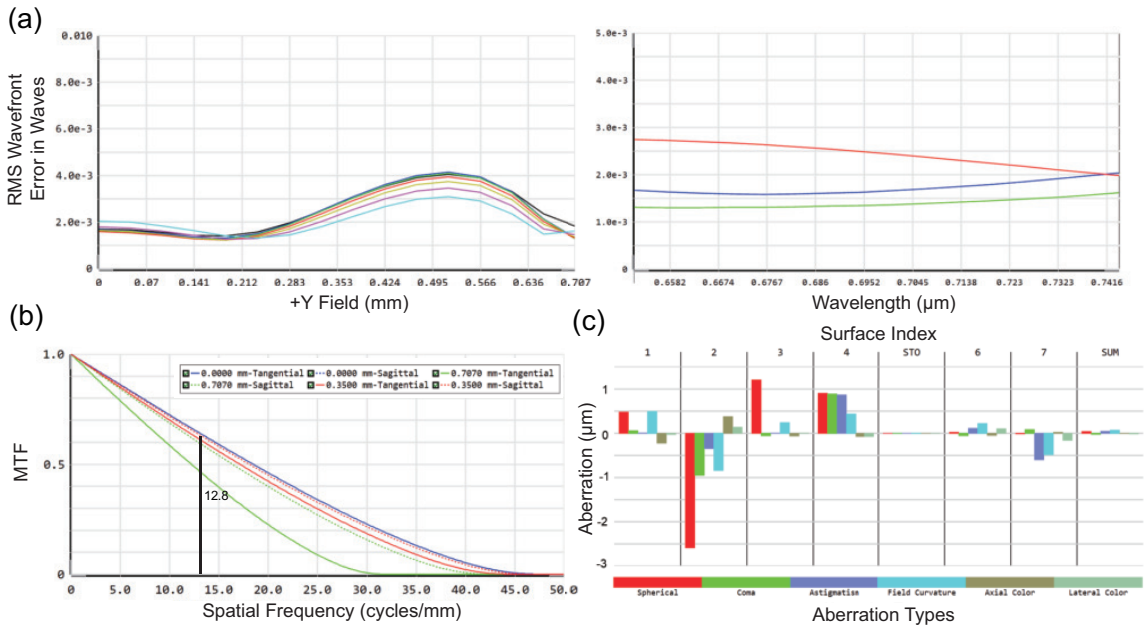


Figure 6.5: Simulated performance of the optimized imaging system. (a) RMS wavefront error as a function of field position (+Y direction) and wavelength, showing consistently low aberrations across the full field of view. (b) Modulation transfer function (MTF) for multiple field points, demonstrating that the system maintains high contrast up to the sensor Nyquist frequency (12.8 cycles/mm in object space). (c) Seidel aberration contributions for each optical surface, indicating that third-order aberrations and chromatic effects are well corrected, with no dominant residual component.

controlled. The total aberration is maintained below 0.1 μm, indicating that the system approaches diffraction-limited performance. These results demonstrate that the imaging module of the compact quantum magnetic camera meets the requirements for high-resolution quantum magnetic microscopy.

Chapter 7: Outlook and Future Experiments

The previous chapters summarize the primary research contributions achieved during my Ph.D. studies. However, six years is a relatively short time for exploring the full potential of this field. In addition to the work presented here, several promising ideas and directions remain unexplored due to time constraints. This chapter outlines potential future research directions motivated by the results of this thesis and ongoing efforts in the field.

The organization of this chapter follows a structure similar to the previous chapters, focusing on prospective advances in DC magnetic sensing, AC sensing, and NV-NMR applications.

7.1 Ramsey DC Sensing Improvement via Decoupling of NV–NV Interactions

As discussed in Section 2.1.1, one effective approach to improving the DC sensitivity of Ramsey magnetometry is to extend the dephasing time T_2^*. Eq. (2.2) summarizes the different contributions to NV spin dephasing. In particular, the electronic spin-bath contribution can be decomposed as

$$\frac{1}{T_2^*\{\text{electronic spin bath}\}} \approx \frac{1}{T_2^*\{\text{P1}\}} + \frac{1}{T_2^*\{\text{NV}^-\}} + \frac{1}{T_2^*\{\text{others}\}}, \tag{7.1}$$

which separates the contributions from P1 centers ($^{15}\text{N}_\text{s}^0$), negatively charged NV centers (NV^-), and other residual electronic spin species.

In Section 2.1.2, we demonstrated using spin-bath driving to decouple dipole–dipole interactions between NV centers and surrounding paramagnetic defects, such as P1 centers and free electrons. While this approach effectively suppresses NV–P1 interactions, residual NV–NV dipolar coupling remains a limiting factor for T_2^*.

Further decoupling of NV–NV interactions could reduce the overall electronic spin-bath noise experienced by each NV center, thereby mitigating dephasing and enabling a longer T_2^*. This would directly translate into enhanced Ramsey sensitivity, providing a promising direction for DC magnetic sensing optimization in the future.

7.1.1 Spin-Bath Driving of Off-Axis NV Centers

Spin-bath driving has been shown to be an effective method for suppressing dephasing induced by surrounding paramagnetic defects, such as P1 centers and other electronic spins. The same idea can, in principle, be extended to the off-axis NV ensembles. In a diamond sample under a bias field aligned to one NV axis, only one quarter of the NV centers are used as the sensing ensemble, while the remaining three quarters form off-axis NV ensembles. These off-axis NV centers constitute an additional electronic spin bath and can therefore contribute to the Ramsey dephasing of the sensing NVs through dipole–dipole interactions. Driving the off-axis NV transitions provides a possible route to average out this interaction and further extend the Ramsey dephasing time T_2^*.

A simple estimate of the potential improvement can be obtained by separating the NV–NV contribution into on-axis and off-axis groups. Following the discussion, the NV-induced dephasing rate may be written as

$$\frac{1}{T_2^*\{\mathrm{NV}^-\}} = \frac{1}{T_2^*\{\mathrm{NV}^-\}_{\parallel}} + \frac{1}{T_2^*\{\mathrm{NV}^-\}_{\nparallel}} = \zeta_{\parallel} A_{\mathrm{NV}^-{}_{\parallel}} [\mathrm{NV}^-]_{\parallel} + \zeta_{\nparallel} A_{\mathrm{NV}^-{}_{\nparallel}} [\mathrm{NV}^-]_{\nparallel}, \tag{7.2}$$

where ζ accounts for imperfect spin initialization, A is the effective dipolar interaction coefficient, and $[\mathrm{NV}^-]$ is the concentration of the corresponding NV subgroup. For the on-axis group, resonant

flip-flop processes enhance the dephasing rate [23], giving

$$A_{\mathrm{NV}^-{}_{\parallel}} = \frac{3}{2} A_{\mathrm{NV}^-{}_{\nparallel}}. \tag{7.3}$$

Assuming the bias field is aligned to one NV orientation, the off-axis NV concentration is approximately three times larger than that of the on-axis group,

$$[\mathrm{NV}^-]_{\nparallel} \approx 3[\mathrm{NV}^-]_{\parallel}. \tag{7.4}$$

Using the same scaling argument as for the P1 spin bath, the interaction coefficient for the off-axis NV bath can be estimated as

$$A_{\mathrm{NV}^-{}_{\nparallel}} \approx \sqrt{\frac{S_{\mathrm{NV}^-}(S_{\mathrm{NV}^-}+1)}{S_{\mathrm{N}_\mathrm{s}^0}(S_{\mathrm{N}_\mathrm{s}^0}+1)}}\, A_{\mathrm{N}_\mathrm{s}^0} \approx \sqrt{\frac{8}{3}}\, A_{\mathrm{N}_\mathrm{s}^0} \approx 165\ \mathrm{ms}^{-1}\,\mathrm{ppm}^{-1}, \tag{7.5}$$

where the last numerical value follows the estimate shown in Ref [17]. For the diamond used in Chapter 2 [39], taking

$$[\mathrm{NV}] \approx 3\ \mathrm{ppm}, \qquad T_2^* \approx 1.55\ \mu\mathrm{s}, \tag{7.6}$$

and assuming complete removal of the off-axis NV contribution, the residual dephasing time can be estimated from

$$\frac{1}{1.55\ \mu\mathrm{s}} = \frac{1}{T_{2,\mathrm{new}}^*} + 0.165 \times 3 \times 0.75\ \mu\mathrm{s}^{-1}, \tag{7.7}$$

which gives

$$T_{2,\mathrm{new}}^* \approx 3.65\ \mu\mathrm{s}. \tag{7.8}$$

This rough estimate suggests that off-axis-NV spin-bath driving could provide a substantial extension of Ramsey coherence time. At the same time, this estimate should be regarded as optimistic, since the effective negatively charged NV concentration may be lower than the total NV concentration, and the initialization factor ζ can be significantly smaller than unity.

To implement this idea experimentally, one can exploit the fact that off-axis NV centers exhibit mixed-spin eigenstates under a bias magnetic field that is not aligned with their symmetry axis. In this regime, the $m_s = \pm 1$ manifolds are mixed, enabling nominally forbidden double-quantum (DQ) transitions between the mixed states. These transitions can be coherently driven by microwave fields and therefore provide a viable control channel for off-axis spin-bath driving. Such transitions have been experimentally observed in previous DEER measurements [105], as shown in Figure 7.1.

Analogous to spin-bath driving of P1 centers, these off-axis NV transitions can be driven using two main protocols. In the CW approach, the bath spins undergo rapid Rabi oscillations; when the Rabi frequency exceeds the dipolar coupling strength, the interaction with the sensing NV ensemble is effectively averaged to zero. Alternatively, in the pulsed driving scheme, a resonant π-pulse is applied to the off-axis NV spins at the midpoint of the Ramsey free-precession interval, refocusing the phase accumulation induced by NV–NV dipolar interactions.

At the current stage, the numerical simulation has focused on the single off-axis NV Hamiltonian and on verifying that the relevant control transitions are experimentally accessible in principle. Starting from the full NV Hamiltonian,

$$\frac{\hat{H}}{\hbar} = D\hat{S}_z^2 + \gamma_e \mathbf{B}\cdot\hat{\mathbf{S}} + \gamma_n \mathbf{B}\cdot\hat{\mathbf{I}} + \hat{\mathbf{S}}\cdot\mathbf{A}\cdot\hat{\mathbf{I}} + Q\hat{I}_z^2 + \cos(\omega t)\sqrt{2}\,\Omega\hat{S}_x, \tag{7.9}$$

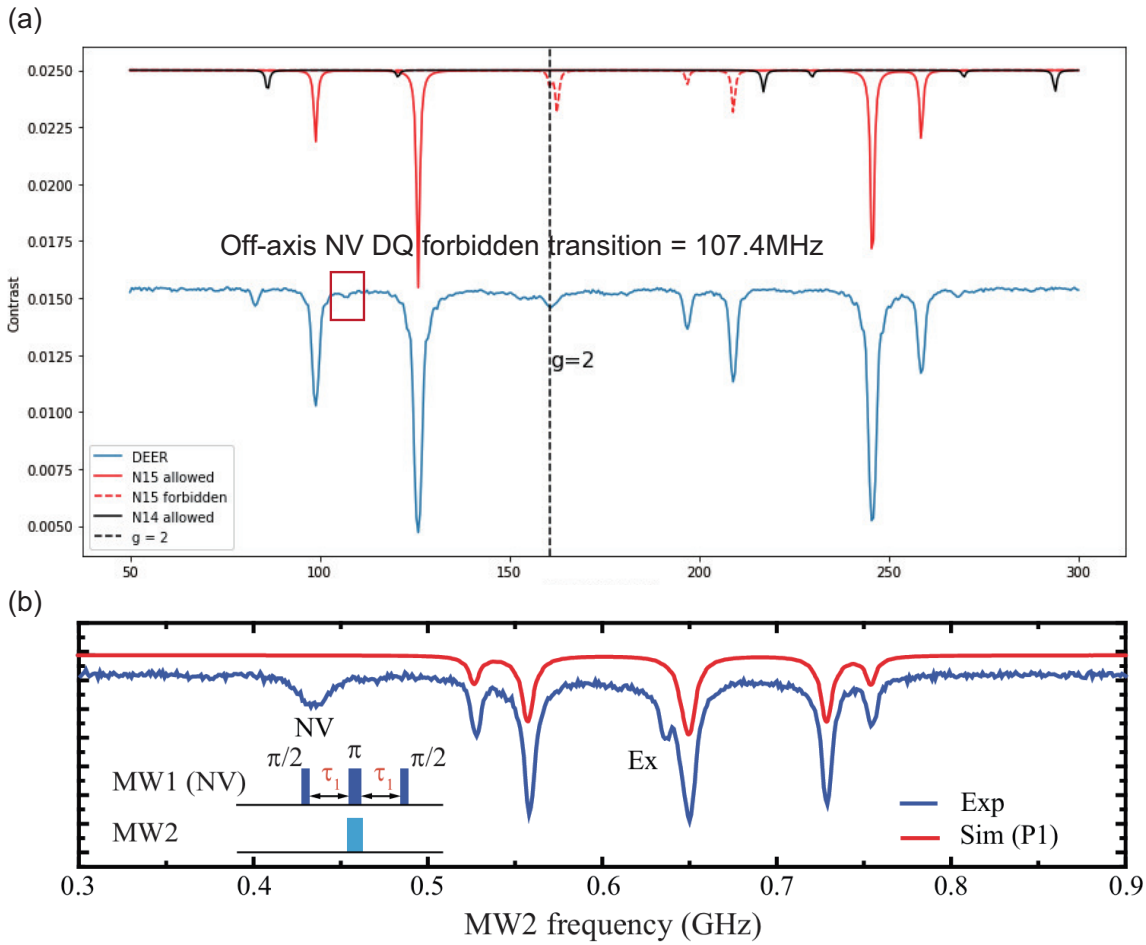


Figure 7.1: Observation of off-axis NV double-quantum (DQ) transitions in DEER experiments. (a) Continuous DEER spectrum similar to Figure 2.1, where a weak off-axis NV transition is observed (red box). (b) DEER measurement reported in Ref. [105], where the off-axis NV transition is more clearly resolved.

the simulation was simplified by retaining only the electronic spin degree of freedom,

$$\frac{\hat{H}}{\hbar} = D\hat{S}_z^2 + \gamma_e \mathbf{B}\cdot\hat{\mathbf{S}} + \cos(\omega t)\sqrt{2}\,\Omega\hat{S}_x. \tag{7.10}$$

As shown in Figure 7.2, using this model, the current simulation successfully reproduced the ESR spectrum of an off-axis NV under a bias field of $B = 200\,\mathrm{G}$ and demonstrated coherent Rabi oscillations between the mixed eigenstates. In other words, the present numerical results verify both the existence and the coherent controllability of the off-axis transition required for spin-bath driving. However, the current simulation does not yet include interactions between the sensing NV and the off-axis NV bath, and therefore does not provide a full prediction of Ramsey dephasing or the corresponding enhancement in T_2^*.

The next step is to extend the model to two interacting NV centers with different crystallographic orientations, as outlined below. In that framework, one NV represents the sensing on-axis spin and the other represents an off-axis bath spin. Neglecting the nuclear degrees of freedom for simplicity, the static Hamiltonian can be written as

$$\frac{\hat{H}}{\hbar} = D_a\hat{S}_{az}^2 + D_b\hat{S}_{bz}^2 + \gamma_e\mathbf{B}\cdot(\hat{\mathbf{S}}_a + \hat{\mathbf{S}}_b) + \frac{\hat{H}_{ab}}{\hbar}, \tag{7.11}$$

where $\hat{H}_{ab}$ is the magnetic dipole–dipole interaction,

$$\frac{\hat{H}_{ab}}{\hbar} = -\frac{\mu_0}{4\pi}\frac{\gamma_e^2\hbar}{r_{ab}^3}\left[\frac{3(\hat{\mathbf{S}}_a\cdot\mathbf{r}_{ab})(\hat{\mathbf{S}}_b\cdot\mathbf{r}_{ab})}{r_{ab}^2} - \hat{\mathbf{S}}_a\cdot\hat{\mathbf{S}}_b\right]. \tag{7.12}$$

Choosing the on-axis NV as the z-axis reference and letting the off-axis NV be rotated by an angle θ,

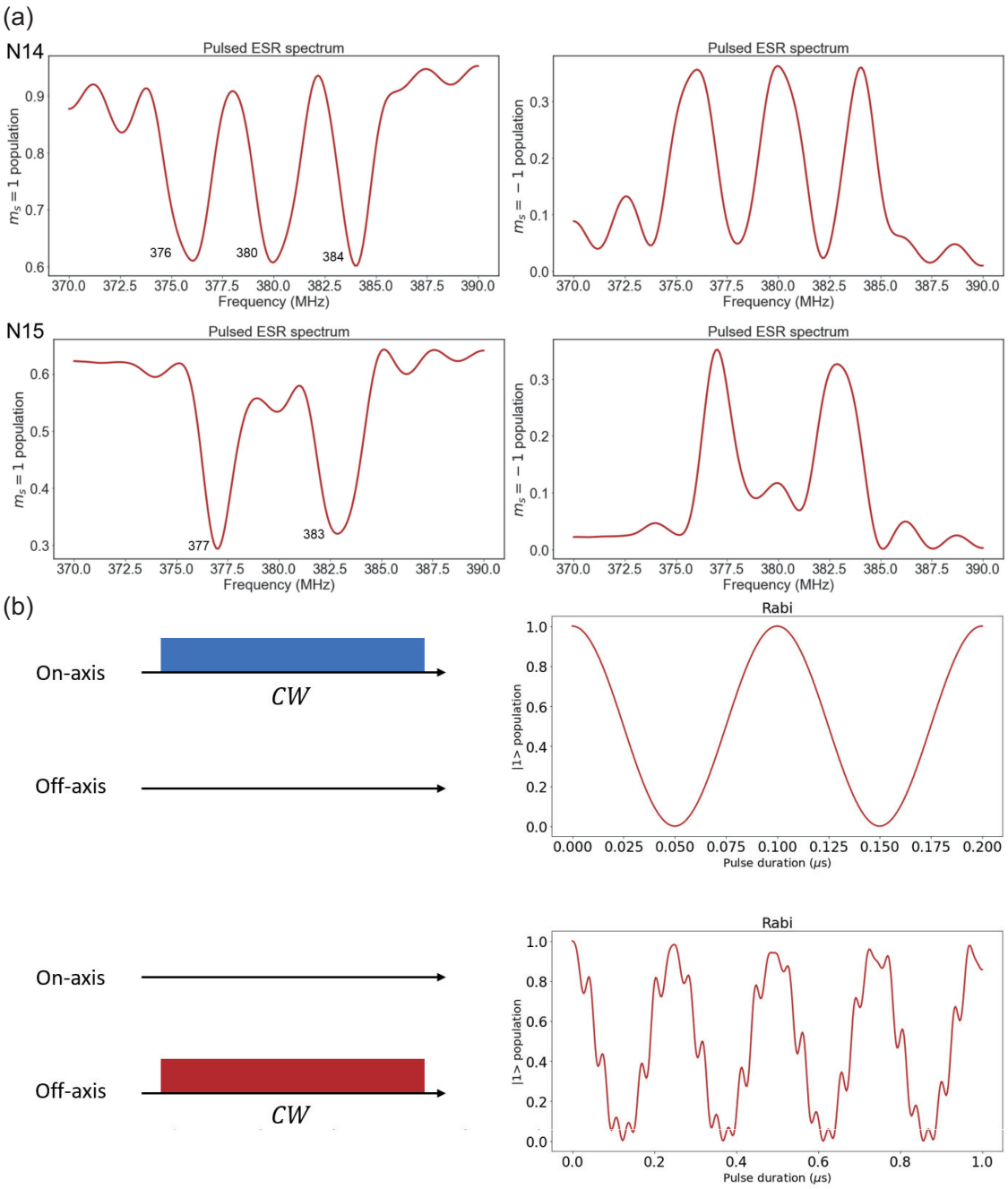


Figure 7.2: Numerical simulation of off-axis NV control at $B = 200\,\mathrm{G}$. (a) Simulated pulsed ESR spectra for off-axis NV centers, showing resolved transitions arising from mixed-spin eigenstates under the applied bias field. (b) Simulated on-axis and off-axis Rabi drive corresponding oscillations

the off-axis spin operators are

$$\hat{S}_{bx} = \cos\theta\,\hat{S}_x + \sin\theta\,\hat{S}_z, \qquad \hat{S}_{by} = \hat{S}_y, \qquad \hat{S}_{bz} = -\sin\theta\,\hat{S}_x + \cos\theta\,\hat{S}_z, \tag{7.13}$$

with relative position vector

$$\mathbf{r}_{ab} = (r\sin\theta,\ 0,\ r\cos\theta). \tag{7.14}$$

Substituting these relations into Eq. 7.12 yields the interaction,

$$\frac{\hat{H}_{ab}}{\hbar} = \frac{\mu_0\gamma_e^2\hbar}{4\pi r^3}\left[3\sin\theta\,\hat{S}_x\otimes\hat{S}_z - \sin\theta\,\hat{S}_z\otimes\hat{S}_x + 2\cos\theta\,\hat{S}_z\otimes\hat{S}_z\right]. \tag{7.15}$$

Including independent microwave drives on the sensing and bath NVs then gives the time-dependent Hamiltonian

$$\begin{aligned}\frac{\hat{H}(t)}{\hbar} &= D(\hat{S}_z^2\otimes\hat{I} + \hat{I}\otimes\hat{S}_z^2) + \gamma_e B\left[\hat{S}_z\otimes\hat{I} + \hat{I}\otimes(-\sin\theta\,\hat{S}_x + \cos\theta\,\hat{S}_z)\right] \\ &\quad + \frac{\mu_0\gamma_e^2\hbar}{4\pi r^3}\left[3\sin\theta\,\hat{S}_x\otimes\hat{S}_z - \sin\theta\,\hat{S}_z\otimes\hat{S}_x + 2\cos\theta\,\hat{S}_z\otimes\hat{S}_z\right] \\ &\quad + \sqrt{2}\left[\cos(\omega_a t)\Omega_a\,\hat{S}_x\otimes\hat{I} + \cos(\omega_b t)\Omega_b\,\hat{I}\otimes\hat{S}_x\right].\end{aligned} \tag{7.16}$$

This two-spin model would allow direct simulation of Ramsey evolution with and without off-axis spin-bath driving. In the absence of bath driving, the sensing NV Ramsey signal should show dephasing and possibly oscillatory features that reflect the coupling strength to the off-axis NV. With resonant CW or pulsed driving applied to the off-axis NV, the same model can be used to test whether the interaction is effectively averaged away and to quantify the resulting extension of the sensing NV coherence time. Such simulations would provide a more rigorous foundation for the T_2^* improvement estimate above and would guide the choice of bias field, microwave frequency, and drive strength for

future experiments.

7.1.2 Magic-Angle Spinning for NV-diamond System

A well-established approach to suppress dipolar interactions in the NMR community is magic-angle spinning [106], in which the sample is physically rotated at a fixed angle β with respect to the static magnetic field $\mathbf{B}_0$. As shown in Figure 7.3(a), the dipole–dipole interaction between spins i and j is described by the secular Hamiltonian

$$H_{dd} = \sum_{i<j} \frac{\mu_0}{4\pi} \frac{\gamma_i \gamma_j \hbar^2}{r_{ij}^3} \left(\mathbf{I}_i \cdot \mathbf{I}_j - 3 I_{iz} I_{jz}\right) \left(3\cos^2\theta_{ij} - 1\right), \tag{7.17}$$

where θ_{ij} is the angle between the internuclear vector $\mathbf{r}_{ij}$ and the quantization axis.

Under sample rotation at angular frequency ω_r, the angle θ_{ij} becomes time-dependent. It can be expressed as

$$\cos\theta_{ij}(t) = \cos\beta\cos\beta'_{ij} + \sin\beta\sin\beta'_{ij}\cos(\omega_r t + \phi_{ij}), \tag{7.18}$$

where β is the rotation angle with respect to $\mathbf{B}_0$, and (β'_{ij}, ϕ_{ij}) define the orientation of $\mathbf{r}_{ij}$ in the rotating frame.

Substituting into the dipolar term $(3\cos^2\theta_{ij} - 1)$ yields a decomposition into time-independent and time-dependent components,

$$3\cos^2\theta_{ij}(t) - 1 = \frac{1}{2}(3\cos^2\beta - 1)(3\cos^2\beta'_{ij} - 1) + O(t), \tag{7.19}$$

where

$$O(t) = \frac{3}{2}\sin 2\beta \sin 2\beta'_{ij}\cos(\omega_r t + \phi_{ij}) + \frac{3}{2}\sin^2\beta \sin^2\beta'_{ij}\cos\big(2(\omega_r t + \phi_{ij})\big). \tag{7.20}$$

are oscillatory terms contain $\cos(\omega_r t)$ and $\cos(2\omega_r t)$ components, which average to zero when ω_r is much larger than the dipolar interaction strength. The remaining time-averaged Hamiltonian is therefore

$$\langle H_{dd}\rangle \propto \frac{1}{2}(3\cos^2\beta - 1). \tag{7.21}$$

By choosing the rotation angle such that

$$3\cos^2\beta - 1 = 0, \tag{7.22}$$

the dipolar interaction is completely averaged out. This condition defines the magic angle

$$\beta = \cos^{-1}\left(\frac{1}{\sqrt{3}}\right) \approx 54.7^\circ. \tag{7.23}$$

At this angle, the secular dipolar interaction vanishes to first order, effectively decoupling spins and significantly extending the dephasing time T_2^*.

However, directly applying magic-angle spinning to NV-diamond systems is impractical. Achieving the required MHz-scale mechanical rotation is technically challenging and incompatible with wide-field imaging modalities such as TIR microscopy. Moreover, physical rotation increases the sensor stand-off distance and limits integration with compact sensing platforms.

To overcome these limitations, an alternative approach is to emulate magic-angle spinning by

applying a rotating magnetic bias field [107], rather than rotating the diamond itself. This approach generates an effective time-dependent quantization axis for the spin system. When the bias field rotates at sufficiently high frequency and is oriented at the magic angle with respect to the NV axis, the dipolar interaction is dynamically averaged, suppressing spin-bath-induced dephasing.

Experimentally, the rotating bias field can be generated using orthogonal Helmholtz coil pairs driven with phase-shifted currents, optionally combined with permanent magnets to provide a static offset field. In this configuration, the sensing NV experiences a time-dependent magnetic field of the form

$$\mathbf{B}(t) = B_0 \left[\sin\beta\cos(\omega t)\,\hat{x} + \sin\beta\sin(\omega t)\,\hat{y} + \cos\beta\,\hat{z}\right], \tag{7.24}$$

which traces a cone at the magic angle.

During the design of the QDM setup, we preserved the flexibility to extend the system toward implementation of a magic-angle rotating bias field, as illustrated in Figure 7.3. In this configuration, the static bias field along the z-axis is generated by a pair of permanent ring magnets, while the transverse magnetic fields along the x and y directions are produced by two orthogonal pairs of Helmholtz coils. By driving the x and y coils with sinusoidal currents that are phase-shifted by 90°, an in-plane rotating magnetic field is generated. When the amplitude of this rotating component satisfies $B_\perp = B_z \tan\beta$, the total magnetic field traces out a cone with opening angle β, thereby realizing a rotating bias field at the magic angle.

Despite its conceptual simplicity, several technical challenges must be addressed to realize this approach in practice. First, generating a sufficiently strong and homogeneous rotating magnetic field at MHz frequencies requires carefully designed, high-bandwidth Helmholtz coils; conventional laboratory coils are typically limited to frequencies below 1 MHz and may not provide adequate field

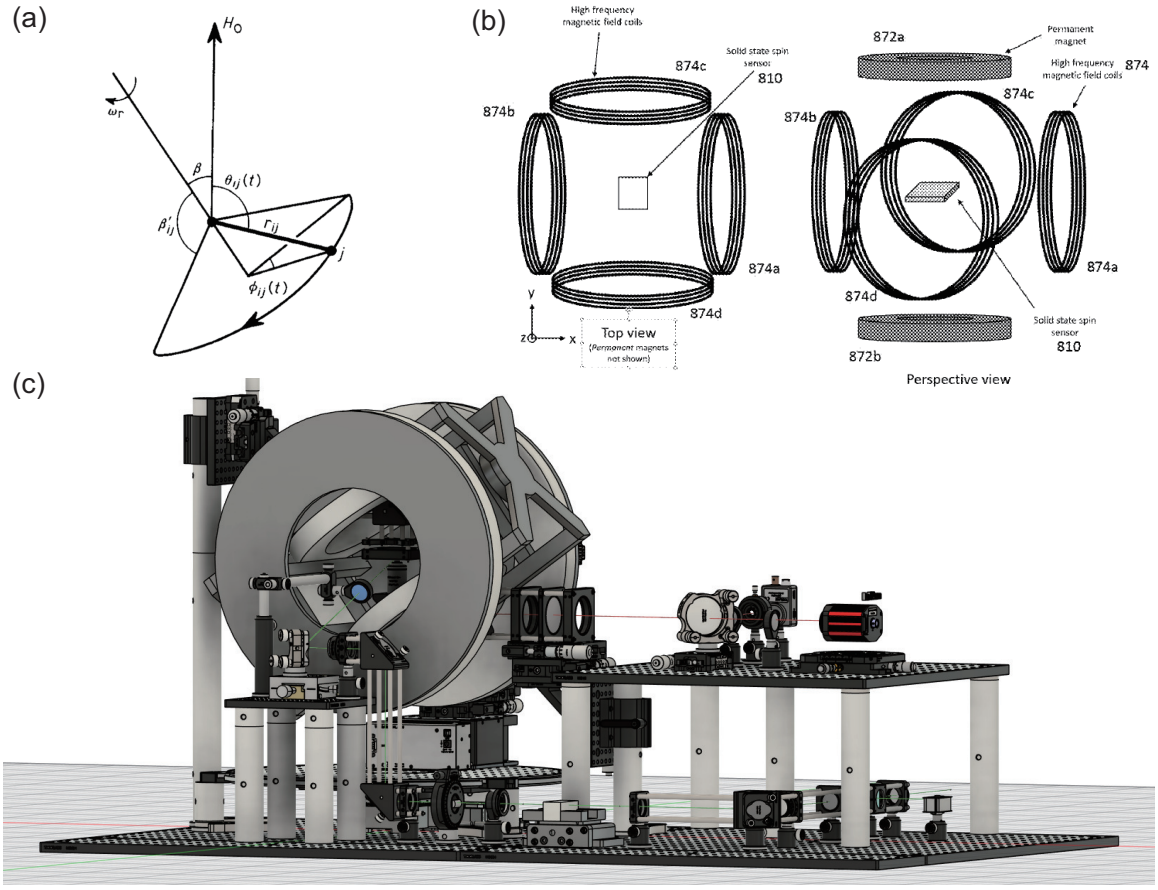


Figure 7.3: (a) Geometry of magic-angle spinning, showing the rotation of the internuclear vector relative to the static magnetic field. (b) Conceptual implementation of a rotating magnetic bias field using orthogonal coil pairs and permanent magnets [107]. (c) Proposed integration of the rotating-bias-field architecture into the QDM platform, enabling magic-angle spin-bath driving without mechanical rotation.

amplitude or spatial uniformity. Second, precise alignment between the rotating field axis and the NV crystallographic axis is essential to ensure effective dipolar averaging and to avoid residual anisotropic interactions. Third, the large drive currents required (e.g., $\sim$15 A to produce $\sim$8 G fields) necessitate high-power RF amplifiers and impedance-matched LC circuits, introducing additional constraints on system stability, thermal management, and integration with optical components.

Taken together, these challenges highlight that the implementation of a magic-angle rotating bias field in NV-based platforms is primarily an engineering problem rather than a fundamental limitation. With continued advances in coil design, high-frequency electronics, and compact integration, this approach offers a promising pathway toward actively controlling the spin bath and extending the effective NV spin dephasing time T_2^*. In particular, the ability to realize spin-bath driving in a wide-field geometry would enable enhanced sensitivity in quantum diamond microscopy without sacrificing spatial resolution, providing a scalable route toward high-performance quantum sensing and imaging.

7.2 Potential Improvements in AC Magnetic Sensing

In Chapter 3, we demonstrated that the QDM is capable of simultaneously imaging the amplitude, frequency, and phase of AC magnetic fields with high sensitivity and spatial resolution. In Chapter 4, we further extended the detection bandwidth by implementing the QFM protocol.

Despite these advances, additional opportunities remain to enhance AC sensing performance. In particular, future improvements may focus on increasing robustness to pulse error and enabling full vector magnetometry. In this section, we discuss several potential approaches toward these goals.

7.2.1 Double-Quantum Dynamical Decoupling Sequences

One of the key limitations in AC magnetic imaging using NV ensembles arises from spatially varying detuning, primarily induced by crystal strain. As shown in Figure 7.4, such detuning leads to pulse errors that distort the AC magnetometry response, introducing amplitude inhomogeneity and phase offsets across the field of view. Rotating-frame simulations of a Hahn spin-echo sequence further indicate that, in the presence of DC detuning, the ideal sinusoidal magnetometry curve becomes distorted, exhibiting non-zero offsets at zero field as well as modified contrast and phase response. These effects become particularly problematic in wide-field imaging, where detuning varies spatially across the diamond.

A straightforward approach to mitigate this issue is to increase the Rabi frequency, thereby making the effective rotation axis less sensitive to detuning. Indeed, simulations indicate that when the ratio of detuning to Rabi frequency is sufficiently small (e.g., $\Delta/\Omega < 0.1$), the magnetometry response approaches the ideal behavior. However, increasing the Rabi frequency is experimentally constrained by microwave delivery efficiency and may introduce additional complications, such as pulse distortions in long dynamical decoupling sequences.

An alternative and more fundamental solution is to employ double quantum (DQ) sensing protocols. As described in Section 2.1.3, in contrast to conventional single quantum (SQ) transitions between $m_s = 0$ and $m_s = \pm 1$, DQ protocols utilize the coherence between the $m_s = +1$ and $m_s = -1$ states. Because these two states experience identical common-mode shifts from strain and other DC perturbations, the DQ transition is intrinsically insensitive to such detuning. This property has been successfully exploited in DC magnetometry, where DQ sequences such as DQ4R suppress strain-induced inhomogeneities [21].

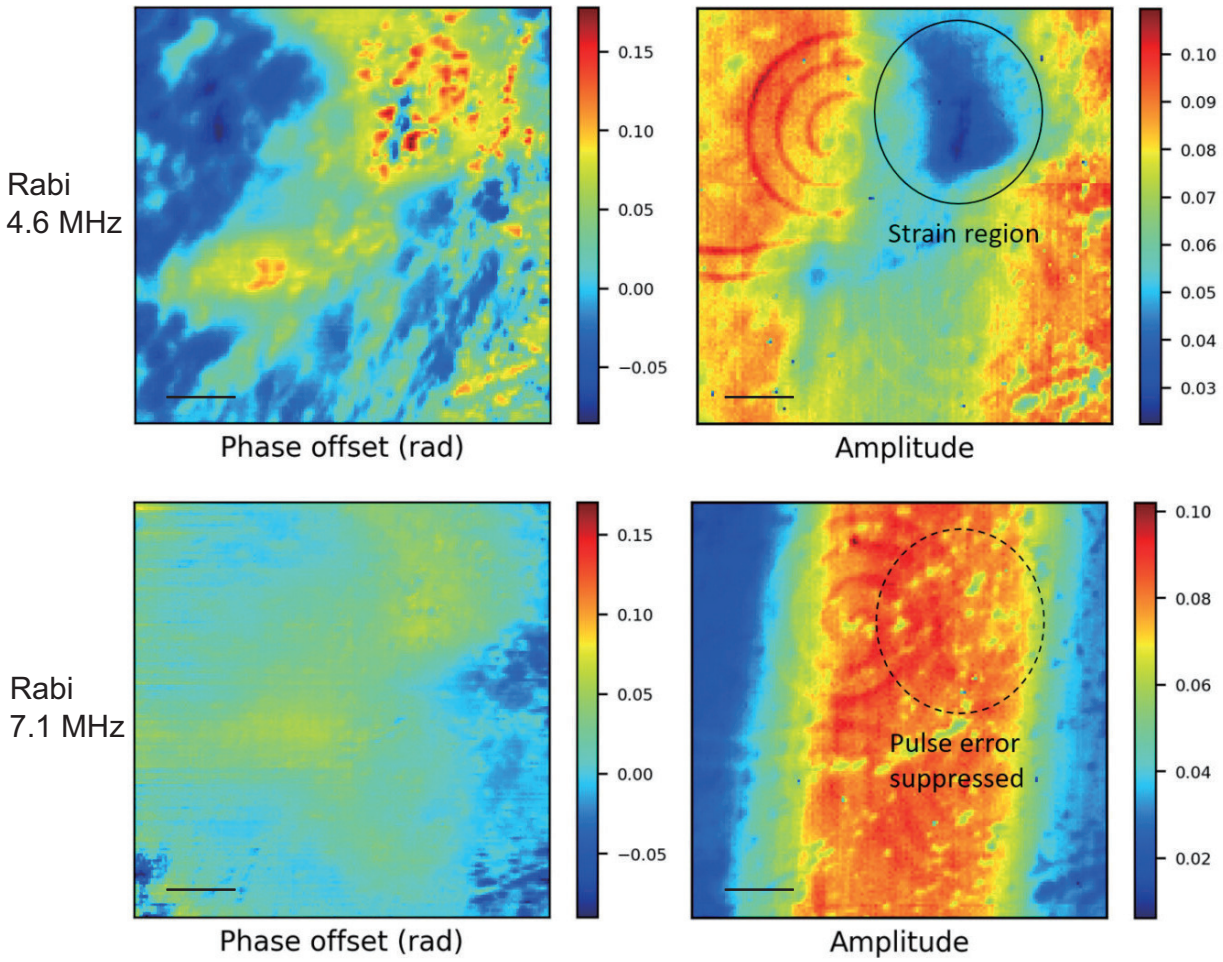


Figure 7.4: Suppression of strain-induced pulse errors in AC magnetic imaging by increasing the Rabi frequency. Top row: phase offset (left) and amplitude (right) images acquired with a Rabi frequency of 4.6 MHz, showing strong spatial inhomogeneity due to strain-induced detuning, highlighted by the circled region. Bottom row: corresponding images acquired with an increased Rabi frequency of 7.1 MHz, demonstrating significantly improved phase uniformity and suppression of amplitude artifacts. These results indicate that stronger microwave driving enhances robustness against detuning-induced pulse errors. The scale bar is 50 μm.

Extending this concept to AC sensing, DQ dynamical decoupling sequences can similarly suppress strain-induced pulse errors in magnetic imaging. While AC magnetometry with photodiode detection is generally insensitive to static detuning due to echo cancellation, the situation differs in wide-field imaging: spatial variations in detuning lead to imperfect pulse rotations and accumulated phase errors. DQ-based AC sensing therefore provides a promising route to eliminate these errors by rejecting common-mode detuning across the ensemble.

Preliminary simulations of DQ spin-echo sequences confirm that the AC magnetometry response retains the desired sinusoidal behavior even in the presence of detuning. Furthermore, modified sequences such as a double-quantum four-pulse echo (DQ4S), as shown in Figure 7.5, analogous to DQ4R in DC sensing, may further suppress residual single-quantum contributions. Although DQ AC sensing has been proposed in earlier work [41], its advantages for mitigating strain-induced errors in wide-field imaging have not been fully explored.

Implementing DQ dynamical decoupling in the QDM platform represents a promising direction for future work. In addition to improving robustness against strain and detuning, DQ protocols may enable more uniform contrast and phase response across the imaging field, thereby enhancing both sensitivity and quantitative accuracy. Systematic experimental validation, including optimization of pulse sequences and direct comparison with SQ-based methods, will be an important next step toward realizing these benefits.

7.2.2 Vector AC Magnetometry

In Chapters 3–5, the AC magnetic sensing protocols are primarily based on dynamical decoupling sequences, which are intrinsically sensitive only to the magnetic field component projected along the

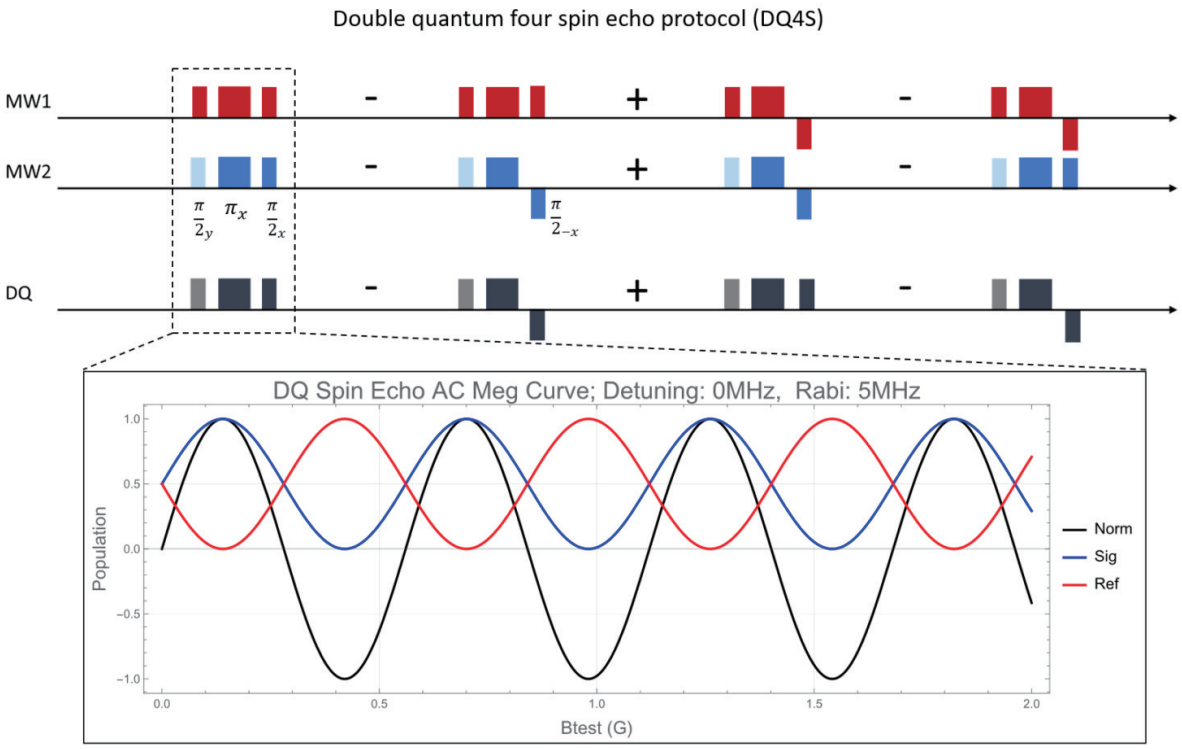


Figure 7.5: Double-quantum four-spin-echo protocol (DQ4S) for AC magnetic sensing. Top: pulse sequence diagram showing two microwave channels (MW1 and MW2) driving the $m_s = \pm 1$ transitions to realize double-quantum control. The sequence combines phase-alternating $\pi/2$ and π pulses to construct an effective double-quantum spin echo. Bottom: simulated AC magnetometry response under zero detuning, demonstrating sinusoidal dependence of the signal (blue) and reference (red) channels, with the normalized contrast (black) retaining high fidelity. The DQ protocol suppresses common-mode detuning effects and preserves the ideal magnetometry response, highlighting its potential for robust wide-field AC magnetic imaging.

NV quantization axis. As a result, the measured signal corresponds to a single vector component of the AC magnetic field, limiting the ability to directly reconstruct the full vector field.

A straightforward approach to realizing vector AC magnetometry is to perform independent measurements along different NV orientations. By combining the projections measured from the four crystallographic NV axes, the full vector magnetic field can, in principle, be reconstructed. However, this approach significantly increases experimental complexity, requiring multiple bias-field configurations or selective addressing of different NV classes. Moreover, off-axis NV experience spin-state mixing under transverse fields, which reduces optical contrast and degrades sensitivity, particularly in wide-field imaging applications.

Beyond dynamical-decoupling-based methods, alternative AC sensing schemes that are directly sensitive to transverse magnetic fields offer a promising pathway toward vector magnetometry. Recent work has demonstrated that transverse AC magnetic fields can drive coherent transitions between NV spin states, enabling direct detection of magnetic field components perpendicular to the NV axis [69, 108]. For example, nanoscale vector AC magnetometry using a single NV center exploits such transverse-field-driven dynamics to reconstruct both the amplitude and direction of the oscillating magnetic field with high precision.

In these approaches, the transverse AC field induces Rabi-like oscillations between spin states, with the transition rate determined by the perpendicular magnetic field amplitude. By analyzing the resulting population dynamics, both the magnitude and orientation of the AC field can be extracted without requiring multiple NV orientations. Similarly, recent developments in multi-frequency and dressed-state sensing protocols further enable simultaneous sensitivity to longitudinal and transverse field components, providing a route toward full vector reconstruction within a single measurement basis.

For wide-field QDM implementations, using such transverse-field-sensitive protocols presents both opportunities and challenges. On one hand, these methods could eliminate the need for multi-orientation measurements and reduce sensitivity degradation associated with off-axis NVs. On the other hand, they typically require precise microwave control, careful calibration of driving fields, and mitigation of additional decoherence channels introduced by transverse coupling.

In the future, integrating transverse-field AC sensing with existing QDM platforms may enable vector magnetic imaging with improved robustness and reduced experimental overhead. Combining these methods with advanced protocols such as quantum frequency mixing or double-quantum sensing could further enhance sensitivity and bandwidth, ultimately enabling comprehensive vector-resolved imaging of complex AC magnetic phenomena.

7.3 Future Directions in QDM-NMR Experiments

In Chapter 5, we demonstrated the current capabilities of our QDM platform for real-space, wide-field NMR imaging, enabling simultaneous spatial and spectral mapping with micrometer-scale resolution. Moving forward, an important direction is to extend these techniques to more complex systems, such as hydrogels and 2D biological platforms, where spatially resolved chemical information is critical. Beyond application-driven studies, emerging NV-NMR methods provide new opportunities to further expand the capabilities of QDM-based imaging.

7.3.1 Diffusion NMR Imaging

One promising direction is the realization of spatially resolved diffusion imaging. While the T_2-weighted imaging demonstrated in Chapter 5 already provides indirect sensitivity to molecular

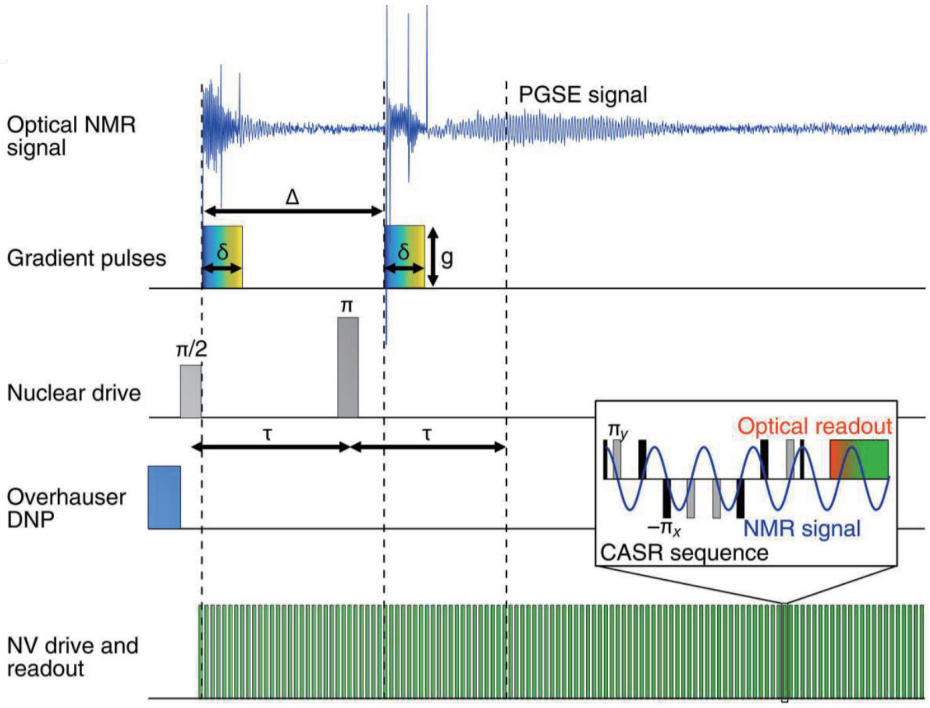


Figure 7.6: [85] Pulse-gradient spin-echo (PGSE) sequence adapted for NV-based NMR detection. Gradient pulses of duration δ and separation Δ encode molecular diffusion into the accumulated phase of nuclear spins. The resulting NMR signal is detected using the CASR protocol with continuous NV optical readout. This approach enables direct measurement of diffusion coefficients. Extending this sequence to wide-field QDM detection would allow spatially resolved diffusion imaging, providing two-dimensional maps of transport dynamics in heterogeneous samples.

diffusion, recent work has shown that NV-NMR can be used to directly measure diffusion coefficients through controlled encoding of molecular motion. In this approach, the diffusion process modulates the accumulated phase of nuclear spins, enabling quantitative extraction of diffusion constants [85].

However, current demonstrations are limited to single-point measurements. By leveraging the intrinsic wide-field capability of the QDM, these diffusion-sensitive protocols can be naturally extended to two-dimensional imaging. This would enable direct acquisition of spatially resolved diffusion maps in a single measurement, providing a powerful tool for studying transport phenomena in heterogeneous systems such as hydrogels, microfluidic environments, and biological tissues.

Such capability would represent a significant advance over conventional NV-NMR, enabling

real-time visualization of diffusion processes with micrometer-scale spatial resolution. Furthermore, combining diffusion imaging with spectral information could allow simultaneous mapping of chemical composition and transport dynamics.

7.3.2 Nutation-Based Longitudinal Sensing for High-Field NMR Imaging

Another important frontier is high-field (tesla-scale) NV-NMR, which provides much greater nuclear spin polarization and larger spectral feature separation arising from chemical shifts. Conventional NV-NMR detection relies on dynamical decoupling sequences that are resonant with the nuclear Larmor frequency. At high magnetic fields, nuclear Larmor frequencies can reach tens of MHz, exceeding the practical bandwidth of dynamical decoupling sequences and requiring extremely fast and high-power microwave control.

One approach to overcome this limitation is the QFM protocol, which down-converts high-frequency signals into the detectable bandwidth of NV sensors. However, as discussed in Chapter 4, QFM protocols typically suffer from reduced sensitivity due to the multi-step frequency conversion process.

Recent advances propose an alternative strategy based on nutation-driven longitudinal sensing, such as the AERIS and DRACAERIS protocols [109, 110]. Instead of detecting transverse nuclear magnetization oscillating at the Larmor frequency, these methods probe the longitudinal magnetization modulated at the nuclear Rabi frequency.

Since the nuclear Rabi frequency can be tuned to the optimal detection range of the NV sensor (typically in the kHz–MHz regime), this approach significantly relaxes the requirements on microwave pulse timing and bandwidth. In particular, the DRACAERIS protocol introduces a rewinding scheme

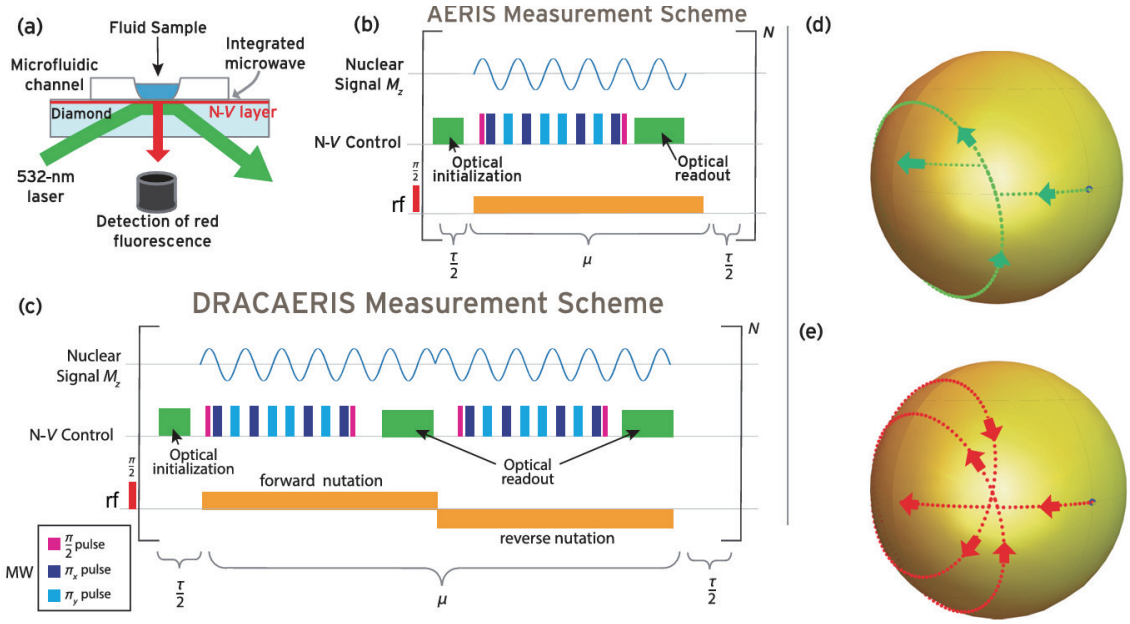


Figure 7.7: (a) Schematic of an NV ensemble NMR apparatus. A fluid sample is placed in close proximity to the NV layer in diamond and detected through optically read out NV fluorescence under microwave and RF control. (b) AERIS pulse sequence [109], where nuclear spin precession is measured through synchronized NV dynamical decoupling during RF nutation. (c) DRACAERIS pulse sequence [110], which introduces an additional reverse-nutation step to suppress common-mode noise and improve measurement robustness. (d,e) Bloch-sphere representation of nuclear spin evolution during AERIS and DRACAERIS protocols. DRACAERIS compensates leading-order off-resonance effects and restores the magnetization to its initial state more accurately.

that suppresses pulse errors and improves spectral fidelity by compensating for off-resonant driving effects.

Integrating nutation-based sensing protocols into the QDM platform could enable wide-field, high-field NMR imaging with both high spectral resolution and relaxed hardware constraints. Combined with the inherent spatial multiplexing of QDM, this approach has the potential to realize real-time, spatially resolved chemical imaging in complex systems.

Appendix A: Lock-in Camera Demodulated CASR

As introduced in Sec. 3.1.2, Coherent Averaged Synchronized Readout (CASR) [38] is a detection protocol for measuring narrowband magnetic signals with ultrahigh spectral resolution, particularly for NMR spectroscopy. CASR provides the spectral selectivity required for NMR by coherently averaging synchronized NV magnetometry measurements over long interrogation times.

CASR has been implemented in both photodiode detection and lock-in camera wide-field imaging modalities throughout Chapters 3–5. Conceptually, CASR can be understood as a low-sampling-rate aliasing process, as illustrated in Fig. A.1. For photodiode-based measurements, the mathematical description follows the treatment presented in Sec. 3.1.2.

However, as described in Sec. 3.1.3, when implementing CASR imaging using the heliCam lock-in camera, the camera performs an internal demodulation process in which multiple CASR readouts are averaged within each internal frame, as shown in Fig. A.1. Therefore, instead of treating the effective CASR sampling rate as simply equal to the camera internal frame rate, the demodulated CASR process should be considered as a double-alias process.

A.1 Double-alias Process

Consider a continuous sinusoidal signal

$$S(t) = A\sin(2\pi f_0 t + \phi), \tag{A.1}$$

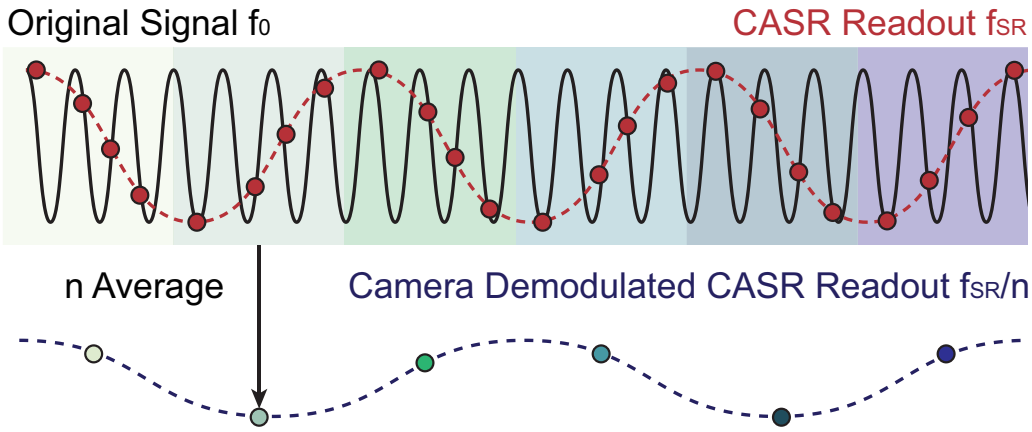


Figure A.1: Conceptual illustration of camera-demodulated CASR readout. A narrowband magnetic signal with frequency f_0 (black curve) is sampled by the CASR protocol at the repetition rate f_{SR}, producing an aliased low-frequency signal (red dashed curve with red sampling points). In the heliCam lock-in camera implementation, the camera internally averages n consecutive CASR readouts within each internal frame (top shaded regions). This internal demodulation produces a reduced set of effective samples (bottom), corresponding to an additional averaging step that lowers the effective sampling rate from f_{SR} to f_{SR}/n. Consequently, the camera-demodulated CASR signal can be interpreted as a two-stage process: first aliasing at the CASR sampling rate, followed by averaging-induced down-sampling that produces a second effective aliasing process.

where A is the amplitude, f_0 is the signal frequency, and ϕ is the phase. The signal is sampled at a sampling rate f_{SR},

$$t_k = kT_s, \qquad T_s = \frac{1}{f_{SR}}. \tag{A.2}$$

The discrete-time sequence becomes

$$S[k] = S(kT_s) = A\sin(2\pi f_0 kT_s + \phi). \tag{A.3}$$

Define the normalized discrete-time frequency

$$\Omega_0 = 2\pi\frac{f_0}{f_{SR}}. \tag{A.4}$$

Because discrete-time frequency is periodic with period 2π, the observed frequency becomes the aliased frequency

$$f_a = f_0 - m f_{SR}, \tag{A.5}$$

where m is the integer that places f_a inside the Nyquist band

$$-\frac{f_{SR}}{2} \leq f_a \leq \frac{f_{SR}}{2}. \tag{A.6}$$

Thus the sampled signal can be written as

$$S[k] = A \sin\left(2\pi \frac{f_a}{f_{SR}} k + \phi\right). \tag{A.7}$$

In the camera demodulation process, n consecutive samples are averaged,

$$S'[m] = \frac{1}{n} \sum_{r=0}^{n-1} S[mn + r]. \tag{A.8}$$

Substituting the sinusoidal signal,

$$S'[m] = \frac{A}{n} \sum_{r=0}^{n-1} \sin\left(2\pi \frac{f_a}{f_{SR}} (mn + r) + \phi\right). \tag{A.9}$$

Using the identity for a finite sinusoidal sum,

$$\sum_{r=0}^{n-1} \sin(\alpha + r\beta) = \frac{\sin\left(\frac{n\beta}{2}\right)}{\sin\left(\frac{\beta}{2}\right)} \sin\left(\alpha + \frac{(n-1)\beta}{2}\right), \tag{A.10}$$

we obtain

$$S'[m] = A\frac{\sin\left(\frac{n\Omega}{2}\right)}{n\sin\left(\frac{\Omega}{2}\right)}\sin\left(\Omega nm + \phi + \frac{(n-1)\Omega}{2}\right), \tag{A.11}$$

where

$$\Omega = 2\pi\frac{f_a}{f_{SR}}. \tag{A.12}$$

The averaging operation introduces an amplitude scaling factor

$$H(\Omega) = \frac{\sin\left(\frac{n\Omega}{2}\right)}{n\sin\left(\frac{\Omega}{2}\right)}, \tag{A.13}$$

which corresponds to the frequency response of a moving-average filter. This filter suppresses high-frequency components relative to the sampling rate. After averaging, the signal is effectively sampled once per block, giving an effective sampling rate

$$f_{\text{eff}} = \frac{f_{SR}}{n}. \tag{A.14}$$

The final signal can therefore be written as

$$S'[m] = AH(\Omega)\sin\left(2\pi\frac{f_a}{f_{\text{eff}}}m + \phi'\right), \tag{A.15}$$

where

$$\phi' = \phi + \frac{(n-1)\Omega}{2}. \tag{A.16}$$

A.2 Optimization of the Modulated-CASR Performance

After sampling and block averaging over n points, the signal amplitude is scaled by the moving-average response

$$A_{\text{eff}} = A \left| \frac{\sin\left(\frac{n\Omega}{2}\right)}{n \sin\left(\frac{\Omega}{2}\right)} \right|, \tag{A.17}$$

where $\Omega = 2\pi \frac{f_a}{f_{SR}}$is the discrete-time angular frequency, f_a is the aliased frequency, and f_{SR} is the sampling rate.

The extrema of the amplitude of $H(\Omega)$ occur when

$$\frac{dH(\Omega)}{d\Omega} = 0. \tag{A.18}$$

Define $u = \frac{\Omega}{2}$, taking the derivative and setting it to zero gives

$$\frac{d}{du}\left(\frac{\sin(nu)}{\sin u}\right) = \frac{n\cos(nu)\sin u - \sin(nu)\cos u}{\sin^2 u} = 0. \tag{A.19}$$

Thus the extrema satisfy

$$n\cos(nu)\sin u = \sin(nu)\cos u. \tag{A.20}$$

Dividing by $\cos(nu)\cos u$ yields

$$\tan(nu) = n\tan u. \tag{A.21}$$

Substituting $u = \pi f_a / f_{SR}$, the extrema condition becomes

$$\tan\left(n\pi \frac{f_a}{f_{SR}}\right) = n\tan\left(\pi \frac{f_a}{f_{SR}}\right). \tag{A.22}$$

The largest amplitude occurs when $f_a \to 0$. In this limit,

$$\lim_{\Omega \to 0} \frac{\sin\left(\frac{n\Omega}{2}\right)}{n \sin\left(\frac{\Omega}{2}\right)} = 1, \tag{A.23}$$

and therefore $A_{\text{eff}} = A$. This occurs when the signal frequency is close to an integer multiple of the sampling rate,

$$f_0 \approx m f_{SR}. \tag{A.24}$$

where m is an integer. This condition corresponds to the synchronization condition proposed in the original CASR paper [38].

Interestingly, this synchronization condition is not strictly required for single-alias CASR when the signal source is coherent. In early experiments, the synchronization constraint arose primarily from experimental hardware limitations. With modern AWGs, photodiode-based CASR measurements do not necessarily require strict synchronization.

However, for heliCam-based CASR imaging, the synchronization condition becomes essential due to the additional averaging performed during camera demodulation. In Chapter 3, the sampling rate was $f_{SR} = 500\,\text{Hz}$, while the signal frequency f_0 was approximately $1\,\text{MHz}$, which naturally satisfied the synchronization condition. Consequently, the system did not suffer significant amplitude degradation from the double-alias process.

In Chapter 5, however, CASR imaging was performed near the $1.69\,\text{MHz}$ NMR Larmor frequency. Under these conditions, the previous camera configuration no longer satisfied the synchronization condition, leading to a significant reduction in signal amplitude. This observation motivated the analysis of the double-alias synchronization condition presented in this appendix.

A.3 Numerical Simulation Results

In our experiments, camera-demodulated CASR is used to image NMR signals near the proton Larmor frequency $f_0 \approx 1.69\,\mathrm{MHz}$. To understand the double-alias behavior described in the previous section, we perform a numerical simulation of the demodulated CASR process.

First, we generate a continuous sinusoidal signal with frequency f_0 and a total duration of 1 s. The signal is sampled at the CASR repetition rate f_{SR}. This sampling step produces the first aliasing process. To simulate the heliCam internal demodulation process, we then perform block averaging on the sampled signal. The minimum demodulation cycle number of our heliCam configuration is four, corresponding to averaging $4 \times 4 = 16$ consecutive CASR readouts. This averaging step models the camera's internal frame demodulation and produces the final demodulated signal sequence.

We then compute the FFT of the resulting time-domain signal and plot the FFT peak amplitude as a function of the CASR sequence length Seq_t $= 1/f_{\mathrm{SR}}$, as shown in Fig. A.2(a). The simulated FFT amplitude exhibits an overall decay with periodically spaced peaks as the sequence time increases. The spacing between adjacent peaks is approximately $0.6\,\mu\mathrm{s}$, which closely matches $1/f_0$. This behavior is consistent with the synchronization condition $f_0 = m f_{\mathrm{SR}}$ derived in the previous section.

Considering the constraints of our experimental pulse sequence, which includes both the AOM laser pulse time and the XY8 sequence duration, we selected a sequence length of Seq_t $= 24.28\,\mu\mathrm{s}$ for the experiment.

We further simulate the dependence of the demodulated signal amplitude on the signal frequency near f_0. The resulting contrast spectrum is shown in Fig. A.2(b). The main peak has a full width at half maximum (FWHM) of approximately $3\,\mathrm{kHz}$. This result indicates that during CASR imaging experiments, the signal frequency must remain within roughly $3\,\mathrm{kHz}$ of the optimized frequency f_0.

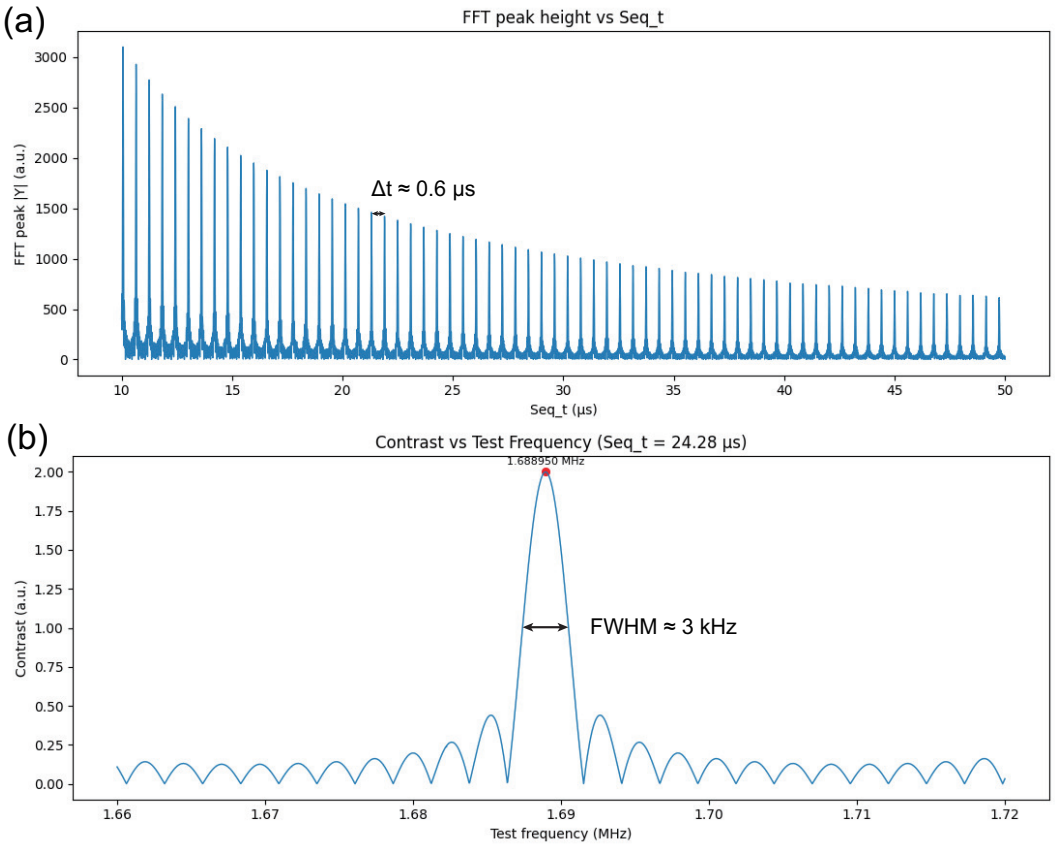


Figure A.2: Numerical simulation of the double-alias behavior in camera-demodulated CASR. (a) Simulated FFT peak amplitude as a function of CASR sequence length $\mathrm{Seq}_t = 1/f_{\mathrm{SR}}$. Periodically spaced maxima appear due to the synchronization condition between the signal frequency and the CASR repetition rate. The peak spacing of approximately $0.6\,\mu\mathrm{s}$ corresponds to $1/f_0$ for $f_0 \approx 1.69\,\mathrm{MHz}$. (b) Simulated contrast spectrum near the signal frequency for an optimized sequence length $\mathrm{Seq_t} = 24.28\,\mu\mathrm{s}$. The resonance peak has a full width at half maximum of approximately $3\,\mathrm{kHz}$, indicating the frequency tolerance of the double-aliased CASR detection scheme.

If the signal frequency drifts beyond this range, the demodulated CASR response becomes strongly suppressed, which significantly reduces the SNR of the reconstructed image or may prevent signal detection entirely.

Appendix B: Bias Magnetic Field Alignment

The bias magnetic field is one of the most critical experimental parameters in ensemble NV experiments. Precise alignment of the bias field with the NV quantization axis is essential: the transverse magnetic field component induces spin-state mixing, while spatial inhomogeneity in the bias field leads to dephasing across the NV ensemble. Therefore, accurate alignment of the bias field is a fundamental and necessary first step in NV-based measurements. In this appendix, we describe practical experimental procedures and techniques used to determine the NV orientation and optimize the bias field alignment.

B.1 Determination of NV Orientation

In the absence of bias-field alignment, the ODMR spectrum of an NV ensemble exhibits eight resonance peaks, corresponding to the Zeeman splitting of the four NV orientations (neglecting hyperfine interactions), as shown in Figure B.1(a).

When working with an NV ensemble of unknown crystal orientation, the first step is to determine the orientation of the diamond lattice. This provides an approximate direction of the NV axes and serves as a starting point for subsequent alignment. Typical NV-diamond samples can generally be classified into two categories: corner-cut diamonds and side-cut diamonds.

As illustrated in Figure B.1(b), for corner-cut diamonds, the NV axes point toward the crystal corners, and the sample typically has six $\langle 100 \rangle$ surfaces. In contrast, side-cut diamonds have NV axes oriented toward the crystal sides, with four $\langle 110 \rangle$ surfaces and top/bottom $\langle 100 \rangle$ surfaces. Diamonds

cut along the $\langle 111 \rangle$ direction are also suitable for NV experiments, as one NV axis is perpendicular to the surface; these samples typically have a prism-like geometry and can be easily distinguished from slab-shaped diamonds.

A direct method to determine the crystal orientation is X-ray diffraction (XRD). However, this requires access to bulk characterization equipment and is not always practical for routine experiments.

Instead, we employ a rapid in-situ method based on polarized laser excitation. Optical excitation of NV centers depends on the projection of the electric field perpendicular to the NV axis (i.e., aligned with the NV transition electronic dipole moment). By continuously rotating the laser polarization, the ODMR contrast associated with each NV orientation varies depending on its geometric projection relative to the excitation field, as shown in Figure B.1(c).

To interpret these measurements, we perform numerical simulations of the laser polarization dependence for both corner-cut and side-cut diamonds, as shown in Figure B.1(d). The simulated signal represents the projection of the laser electric field onto each NV electron dipole. For corner-cut diamonds, the four NV orientations form two pairs exhibiting in-phase oscillations with similar amplitudes. In contrast, for side-cut diamonds, one pair exhibits weak in-phase oscillations, while another pair shows strong out-of-phase oscillations.

By comparing the experimental data with these simulations, we identify the diamond used in our experiments as a side-cut diamond. This information allows us to estimate the NV axis direction and provides an effective starting point for bias field alignment.

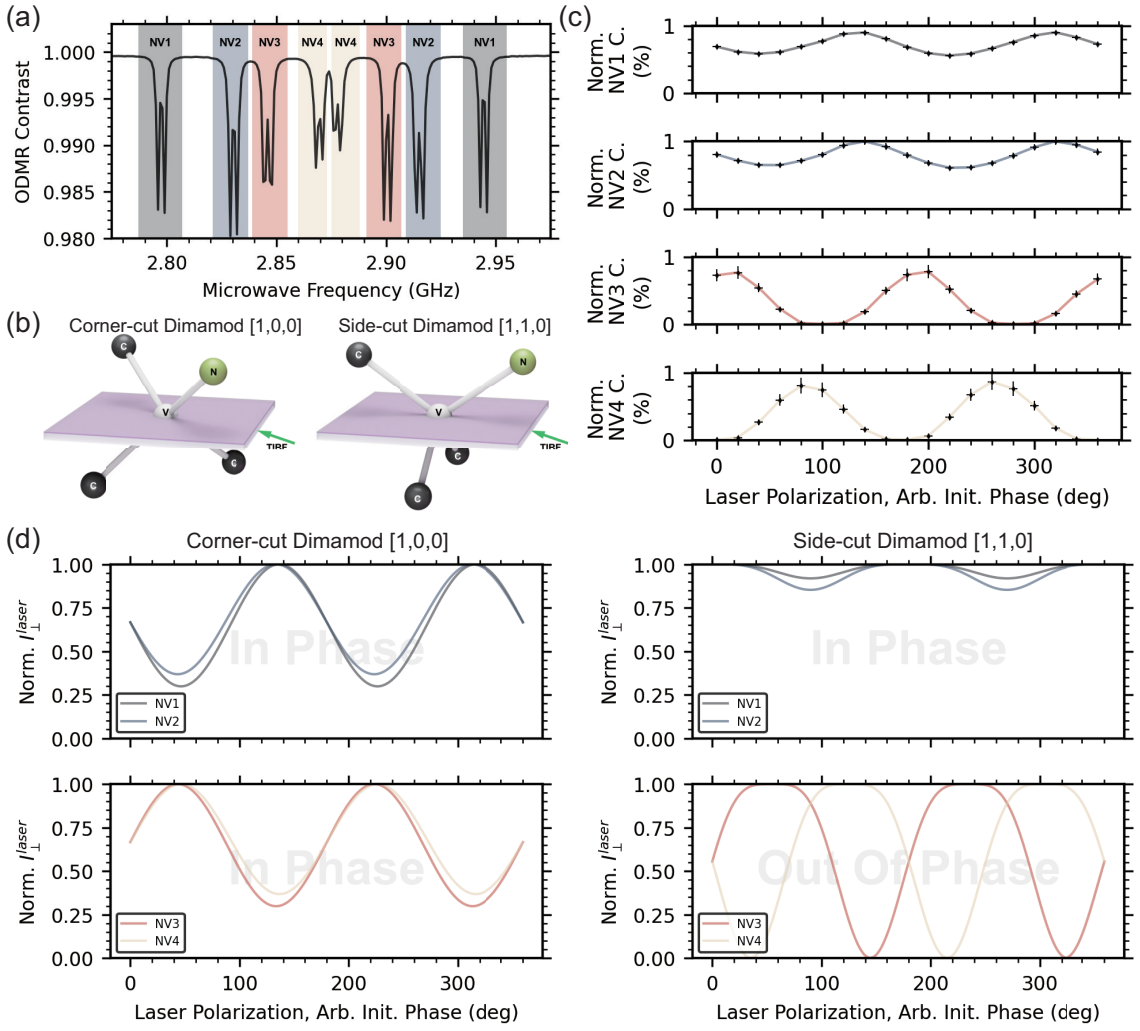


Figure B.1: Characterization of NV orientation and diamond crystal geometry. (a) Representative ODMR spectrum of an NV ensemble without bias-field alignment, showing eight resonance dips corresponding to the Zeeman splitting of the four NV orientations (labeled NV1–NV4), neglecting hyperfine interactions. (b) Schematic illustration of two typical diamond geometries used in experiments. Laser incident into the diamond side with a total internal reflection (TIR) labeled as green arrow. (c) Measured polarization-dependent ODMR contrast for the four NV orientations as the laser polarization is rotated. The contrast modulation reflects the projection of the laser electric field onto each NV dipole, enabling identification of the crystal orientation. (d) Numerical simulation of the polarization dependence for corner-cut (left) and side-cut (right) diamonds. For corner-cut diamonds, NV orientations form two pairs with in-phase oscillations and similar amplitudes. For side-cut diamonds, one pair exhibits weak in-phase oscillations, while another pair shows strong out-of-phase oscillations.

B.2 Alignment and Optimization of the Bias Field

In a typical NV experimental setup, the bias magnetic field alignment involves five degrees of freedom: three translational degrees (Cartesian x, y, z) and two rotational degrees (polar and azimuthal angles, θ and ϕ). Using the estimated NV axis orientation obtained in the previous section, we first perform a coarse alignment by adjusting the rotational angles and positioning the diamond approximately at the center of the magnetic field.

Fine alignment of the field direction is then performed by tuning the angular degrees of freedom. Specifically, we adjust θ and ϕ to merge the six off-axis ODMR resonances into two peaks corresponding to the $m_s = \pm 1$ transitions. Subsequently, we zoom into the hyperfine structure and further refine the alignment to ensure that the hyperfine splittings are symmetric and well-resolved.

After optimizing the field direction, the next step is to minimize magnetic field gradients to achieve a homogeneous field across the field of view. Based on numerical simulations reported in Ref. [20], the optimal homogeneity occurs near the saddle point of the magnetic field distribution along the x, y, and z axes, as illustrated in Figure B.2(a).

Experimentally, we locate this saddle point through a systematic scanning procedure, as shown in Figure B.2(b). We first perform ODMR measurements while sweeping the x and z positions, generating a set of frequency-versus-z curves for different x values. The intersection point of these curves determines the optimal z position, while the flattest curve identifies the optimal x position. In our experiment, this yields $z = 23.15\,\text{mm}$ and $x = 5.2\,\text{mm}$.

With x and z fixed, we then sweep along the y direction to locate the saddle point, obtaining an optimal position of $y = 18.5\,\text{mm}$. At this point, the magnetic field gradient is minimized, resulting in improved coherence and uniformity across the NV ensemble.

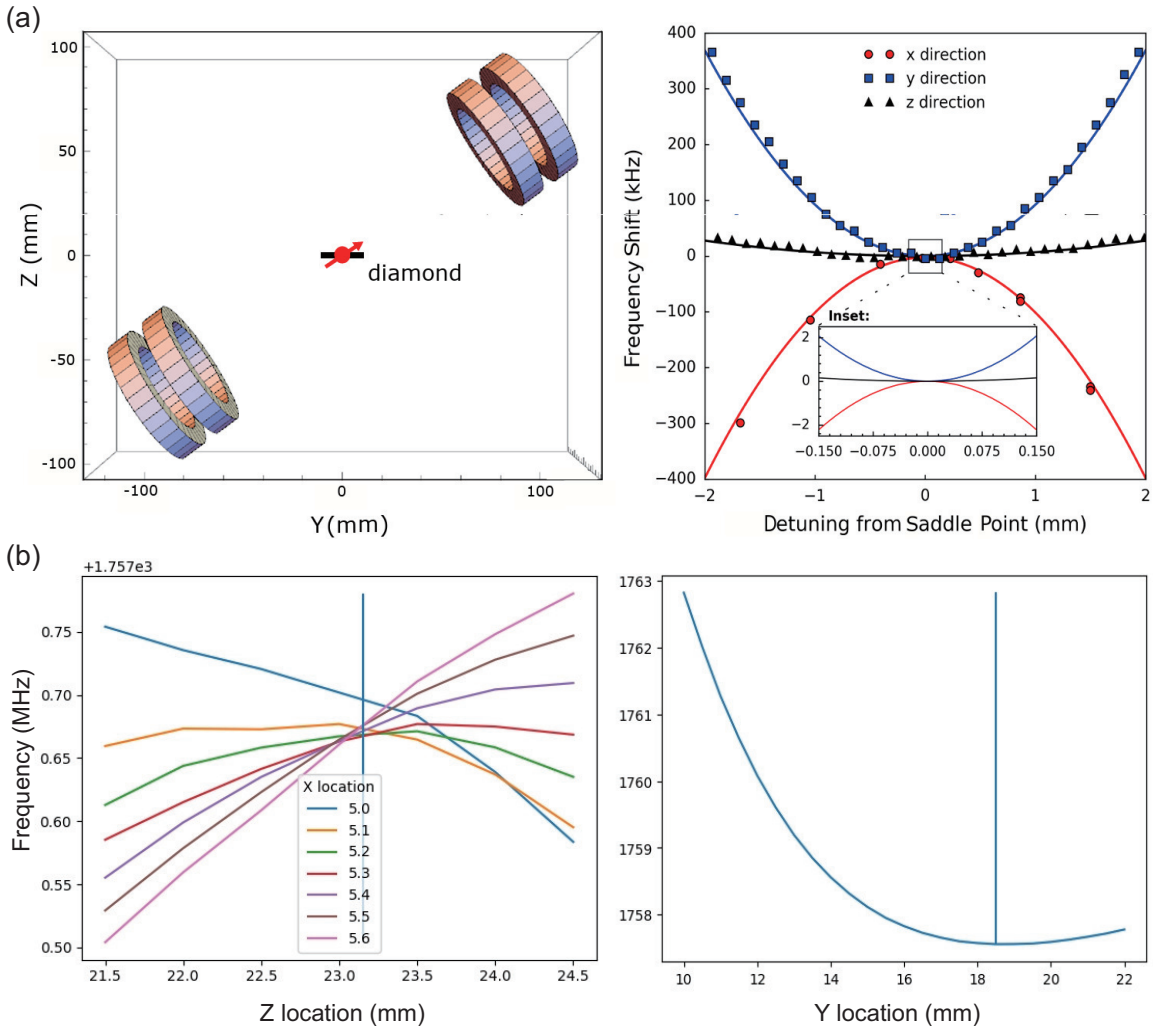


Figure B.2: Bias magnetic field homogeneity optimization via saddle-point alignment. (a) Left: magnet configuration and diamond position. Right: simulated ODMR frequency shift versus spatial detuning along x, y, and z, showing a saddle point where first-order field gradients vanish. (b) Experimental identification of the saddle point. Left: ODMR frequency versus z for different x, where the curve intersection and flattest trace determine the optimal (x, z). Right: frequency versus y with (x, z) fixed, where the minimum locates the saddle point.

Appendix C: MW CPW and Phantom Fabrication

In Section 2.2.1, we described the design and electromagnetic simulation of the Ω-shaped microwave (MW) antenna and the coplanar waveguide (CPW) used for microwave delivery. This MW structure is employed throughout this thesis as a fundamental component of the NV experimental platform, providing strong and spatially homogeneous microwave driving fields for coherent spin manipulation.

In this appendix, we present the detailed fabrication procedures for the MW CPW and the associated phantom structures. The fabrication follows a standard multi-layer photolithography and metal deposition process as shown in Figure C.1. Although different geometries are used throughout this thesis (e.g., terrapin-shaped phantom in Chapter 2 and double-spiral microcoil in Chapter 3), the fabrication methodology remains identical.

C.1 Phantom Layer Fabrication

The phantom layer defines the magnetic-field-generating structure used for calibration and imaging experiments. This layer is typically fabricated using a thin palladium (Pd) film with an adhesion layer.

The fabrication begins with wafer cleaning using sequential solvent rinses (acetone, methanol, and IPA), followed by dehydration baking to remove residual moisture. A positive photoresist (S1813) is then spin-coated onto the wafer, preceded by an HMDS adhesion layer. The coated wafer is soft-baked to stabilize the resist.

Photolithography is performed using a UV mask aligner to define the phantom pattern. The exposure parameters are carefully optimized to balance feature resolution and resist development.

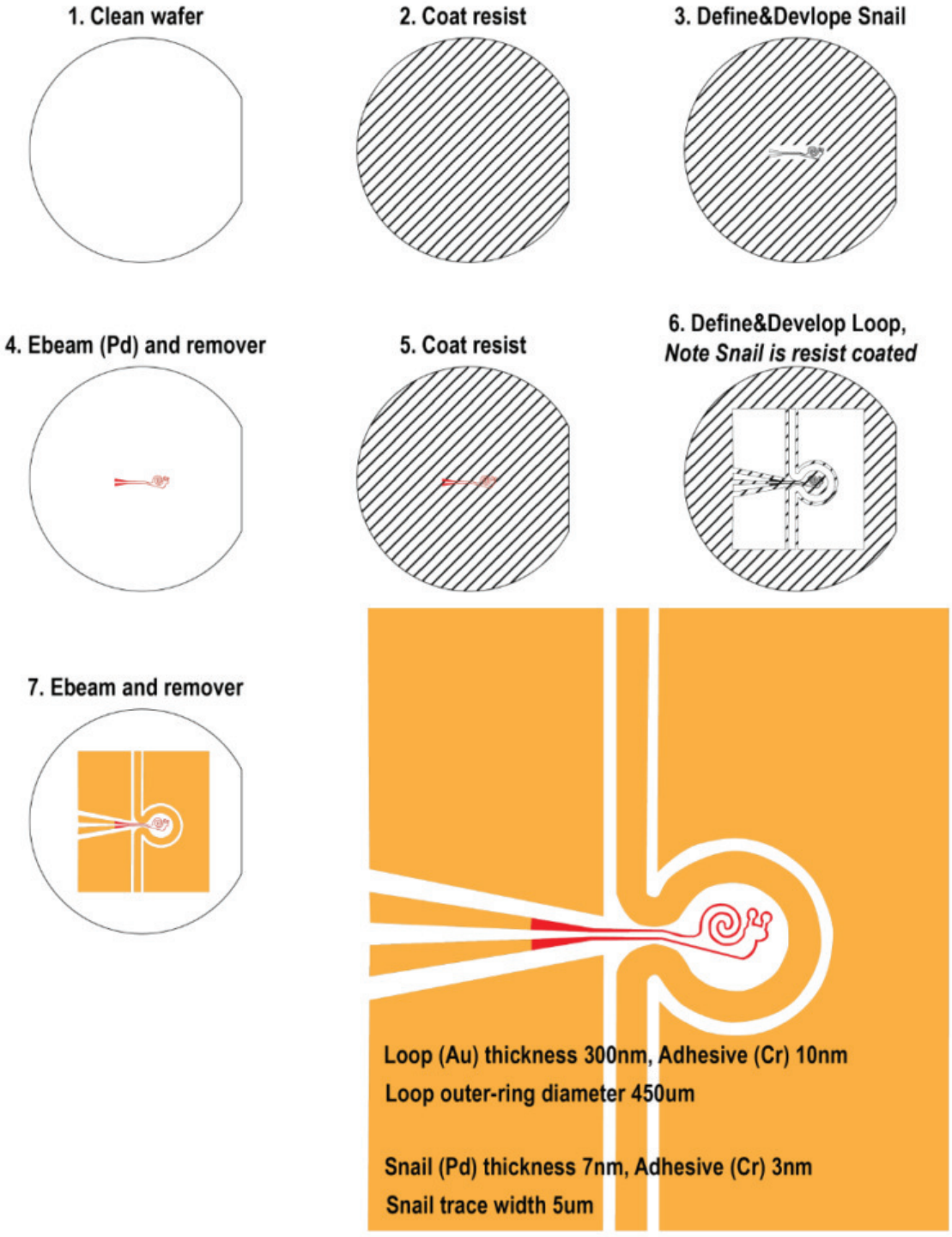


Figure C.1: Schematic illustration of the multi-layer fabrication process for the phantom and Ω loop structures. The process consists of seven main steps. The final device integrates a thin Pd phantom layer (typically $\sim$7 nm with $\sim$3 nm Cr adhesion) and a thicker Au microwave layer (typically $\sim$300 nm with $\sim$10 nm Cr adhesion), enabling simultaneous magnetic field generation and microwave delivery.

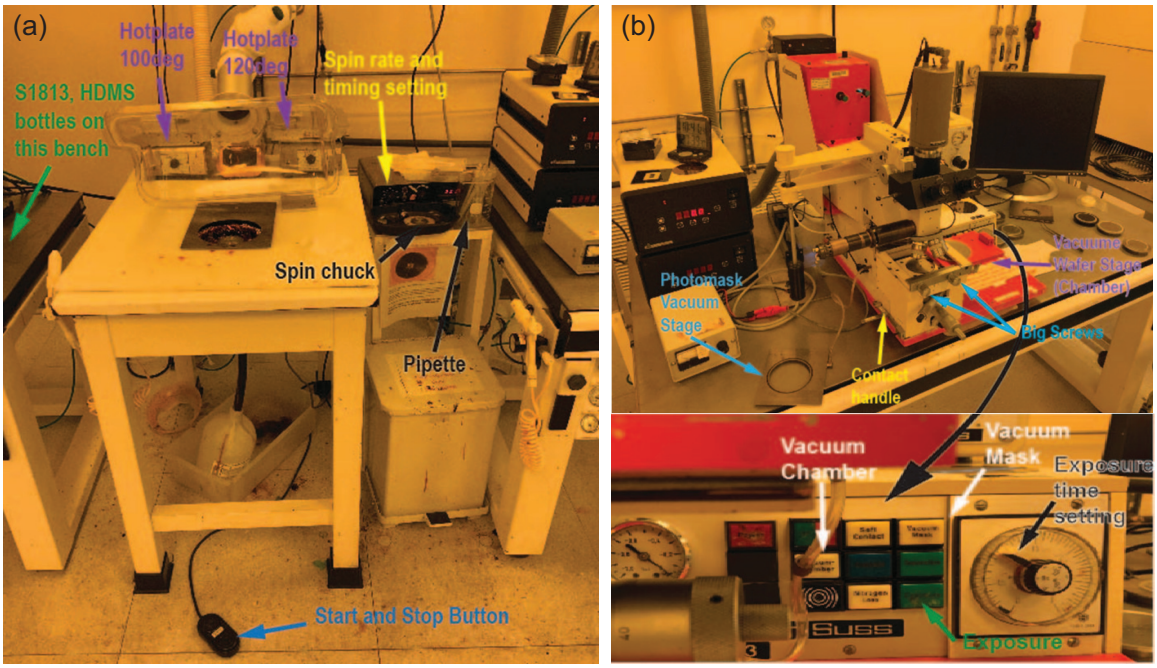


Figure C.2: Photolithography setup used for patterning the phantom layer. (a) Spin-coating station for applying HMDS adhesion layer and S1813 photoresist, showing the spin chuck, pipetting process, and programmable spin timing. (b) UV mask aligner (Süss MicroTec MJB-3) used for pattern transfer, including photomask and wafer vacuum stages, alignment controls, and exposure timing module. These tools enable precise control of resist thickness, feature definition, and alignment accuracy in the multi-layer fabrication process.

After exposure, the wafer is developed using CD26 developer, revealing the patterned resist structure.

Metal deposition is carried out using electron-beam evaporation. A thin chromium (Cr) adhesion layer is first deposited, followed by the Pd layer that forms the phantom structure.

Finally, a lift-off process is performed to remove excess metal and photoresist, leaving only the patterned phantom structure on the substrate.

C.2 Ω Loop Layer Fabrication

The Ω loop layer forms the microwave delivery structure and is fabricated as a second metal layer aligned to the phantom structure. This layer typically consists of a thicker gold (Au) film with a

chromium adhesion layer.

The process begins with a second round of photoresist coating, identical to the phantom layer fabrication. Precise alignment between the previously fabricated phantom structure and the Ω loop pattern is achieved using a mask aligner. In practice, alignment is facilitated by directly imaging both layers within the same field of view.

After alignment, UV exposure and development are performed to define the Ω loop pattern. Metal deposition is then carried out using electron-beam evaporation, with a thicker Cr adhesion layer followed by a gold layer to ensure low-resistance microwave transmission.

Lift-off is subsequently performed to complete the formation of the Ω loop and CPW structure.

C.3 Post-Fabrication Process

After fabrication, the device undergoes several post-processing steps to enable experimental use.

First, the device is connectorized by attaching microwave connectors to the CPW pads. Care must be taken to avoid excessive mechanical stress during connector attachment.

Next, electrical and microwave characterization is performed. The scattering parameters (S_{11} and S_{21}) are measured using a vector network analyzer to evaluate reflection and transmission properties. A low S_{11} indicates efficient impedance matching, while a high and flat S_{21} ensures effective microwave delivery.

Finally, the resistance of the phantom structure is measured using a multimeter to verify fabrication consistency. These post-fabrication characterizations confirm the functionality of the device and ensure reliable performance in subsequent NV-based magnetic imaging experiments.

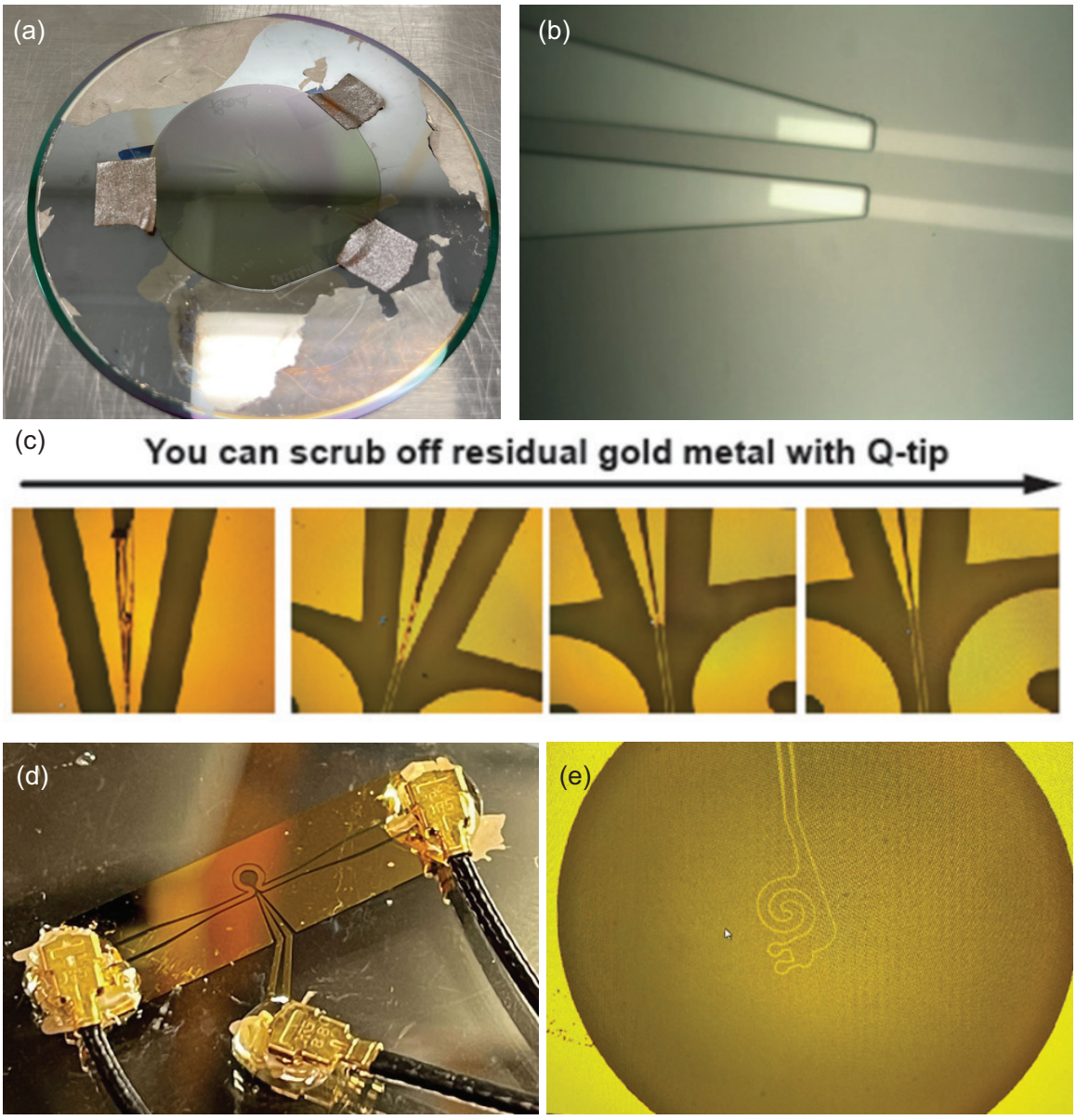


Figure C.3: Fabrication results and post-processing details of the MW CPW and phantom device. (a) Photograph of the fabricated wafer after metal deposition and lift-off, showing the patterned device region at the center. (b) Optical microscope image of the CPW and Ω loop structure, highlighting the tapered microwave traces. (c) Sequential optical images illustrating removal of residual metal after lift-off using a solvent-wetted swab (Q-tip), which improves pattern cleanliness and electrical isolation. (d) Fully connectorized device with microwave connectors attached to the CPW pads for experimental integration. (e) Optical microscope image of the completed phantom structure, showing the spiral (snail) geometry used to generate controlled magnetic field distributions.

Bibliography

[1] J. M. Taylor, P. Cappellaro, L. Childress, L. Jiang, D. Budker, P. R. Hemmer, A. Yacoby, R. Walsworth, and M. D. Lukin, "High-sensitivity diamond magnetometer with nanoscale resolution", Nature Physics **4**, 810 (2008).

[2] M. W. Doherty, N. B. Manson, P. Delaney, F. Jelezko, J. Wrachtrup, and L. C. Hollenberg, "The nitrogen-vacancy colour centre in diamond", Physics Reports **528**, The nitrogen-vacancy colour centre in diamond, 1 (2013).

[3] M. W. Doherty, F. Dolde, H. Fedder, F. Jelezko, J. Wrachtrup, N. B. Manson, and L. C. L. Hollenberg, "Theory of the ground-state spin of the nv^- center in diamond", Phys. Rev. B **85**, 205203 (2012).

[4] V. M. Acosta, A. Jarmola, E. Bauch, and D. Budker, "Optical properties of the nitrogen-vacancy singlet levels in diamond", Phys. Rev. B **82**, 201202 (2010).

[5] N. B. Manson, X.-F. He, and P. T. H. Fisk, "Raman heterodyne detected electron-nuclear-double-resonance measurements of the nitrogen-vacancy center in diamond", Opt. Lett. **15**, 1094 (1990).

[6] N. B. Manson, X.-F. He, and P. T. Fisk, "Raman heterodyne studies of the nitrogen-vacancy centre in diamond", Journal of Luminescence **53**, 49 (1992).

[7] J. Michl, J. Steiner, A. Denisenko, A. Bülau, A. Zimmermann, K. Nakamura, H. Sumiya, S. Onoda, P. Neumann, J. Isoya, and J. Wrachtrup, "Robust and accurate electric field sensing with solid state spin ensembles", Nano Letters **19**, PMID: 31348669, 4904 (2019).

[8] A. Barfuss, M. Kasperczyk, J. Kölbl, and P. Maletinsky, "Spin-stress and spin-strain coupling in diamond-based hybrid spin oscillator systems", Phys. Rev. B **99**, 174102 (2019).

[9] M. C. Marshall, R. Ebadi, C. Hart, M. J. Turner, M. J. Ku, D. F. Phillips, and R. L. Walsworth, "High-precision mapping of diamond crystal strain using quantum interferometry", Phys. Rev. Appl. **17**, 024041 (2022).

[10] K. Arai, J. Lee, C. Belthangady, D. R. Glenn, H. Zhang, and R. L. Walsworth, "Geometric phase magnetometry using a solid-state spin", Nature Communications **9**, 4996 (2018).

[11] L. J. Rogers, M. W. Doherty, M. S. J. Barson, S. Onoda, T. Ohshima, and N. B. Manson, "Singlet levels of the nv centre in diamond", New Journal of Physics **17**, 013048 (2015).

[12] L. Robledo, H. Bernien, T. v. d. Sar, and R. Hanson, "Spin dynamics in the optical cycle of single nitrogen-vacancy centres in diamond", New Journal of Physics **13**, 025013 (2011).

[13] T.-L. Wee, Y.-K. Tzeng, C.-C. Han, H.-C. Chang, W. Fann, J.-H. Hsu, K.-M. Chen, and Y.-C. Yu, "Two-photon excited fluorescence of nitrogen-vacancy centers in proton-irradiated type ib diamond", The Journal of Physical Chemistry A **111**, PMID: 17705460, 9379 (2007).

[14] A. Dréau, M. Lesik, L. Rondin, P. Spinicelli, O. Arcizet, J.-F. Roch, and V. Jacques, "Avoiding power broadening in optically detected magnetic resonance of single nv defects for enhanced dc magnetic field sensitivity", Phys. Rev. B **84**, 195204 (2011).

[15] Z. Yin, J. Tang, C. A. Hart, J. W. Blanchard, X. Xiang, S. Satyajit, S. Bhalerao, T. Tao, S. J. DeVience, and R. L. Walsworth, "Quantum diamond microscope for narrowband magnetic imaging with high spatial and spectral resolution", Phys. Rev. Appl. **22**, 054050 (2024).

[16] C. L. Degen, F. Reinhard, and P. Cappellaro, "Quantum sensing", Rev. Mod. Phys. **89**, 035002 (2017).

[17] J. F. Barry, J. M. Schloss, E. Bauch, M. J. Turner, C. A. Hart, L. M. Pham, and R. L. Walsworth, "Sensitivity optimization for nv-diamond magnetometry", Rev. Mod. Phys. **92**, 015004 (2020).

[18] E. V. Levine, M. J. Turner, P. Kehayias, C. A. Hart, N. Langellier, R. Trubko, D. R. Glenn, R. R. Fu, and R. L. Walsworth, Nanophotonics **8**, 1945 (2019).

[19] N. F. Ramsey, "A molecular beam resonance method with separated oscillating fields", Phys. Rev. **78**, 695 (1950).

[20] E. Bauch, C. A. Hart, J. M. Schloss, M. J. Turner, J. F. Barry, P. Kehayias, S. Singh, and R. L. Walsworth, "Ultralong dephasing times in solid-state spin ensembles via quantum control", Phys. Rev. X **8**, 031025 (2018).

[21] C. A. Hart, J. M. Schloss, M. J. Turner, P. J. Scheidegger, E. Bauch, and R. L. Walsworth, "N-V–diamond magnetic microscopy using a double quantum 4-ramsey protocol", Phys. Rev. Appl. **15**, 044020 (2021).

[22] E. L. Hahn, "Spin echoes", Phys. Rev. **80**, 580 (1950).

[23] E. Bauch, S. Singh, J. Lee, C. A. Hart, J. M. Schloss, M. J. Turner, J. F. Barry, L. M. Pham, N. Bar-Gill, S. F. Yelin, and R. L. Walsworth, "Decoherence of ensembles of nitrogen-vacancy centers in diamond", Phys. Rev. B **102**, 134210 (2020).

[24] Ł. Cywi ński, R. M. Lutchyn, C. P. Nave, and S. Das Sarma, "How to enhance dephasing time in superconducting qubits", Phys. Rev. B **77**, 174509 (2008).

[25] R. de Sousa, **in***Electron spin resonance and related phenomena in low-dimensional structures* **volume** 115, edited by M. Fanciulli, Topics in Applied Physics (Springer, Berlin, Heidelberg, 2009), **pages** 183–220.

[26] G. Wang, Y.-X. Liu, J. M. Schloss, S. T. Alsid, D. A. Braje, and P. Cappellaro, "Sensing of arbitrary-frequency fields using a quantum mixer", Phys. Rev. X **12**, 021061 (2022).

[27] Z. Yin, J. J. Welter, C. A. Hart, P. V. Petruzzi, and R. L. Walsworth, "High-resolution and wide-frequency-range magnetic spectroscopy with solid-state spin ensembles", npj Quantum Information **11**, 190 (2025).

[28] S. T. Alsid, J. M. Schloss, M. H. Steinecker, J. F. Barry, A. C. Maccabe, G. Wang, P. Cappellaro, and D. A. Braje, "Solid-state microwave magnetometer with picotesla-level sensitivity", Phys. Rev. Appl. **19**, 054095 (2023).

[29] Z. Wang, F. Kong, P. Zhao, Z. Huang, P. Yu, Y. Wang, F. Shi, and J. Du, "Picotesla magnetometry of microwave fields with diamond sensors", Sci. Adv **8**, 8158 (2022).

[30] A. Horsley, P. Appel, J. Wolters, J. Achard, A. Tallaire, P. Maletinsky, and P. Treutlein, "Microwave device characterization using a widefield diamond microscope", Phys. Rev. Appl. **10**, 044039 (2018).

[31] B. Naydenov, F. Dolde, L. T. Hall, C. Shin, H. Fedder, L. C. L. Hollenberg, F. Jelezko, and J. Wrachtrup, "Dynamical decoupling of a single-electron spin at room temperature", Phys. Rev. B **83**, 081201 (2011).

[32] K. J. Rietwyk, A. Shaji, I. O. Robertson, A. J. Healey, P. Singh, S. C. Scholten, P. Reineck, D. A. Broadway, and J.-P. Tetienne, "Practical limits to spatial resolution of magnetic imaging with a quantum diamond microscope", AVS Quantum Science **6**, 044402 (2024).

[33] M. J. H. Ku, T. X. Zhou, Q. Li, Y. J. Shin, J. K. Shi, C. Burch, L. E. Anderson, A. T. Pierce, Y. Xie, A. Hamo, U. Vool, H. Zhang, F. Casola, T. Taniguchi, K. Watanabe, M. M. Fogler, P. Kim, A. Yacoby, and R. L. Walsworth, "Imaging viscous flow of the Dirac fluid in graphene", Nature **583**, 537 (2020).

[34] D. Le Sage, K. Arai, D. R. Glenn, S. J. DeVience, L. M. Pham, L. Rahn-Lee, M. D. Lukin, A. Yacoby, A. Komeili, and R. L. Walsworth, "Optical magnetic imaging of living cells", Nature **496**, 486 (2013).

[35] D. R. Glenn, R. R. Fu, P. Kehayias, D. Le Sage, E. A. Lima, B. P. Weiss, and R. L. Walsworth, "Micrometer-scale magnetic imaging of geological samples using a quantum diamond microscope", Geochemistry, Geophysics, Geosystems **18**, 3254 (2017).

[36] M. J. Turner, N. Langellier, R. Bainbridge, D. Walters, S. Meesala, T. M. Babinec, P. Kehayias, A. Yacoby, E. Hu, M. Lon čar, R. L. Walsworth, and E. V. Levine, "Magnetic field fingerprinting of integrated-circuit activity with a quantum diamond microscope", Phys. Rev. Appl. **14**, 014097 (2020).

[37] S. J. DeVience, L. M. Pham, I. Lovchinsky, A. O. Sushkov, N. Bar-Gill, C. Belthangady, F. Casola, M. Corbett, H. Zhang, M. Lukin, H. Park, A. Yacoby, and R. L. Walsworth, "Nanoscale NMR spectroscopy and imaging of multiple nuclear species", Nature Nanotechnology **10**, 129 (2015).

[38] D. R. Glenn, D. B. Bucher, J. Lee, M. D. Lukin, H. Park, and R. L. Walsworth, "High-resolution magnetic resonance spectroscopy using a solid-state spin sensor", Nature **555**, 351 (2018).

[39] J. Tang, Z. Yin, C. A. Hart, J. W. Blanchard, J. T. Oon, S. Bhalerao, J. M. Schloss, M. J. Turner, and R. L. Walsworth, "Quantum diamond microscope for dynamic imaging of magnetic fields", AVS Quantum Science **5**, 044403 (2023).

[40] J. M. Schloss, "Optimizing nitrogen-vacancy diamond magnetic sensors and imagers for broadband sensitivity", Advisors: Ronald L. Walsworth and Isaac L. Chuang, Ph.D. thesis (Massachusetts Institute of Technology, Cambridge, MA, 2019).

[41] H. J. Mamin, M. H. Sherwood, M. Kim, C. T. Rettner, K. Ohno, D. D. Awschalom, and D. Rugar, "Multipulse double-quantum magnetometry with near-surface nitrogen-vacancy centers", Phys. Rev. Lett. **113**, 030803 (2014).

[42] G. De Lange, T. Van Der Sar, M. Blok, Z.-H. Wang, V. Dobrovitski, and R. Hanson, "Controlling the quantum dynamics of a mesoscopic spin bath in diamond", Sci. Rep. **2**, 1 (2012).

[43] A. Cox, M. Newton, and J. Baker, "^{13}C, ^{14}N and ^{15}N endor measurements on the single substitutional nitrogen centre (P1) in diamond", Journal of Physics: Condensed Matter **6**, 551 (1994).

[44] A. M. Edmonds, C. A. Hart, M. J. Turner, P.-O. Colard, J. M. Schloss, K. S. Olsson, R. Trubko, M. L. Markham, A. Rathmill, B. Horne-Smith **andothers**, "Characterisation of CVD diamond with high concentrations of nitrogen for magnetic-field sensing applications", Mater. Quantum Technol. **1**, 025001 (2021).

[45] *Heliotis AG heliCam™ C3 Lock-in Camera*, 2023.

[46] R. R. Fu, B. A. Maher, J. Nie, P. Gao, T. Berndt, E. Folsom, and T. Cavanaugh, "Pinpointing the mechanism of magnetic enhancement in modern soils using high-resolution magnetic field imaging", Geochem. Geophys. Geosyst. **24**, e2022GC010812 (2023).

[47] J. F. Barry, M. J. Turner, J. M. Schloss, D. R. Glenn, Y. Song, M. D. Lukin, H. Park, and R. L. Walsworth, "Optical magnetic detection of single-neuron action potentials using quantum defects in diamond", Proc. Natl. Acad. Sci. U.S.A. **113**, 14133 (2016).

[48] Ł. Cywiński, R. M. Lutchyn, C. P. Nave, and S. D. Sarma, "How to enhance dephasing time in superconducting qubits", Physical Review B **77**, 174509 (2008).

[49] N. R. Reed, D. Bhutto, M. J. Turner, D. M. Daly, S. M. Oliver, J. Tang, K. S. Olsson, N. Langellier, M. J. Ku, M. S. Rosen, and R. L. Walsworth, "Machine learning for improved current-density reconstruction from two-dimensional vector magnetic images", Phys. Rev. Appl. **23**, 034035 (2025).

[50] L. M. Pham, D. L. Sage, P. L. Stanwix, T. K. Yeung, D. Glenn, A. Trifonov, P. Cappellaro, P. R. Hemmer, M. D. Lukin, H. Park, A. Yacoby, and R. L. Walsworth, "Magnetic field imaging with nitrogen-vacancy ensembles", New Journal of Physics **13**, 045021 (2011).

[51] L. M. Pham, N. Bar-Gill, C. Belthangady, D. Le Sage, P. Cappellaro, M. D. Lukin, A. Yacoby, and R. L. Walsworth, "Enhanced solid-state multispin metrology using dynamical decoupling", Phys. Rev. B **86**, 045214 (2012).

[52] N. Arunkumar, K. S. Olsson, J. T. Oon, C. A. Hart, D. B. Bucher, D. R. Glenn, M. D. Lukin, H. Park, D. Ham, and R. L. Walsworth, "Quantum logic enhanced sensing in solid-state spin ensembles", Physical Review Letters **131**, 100801 (2023).

[53] A. M. Edmonds, C. A. Hart, M. J. Turner, P.-O. Colard, J. M. Schloss, K. S. Olsson, R. Trubko, M. L. Markham, A. Rathmill, B. Horne-Smith **andothers**, "Characterisation of CVD diamond with high concentrations of nitrogen for magnetic-field sensing applications", Mater. Quantum Technol. **1**, 025001 (2021).

[54] G. Wang, F. Madonini, B. Li, C. Li, J. Xiang, F. Villa, and P. Cappellaro, "Fast wide-field quantum sensor based on solid-state spins integrated with a spad array", Advanced Quantum Technologies **6**, 2300046 (2023).

[55] D. B. Bucher, D. R. Glenn, H. Park, M. D. Lukin, and R. L. Walsworth, "Hyperpolarization-enhanced nmr spectroscopy with femtomole sensitivity using quantum defects in diamond", Phys. Rev. X **10**, 021053 (2020).

[56] N. Arunkumar, D. B. Bucher, M. J. Turner, P. TomHon, D. Glenn, S. Lehmkuhl, M. D. Lukin, H. Park, M. S. Rosen, T. Theis, and R. L. Walsworth, "Micron-scale nv-nmr spectroscopy with signal amplification by reversible exchange", PRX Quantum **2**, 010305 (2021).

[57] K. D. Briegel, N. R. von Grafenstein, J. C. Draeger, P. Blümler, R. D. Allert, and D. B. Bucher, "Optical widefield nuclear magnetic resonance microscopy", Nature Communications **16**, 1281 (2025).

[58] X.-Y. Zhang, Y.-X. Wang, T. A. Tartaglia, T. Ding, M. J. Gray, K. S. Burch, F. Tafti, and B. B. Zhou, "Ac susceptometry of 2d van der waals magnets enabled by the coherent control of quantum sensors", PRX Quantum **2**, 030352 (2021).

[59] C. Wang, M. Fan, B. Cao, B. Ye, and W. Li, "Novel noncontact eddy current measurement of electrical conductivity", IEEE Sensors Journal **18**, 9352 (2018).

[60] S. M. Oliver, D. J. Martynowych, M. J. Turne, D. A. Hopper, R. L. Walswort, and E. V. Levine, "Vector Magnetic Current Imaging of an 8 nm Process Node Chip and 3D Current Distributions Using the Quantum Diamond Microscope", ISTFA 2021, 96 (2021).

[61] P. Kehayias, J. Walraven, A. L. Rodarte, and A. M. Mounce, "High-resolution short-circuit fault localization in a multilayer integrated circuit using a quantum diamond microscope", Phys. Rev. Appl. **20**, 014036 (2023).

[62] M. Ashok, M. J. Turner, R. L. Walsworth, E. V. Levine, and A. P. Chandrakasan, "Hardware trojan detection using unsupervised deep learning on quantum diamond microscope magnetic field images", J. Emerg. Technol. Comput. Syst. **18**, 1 (2022).

[63] P. Kehayias, E. V. Levine, L. Basso, J. Henshaw, M. Saleh Ziabari, M. Titze, R. Haltli, J. Okoro, D. R. Tibbetts, D. M. Udoni, E. Bielejec, M. P. Lilly, T.-M. Lu, P. D. D. Schwindt, and A. M. Mounce, "Measurement and simulation of the magnetic fields from a 555 timer integrated circuit using a quantum diamond microscope and finite-element analysis", Phys. Rev. Appl. **17**, 014021 (2022).

[64] R. Bounik, F. Cardes, H. Ulusan, M. M. Modena, and A. Hierlemann, "Impedance imaging of cells and tissues: design and applications", BME Frontiers **2022**, 9857485 (2022).

[65] J. M. Schloss, J. F. Barry, M. J. Turner, and R. L. Walsworth, "Simultaneous broadband vector magnetometry using solid-state spins", Phys. Rev. Appl. **10**, 034044 (2018).

[66] H. Zhou, J. Choi, S. Choi, R. Landig, A. M. Douglas, J. Isoya, F. Jelezko, S. Onoda, H. Sumiya, P. Cappellaro, H. S. Knowles, H. Park, and M. D. Lukin, "Quantum metrology with strongly interacting spin systems", Physical Review X **10**, 031003 (2020).

[67] J. Choi, H. Zhou, H. S. Knowles, R. Landig, S. Choi, and M. D. Lukin, "Robust dynamic hamiltonian engineering of many-body spin systems", Physical Review X **10**, 031002 (2020).

[68] L. Viola, E. Knill, and S. Lloyd, "Dynamical decoupling of open quantum systems", Phys. Rev. Lett. **82**, 2417 (1999).

[69] G. Wang, Y.-X. Liu, Y. Zhu, and P. Cappellaro, "Nanoscale vector ac magnetometry with a single nitrogen-vacancy center in diamond", Nano Letters **21**, PMID: 34086471, 5143 (2021).

[70] J. C. Hermann, R. Rizzato, F. Bruckmaier, R. D. Allert, A. Blank, and D. B. Bucher, "Extending radiowave frequency detection range with dressed states of solid-state spin ensembles", npj Quantum Information **10**, 103 (2024).

[71] S. J. Karlson, P. Kehayias, J. M. Schloss, A. C. Maccabe, A. Libson, D. F. Phillips, G. Wang, P. Cappellaro, and D. A. Braje, "Quantum frequency mixing using an N-V diamond microscope", Phys. Rev. Appl. **22**, 064051 (2024).

[72] S. Maas, *Microwave mixers*, Artech House microwave library (Artech House, 1993).

[73] C. P. Slichter, *Principles of magnetic resonance*, **volume** 1 (Springer Science & Business Media, 2013).

[74] J. Meinel, V. Vorobyov, B. Yavkin, D. Dasari, H. Sumiya, S. Onoda, J. Isoya, and J. Wrachtrup, "Heterodyne sensing of microwaves with a quantum sensor", Nature Communications **12**, 2737 (2021).

[75] F. Bloch, W. W. Hansen, and M. Packard, "The nuclear induction experiment", Phys. Rev. **70**, 474 (1946).

[76] E. M. Purcell, N. Bloembergen, and R. V. Pound, "Resonance absorption by nuclear magnetic moments in a single crystal of caF_2", Phys. Rev. **70**, 988 (1946).

[77] R. R. Ernst, G. Bodenhausen, and A. Wokaun, *Principles of nuclear magnetic resonance in one and two dimensions* (Oxford university press, 1990).

[78] P. T. Callaghan, *Principles of nuclear magnetic resonance microscopy* (Clarendon press, 1993).

[79] E. M. Haacke, "Magnetic resonance imaging: physical principles and sequence design", (No Title) (1999).

[80] D. Hoult, and R. Richards, "The signal-to-noise ratio of the nuclear magnetic resonance experiment", Journal of Magnetic Resonance (1969) **24**, 71 (1976).

[81] H. J. Mamin, M. Kim, M. H. Sherwood, C. T. Rettner, K. Ohno, D. D. Awschalom, and D. Rugar, "Nanoscale nuclear magnetic resonance with a nitrogen-vacancy spin sensor", Science **339**, 557 (2013).

[82] T. Staudacher, F. Shi, S. Pezzagna, J. Meijer, J. Du, C. A. Meriles, F. Reinhard, and J. Wrachtrup, "Nuclear magnetic resonance spectroscopy on a (5-nanometer)¡sup¿3¡/sup¿ sample volume", Science **339**, 561 (2013).

[83] I. Lovchinsky, A. O. Sushkov, E. Urbach, N. P. de Leon, S. Choi, K. D. Greve, R. Evans, R. Gertner, E. Bersin, C. Müller, L. McGuinness, F. Jelezko, R. L. Walsworth, H. Park, and M. D. Lukin, "Nuclear magnetic resonance detection and spectroscopy of single proteins using quantum logic", Science **351**, 836 (2016).

[84] K. S. Liu, A. Henning, M. W. Heindl, R. D. Allert, J. D. Bartl, I. D. Sharp, R. Rizzato, and D. B. Bucher, "Surface nmr using quantum sensors in diamond", Proceedings of the National Academy of Sciences **119**, e2111607119 (2022).

[85] F. Bruckmaier, R. D. Allert, N. R. Neuling, P. Amrein, S. Littin, K. D. Briegel, P. Schätzle, P. Knittel, M. Zaitsev, and D. B. Bucher, "Imaging local diffusion in microstructures using nv-based pulsed field gradient nmr", Science Advances **9**, eadh3484 (2023).

[86] R. Rizzato, N. R. von Grafenstein, and D. B. Bucher, "Quantum sensors in diamonds for magnetic resonance spectroscopy: Current applications and future prospects", Applied Physics Letters **123**, 260502 (2023).

[87] S. Ishikawa, T. Yasuda, Y. Iwanaga, and T. Sakai, "Gel–gel phase separation in clustered poly(ethylene glycol) hydrogel with enhanced hydrophobicity", ACS Macro Letters **13**, 1369 (2024).

[88] M. P. Herrling, S. Lackner, H. Nirschl, H. Horn, and G. Guthausen, **in volume** 97, edited by G. A. Webb, Annual Reports on NMR Spectroscopy (Academic Press, 2019), **pages** 163–213.

[89] J. W. Costerton, Z. Lewandowski, D. DeBeer, D. Caldwell, D. Korber, and G. James, "Biofilms, the customized microniche", Journal of bacteriology **176**, 2137 (1994).

[90] A. Mai-Prochnow, F. Evans, D. Dalisay-Saludes, S. Stelzer, S. Egan, S. James, J. S. Webb, and S. Kjelleberg, "Biofilm development and cell death in the marine bacterium pseudoalteromonas tunicata", Applied and Environmental Microbiology **70**, 3232 (2004).

[91] A. A. Gorbushina, "Life on the rocks", Environmental microbiology **9**, 1613 (2007).

[92] L. Hall-Stoodley, and P. Stoodley, "Evolving concepts in biofilm infections", Cellular microbiology **11**, 1034 (2009).

[93] T. R. Neu, B. Manz, F. Volke, J. J. Dynes, A. P. Hitchcock, and J. R. Lawrence, "Advanced imaging techniques for assessment of structure, composition and function in biofilm systems", FEMS microbiology ecology **72**, 1 (2010).

[94] M. P. Herrling, J. Weisbrodt, C. M. Kirkland, N. H. Williamson, S. Lackner, S. L. Codd, J. D. Seymour, G. Guthausen, and H. Horn, "Nmr investigation of water diffusion in different biofilm structures", Biotechnology and bioengineering **114**, 2857 (2017).

[95] F. Ranzinger, M. P. Herrling, S. Lackner, V. W. Grande, A. Baniodeh, A. K. Powell, H. Horn, and G. Guthausen, "Direct surface visualization of biofilms with high spin coordination clusters using magnetic resonance imaging", Acta biomaterialia **31**, 167 (2016).

[96] B. Ramanan, W. M. Holmes, W. T. Sloan, and V. R. Phoenix, "Magnetic resonance imaging of mass transport and structure inside a phototrophic biofilm", Current microbiology **66**, 456 (2013).

[97] S. E. Abed, S. K. Ibnsouda, H. Latrache, and F. Hamadi, "Scanning electron microscopy (sem) and environmental sem: suitable tools for study of adhesion stage and biofilm formation", **in** (2012).

[98] L. Ciobanu, and C. Pennington, "3d micron-scale mri of single biological cells", Solid State Nuclear Magnetic Resonance **25**, 31st Congress Ampere, Magnetic Resonance and Related Phenomena, 138 (2004).

[99] D. Kim, M. I. Ibrahim, C. Foy, M. E. Trusheim, R. Han, and D. R. Englund, "A cmos-integrated quantum sensor based on nitrogen–vacancy centres", Nature Electronics **2**, 284 (2019).

[100] F. M. Stürner, A. Brenneis, T. Buck, J. Kassel, R. Rölver, T. Fuchs, A. Savitsky, D. Suter, J. Grimmel, S. Hengesbach, M. Förtsch, K. Nakamura, H. Sumiya, S. Onoda, J. Isoya, and F. Jelezko, "Integrated and portable magnetometer based on nitrogen-vacancy ensembles in diamond", Advanced Quantum Technologies **4**, 2000111 (2021).

[101] Z. Zhang, R. Xu, Y. Zhang, B. Du, K. Huang, and L. Cheng, "Design of nv centers integrated magnetometer and high-resolution output module based on the odmr system", IEEE Sensors Journal **23**, 6150 (2023).

[102] J. Pogorzelski, L. Horsthemke, J. Homrighausen, D. Stiegekötter, M. Gregor, and P. Glösekötter, "Compact and fully integrated led quantum sensor based on nv centers in diamond", Sensors **24**, 10.3390/s24030743 (2024).

[103] Z. Yin, P. D. Schmalenberg, and E. M. Dede, "Compact quantum camera for wide-field magnetic imaging" (2025), US patent application under review.

[104] R. Albrecht, A. Bommer, C. Deutsch, J. Reichel, and C. Becher, "Coupling of a single nitrogen-vacancy center in diamond to a fiber-based microcavity", Phys. Rev. Lett. **110**, 243602 (2013).

[105] S. Li, H. Zheng, Z. Peng, M. Kamiya, T. Niki, V. Stepanov, A. Jarmola, Y. Shimizu, S. Takahashi, A. Wickenbrock, and D. Budker, "Determination of local defect density in diamond by double electron-electron resonance", Phys. Rev. B **104**, 094307 (2021).

[106] A. Abragam, *The principles of nuclear magnetism* (Oxford University Press, Oxford, 1961).

[107] J. F. Barry, D. A. Braje, E. R. Eisenach, C. M. McNally, M. F. O'Keeffe, and L. M. Pham, "Stationary magic angle spinning enhanced solid state spin sensor", U.S. Patent US10705163B2 (2020).

[108] D. Louzon, G. T. Genov, N. Staudenmaier, F. Frank, J. Lang, M. L. Markham, A. Retzker, and F. Jelezko, "Robust noise suppression and quantum sensing by continuous phased dynamical decoupling", Phys. Rev. Lett. **134**, 120802 (2025).

[109] C. Munuera-Javaloy, A. Tobalina, and J. Casanova, "High-resolution nmr spectroscopy at large fields with nitrogen vacancy centers", Phys. Rev. Lett. **130**, 133603 (2023).

[110] D. Daly, S. J. DeVience, E. Huckestein, J. W. Blanchard, J. Cremer, and R. L. Walsworth, "Nutation-based longitudinal-sensing protocols for high-field nmr with nitrogen-vacancy centers in diamond", Phys. Rev. Appl. **22**, 024043 (2024).